



JAEA-Conf 2020-001

INDC(JPN)-206

DOI:10.11484/jaea-conf-2020-001

**Proceedings of the 2019 Symposium on Nuclear Data  
November 28-30, 2019,  
Kyushu University,  
Chikushi Campus, Fukuoka, Japan**

(Eds.) Yukinobu WATANABE, Nobuhiro SHIGYO, Tadahiro KIN  
and Osamu IWAMOTO

Nuclear Science and Engineering Center  
Sector of Nuclear Science Research

December 2020

Japan Atomic Energy Agency

日本原子力研究開発機構

JAEA-Conf

本レポートは国立研究開発法人日本原子力研究開発機構が不定期に発行する成果報告書です。  
本レポートの入手並びに著作権利用に関するお問い合わせは、下記あてにお問い合わせ下さい。  
なお、本レポートの全文は日本原子力研究開発機構ホームページ (<https://www.jaea.go.jp>)  
より発信されています。

国立研究開発法人日本原子力研究開発機構 研究連携成果展開部 研究成果管理課  
〒319-1195 茨城県那珂郡東海村大字白方2番地4  
電話 029-282-6387, Fax 029-282-5920, E-mail:ird-support@jaea.go.jp

This report is issued irregularly by Japan Atomic Energy Agency.  
Inquiries about availability and/or copyright of this report should be addressed to  
Institutional Repository Section,  
Intellectual Resources Management and R&D Collaboration Department,  
Japan Atomic Energy Agency.  
2-4 Shirakata, Tokai-mura, Naka-gun, Ibaraki-ken 319-1195 Japan  
Tel +81-29-282-6387, Fax +81-29-282-5920, E-mail:ird-support@jaea.go.jp

© Japan Atomic Energy Agency, 2020

JAEA-Conf 2020-001

INDC(JPN)-206

## Proceedings of the 2019 Symposium on Nuclear Data

November 28-30, 2019,

Kyushu University,

Chikushi Campus, Fukuoka, Japan

(Eds.) Yukinobu WATANABE\*, Nobuhiro SHIGYO\*, Tadahiro KIN\*,  
and Osamu IWAMOTO

Nuclear Science and Engineering Center, Sector of Nuclear Science Research,  
Japan Atomic Energy Agency,  
Tokai-mura, Naka-gun, Ibaraki-ken  
(Received August 24, 2020)

The 2019 Symposium on Nuclear Data was held at Chikushi Campus Cooperation Building (C-Cube), Kyushu University, on November 28 to 30, 2019. The symposium was organized by the Nuclear Data Division of the Atomic Energy Society of Japan (AESJ) in cooperation with Sigma Investigative Advisory Committee of AESJ, Nuclear Science and Engineering Center of Japan Atomic Energy Agency, Kyushu Branch of AESJ, and Center for Accelerator and Beam Applied Science of Kyushu University. In the symposium, there were one tutorial, “From the resonance theory to statistical model”, and five sessions, “Study on Nuclear Data and related topics”, “Reactor physics”, “International Cooperation”, “Nuclear Physics”, and “High Energy Nuclear Data and their Application”. In addition, recent research progress on experiments, nuclear theory, evaluation, benchmark and applications was presented in the poster session. Among 85 participants, all presentations and following discussions were very active and fruitful. This report consists of total 42 papers including 13 oral and 29 poster presentations.

Keywords: Nuclear Data Symposium 2019, Experiments, Nuclear Theory, Nuclear Data Evaluation,  
Benchmark Test, Nuclear Data Applications

---

\*Kyushu University

Organizers: Yukinobu Watanabe (Chair, Kyushu Univ.), Hideaki Otsu (Co-chair, RIKEN), Toshiya Sanami (KEK), Tatsuya Katabuchi (Tokyo Tech.), Atsushi Kimura (JAEA), Katsuhisa Nishio (JAEA), Go Chiba (Hokkaido Univ.), Satoshi Kunieda (JAEA), Takanori Kitada (Osaka Univ.), Shin-ichiro Meigo (JAEA), Futoshi Minato (JAEA), Satoshi Chiba (Tokyo Tech.)

## 2019 年度核データ研究会報告集

2019 年 11 月 28 日～30 日

九州大学 筑紫キャンパス 福岡県

日本原子力研究開発機構 原子力科学研究部門 原子力基礎工学研究センター

(編) 渡辺 幸信\*、執行 信寛\*、金 政浩\*、岩本 修

(2020 年 8 月 24 日受理)

2019 年度核データ研究会は、2019 年 11 月 28 日～30 日に、福岡県春日市にある九州大学筑紫キャンパスの総合研究棟(C-Cube)にて開催された。本研究会は、日本原子力学会核データ部会が主催、日本原子力学会「シグマ」調査専門委員会、日本原子力研究開発機構原子力基礎工学研究センター、日本原子力学会九州支部、九州大学加速器・ビーム応用科学センターが共催した。今回、チュートリアルとして「共鳴理論から統計模型へ」を、講演・議論のセッションとして、「核データ研究及び関連トピックス」、「炉物理研究」、「国際協力」、「原子核物理」、「高エネルギー核データと応用」の 5 セッションを企画し実施した。さらに、ポスターセッションでは、実験、理論、評価、ベンチマーク、応用等、幅広い研究内容について発表が行われた。参加者総数は 85 名、それぞれの口頭発表及びポスター発表では活発な質疑応答が行われた。本報告集は、本研究会における口頭発表 13 件、ポスター発表 29 件の論文を掲載している。

キーワード：2019 年度核データ研究会、実験、原子核理論、核データ評価、ベンチマークテスト、核データ応用

---

原子力科学研究所：〒319-1195 茨城県那珂郡東海村大字白方 2-4

\*九州大学

2019 年度核データ研究会実行委員会：

渡辺幸信(委員長、九大)、大津秀暁(副委員長、理研)、佐波俊哉(KEK)、片渕竜也(東工大)、木村敦(原子力機構)、西尾勝久(原子力機構)、千葉豪(北大)、国枝賢(原子力機構)、北田孝典(阪大)、明午伸一郎(原子力機構)、湊太志(原子力機構)、千葉敏(東工大)

## Contents

1.	2019 Symposium on Nuclear Data - Programme	1
<b>Papers Presented at Oral Sessions</b>		
2.	Neutron Capture Cross Section Measurement of Minor Actinides in Fast Neutron Energy Region for Study on Nuclear Transmutation System Tatsuya KATABUCHI (Tokyo tech.) <i>et al.</i>	5
3.	Recent Progress and Future Plan on the JENDL Project Osamu IWAMOTO (JAEA)	11
4.	A Consideration on Nuclear Data Needs for 1F Decommissioning Tokio FUKAHORI (JAEA)	17
5.	Fundamental Physics using Neutron at J-PARC and Accelerator-driven Neutron Source Tamaki YOSHIOKA (Kyushu Univ.)	21
6.	Recent R&D of HTGR and Requirement for Nuclear Data Yuji FUKAYA (JAEA) <i>et al.</i>	27
7.	Performance of a Gas-cooled Reactor as a Tritium Production Device for Fusion Reactors Hideaki MATSUURA (Kyushu Univ.)	33
8.	Research and Development of an Innovative Transmutation System of LLFP by Fast Reactors Satoshi CHIBA (Tokyo tech.)	39
9.	Nuclear Data Activities and Related Database Services at the IAEA Nuclear Data Section Shin OKUMURA (IAEA)	45
10.	Status of the Nuclear Energy Agency Data Bank – Services for Nuclear Data and Computer Programs Kenya SUYAMA (OECD/NEA) <i>et al.</i>	51
11.	From the Resonance Theory to the Statistical Model Toshihiko KAWANO (LANL)	55
12.	Current Status of Search for Element 119 Satoshi SAKAGUCHI (Kyushu Univ.) <i>et al.</i>	61
13.	Application of CDCC to Many-body Breakup Reaction Takuma MATSUMOTO (Kyushu Univ.)	63
14.	Topics from Radiation Safety Design of J-PARC Hiroshi NAKASHIMA (JAEA)	69

**Poster Session**

15. Production Cross Sections of  $^{45}\text{Ti}$  via Deuteron-induced Reaction on  $^{45}\text{Sc}$  ..... 75  
Tsoodol ZOLBADRAL (Hokkaido Univ., National Univ. of Mongolia) *et al.*
16. Production of  $^{169}\text{Yb}$  by the Proton-induced Reaction on  $^{169}\text{Tm}$  ..... 79  
Moemi SAITO (Hokkaido Univ.) *et al.*
17. Measurements of Nuclear Cross Section Data for Proton-induced Reactions on Bi and Pb Targets at Intermediate Energy ..... 83  
Mahdi BAKHTIARI (POSTECH) *et al.*
18. Measurement of Nuclide Production Cross Sections for  $Z = 26-30$  Elements Irradiated with 0.4 - 3.0 GeV Proton in J-PARC ..... 89  
Hiroki MATSUDA (JAEA) *et al.*
19. Study of an Angular Correlation of  $\gamma$ -rays Emitted by  $^{117}\text{Sn}(n,\gamma)$  Reactions for T-violation Search ..... 95  
Jun KOGA (Kyushu Univ.) *et al.*
20. Measurement of the Photon Strength Function in  $^{115}\text{In}$  at the  $\gamma\text{ELBE}$  Facility ..... 101  
Ayano MAKINAGA (Teikyo Univ., JIFS, Hokkaido Univ.) *et al.*
21. Comparison between Experimental and Calculation Neutron Spectra of the  $^{197}\text{Au}(\gamma,\text{sn})$  Reaction for 17 MeV Polarized Photon ..... 107  
Tran Kim TUYET (SOKENDAI, KEK) *et al.*
22. Measurement of Neutron Total Cross-section of  $^{93}\text{Nb}$  at J-PARC MLF ANNRI ..... 113  
Shunsuke ENDO (JAEA) *et al.*
23. High-Energy Measurement of the Neutron Capture Cross Section of  $^{237}\text{Np}$  ..... 119  
Gerard Rovira LEVERONI (Tokyo tech.) *et al.*
24. New Methods to Reduce Systematic Uncertainties of Capture Cross Section Measurement Using a Sample Rotation System ..... 127  
Yu KODAMA (Tokyo tech.) *et al.*
25. Proton Spectra with Low-Energy-Threshold from 40- and 70-MeV Proton-Induced Reactions ..... 131  
Yuji YAMAGUCHI (Kyushu Univ.) *et al.*
26. Charged Particle Emission Reactions Induced by 100-MeV/u  $^{12}\text{C}$  ions ..... 137  
Kazuhito YOSHIDA (Kyushu Univ.) *et al.*
27. Measurement of Neutron Energy Spectra of 345 MeV/u  $^{238}\text{U}$  Incidence on a Copper Target ..... 143  
Kenta SUGIHARA (Kyushu Univ., RIKEN) *et al.*
28. Measurement of the Energy Spectra of Hydrogen Isotopes from Nuclear Muon Capture in  $^{\text{nat}}\text{Si}$  ..... 147  
Seiya MANABE (Kyushu Univ.) *et al.*
29. Detailed Examination of Benchmark Method for Large Angle Scattering Reaction Cross Section at 14MeV for a flake target ..... 153  
Kazuki FUKUI (Osaka Univ.) *et al.*

30. Integration Test with a Gaseous Detector and a Solenoidal Magnet for the Precise Neutron Lifetime Measurement.....	159
Kodai YANO (Kyushu Univ.) <i>et al.</i>	
31. HUNS Upgrade; Simulation of the Beam Profile for a Thermal Neutron Source in HUNS-2.....	165
Kaoru Y. HARA (Hokkaido Univ.) <i>et al.</i>	
32. Preliminary Experiment on Characterization of RANS-II Neutron Production via the ${}^7\text{Li}(p, n){}^7\text{Be}$ Reaction with 2.49 MeV Proton Injection .....	171
Shogo IZUMITANI (Kyushu Univ.) <i>et al.</i>	
33. Development of a Neutron Beam Monitor for Nuclear Data Measurement using Spallation Neutron Source .....	177
Hideto NAKANO (Tokyo tech.) <i>et al.</i>	
34. Model Analysis of Isotope-Production Cross Sections for Proton- and Deuteron-Induced Reactions on ${}^{93}\text{Zr}$ .....	181
Keita NAKANO (Kyushu Univ.) <i>et al.</i>	
35. Systematical Calculation of Probabilities of Beta-delayed Neutron Emission and Fission in the Entire Region of Nuclear Chart.....	187
Hiroyuki KOURA (JAEA) <i>et al.</i>	
36. Development of Multi-group Neutron Activation Cross-section Library from JENDL/AD-2017 .....	193
Chikara KONNO (JAEA)	
37. Quantification of Integral Data Effectiveness using the Concept of Active Sub-Space in Nuclear Data Testing .....	199
Go CHIBA (Hokkaido Univ.) <i>et al.</i>	
38. Uncertainty Estimation of Conventional Neutron-spectrum Unfolding Codes with Monte-Carlo Based Method.....	205
Katsumi AOKI (Kyushu Univ.) <i>et al.</i>	
39. The Influence of B and Li Burnable Poison on Effective Multiplication Factor in the HTGR .....	211
Yuki KOGA (Kyushu Univ.) <i>et al.</i>	
40. Evaluation of Radioactive Concentration Produced in Electric Equipments and Materials on the Decommissioning of Nuclear Power Plants .....	217
Hirokuni YAMANISHI (Kindai Univ.) <i>et al.</i>	
41. Evaluation of Scattered Radiation on the Contralateral Breast in Breast-conserving Therapy .....	221
Rikuto HARA (Teikyo Univ.) <i>et al.</i>	
42. Burnup Calculation with Different Fission Yield Data .....	225
Atsuya ISO (Osaka Univ.) <i>et al.</i>	
43. Improvement of Fuel Ion Ratio Diagnostics Performance using Anisotropic Neutron Emission Spectrum in NBI Heating Deuterium-tritium Plasma .....	231
Tomoki URAKAWA (Kyushu Univ.) <i>et al.</i>	

## 目次

1. 2019 年度核データ研究会プログラム .....	1
<b>口頭発表論文</b>	
2. 長寿命 MA 核種の高速中性子捕獲反応データに関する研究 .....	5
片渕 竜也 (東工大) 他	
3. JENDL プロジェクトの最近の進展と計画 .....	11
岩本 修 (原子力機構)	
4. 1F 廃炉のための核データニーズに関する一考察 .....	17
深堀 智生 (原子力機構)	
5. J-PARC での中性子基礎物理実験と小型中性子源 .....	21
吉岡 瑞樹 (九州大学)	
6. 最近の高温ガス炉の研究開発と核データへの要求 .....	27
深谷 裕司 (原子力機構) 他	
7. 核融合炉用トリチウム製造に対する高温ガス炉の特性 .....	33
松浦 秀明 (九州大学)	
8. 高速炉を活用した LLFP 核変換システムの研究開発 .....	39
千葉 敏 (東工大)	
9. IAEA 核データセクションにおける核データ活動及びデータベースサービス .....	45
奥村 森 (国際原子力機関)	
10. OECD NEA データバンクの現状 - 核データとコンピュータプログラムサービスを中心に ..	51
須山 賢也 (経済協力開発機構/原子力機関) 他	
11. 共鳴理論から統計模型まで .....	55
河野 俊彦 (ロスアラモス国立研究所)	
12. 新 119 番元素合成実験の現状 .....	61
坂口 聡志 (九州大学) 他	
13. CDCC 理論と多体分解反応への応用 .....	63
松本 琢磨 (九州大学)	
14. J-PARC における放射線安全設計からの話題 .....	69
中島 宏 (原子力機構)	

## ポスター発表論文

15. Production cross sections of  $^{45}\text{Ti}$  via deuteron-induced reaction on  $^{45}\text{Sc}$  ..... 75  
Tsoodol ZOLBADRAL (北海道大学 / モンゴル国立大学) 他
16. ツリウム標的への陽子入射反応による  $^{169}\text{Yb}$  生成 ..... 79  
齋藤 萌美 (北海道大学) 他
17. Measurements of nuclear cross section data for proton-induced reactions on Bi and Pb targets at intermediate energy ..... 83  
Mahdi BAKHTIARI (浦項工科大学) 他
18. J-PARC における 0.4 GeV – 3.0 GeV 陽子を用いた  $Z=26-30$  元素に対する核種生成断面積測定 ..... 89  
松田 洋樹 (原子力機構) 他
19. 時間反転対称性の破れ探索に向けた  $^{117}\text{Sn}(n,\gamma)$  反応による  $\gamma$  線角相関に関する研究 ..... 95  
古賀 淳 (九州大学) 他
20.  $\gamma$ ELBE 施設における In-115 の  $\gamma$  線強度関数測定 ..... 101  
牧永 あや乃 (帝京大学 / NPO 法人あいんしゅたいん / 北海道大学) 他
21. Comparison between experimental and calculation neutron spectra of the  $^{197}\text{Au}(\gamma,sn)$  reaction for 17 MeV polarized photon ..... 107  
Tran Kim TUYET (総研大 / 高エネ研) 他
22. J-PARC MLF ANNRI を用いた  $^{93}\text{Nb}$  の中性子全断面積の測定 ..... 113  
遠藤 駿典 (原子力機構) 他
23. High-Energy Measurement of the Neutron Capture Cross Section of  $^{237}\text{Np}$  ..... 119  
Gerard Rovira LEVERONI (東工大) 他
24. 試料回転法を用いた中性子捕獲断面積の高精度化のための新たな手法 ..... 127  
児玉 有 (東工大) 他
25. 40 MeV 及び 70 MeV 陽子入射反応における低エネルギー下限陽子スペクトル ..... 131  
山口 雄司 (九州大学) 他
26. 100MeV/u  $^{12}\text{C}$  ビーム入射荷電粒子生成反応の研究 ..... 137  
吉田 和人 (九州大学) 他
27. 銅標的に対する 345 MeV/u ウラン入射により生成する中性子エネルギースペクトルの測定 ..... 143  
杉原 健太 (九州大学 / 理研) 他
28. Si に対する負ミューオン原子核捕獲反応からの放出水素イオンエネルギースペクトル測定 ..... 147  
真鍋 征也 (九州大学) 他
29. フレック状ターゲットの 14MeV での後方散乱反応断面積のベンチマーク実験法の詳細検討 ..... 153  
福井 和輝 (大阪大学) 他
30. 中性子の精密寿命測定のためのガス検出器とソレノイド磁石の総合試験 ..... 159  
矢野 浩大 (九州大学) 他

31. HUNS アップグレード ; HUNS-2 熱中性子源のためのビームプロファイルのシミュレーション .....	165
原  かつお (北海道大学) 他	
32. 2.49 MeV 陽子入射による ${}^7\text{Li}(p, n){}^7\text{Be}$ 反応を用いた RANS-II の中性子生成特性に関する予備実験 .....	171
泉谷  祥伍 (九州大学) 他	
33. 核破砕中性子源を利用した核データ測定のための中性子ビームモニターの開発 ..... 177	177
中野  秀仁 (東工大) 他	
34. ${}^{93}\text{Zr}$ に対する陽子・重陽子入射反応における同位体生成断面積の理論モデル解析 ..... 181	181
中野  敬太 (九州大学) 他	
35. $\beta$ 崩壊遅発中性子放出および $\beta$ 崩壊遅延核分裂の核図表全体における系統的な計算 ..... 187	187
小浦  寛之 (原子力機構) 他	
36. JENDL/AD-2017 の多群中性子放射化断面積ライブラリ開発 ..... 193	193
今野  力 (原子力機構)	
37. 核データ検証における有効部分空間法による積分データの有効性の定量化 ..... 199	199
千葉  豪 (北海道大学) 他	
38. アンフォールディングコードにおけるモンテカルロ手法を用いた中性子スペクトルの不確かさ推定 .....	205
青木  勝海 (九州大学) 他	
39. 高温ガス炉におけるホウ素可燃性毒物と T 製造用 Li ロッドの実効増倍率経時変化に及ぼす影響 .....	211
古賀  友稀 (九州大学) 他	
40. 原子力発電所廃止措置における電機品の放射性物質濃度の評価 ..... 217	217
山西  弘城 (九州大学) 他	
41. 乳房温存療法における対側乳房に影響する散乱線量の評価 ..... 221	221
原  陸人 (九州大学) 他	
42. 異なる核分裂収率データを用いた燃焼計算 ..... 225	225
磯  敦也 (大阪大学) 他	
43. NBI 加熱 DT プラズマにおける、中性子の非等方放出スペクトルを用いた燃料イオン比診断の測 定性能改善 ..... 231	231
浦川  知己 (九州大学) 他	

# 1 2019 Symposium on Nuclear Data - Programme

Chikushi Hall, Chikushi Campus, Kyushu University, Nov 28–29, 2019.

## Thursday, November 28

### Opening Address (13:00–13:10)

Prof. Yukinobu Watanabe (Kyushu University)

### Study on Nuclear Data (13:10–15:10)

Chair: Prof. Yukinobu Watanabe

#### 13:10 Neutron Capture Cross Section Measurement of Minor Actinides in Fast Neutron Energy Region for Study on Nuclear Transmutation System

Prof. Tatsuya Katabuchi (Tokyo Institute of Technology)

#### 13:40 Recent progress and future plan on the JENDL project

Dr. Osamu Iwamoto (Japan Atomic Energy Agency)

#### 14:10 A Consideration on Nuclear Data Needs for 1F Decommissioning

Dr. Tokio Fukahori (Japan Atomic Energy Agency)

#### 14:40 Fundamental physics using neutron at J-PARC and accelerator-driven compact neutron source

Dr. Tamaki Yoshioka (Kyushu University)

### Coffee Break (15:10–15:30)

*Group photos will be taken at the entrance of the C-Cube building.*

### Poster Session - Gallery, C-Cube 3<sup>rd</sup> Floor (15:30–17:00)

### Social Gathering - Restaurant Sonne (17:15–19:15)

---

## Friday, November 29

### Reactor Physics (9:30–11:00)

Chair: Prof. Go Chiba (Hokkaido University)

#### 9:30 Recent R&D of HTGR and Requirement for Nuclear Data

Dr. Yuji Fukaya (Japan Atomic Energy Agency)

#### 10:00 Performance of a gas-cooled reactor as a tritium production device for fusion reactors

Dr. Hideaki Matsuura (Kyushu University)

#### 10:30 Research and development of an innovative transmutation system of LLFP by fast reactors

Prof. Satoshi Chiba (Tokyo Institute of Technology)

### **International Cooperation (11:10–12:10)**

Chair: Dr. Tokio Fukahori (Japan Atomic Energy Agency)

#### **11:10 Nuclear Data Activities and Related Database Services at the IAEA Nuclear Data Section**

Dr. Shin Okumura (International Atomic Energy Agency)

#### **11:40 Status of the OECD NEA Data Bank – Services for Nuclear Data and Computer Program**

Dr. Kenya Suyama (OECD NEA Data Bank)

### **Tutorial (13:20–14:30)**

Chair: Dr. Osamu Iwamoto (Japan Atomic Energy Agency)

#### **13:20 From the resonance theory to the statistical model**

Dr. Toshihiko Kawano (Los Alamos National Laboratory)

### **Nuclear Physics (14:45–16:00)**

Chair: Dr. Hideaki Otsu (RIKEN Nishina Center)

#### **14:45 Current status of search for new element 119**

Prof. Satoshi Sakaguchi (Kyushu University)

#### **15:15 Application of CDCC to many-body breakup reaction**

Dr. Takuma Matsumoto (Kyushu University)

### **High Energy Nuclear Data and Application (16:10–17:40)**

Chair: Dr. Nobuhiro Shigyo (Kyushu University)

#### **16:10 Topics from Radiation Safety Design of J-PARC**

Dr. Hiroshi Nakashima (Japan Atomic Energy Agency)

#### **16:40 Present Status and Outlook of IFMIF and A-FNS**

Dr. Atsushi Kasugai (National Institutes for Quantum and Radiological  
Science and Technology)

#### **17:10 Construction status and future plan for RAON and its nuclear data production system**

Prof. Moses Chung (Ulsan National Institute of Science and Technology)

### **Poster Award and Closing Address (17:40–18:00)**

Prof. Yukinobu Watanabe (Kyushu University), Dr. Hideaki Otsu (RIKEN Nishina  
Center)

---

## **Saturday, November 30**

### **Accelerator Facility Tour (10:00–11:10)**

Dr. Nobuhiro Shigyo (Kyushu University)

## 2019 Symposium on Nuclear Data - Poster List

#	Name	Title
1	TSOODOL, Zoldabrai (Hokkaido U)	Production cross sections of $^{45}\text{Ti}$ via deuteron-induced reaction on $^{45}\text{Sc}$
2	SAITO, Moemi (Hokkaido U)	Production of $^{169}\text{Yb}$ by the proton-induced reaction on $^{169}\text{Tm}$
3	HWANG, Jongwon (CNS, U Tokyo)	Proton-induced reactions of $^{93}\text{Zr}$ using the OEDO beamline
4	BAKHTIARI, Mahdi (POSTECH)	Measurements of nuclear cross section data for proton-induced reactions on Bi and Pb targets at intermediate energy
5	MATSUDA, Hiroki (J-PARC/JAEA)	Measurement of nuclide production cross sections for $Z = 26-30$ elements irradiated with 0.4 - 3.0 GeV proton in J-PARC
6	KOGA, Jun (Kyushu U)	Study of an angular correlation of $\gamma$ -rays emitted by $^{117}\text{Sn}(n,\gamma)$ reactions for T-violation search
7	MAKISE, So (Kyushu U)	Measurement of $\gamma$ ray angular distribution to come from 4.53 eV p-wave resonance of $^{111}\text{Cd}$ in compound nuclear reaction
8	MAKINAGA, Ayano (Teikyo U)	Measurement of photon strength function in In-115 at gELBE facility
9	TRAN, Kim Tuyet (SOKENDAI)	Comparison between experimental and calculation neutron spectra of the $^{197}\text{Au}(\gamma,n)$ reaction for 17 MeV polarized photon
10	ENDO, Shunsuke (JAEA)	Measurement of total neutron cross section of Niobium at J-PARC MLF ANNRI
11	ROVIRA LEVERONI, Gerard (Tokyo Tech)	High-Energy Measurement of the Neutron Capture Cross Section of $^{237}\text{Np}$
12	KODAMA, Yu (Tokyo Tech)	New Methods to Reduce Systematic Uncertainties of Capture Cross Section Measurement Using a Sample Rotation System
13	YAMAGUCHI, Yuji (Kyushu U)	Proton Spectra with Low-Energy-Threshold from 40- and 70-MeV Proton-Induced Reactions
14	YOSHIDA, Kazuhito (Kyushu U)	Charged particle emission reactions induced by 100-MeV/u $^{12}\text{C}$ ions
15	MOON, Dalho (Sunkyunkwan U)	Neutron Production Double-differential cross section from Carbon and Niobium targets bombarded with 290 MeV/u $^{136}\text{Xe}$ ions
16	SUGIHARA, Kenta (Kyushu U/RIKEN)	Measurement of Neutron Energy Spectra of 345 MeV/u $^{238}\text{U}$ Incidence on a Cu Target
17	MANABE, Seiya (Kyushu U)	Measurement of the energy spectra of hydrogen isotopes from nuclear muon capture in $^{\text{nat}}\text{Si}$
18	FUKUI, Kazuki (Osaka U)	Detailed examination of benchmark experimental method for large angle scattering reaction cross section at 14MeV for a flake target
19	YANO, Kodai (Kyushu U)	Integration test with a Gaseous Detector and a Solenoidal Magnet for the Precise Neutron Lifetime Measurement

#	Name	Title
20	HARA, Kaoru (Hokkaido U)	HUNS upgrade; Simulation of the beam profile for a thermal neutron source in HUNS-2
21	IZUMITANI, Shogo (Kyushu U)	Preliminary experiment on characterization of RANS-II neutron production via the ${}^7\text{Li}(p, n){}^7\text{Be}$ reaction with 2.49 MeV proton injection
22	NAKANO, Hideto (Tokyo Tech)	Development of a neutron beam monitor for nuclear data measurement using spallation neutron source
23	NAKANO, Keita (Kyushu U)	Model analysis of isotope-production cross sections for proton- and deuteron-induced reactions on Zr-93
24	FUJIO, Kazuki (Tokyo Tech)	Dependence of the potential energy surface of U-236 system on effective nucleon-nucleon interactions
25	ZHANG, Xuan (Tokyo Tech)	Fission study using four-dimensional Langevin model - Nuclear shape of fission fragments
26	KOURA, Hiroyuki (JAEA)	Systematical calculation of probabilities of beta-delayed neutron emission and fission in the entire region of nuclear chart
27	INAKURA, Tsunenori (Tokyo Tech)	Estimation of covariance of the neutron cross section of the long-lived fission product
28	AMITANI, Tatsuki (Tokyo Tech)	Estimation of Covariance of Neutron Cross Sections for Decommissioning
29	KONNO, Chikara (JAEA)	Development of multi-group neutron activation cross-section library from JENDL/AD-2017
30	CHIBA, Go (Hokkaido U)	Quantification of Integral Data Effectiveness Using the Concept of Active Sub-Space in Nuclear Data Testing
31	AOKI, Katsumi (Kyushu U)	Uncertainty estimation of conventional neutron-spectrum unfolding codes with Monte Carlo based method
32	KOGA, Yuki (Kyushu U)	The Influence of B Burnable poison and T Production Li rod on Effective Multiplication Factor in the HTGR
33	YAMANISHI, Hirokuni (Kindai U)	Evaluation of radioactive concentration produced in electric equipments and materials on the decommissioning of nuclear power plants
34	HARA, Rikuto (Teikyo U)	Evaluation of scattered radiation on the contralateral breast in breast-conserving therapy
35	ISO, Atsuya (Osaka U)	Burnup calculation with different fission yield data
36	URAKAWA, Tomoki (Kyushu U)	Improvement of fuel ion ratio diagnostics performance using anisotropic neutron emission spectrum in NBI heating deuterium-tritium plasma

## 2 Neutron Capture Cross Section Measurement of Minor Actinides in Fast Neutron Energy Region for Study on Nuclear Transmutation System

Tatsuya KATABUCHI<sup>1)\*</sup>, Jun-ich HORI<sup>2)</sup>, Nobuyuki IWAMOTO<sup>3)</sup>, Osamu IWAMOTO<sup>3)</sup>, Atsushi KIMURA<sup>3)</sup>, Shoji NAKAMURA<sup>3)</sup>, Yuji SHIBAHARA<sup>2)</sup>, Kazushi TERADA<sup>1)</sup>, Kenichi TOSAKA<sup>1)</sup>, Shunsuke ENDO<sup>3)</sup>, Gerard ROVIRA<sup>1)</sup>, Yu KODAMA<sup>1)</sup>, Hideto NAKANO<sup>1)</sup>

1) Tokyo Institute of Technology,

2) Kyoto University

3) Japan Atomic Energy Agency

\*E-mail: buchi@lane.iir.titech.ac.jp

A research project entitled “*Study on accuracy improvement of fast-neutron capture reaction data of long-lived MAs for development of nuclear transmutation systems*” started in 2017 as a four-year project. The purpose of the project is to improve the neutron capture cross sections of minor actinides in the fast neutron energy region that is particularly important for study on a nuclear transmutation system. The outline of the project and the current progress are reported.

### 1. Introduction

Disposal of high-level nuclear waste from nuclear power plants has been a long-standing issue in the nuclear industries. Nuclear waste contains long-lived minor actinides (MAs), some of which keep their radiotoxicities for more than thousand years. Currently planned geological disposal of high-level nuclear waste has been in deadlock due to the difficulty of public acceptance for many years. In order to solve this issue, nuclear transmutation, by which long-lived MAs are converted to stable or shorter-lived nuclides via neutron-induced reactions, has been investigated. In recent years, accelerator-driven systems (ADS) are considered as feasible candidates of MA burners and several ADS projects are ongoing or planned. Detailed core design of an ADS requires accurate, reliable nuclear reaction data of MAs but the uncertainties of the current cross section data in evaluated nuclear data libraries in the fast neutron energy region that is most relevant for ADS are not small enough to satisfy the requirement [1,2].

A research project entitled “*Study on accuracy improvement of fast-neutron capture reaction data of long-lived MAs for development of nuclear transmutation systems*” started in 2017. The project aims at improving the accuracies of neutron capture cross sections of MAs ( $^{237}\text{Np}$ ,  $^{241}\text{Am}$ ,  $^{243}\text{Am}$ ) in the fast neutron energy region. The target uncertainty of cross section measurement in this project is 5%. To improve the capture reaction data of MAs, an intense pulsed neutron beam from a spallation neutron source of the Japan Proton Accelerator Research Complex (J-PARC) is utilized in time-of-flight (TOF) experiments to measure capture cross sections. In previous research projects, we worked on building and commissioning the Accurate Neutron Nucleus Reaction Measurement Instrument (ANNRI), a neutron beam line for nuclear data measurement in the Materials and Life Science Experimental Facility (MLF) of J-PARC [3]. ANNRI now becomes one of the leading neutron beam lines for nuclear data measurement in the world.

One of the major reasons that previous measurements of MA capture cross sections were not able to achieve high accuracies is that MA samples were radioactive. A radioactive sample emits decay  $\gamma$ -rays that become background for the detection of neutron capture  $\gamma$ -rays. The large decay  $\gamma$ -ray background hinders accurate capture  $\gamma$ -ray measurement. The J-PARC high-intensity pulsed neutron beam solves the issue by increasing neutron capture reaction rates in a sample. The rate of capture events to background events can be improved, consequently achieving small uncertainties of cross sections.

This project consists of four tasks: (1) development of a neutron beam filter system to solve the so-called double bunch issue of a neutron beam in J-PARC, (2) neutron capture cross section measurement, (3) sample characteristic assay, and (4) theoretical reaction model study. The following sections describe details of the tasks.

## 2. Neutron Beam Filter System

The neutron beam filter is designed to solve the double bunch issue of a neutron beam from the J-PARC spallation neutron source. The spallation neutron source is operated at a repetition rate of 25 Hz. Hence, neutrons are generated every 40 ms. The J-PARC accelerator adopts a special operational pattern called double bunch operation, in which two proton beam pulses with a separation time of 0.6  $\mu\text{s}$  are injected into the spallation neutron target for each neutron burst cycle. The purpose of this operation is to increase the thermal neutron intensity, important for most of measurements with the neutron beam lines in MLF. In the thermal neutron TOF range, the time structure of the incident proton beam is negligible. The Doppler broadening effect and moderation time in a moderator erase the proton beam time structure in the thermal neutron TOF region over 12 ms. On the other hand, this double bunch mode is very problematic for measurements in the high energy region above 100 eV, where the double bunch structure appears in TOF spectra. Neutrons having two different energies originating

from two incident proton pulses overlap at the same TOF channel in measurement. The capture yield at each TOF channel is contributed by two different neutron energies and the results cannot be deconvoluted easily.

A neutron beam filter system solves this issue. The neutron beam filter method is often used in nuclear reactor experiments [4,5]. A reactor neutron beam which has a continuous energy distribution can be tailored to be mono or quasi-mono energetic through filter materials that have sharp resonance dips of total cross section at certain resonance energies. In this project, the neutron filter technique is combined with the TOF technique to separate out coexisting different energy neutrons at the same TOF. The neutron beam filter system is under development. Filter materials Fe, Bi, Al, Si, Cr and Sc were chosen and tested in 2018. Based on the test results, the system was designed and installed in the ANNRI beam line of J-PARC MLF. A measured neutron energy spectrum filtered with Fe is shown in Fig. 1. A neutron spectrum with no filter is also shown for comparison. As seen in Fig. 1, a prominent peak is clearly observed at an energy of 24 keV.

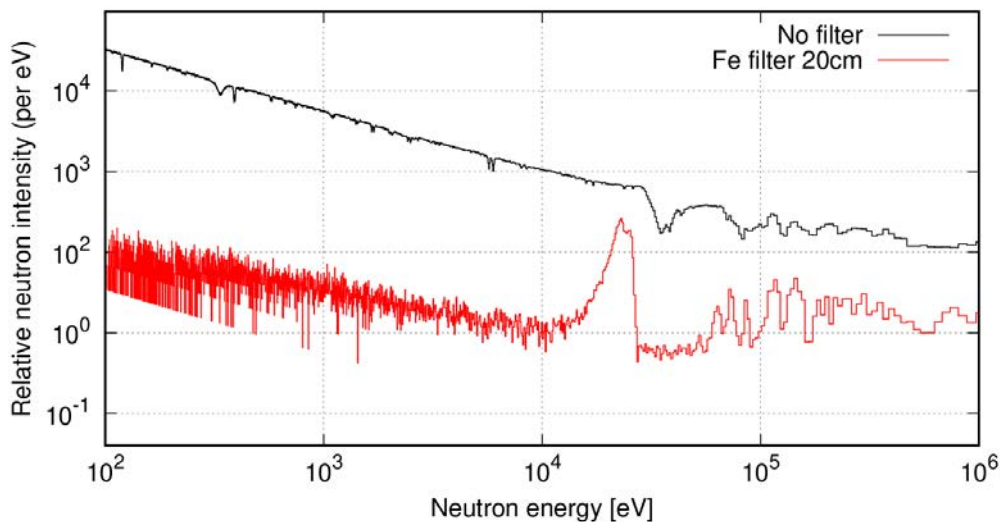


Fig. 1 Neutron energy spectrum filtered with Fe (red). A neutron spectrum with no filter (black) is shown for comparison.

### 3. Neutron Capture Cross Section Measurement

This project focuses on fast-neutron capture cross section data of MA. This requires a fast detection and data acquisition systems. Fast neutron events appear in fast TOF region close to the gamma flash, an intense  $\gamma$ -ray emission produced at the moment that the incident proton beam pulse reaches the spallation neutron target. The gamma flash overwhelms the detection system and detection signals are distorted for  $\mu$ s (sometimes ms) after the gamma flash. To detect neutron capture events in the fast TOF region, the system needs to recover quickly from the distortion caused by the gamma flash. In addition to the gamma-flash, an

intense neutron beam from the J-PARC spallation neutron source increase the detector counting rate, leading to large count loss due to the system dead time.

We plan to measure the neutron capture cross sections of MAs using NaI(Tl) detectors of ANNRI. NaI(Tl) detectors are suitable for the measurement in fast TOF region [6]. Scintillation detectors have faster response than semiconductor detectors, and what's more, an NaI(Tl) detector can measure a  $\gamma$ -ray spectrum. The pulse height weighting technique to derive neutron capture cross sections is well established for a NaI(Tl) detector [7].

In addition, we developed a new method to determine the absolute neutron capture yields using a sample rotation system. The effective sample thickness can be changed by tilting the sample with respect to the beam axis. The self-shielding factor changes with the effective sample thickness. The absolute neutron capture yield is determined from the self-shielding factor that is calculated from change of capture yield by tilting the sample.

#### 4. Sample Characteristic Assay

Sample characteristic assay is an important task to improve the accuracy of cross sections. Uncertainties of sample characteristics such as total mass, isotope composition and impurities can be crucial systematic uncertainties. In this project, we plan to analyze the isotope composition and impurities of MA samples by thermal ionization mass spectrometry (TIMS) at the Institute of Integrated Radiation and Nuclear Science of Kyoto University. The target accuracy of analysis is set at less than 1% in this project. The key to achieving such a high accuracy is the stability of ion emission from a filament of the TIMS ion source. To stabilize the ion emission, the monitoring method of the filament temperature, most dominant factor for ion emission, was improved in 2018. A test experiment showed significant improvement of ion emission control. TIMS analysis of MA samples is planned to conduct in 2020.

#### 5. Theoretical Reaction Model Study

Theoretical nuclear reaction models can predict neutron capture cross sections. Combined with experimental data, theoretical reaction models become powerful tools in nuclear data evaluation. In this project, neutron capture  $\gamma$ -ray spectra measured with the ANNRI-NaI(Tl) detectors are used to refine theoretical model prediction. Capture  $\gamma$ -ray spectra give more information on reaction mechanisms than only from capture cross section. Comparing theoretical calculations with the measured  $\gamma$ -ray spectra, model parameters such as gamma-ray strength function and level density can be determined. However, direct output spectra from experiments cannot be compared with theoretical capture  $\gamma$ -ray spectra because measured spectra convolute detector response. Unfolding measured spectra with detector response function is often performed to compare with theoretical spectra [7] but the unfolding

process adds uncertainties to experimental data. Instead, we adopted the reverse process for comparison. We fold theoretical spectra with detector response and then compare them to experimental data. Folding process is less ambiguous than unfolding process. We built a geometrical model of the ANNRI-NaI(Tl) detectors for the Monte Carlo simulation code PHITS [8] and calculated the detector response matrix. For a benchmark calculation, the capture  $\gamma$ -ray spectrum of  $^{197}\text{Au}$  was calculated with the theoretical reaction model code CCONE [9] and then folded the calculated spectrum with the detector response matrix

## 6. Summary and Future Prospect

The project entitled “*Study on accuracy improvement of fast-neutron capture reaction data of long-lived MAs for development of nuclear transmutation systems*” started in 2017 as a four-year project. The first two years were spent for development of the neutron beam filter system, fast data acquisition method for the ANNRI-NaI(Tl) detectors and MA sample characteristic assay. The neutron filter system and the sample rotation system were installed in ANNRI. Now the project is in the actual experimental phase to measure the capture cross sections and capture  $\gamma$ -ray spectra of MAs.

## Acknowledgements

This work is supported by the Innovative Nuclear Research and Development Program from the Ministry of Education, Culture, Sports, Science and Technology of Japan. The neutron experiment at the MLF of the J-PARC was performed under the user program (Proposal No. 2018A0213 and 2018B0011).

## References

- [1] M. Salvatores *et al.*, OECD/NEA Report No.6410 (2008).
- [2] H. Iwamoto *et al.*, J. Nucl. Sci. Technol., **50**, 856 (2013).
- [3] K. Kino *et al.*, Nucl. Instr. Meth. A, **736**, 66 (2014).
- [4] O. D. Simpson and L. G. Miller, Nucl. Instr. Meth, **61**, 245 (1968).
- [5] A. T. Tran *et al.*, Ann. Nucl. En., **113**, 420 (2018).
- [6] T. Katabuchi *et al.*, Nucl. Instr. Meth. A, **764**, 369 (2014).
- [7] S. Mizuno *et al.*, J. Nucl. Sci Technol., **36**, 493 (1999).
- [8] T. Sato *et al.*, J. Nucl. Sci Technol., **55**, 684 (2018).
- [9] O. Iwamoto *et al.*, Nucl. Data Sheets, **131**, 259 (2016).

This is a blank page.

### 3 Recent progress and future plan on the JENDL project

Osamu IWAMOTO

Nuclear Data Center, Japan Atomic Energy Agency

Tokai-mura, Naka-gun, Ibaraki-ken 319-1195 Japan

e-mail: iwamoto.osamu@jaea.go.jp

The JENDL project has been developing evaluated nuclear data libraries to meet the needs of nuclear science and engineering. JENDL provides general and special purpose files generally for nuclear reactor applications and topically for other applications that cannot be covered by the general purpose file, respectively. Owing to the broadened needs of the nuclear data, many special purpose files have been released since 2010 in which JENDL-4.0 was released. Concerning the general purpose file, development of the next version JENDL-5 is in progress. In addition to the revision of the data ranging from light to heavy nuclei, the new evaluation for whole stable isotopes lacked in JENDL-4.0 are being undertaken to meet the needs for various applications. The test libraries of JENDL-5 are produced to get feedbacks from integral experimental data. The recent progress of JENDL is summarized in this report.

#### 1. Introduction

The latest version of JENDL general purpose file, *i.e.* JENDL-4.0, was released in 2010 [1]. It was developed intending to improve the data of fission products and minor actinides that would be important for research and development of light water reactors with high burn-up and MOX fuels as well as of innovative reactors such as accelerator driven system. Since then, many special purpose files have been released: JENDL FP Decay Data File 2011 (JENDL/FPD-2011), JENDL FP Fission Yields Data File 2011 (JENDL/FPY-2011), JENDL-4.0 High Energy File (JENDL-4.0/HE), JENDL Decay Data File 2015 (JENDL/DDF-2015), JENDL Photonuclear Data File 2016 (JENDL/PD-2016), JENDL Activation Cross Section File for Nuclear Decommissioning 2017 (JENDL/AD-2017), JENDL LLFP Transmutation Cross Section File 2018 (JENDL/ImPACT-2018) [2]. These files were developed to meet needs from expanding fields of applications such as backends of nuclear energy and accelerator utilizations.

As well as the special purpose files, development of the next version of general-purpose file JENDL-5 is in progress. JENDL-5 is aiming at increasing completeness and reliability from JENDL-4.0 in viewpoints of target nuclide species and data uncertainties. The data will be evaluated with reflecting current knowledge of cross section measurements, nuclear theory and integral benchmark tests. A new R-matrix theory code AMUR has been developed and applied to the resonance analysis for light nuclides [3]. Structural materials and medium-heavy nuclides have been evaluated using the modern nuclear reaction model code CCONE [4,5]. The first test library JENDL-5 $\alpha$ 1 was created last year and its integral benchmark tests were

performed. The next version of the test file JENDL-5 $\alpha$ 2 is being prepared. JENDL-5 is planned to be released in FY 2021.

## 2. Special purpose file

### 2.1 JENDL/PD-2016

Photonuclear data are important for shielding design of electron accelerator as well as gamma-ray therapy. Since the number of nuclei in the previous version of photonuclear data library JENDL/PD-2004 [6] was limited to 68, the new version JENDL/PD-2016 [7] was developed with increasing the number of target nuclides applying the current theoretical models and available experimental data. JENDL/PD-2016 provides 2681 nuclides in total from  $Z=1$  to 93 covering unstable isotopes in the expanded version, and the standard version with the data for 181 nuclides along the beta-stability line is also prepared for convenience. The secondary particle productions with energy-angle distributions have been evaluated for nucleons and light ions. The data of production cross sections of residual nuclides are also stored. The incident photon energy ranges from 1 to 140 MeV.

In connection with the Coordinated Research Project about update of photonuclear data library of IAEA, new evaluations of photonuclear data have been performed using newly measured data. Updating the data of JENDL/PD-2016 with these new evaluations, the revised version JENDL/PD-2016.1 was released in February 2020 [2].

### 2.2 JENDL/AD-2017

For decommissioning of nuclear installations that is expected to increase remarkably in near future, reliable evaluation of activation inventories of the facilities is essential to implement reasonable plan according to levels of the activities. The activation cross sections of the constituent materials are needed for this evaluation. However, more than 20 years have already passed since JENDL released the previous version of the activation file JENDL/A-96 [8] in 1996. We started development of a new activation cross section library focusing on the decommissioning of light water reactors with the framework of the joint research with Japan Atomic Power Company in 2011. The 221 radioactive isotopes were selected in terms of importance for dose and clearance evaluations having half-lives longer than 30 days. The cross sections for 311 nuclides which would produce those isotopes were compiled into the ENDF-6 format and was released as JENDL/AD-2017 [9]. While some data were updated based on the latest version of general-purpose file JENDL-4.0 and supplemented with JEFF-3.1/A, a large part of the data were newly evaluated with the available measurements and the current theoretical model. The library provides the point-wise cross sections at 0 K and 293.6 K for energy range from  $10^{-5}$  eV to 20 MeV for production of radioactive nuclei including isomers.

### 2.3 JENDL/ImPACT-2018

Fission product nuclear data library JENDL/ImPACT-2018 [10] was developed under the program “Reduction and Resource Recycling of High-level Radioactive Wastes through Nuclear Transmutation”

funded by the ImPACT Program of the Council for Science, Technology and Innovation (Cabinet Office, Government of Japan). This ImPACT program aimed at producing innovations on issues of high-level radioactive wastes by reducing and recycling long-lived fission products by transmutation using accelerators. In addition to the data for LLFPs of  $^{79}\text{Se}$ ,  $^{93}\text{Zr}$ ,  $^{107}\text{Pd}$  and  $^{135}\text{Cs}$ , JENDL/ImPACT-2018 covers the data for secondary products that would be produced via transmutation of LLFP using reactions in hundreds MeV region. The library provides the data of energy-angle distributions for nucleon and light particle emissions as well as cross sections of residual nuclei productions up to 200 MeV. The data was evaluated using the comprehensive nuclear reaction evaluation code CCONE with enhancing prediction accuracies for residual nuclide productions of proton induced reactions around a few hundred MeV that were measured by inverse kinematics at RIKEN under the same program [11, 12].

### 3. General purpose file

The next version of general purpose file JENDL-5 is under development. The data in wide range of nuclides from light to heavy nuclides have been being evaluated.

Regarding light nuclides, the neutron resonance data of  $^{16}\text{O}$ ,  $^{15}\text{N}$  and  $^{19}\text{F}$  were analyzed using the newly developed R-matrix code system AMUR. Taking account of the data for inverse channels creating the same compound nucleus, the reliability of the data has been increased. From the resonance analysis, the resonance cross sections as well as their covariances were deduced. JENDL-4.0 contains old data for structural materials that were evaluated in 1980's in spite of several revisions from the first evaluation. The CCONE code has been used to update those data taking account of available experimental data of isotopes of Mn, Cu, Zr and Nb [13-15].

Increase of reliability of the data for fission products and minor actinides is still important because of their large uncertainties in evaluated data and needs of managements of those nuclear wastes. Due to the large number of nuclides in the fission products, a part of them were not yet revised in the release of JENDL-4.0 in spite of making much efforts on the revision of them. Remaining nuclides of fission products of Ga, Tc, Sb, Te, I and Er isotopes have been evaluated for JENDL-5 [16-19]. Concerning minor actinides, intensive works to improve accuracy of nuclear data especially on  $^{241,243}\text{Am}$  were conducted under the AIMAC project [20]. The accurate data taken by ANNRI at J-PARC under this project have been used to revise the resonance parameters of Am isotopes.

New experimental data recently becomes available not only for Am but also for other actinides. Fission cross section for  $^{242}\text{Pu}$ , which is listed in NEA Nuclear Data High Priority Request List, was measured at several facilities in the world after around 2010. Some of those measurements suggest the current evaluated data are overestimated. The integral experiments of fission reaction rate with fast reactors also suggest overestimation of  $^{242}\text{Pu}$  fission cross section in JENDL-4.0. Taking into account the recent measurements, the fission cross section has been reevaluated with the least squares fitting code SOK [21]. The evaluated results are compared with recent experimental data and the evaluation of JENDL-4.0 in Fig. 1. While the evaluated result with all experimental data is very close to that of JENDL-4.0, the cross section deduced from

recent experimental data significantly decreases around 1 MeV. The fission reaction rate ratio of  $^{242}\text{Pu}$  to  $^{239}\text{Pu}$  is estimated using evaluated data from recent measurement with the sensitivity matrix of fission cross section of  $^{242}\text{Pu}$  prepared for ADJ2017 and cross section differences from JENDL-4.0. The deduced results are shown in Fig. 2. The overestimations seen in JENDL-4.0 clearly become small. As some overestimations still exist for FCA experiments, further study including contribution from other nuclear data would be needed.

The first test library of JENDL-5 $\alpha$ 1 was created in FY 2018 and the second one JENDL-5 $\alpha$ 2 is being prepared in FY 2019. They include the updated and newly-evaluated data for more than 90 isotopes. The preliminary evaluation of fission cross sections of major actinides *i.e.* uranium and plutonium isotopes for the fast neutrons are included. The results of the recent international collaboration CIELO [22] are taken for these test versions. The thermal scattering law data evaluated by Abe *et al.* [23] is adopted. Feedbacks from benchmark results for reactors will be taken into accounts in the revision of the JENDL-5 evaluations.

#### 4. Conclusion

Recent progress and future plan of JENDL are summarized. The JENDL project has released many special purpose files in this decade. Outlines of the most recent 3 files, JENDL/PD-2016, JENDL/AD-2017 and JENDL/ImPACT-2018 are reported. The next version of general purpose file, JENDL-5, is under development with the plan of the release in FY 2021. Evaluations from light to heavy nuclides are in progress. Test libraries are being produced with including new evaluations for light nuclei, structure materials, fission products, actinides etc.

#### References

- [1] K. Shibata, O. Iwamoto, T. Nakagawa, N. Iwamoto, A. Ichihara, S. Kunieda, S. Chiba, K. Furutaka, N. Otuka, T. Ohsawa, T. Murata, H. Matsunobu, A. Zukeran, S. Kamada, J. Katakura, "JENDL-4.0: A New Library for Nuclear Science and Engineering", *J. Nucl. Sci. Technol.*, **48**(1), 1-30 (2011).
- [2] <https://www.ndc.jaea.go.jp/jendl/jendl.html#jendl-sp> (accessed 2020/09/23).
- [3] S. Kunieda, "Status of the R-matrix Code AMUR toward a consistent cross-section evaluation and covariance analysis for the light nuclei", *EPJ Web of Conferences*, **146**, 12029 (2017).
- [4] O. Iwamoto, "Development of a Comprehensive Code for Nuclear Data Evaluation, CCONE, and Validation Using Neutron-Induced Cross Sections for Uranium Isotopes", *J. Nucl. Sci. Technol.*, **44**(5), 687-698 (2007).
- [5] O. Iwamoto, N. Iwamoto, S. Kunieda, F. Minato, K. Shibata, "The CCONE Code System and its Application to Nuclear Data Evaluation for Fission and Other Reactions", *Nucl. Data Sheets* **131**, 259-288 (2016).
- [6] N. Kishida *et al.*, "JENDL Photonuclear Data File", *Proceedings of International Conference on Nuclear Data for Science and Technology*, Santa Fe, New Mexico, USA, Sep. 26 - Oct. 1, 2004, 1, 199 (2004).
- [7] N. Iwamoto, K. Kosako, T. Murata, "Photonuclear Data File", *JAEA-Conf 2016-004*, 53-58 (2016).
- [8] Y. Nakajima, JNDC WG on Activation Cross Section Data, "JENDL Activation Cross Section File",

- Proc. the 1990 Symposium on Nuclear Data, JAERI-M 91-032, 43 (1991).
- [9] K. Shibata, N. Iwamoto, S. Kunieda, F. Minato, O. Iwamoto, “Activation Cross-section File for Decommissioning of LWRs”, JAEA-Conf 2016-004, 47-52 (2016).
- [10] S. Kunieda, N. Furutachi, F. Minato, N. Iwamoto, O. Iwamoto, S. Nakayama, S. Ebata, T. Yoshida, K. Nishihara, Y. Watanabe, K. Niita, “JENDL/ImPACT-2018: A New Nuclear Data Library for Innovative Studies on Transmutation of Long-lived Fission Products”, J. Nucl. Sci. Technol., **56**(12), 1073-1091 (2019).
- [11] H. Wang, H. Otsu, H. Sakurai *et al.*, “Spallation reaction study for the long-lived fission product  $^{107}\text{Pd}$ ”, Prog. Theor. Exp. Phys., **2017**(2), 021D01 (2017).
- [12] S. Kawase, K. Nakano, Y. Watanabe *et al.*, “Study of proton- and deuteron-induced spallation reactions on the long-lived fission product  $^{93}\text{Zr}$  at 105 MeV/nucleon in inverse kinematics”, Prog. Theor. Exp. Phys., **2017**, 093D03 (2017).
- [13] N. Nakayama, “Calculation of neutron cross-sections on copper-63 and -65”, J. Nucl. Sci. Technol., **55**(6), 614-622 (2018).
- [14] A. Ichihara, “Theoretical calculation of neutron cross sections for  $^{90,91,92,94,96}\text{Zr}$  in the incident energy range between 200 keV and 20 MeV”, J. Nucl. Sci. Technol., **55**(9), 1087-1098 (2018).
- [15] A. Ichihara, “Calculation of cross sections for metastable state production in the (n, $\gamma$ ), (n,n'), (n,2n) and (n,3n) reactions of  $^{93}\text{Nb}$ ”, J. Nucl. Sci. Technol., **53**(12), 2049-2055 (2016).
- [16] K. Shibata, “Evaluation of neutron nuclear data for gallium”, J. Nucl. Sci. Technol., **50**(3), 277-286 (2013).
- [17] K. Shibata, “Evaluation of neutron nuclear data on antimony isotopes”, J. Nucl. Sci. Technol., **51**(4), 425-436 (2014).
- [18] K. Shibata, “Evaluation of neutron nuclear data on tellurium isotopes”, J. Nucl. Sci. Technol., **52**(4), 490-502 (2015).
- [19] K. Shibata, “Evaluation of neutron nuclear data on iodine isotopes”, J. Nucl. Sci. Technol., **52**(9), 1174-1185 (2015).
- [20] H. Harada, O. Iwamoto, N. Iwamoto, A. Kimura *et al.*, “Research and development for accuracy improvement of neutron nuclear data on minor actinides”, EPJ Web of Conferences, **146**, 11001 (2017).
- [21] T. Kawano, H. Matsunobu, T. Murata *et al.*, “Evaluation of Fission Cross Sections and Covariances for  $^{233}\text{U}$ ,  $^{235}\text{U}$ ,  $^{238}\text{U}$ ,  $^{239}\text{Pu}$ ,  $^{240}\text{Pu}$ , and  $^{241}\text{Pu}$ ”, JAERI-Research 2000-004 (2000).
- [22] M.B. Chadwick *et al.*, “CIELO Collaboration Summary Results: International Evaluations of Neutron Reactions on Uranium, Plutonium, Iron, Oxygen and Hydrogen”, Nucl. Data Sheets, **148**, 189 (2018).
- [23] Y. Abe, “Evaluation of the neutron scattering cross-section for light water by molecular dynamics”, Nucl. Instrum. methods Phys. Res. A, **735**, 568 (2014).

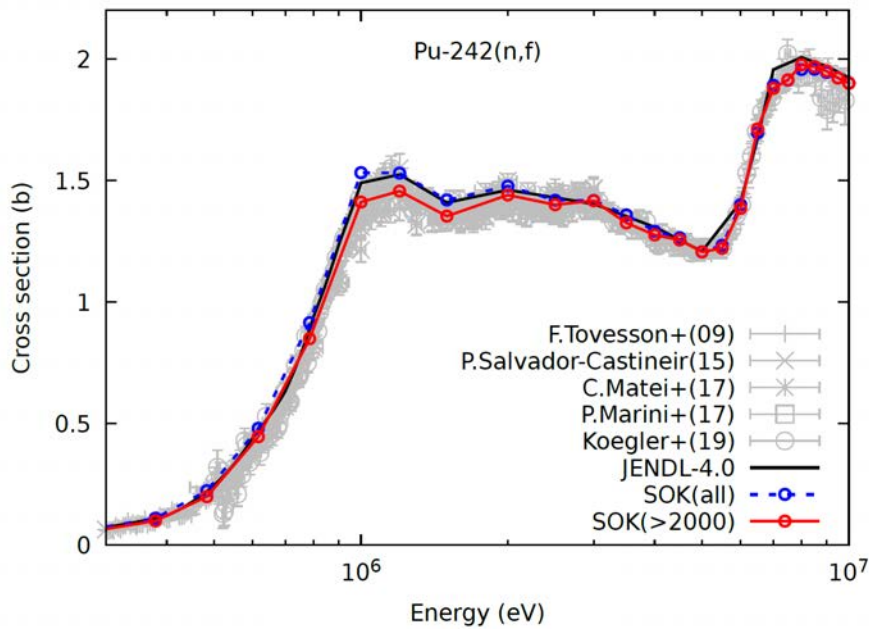


Fig. 1 Neutron induced fission cross section of  $^{242}\text{Pu}$ . Blue and red curves with circles shows the evaluated results with all experimental data and ones limited after 2000, respectively. Black line indicates JENDL-4.0. Recent experimental data are shown by gray symbols.

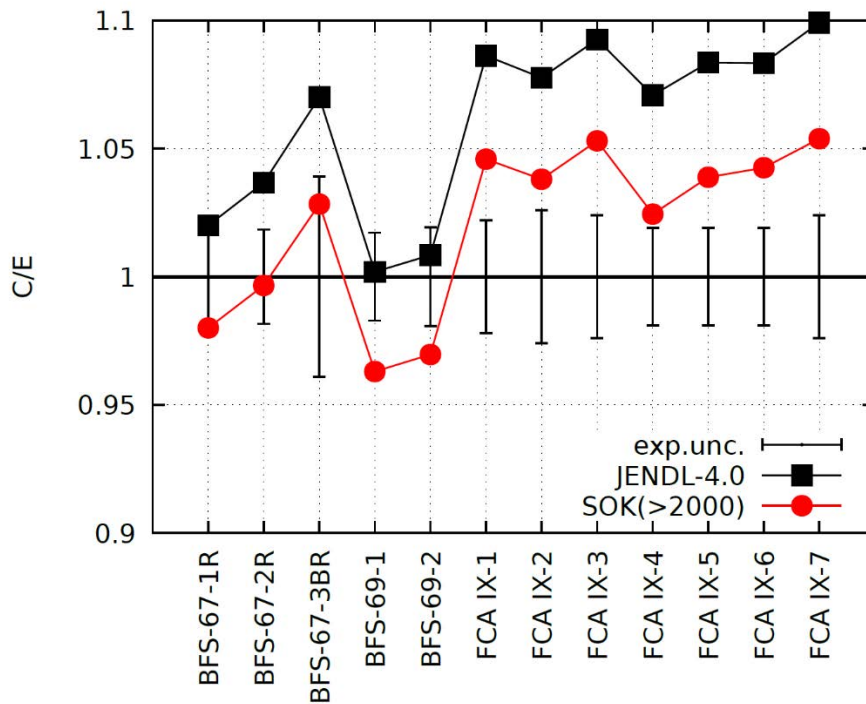


Fig. 2 Fission reaction rate ratio of  $^{242}\text{Pu}$  to  $^{239}\text{Pu}$  for fast reactors. C/E values for JENDL-4.0 is shown by black squares and estimation for new evaluation with sensitivities is indicated by red circles.

## 4 A Consideration on Nuclear Data Needs for 1F Decommissioning

Tokio FUKAHORI

Fukushima Research Institute, Japan Atomic Energy Agency

Taira Central Building, Iwaki, Fukushima, 970-8026 Japan

e-mail: fukahori.tokio@jaea.go.jp

After 8 years from the accident at TEPCO Fukushima Daiichi Nuclear Power Station, the “on-site” research and development (R&D) situation has been changed into new phase. It can be considered from understanding to predicting by many direct and indirect measurements and analyses. In this presentation, nuclear data needs for 1F decommissioning are revisited according to these situation. The needs for accident evolution characteristics, criticality management, debris storage, waste management, etc. are considered with the view point of R&D on prediction what is going on and will be happened in each stage of decommissioning.

### 1. Introduction

The accident at TEPCO Fukushima Daiichi Nuclear Power Station (1F) was triggered by the earthquake named “Great East Japan Earthquake” on March 11, 2011. The research and development (R&D) situation for 1F decommissioning and environment remediation has been changed into new phase and weight of the R&D is getting to shift into the “on-site”, since the situation related to “off-site” is getting more stable. For example, the dose rate at many places has been down to the normal level compared with other cities[1], the number of evacuating people is decreased to 1/4[2], and the evacuation area is reduced 1/3[2,3].

On the other hand, the locations of debris in the unit 1-3 are believed now to be understood much better than before. The fuels in spent fuel pools have been started to move out. The piece being seemed debris has been directly touched by the new equipment. The condition inside the reactor buildings can be considered to change from understanding to predicting by many direct and indirect measurements and analyses.

In this presentation, nuclear data needs for 1F decommissioning are revisited according to the situation mentioned above. The needs for understanding accident development, understanding current situation in the reactor building and waste management of rubble and fuel debris are tried to be considered with the view point of R&D on prediction what is going on and will be happened in each stage of decommissioning. A consideration by the author about above items with seeing criticality management, debris storage, waste management, heat reduction, radiation shielding, hydrogen production by radiolysis, etc.

## **2. Understanding Accident Progression**

For understanding accident progression, the calculation starts at the point of final burn-up condition. The decay heat makes cooling water evaporating and fuel rods and structural materials melting. To estimate final burn-up condition, ordinal burn-up calculation is enough. For this purpose, quantities related to fission reaction for reactor operation are needed as well as fission yields and decay data for fission product (FP) accumulation which is source of decay heat. It seems to be considered these nuclear data have enough accuracy, while the information of reactor operation, fuel combination and shuffling is more important for more precise calculation.

The fuel debris composition can be estimated by melted materials' transfer. This calculation strongly depends on the accident progression calculation results mentioned above. It is also important to consider debris re-melting after solidification. For this calculation, fission yields and decay data are also important, because of heating source estimation. These nuclear data and nuclear structure data are also useful for the heat reduction (cooling) calculation.

## **3. Understanding Current Situation inside Reactor Building**

To estimate current situation inside the reactor buildings, simulation of source term, criticality, decay heat and radiation distribution are necessary. For source term calculation, information of fuel debris and FP nuclide locations is needed to be estimated. For this purpose, data of quantities related to fission reaction, fission yields and decay data are needed.

For the criticality management, amount and location of fissionable nuclides are needed to be obtained as well as FP nuclides for burn-up credit calculation. Quantities related to fission reaction and fission yields are important information. To monitor criticality, high energy gamma-ray from capture state is useful, since it has lower background comparing to the low energy one. It is also used for "Capture Credit" estimation[4,5]. To estimate the high energy gamma-ray production, capture cross section and its gamma-ray emission spectra are necessary. Unfortunately, it is hard to say the gamma-ray spectrum data are enough both qualitatively and quantitatively at this moment.

Heat reduction is important to control the temperature of cooling water. To calculate heat source, the data of fission yields, decay and nuclear structure data are necessary. They are also used for radiation shielding calculation with total cross sections of structural materials.

## **4. Waste Management of Rubble and Fuel Debris**

The waste management is important to be considered before starting the rubble and fuel debris bring-out procedure. Considered are criticality management of debris storage, radiation shielding, heat reduction, radiolysis, etc. For the criticality management, nuclear data needs are same as mentioned in "3. Understanding Current Situation inside Reactor Building".

For estimation of radiation production, the composition of fuel debris and FP production data are necessary as radioactive sources. Considering activation cross sections for structural materials are also important for radiation shielding calculation. In the case of the radiation shielding and heat reduction needs similar nuclear data as well as total cross section of structural materials.

Radiolysis[6], especially hydrogen-gas production, must become important for safety storage, since the waste at 1F has significant radioactivity. For radiation source estimation, fission yields, decay and nuclear structure data are needed. In addition, emitted particle spectra, especially for alpha-particles, are necessary to calculate hydrogen-gas production rate in the water included inside the storage. The alpha-particle spectra are also used to detect U/Pu particles[7] which are alpha emitter. It is important for Pu-signal separation from those of radon progeny to identify the higher energy alpha-particles. The spectra can be used for calculations of alpha-particle transport both in the debris and water.

## 5. Summary

One of considerations on nuclear data needs for 1F decommissioning is introduced for understanding accident development, understanding current situation inside reactor building and waste management of rubble and fuel debris. As the summary of nuclear data need, following physical quantities are picked up.

- Quantities Related to Fission Reaction
- Fission Yields
- Decay and Nuclear Structure Data
- Total Cross Section for Structural Materials
- Activation Cross Section for Structural Materials
- High Energy Gamma Production from Capture State
- Emitted Particle Spectra (especially for Alpha-particle)

Those above are one of considerations by the author. More needs might be hidden according to development of new technology for decommissioning.

## References

- [1] Fukushima Prefecture Radioactivity Measurement Map, <http://fukushima-radioactivity.jp/pc/> (those of foreign cities <https://www.env.go.jp/chemi/rhm/h30kisoshiryo/h30kiso-02-05-07.html>) (accessed 2020/07/03).

- [2] Fukushima Prefecture, “Steps for Revitalization in Fukushima 26th edition <August 5, 2019>” and “Damage Report <October 7, 2019>”,  
<https://www.pref.fukushima.lg.jp/site/portal-english/ayumi-en-15.html> (accessed 2020/07/03).
- [3] Ministry of Economy, Trade and Industry of Japan, “Evacuation Areas”,  
[https://www.meti.go.jp/english/earthquake/nuclear/roadmap/evacuation\\_areas.html](https://www.meti.go.jp/english/earthquake/nuclear/roadmap/evacuation_areas.html)  
(accessed 2020/07/03).
- [4] Y. Nauchi, “Nuclear Data Required for Measurements of Reactivity and Nuclear Material Composition”, JAEA-Conf 2019-001, p.41-46 (2019).
- [5] Y. Nauchi, “Nuclear Data Needs Related to Estimation of Fuel Debris Nuclear Characteristics -Measurement of Gamma-ray Spectrum by Neutron Irradiated Nuclear Reaction -”, Nuclear Data News (ISSN 0385-4876), No.122, p.54-66 (2019) in Japanese.
- [6] R. Nagaishi, “Hydrogen Production in Storage of Fuel Debris”, private communication.
- [7] Y. Morishita, T. Torii, H. Usami, H. Kikuchi, W. Utsugi and S. Takahahira, “Detection of Alpha Particle Emitters Originating from Nuclear Fuel inside Reactor Building of Fukushima Daiichi Nuclear Power Plant”, Scientific Reports (URL: [www.nature.com/scientificreports](http://www.nature.com/scientificreports)), DOI: 10.1038/s41598-018-36962-4 (2019).

## 5 Fundamental physics using neutron at J-PARC and accelerator-driven neutron source

Tamaki YOSHIOKA<sup>1</sup>

<sup>1</sup>*Kyushu University, 744 Motoooka, Nishi-ku, Fukuoka 819-0395, Japan*

*E-mail: yoshioka@phys.kyushu-u.ac.jp*

Precise measurements using low energy neutron give complementary information to the collider experiments using high energy accelerators. Moreover, it is also sensitive to a new physics in high energy regions where the collider experiments may not reach. A high-quality neutron beam can be provided to an experimental apparatus by using the neutron optics, which has been greatly advanced in recent years. A beamline BL05, which is intended for the fundamental physics using low energy neutron, has been constructed at the J-PARC/MLF, and successfully started the operation at the end of 2008. In this article, the experiments using low energy neutron conducted at the J-PARC/MLF/BL05 will be given. In addition, the recent situation of an accelerator-driven compact neutron source will also be presented in this article.

### 1. Introduction

The Higgs boson, which is the last piece predicted in the Standard Model (SM) of the particle physics, was discovered in 2012 [1, 2]. Some phenomena are known that can not be explained by the SM, such as the existence of the dark matter. There is, however, no evidence for a physics beyond the SM (BSM) despite the intensive search at Large Hadron Collider (LHC). So-called the energy frontier experiment is aiming to explore the BSM directly by using the high energy accelerator such as the LHC, as stated above. In contrast, the search for the BSM by the precision experiment using high-intensity secondary particles such as the neutron is an indirect approach. They are complementary with each other, but the indirect search sometimes more sensitive than the direct approach for some specific BSM models.

The Japan Proton Accelerator Research Complex (J-PARC) is a joint project of the Japan Atomic Energy Agency (JAEA) and High Energy Accelerator Research Organization (KEK) and is constructed at Tokai-village, Ibaraki-prefecture [3]. Figure 1 is a schematic view of the J-PARC, and a fundamental physics experiment using low energy neutron is conducted at the Material and Life science Facility (MLF) located at the center of the figure.

### 2. Fundamental physics using low energy neutron

The neutron was discovered by Chadwick in 1932 and is a composite particle consisting of two up quarks and one down quark. The neutron has a spin of  $1/2$  and a mass of about  $1 \text{ GeV}/c^2$ , and decays to an electron and two neutrinos via weak interaction with a lifetime of 880.3 seconds [4]. The classification of neutrons, according to their energy, is shown in Fig. 2. Cold neutrons, which are often used in fundamental physics experiments at J-PARC, have an energy of about meV. Fundamental physics experiments also use very cold and ultracold neutrons in the even lower energy range, and such low energy neutrons have unique features. Low-energy neutrons can be confined to a material bottle because they are totally reflected by the nuclear potential called the Fermi potential which is about several hundred neV for various materials. As mentioned earlier, the neutron has a spin  $1/2$ , and the potential difference between the spin-up and spin-down states is about 120 neV in a magnetic field of 1 T, which is easily achievable in the laboratory. The gravitational interaction is usually ignored in particle physics, but the

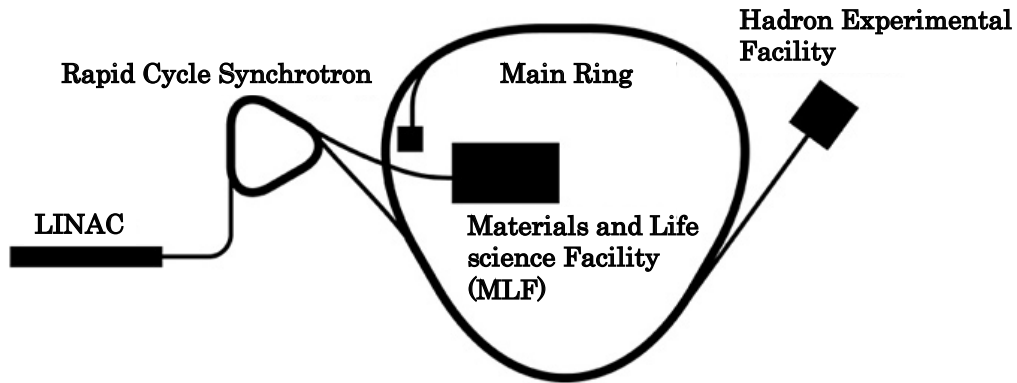


**Fig. 1.** A schematic view of the J-PARC. A building located at the center of the figure is called Materials and Life science Facility (MLF) where fundamental physics experiment using low energy neutron is conducted.

positional energy acquired by neutrons is about 100 neV/m, which is the same order of magnitude as the interactions described above. Moreover, as also mentioned earlier, neutrons decay through weak interactions but have an extremely long lifetime for an unstable particle. We prove the high-energy phenomena in the quantum loop via the precise measurement by utilizing these unique features.

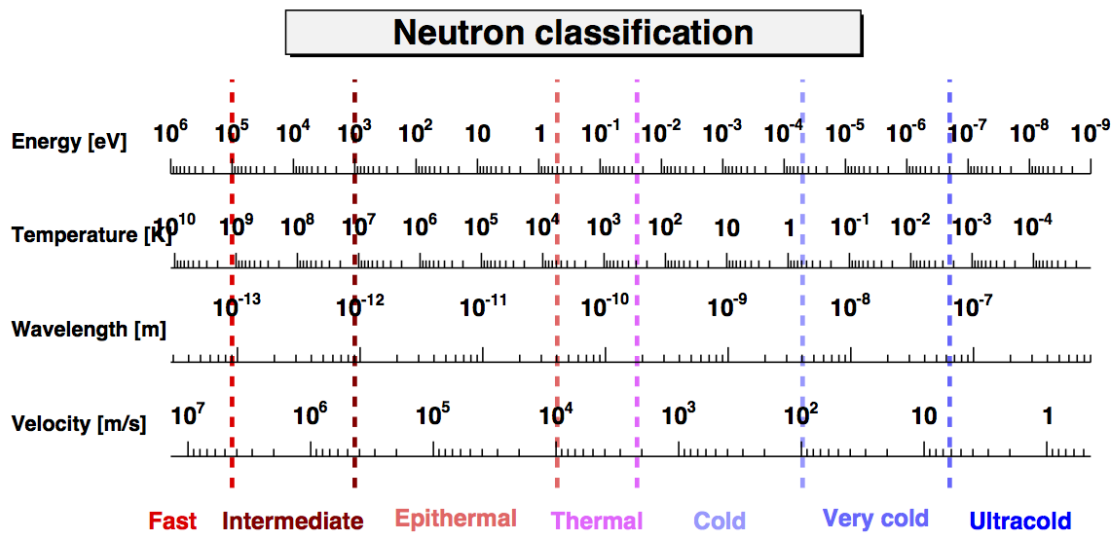


**Fig. 2.** Classification of neutrons according to their energy. Cold neutrons, which are often used in fundamental physics experiments at J-PARC, have an energy of about meV.

In the J-PARC/MLF, a proton beam from the Rapid Cycle Synchrotron shown in Fig. 1 is irradiated to a mercury target to produce neutrons, which are moderated by a hydrogen moderator and transported to each beamline. There are 23 beamlines in total in MLF, among which beamline number 5 (BL05) named Neutron Optics and Physics (NOP) is a beamline dedicated to fundamental physics experiments using low energy neutrons [5]. The BL05 has a feature of dividing a neutron beam from a mercury target to three different beam branches by a neutron optics device called a super mirror bender. Figure 3 shows a picture of the super mirror bender before being installed inside the concrete shield. From the left, there are polarization beam branch, un-polarized beam branch, and low-divergence beam branch, and the neutron beam from the mercury target is injected from the front of the photograph. As can be seen from the picture, each beam branch is curved to reflect low energy neutrons and transport them to the experimental area. A number of physics experiments and device R&D have been carried out at BL05 [6–9]. Among them, the flagship experiment, precision measurement of the neutron lifetime using a polarized beam branch, is described in the next section.

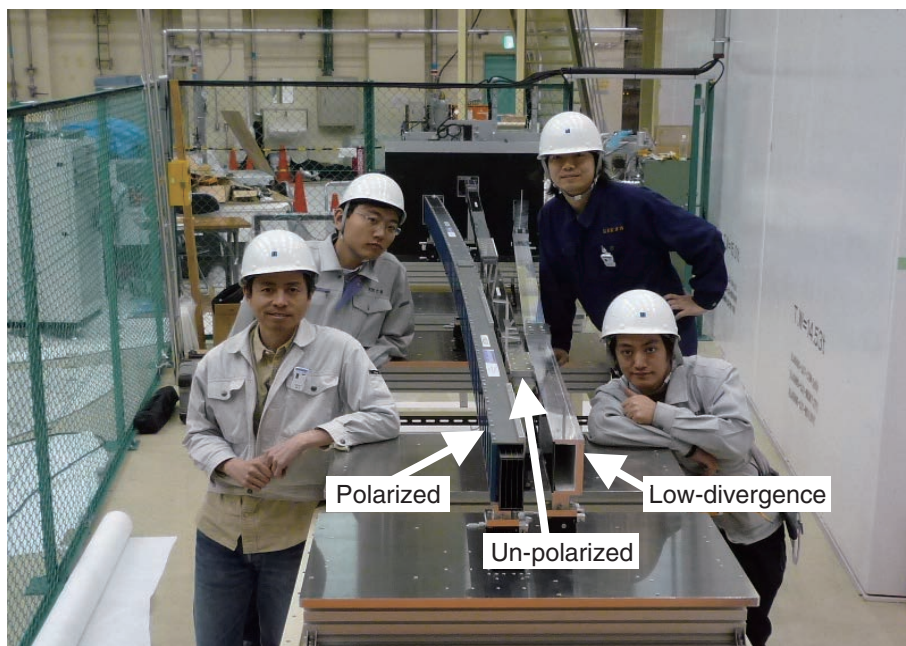


**Fig. 3.** A picture of the super mirror bender before being installed inside the concrete shield. From the left, there are polarized beam branch, un-polarized beam branch, and low-divergence beam branch, and the neutron beam from the mercury target is injected from the front of the photograph.

### 3. Precise measurement of neutron lifetime

The neutron lifetime has been measured for more than 50 years since its discovery. The neutron lifetime is an important input parameter for the Big Bang Nucleosynthesis (BBN). It can also be used for a test of the unitarity of the Cabibbo-Kobayashi-Makawa (CKM) matrix. There are historically two types of methods to measure the neutron lifetime; storage method and beam method. The former confines the ultracold neutron in a material bottle as described earlier for a certain period of time and counts the number of the survived neutron. The latter utilizes the cold neutron beam and counts the number of incident neutrons and decay protons. Each method has a measurement precision of less than 1%, however, there is a long-standing significant discrepancy corresponds to 8.5 sec. or 4.0 standard deviation. Recently, there is an attempt to explain this discrepancy by the BSM. It cannot be, however, ruled out that the difference is due to some unknown systematics, a new type of experiment is therefore desired in this regard.

The precise measurement of the neutron lifetime at J-PARC is a kind of beam method, but we count electrons instead of decay protons. In addition, in the previous beam method, the incident neutrons and decay protons were counted with different detectors, and the resulting uncertainty was considered to be dominant. In our experiment, the incident neutrons and decay electrons are measured simultaneously with a single gaseous detector called a Time-Projection Chamber (TPC). Originally, this type of experiment was developed by Kossakowski *et al.* [10], the following cares are employed in our experiment in order to suppress background events. The TPC is made of a material with small radioactive material contamination [11]. The neutron beam provided by the polarization branch is further chopped by using a special device called Spin Flip Chopper (SFC) so that the neutron bunches are fully contained in the TPC. We started data taking in 2014, and the first result was obtained with an accuracy of a couple of percents. In the future, we are aiming to achieve 0.1% accuracy with an improvement of the SFC and a suppression of the dominant background caused by the TPC operation gas.

We are also planning yet another neutron lifetime measurement using a superconducting magnet. In the course of the data analysis in the current experiment, we found the dominant background source is originated from the TPC operation gas, as mentioned above. Geant4 simulation shows that this background can be significantly suppressed to achieve 0.1% accuracy with a 600 mT magnetic field. The idea of this experiment can be found in Ref. [12] in detail. A dedicated TPC with non-magnetism materials was constructed at Kyushu University for this experiment. An integration test with the TPC and superconducting magnet was conducted at KEK using cosmic rays and a radioactive source. Figure 4 shows the integration test at the KEK. The TPC is installed on the dedicated stand shown in the center of the photograph. Behind the TPC, the superconducting magnet can be seen, and a vacuum chamber is installed inside of the magnet. In this test, we confirmed that the TPC has the expected performance in a magnetic field. As of this written, the TPC and superconducting magnet are installed at the BL05 beamline. The magnet excitation test was successfully done, and we took a first commissioning data with the neutron beam.

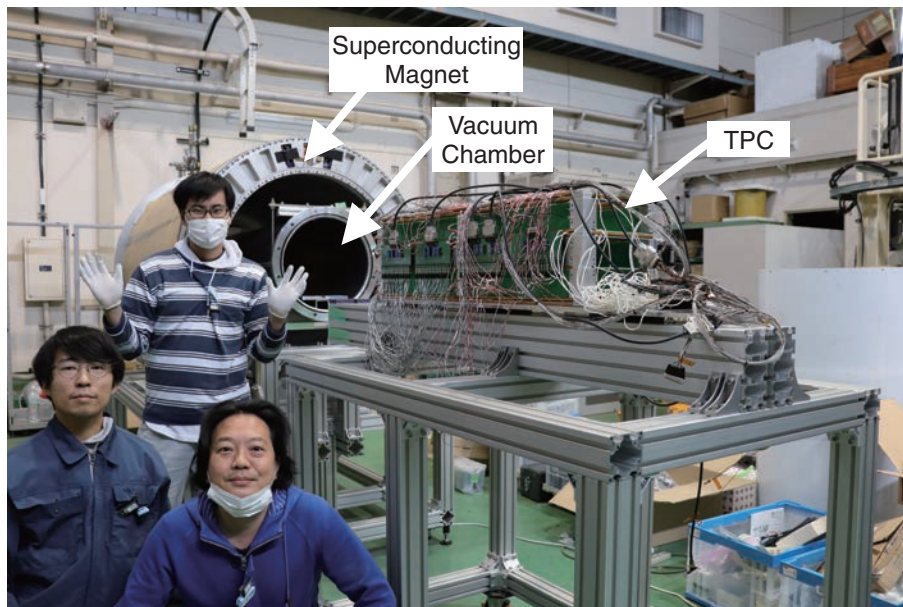


**Fig. 4.** Integration test at KEK. The TPC is installed on the dedicated stand shown in the center of the photograph. Behind the TPC, the superconducting magnet can be seen and a vacuum chamber is installed inside of the magnet.

#### 4. Accelerator-driven compact neutron source at Kyushu University

Neutron beam has been used not only in particle and nuclear physics experiments but also for industrial and medical applications, recently. As described earlier, a high-intensity spallation neutron source has been in operation at J-PARC since 2008. Although such a large facility enables ultra-precise measurements with high-intensity beams, it takes several months from the proposal submission to the actual experiment, and the allocated machine time is rather limited. Comparisons between large and small facilities are summarized in the Table I. As shown in the table, they are complementary to each other, which is similar to the relationship between SPring-8, a large synchrotron radiation facility, and an X-ray device in a university laboratory as a small facility. Although the development of compact neutron sources is widely spreading, it is inefficient to develop in one institute/laboratory since there are a number of R&D items. The Japan Collaboration of Accelerator-driven Neutron Sources (JCANS) was consolidated to activate a nation-wide network of individual research activity on neutron source and moderators. Accelerator-driven compact neutron sources are already in operation at Hokkaido University, Kyoto University, and RIKEN, and are now being developed at Nagoya University [13].

Fast neutrons have been produced so far by using the tandem accelerator at Kyushu University. Fast neutrons are useful for testing a soft error of semiconductor, but lower energy (thermal and cold) neutrons are preferred in particle physics and materials science. We have firstly demonstrated to produce the thermal neutrons at Kyushu University in July 2019. An aluminum duct was connected to downstream of the scattering chamber in the experimental hall. A blank flange was attached to downstream of the duct, and a neutron production target was placed inside of the flange. Fast neutrons produced by the proton beam irradiation from the tandem accelerator are slowed down by a polyethylene moderator installed downstream of the target, and the thermal neutrons are detected by a neutron detector located at the most downstream of the beamline. We chose a Beryllium metal as a neutron production target. We expect  $4 \times 10^7$  neutrons/sec by assuming proton energy of 13 MeV and the beam current of 1 nA of the tandem accelerator. Figure 5 is an image of the two-dimensional detector, in which a cadmium plate with a "Q" shape is attached to the center of the surface of the detector, and a boron gum is attached to the bottom of the detector. Left figure of Fig. 5 shows a detector image with the polyethylene moderator, and the shadows of cadmium and boron gum can be seen due to the absorption of thermal neutrons. Right figure of Fig. 5 is the case without the moderator, and the shadows can not be seen because fast neutrons transmitted the cadmium and boron gum. This indicates that the produced fast neutrons were successfully slowed down in the moderator and became thermal neutrons. In the next step, we will install a mechanical chopper to measure the time of flight. We are also aiming to produce the cold neutrons by farther cooling the thermal neutrons in the future.

**Table I.** Pros and cons of the accelerator-driven compact neutron source.

	Large Facility	Small Facility
Pros	<ul style="list-style-type: none"> <li>• Precision measurement thanks to high intensity beam</li> <li>• Well maintained beamline</li> </ul>	<ul style="list-style-type: none"> <li>• Relatively plenty/flexible beam time</li> <li>• Education use</li> <li>• Test experiment</li> </ul>
Cons	<ul style="list-style-type: none"> <li>• Limited resource/beam time/operation mode</li> <li>• Take long time from proposal stage</li> </ul>	<ul style="list-style-type: none"> <li>• Weak beam intensity</li> <li>• Need setup every time</li> </ul>

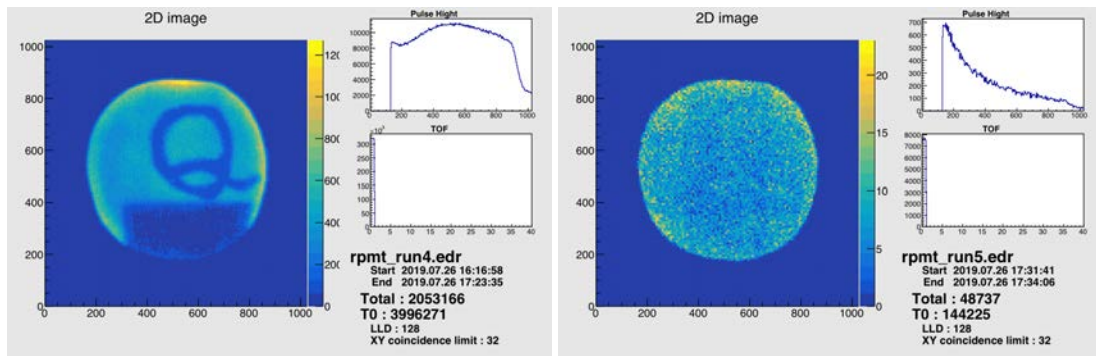


**Fig. 5.** Results of the experiment of thermal neutron production at Kyushu University. Left (Right) figure shows a 2D detector image with (without) a polyethylene moderator.

## 5. Summary

Precise measurements using low-energy neutrons provide complementary information to the collider experiments using the energy frontier accelerator. A beamline named BL05 for the fundamental physics using low energy neutron has been constructed in the MLF of the J-PARC and operated since 2008. Currently, a precise measurement of the neutron lifetime is on-going at the J-PARC/MLF/BL05 as a flagship experiment. The accelerator-driven compact neutron source is useful for such as a detector R&D before conducting an experiment at the J-PARC. A test experiment of the thermal neutron production has been successfully carried out by using the tandem accelerator at Kyushu University. We will try to produce cold neutrons in the future.

## References

- [1] ATLAS Collaboration, Phys. Lett. B 716, 1 (2012).
- [2] CMS Collaboration, Phys. Lett. B 716, 30 (2012).
- [3] J-PARC web site (available at <https://j-parc.jp/c/en/index.html>, date last accessed March 31, 2020).
- [4] M. Tanabashi *et al.* (Particle Data Group), Phys. Rev. D 98, 03001 (2018).
- [5] K. Mishima *et al.*, Nucl. Instrum. Meth. A 600, 342 (2009).
- [6] R. Kitahara *et al.*, Prog. Theor. Exp. Phys. 9, 093C01 (2019).
- [7] C. C. Haddock *et al.*, Phys. Rev. C 100, 064002, (2019)
- [8] C. C. Haddock *et al.*, Phys. Rev. D 97, 062002, (2018)
- [9] N. Nagakura *et al.*, Proceedings of Science, 191 (2016).
- [10] R. Kossakowski *et al.*, Nuclear Physics A 503, 473 (1989).
- [11] Y. Arimoto *et al.*, Nucl. Instrum. Meth. A 799, 187 (2015).
- [12] H. Otono, Nucl. Instrum. Meth. A 845, 278 (2017).
- [13] K. Hirota *et al.*, EPJ Web Conferences 231, 05002 (2020).

## 6 Recent R&D of HTGR and Requirement for Nuclear Data

Y. Fukaya\*, M. Goto, S. Nakagawa

Sector of Fast Reactor and Advanced Reactor Research and Development

Japan Atomic Energy Agency (JAEA)

4002 Narita-cho, Oarai-machi, Higashiibaraki-gun, Ibaraki 311-1393, Japan

\*E-mail: fukaya.yuji@jaea.go.jp

Recently, HTGR attracts a particular attention due to the outstanding safety features especially after the Fukushima Daiichi nuclear disaster, and the R&D is significantly promoted. In this presentation, we introduce the R&D plan of HTGR and the activities related to reactor physics and nuclear data including an experiment by using KUCA. Furthermore, requirement for nuclear data from the HTGR design is discussed.

### 1. Introduction

Japan Atomic Energy Agency (JAEA) has been performed the Research and Development (R&D) of High Temperature Gas-cooled Reactor (HTGR) to utilize the high temperature for multi-purpose heat utilization and electricity generation with high thermal efficiency. Nuclear power generation including HTGR is an attractive energy source of clean-air and carbon-free electricity, that produces no greenhouse gases or air pollutants unlike power generation with fossil fuel. Moreover, HTGR heat utilization of hydrogen generation is expected to reduce the greenhouse gases by replacing the fossil fuel utilization.

Moreover, HTGR has outstanding safety features such as an excellent heat removal function and inherent safety feature so called self-regulation due to the graphite core structure. Graphite has high thermal conductivity and neutron moderation function which realize safety feature of thermal reactor. After the Fukushima Daiichi nuclear disaster, HTGR attracts a particular attention due to the outstanding safety features. The failure of decay heat removal of the unit 1 of Fukushima Daiichi lead to the hydrogen explosion. On the contrary, in HTGR, the decay heat can be removed successfully to final heat sink such as air and soil in any circumstances even in depressurization accident where the coolant flows out from the ruptured pipe. The integrity of Coated Fuel Particle (CFP) remains in any situations. Therefore, the significant Fission Products (FPs) release is never occurred in HTGR.

Under the circumstances, recently, the R&D of HTGR is significantly promoted such as a description in policy and international corporations. Furthermore, the R&D of reactor physics technique with criticality experiment is also started. Those are reported in this article.

## 2. History of HTGR R&D and Future Plan

First, JAEA had completed the design of High Temperature engineering Test Reactor (HTTR) with the demonstrate the elemental technologies and code validation. For fuel material, in-pile helium loop named OGL-1 was built and operated. The loop was deployed into the core of Japan Material Testing Reactor (JMTR), and the actual CFPs are loaded in the similar condition in the HTGR core. For reactor physics, Very High Temperature Reactor Critical Assembly (VHTRC) was built, and criticality experiment was performed. For thermal hydraulics, Helium EngiNeering Demonstration Loop (HENDL) was built, and thermal hydraulics experiment was performed. Experimental correlation formulas relating to Nusselt number and Reynolds number for the particular coolant flow path of HTTR were determined, and flow distribution was measured. By using the validated code and the experimental correlation formulas, HTTR was designed, licensed and constructed. The first criticality was achieved in 1998. In 2010, Loss Of Forced Cooling (LOFC) test was performed as OECD/NEA project. Without scrum, the reactor power is safely reduced by Doppler effect and the decay heat is successfully removed without the forced cooling. The result attracts the particular attention as the evidence of the outstanding safety features of HTGR after the Fukushima Daiichi nuclear accident.

Next, JAEA had completed the design for the commercial use of high temperature gas reactor by introducing the HTGR concept, called GTHTR300. It is planned to start the construction from 2030. The thermal output is 600MW, and the electricity output is approximately 300MW. By employing direct gas-turbine system, the cheaper electricity cost than Light Water Reactor (LWR) can be achievable. By using the high temperature, hydrogen generation is also available.

## 3. Recent Promotion of R&D of HTGR

Due to the outstanding safety and advantage of hydrogen generation, the R&D was recommended in “Strategic Energy Plan”, which was formulated by the government of Japan on April 11, 2014. In this document, the R&D of HTGR with international corporation was recommended. As a result, the corporation with Poland was established. The Polish government published “Strategy for responsible development” in 2017. In the policy, preparation of HTGR development for industrial heat production in cogeneration was planned. The Polish ministry of energy accept the report “HTGR development strategy” proposed by HTGR committee and published it in 2018. The development roadmap and the specification of HTGR were clearly determined. The experimental reactor with output of 10MWt is planned to be built in 2025. The commercial reactor with output of 165MWt is planned to be built in 2030. JAEA have also investigated the experimental reactor and commercial reactor, now. In this study, we report the R&D relating to reactor physics.

#### 4. Recent R&D Activity Relating to Reactor Physics

The R&D have been performed by using Kyoto University Criticality Assembly (KUCA) experiment. There are two objectives for the R&D. First one is to introduce noise analysis technique in HTTR experiment to determine subcriticality and neutron source strength independently. This is necessary to elucidate the re-criticality of the LOFC experiment of HTTR. It is very important for the commercial HTGR design because the temperature increase by the tiny power burst due to the re-criticality exceeds a safety limitation. The neutron source sustains the power level during the subcriticality, and the power level determines the timing to occur the power burst and its height. However, the neutron source strength, in other words, number of Bq, is not equal to that of the point-kinetics, which is employed for safety analysis of licensing. To evaluate the source strength of point-kinetics, the value should be weighted by forward and adjoint flux. The forward flux cannot be evaluated by a criticality calculation, because the profile is exponential in a subcriticality state. For the adjoint flux, there are several definitions in a subcriticality state. Measurement of source strength is preferable from the viewpoint of accuracy. Furthermore, by inverse kinetics, which is widely employed as reactivity meter, it cannot be determined independently from subcriticality. Therefore, we are planning to develop noise analysis method which can determine the subcriticality independently from neutron source strength. With the relation between the measured power, neutron source, and subcriticality in a steady state, the neutron source strength can be determined as well.

For first of a kind HTGR, propagation of the error of the nuclear data may have to be considered for safety analysis for licensing. Therefore, its reduction method may have to be introduced. Representative one is bias method, which needs full-scale mock-up experiment. It needs a huge budget. On the contrary, by using Generalized Bias Method (GBM), the error propagation can be reduced by synthesizing the sensitivity coefficient to close to that of the target design. GBM needs the several criticality experiment data. Fortunately, the scale effect is not significant. The database can be established by small scale criticality experiment.

For the two objectives, KUCA experiments was performed from 2018. The experiment was planned to be performed for three years.

#### 5. Criticality Experiment in KUCA

The experiment performed in 2018 is reported. The detail will be published in PYHSOR 2020. The core should realize the similar characteristics of HTGR. Here, HTTR is assumed to be a representative one. In this experiment, the graphite-moderation core is composed in solid moderator system rack of KUCA so called “B-rack” to mimic the HTTR core. The enrichment is mimicked by the combination of Highly Enrichment Uranium (HEU) plate

which is composed of the alloy of 93 wt% HEU and aluminum, and Natural Uranium (NU) metal plate. The average enrichment is 5.41 wt%. It is similar to the HTTR's of 5.9 wt%. The HEU plate and NU plate are assembled with moderator plate to realize the spectrum of HTGR. Graphite is also employed as the moderator for the core in B-rack. However, the volume fraction of fuel material in HTGR is very small because the CFPs distribute in the graphite structure. The Vm/Vf ratio is 76.8 in HTTR. To realize the soft spectrum of HTGR, polyethylene moderator is necessary in addition to the graphite moderator because the size of the B-rack is small. Moreover, to achieve criticality with the large leakage core, driver fuel assembly composed of HEU plate and polyethylene plate are deployed around the core.

The configuration of the fuel assemblies is shown in Fig.1, and the core configuration is shown in Fig.2. "F" is the fuel assembly composed of 8 unit cells, which include a 1/16" thickness HEU plate, a 1 mm thickness NU plate, three 1/2" thickness graphite plates, a 1/4" thickness graphite plate, and two 1/8" thickness polyethylene plates, with axial graphite reflectors. The fuel plates were designed to realize the averaged fuel enrichment of HTTR as described above. The polyethylene plate was used to mimic the HTTR spectrum. "D" stands for the driver fuel assemblies composed of 38 unit cells, which include a 1/16" thickness enriched uranium plate, and, three 1/8" thickness of polyethylene, with axial graphite reflector. "d" stands for the partial length driver fuel to adjust criticality.

The BF<sub>3</sub> detectors were deployed to observe reactor noise. By using the data, noise analysis method based on Feynman- $\alpha$  method was developed. For the GBM, the criticality experiment data can be regarded as representative core. The neutron spectrum similar to HTTR's can be realized and similar sensitivity coefficient is also expected.

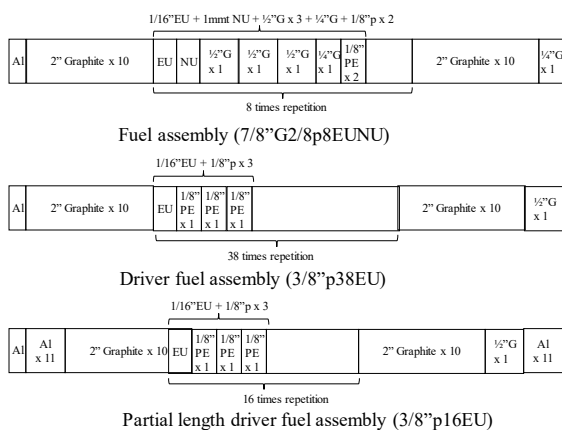


Fig.1 Configuration of fuel assemblies

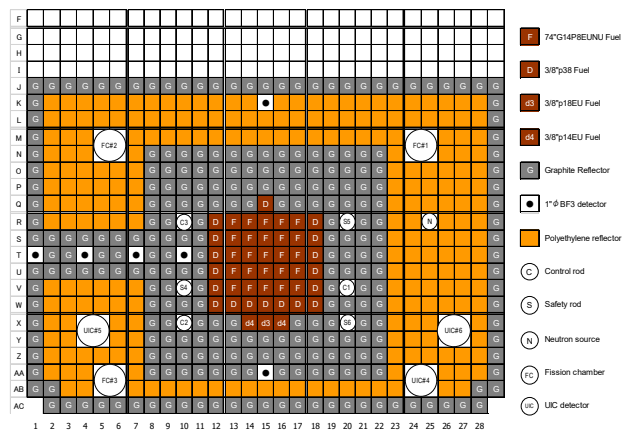


Fig. 2 Configuration of core

## 6. Nuclear Data for HTGR and Requirement

For HTGR design, the nuclear data of graphite, namely cross-section of carbon and the neutron scattering law in graphite, are important. Table 1 shows the history of the modification of the capture cross-section of carbon. The first JENDL was published in 1977 and its capture cross-section of carbon is 3.40 mb. In 1989, JENDL-3 was published, and the capture cross-section of carbon was modified to 3.53 mb. Before JEDNL-4.0 was published, we reported our HTTR criticality analyses results to the nuclear data center of JAEA. In 2010, JENDL-4.0 was published, and the capture cross-section of carbon was modified to 3.85 mb based on the latest measurement data. ENDF/B-VI was published in 1974, and its capture cross-section of carbon was 3.36 mb. The latest ENDF is ENDF/B-VII.0 and its value is same as the ENDF/B-VI, so this value was not modified for 36 years at least.

Table 1 Capture cross-section of carbon

		Japan	U.S.A.	Europe	
		Capt. X-sec of C-nat.	Capt. X-sec of C-nat.	Capt. X-sec of C-nat.	
1974			ENDF/B-IV	3.36mb	
77	JENDL-1	3.40mb	ENDF/B-V		
78				JEF-1	3.36mb
82	JENDL-2		ENDF/B-VI		
89	JENDL-3	3.53mb		JEF-2.2	
90	JENDL-3.1			JEFF-3.1	
92					
94	JENDL-3.2				
2001			ENDF/B-VII		
2	JENDL-3.3			JEFF-3.1.1	
5					
6					
8					
10	JENDL-4.0	3.85mb			3.36mb

Ref. <http://www.ndc.jaea.go.jp/ndd/symposium/2010/program.html>

Table 2 Multiplication factors evaluated by criticality calculation for KUCA experiment

	JENDL-4.0	JEFF-3.2	ENDF/B-VII.0
Critical state 1	0.99835 ± 0.00018	1.00043 ± 0.00018	1.00100 ± 0.00018
Critical state 2	0.99808 ± 0.00018	1.00059 ± 0.00018	1.00103 ± 0.00018
Critical state 3	0.99828 ± 0.00018	1.00069 ± 0.00018	1.00097 ± 0.00018
Critical state 4	0.99804 ± 0.00018	1.00048 ± 0.00018	1.00094 ± 0.00018
Critical state 5	0.99826 ± 0.00018	1.00046 ± 0.00018	1.00088 ± 0.00018

The criticality calculations for the KUCA experiment is performed by MVP code, which is neutron transport calculation code based on Monte Carlo method with recent nuclear data JENDL-4.0, JEFF-3.2, and ENDF/B-VII.0. The multiplication factors are listed in table 2. The calculations are performed for each criticality condition to measure each control rod worth. The result should coincide with unity. The difference is supposed due to the capture cross-section of carbon, which is 3.85, 3.81, and 3.36 mbarn, respectively. Therefore, calculations based on JENDL-4.0 in which only the carbon cross-sections are changed to that of each library is performed, and similar tendency was confirmed. It comes from the difference of the cross-section. The result of JEFF-3.2 shows a good agreement with the criticality experiment. The cross-section of C-12 is 3.86 mbarn, but that of C-nat. is reduced

to 3.81 mbarn with considering the abundance of C-13. In addition, the cross-section of ENDF/B-7.1 is also increased to 3.86 mbarn. The result of JENDL-4.0 shows slightly lower criticality.

Recently, neutron scattering law data for graphite is revised in ENDF/B-8.0. The change is to consider the porosity of the graphite. By this change, the criticality may be slightly changed. With this change, the cross-section may have to be changed. In addition, neutron scattering law data for SiC, which is also employed in recent HTGR design due to the high oxidation durability, was also evaluated. These data are expected to be added to JENDL-5.0. We are planning to validate the data for the HTGR design.

## 7. Summary

In this report, the history, recent, and future plan of R&D of HTGR are described, and the requirement for nuclear data is introduced. The major points are as follows:

- The LOFC experiment demonstrated the outstanding safety feature of HTGR, and it attracted a particular attention especially after the Fukushima Daiichi Nuclear Accident.
- The R&D of HTGR with international cooperation have been recommended by the “Strategic Energy Plan” formulated by the government of Japan due to the attention to the outstanding safety feature and hydrogen generation.
- The R&D corporation with Poland was established. The plan to build commercial HTGR is clearly described in the report.
- To elucidate re-criticality in LOFC experiment is important for the commercial HTGR design. And, GBM may be necessary to avoid full scale mock-up experiment, which may be requested from the viewpoint of licensing of first of a kind commercial HTGR.
- The R&D of noise analysis needed by the LOFC experiment and that of GBM started by using KUCA in 2018.
- The neutron scattering law of graphite should be improved by using ENDF/B-8.0 with considering porosity. With this revision, the capture cross-section may have to be reduced. And, we are planning to validate the data for HTGR design.

With high expectations, recently R&D of HTGR are rapidly promoted. We should promote the R&D related to reactor physics and nuclear data as well.

## Acknowledgement

Authors appropriate to Dr. T. Sano, Dr. A. Sakon, and the Prof. K. Hashimoto of Kindai Univ., who corporate the KUCA experiment, and also to operators of HTTR who corporates the R&D of noise analysis system. This project is founded by the president of JAEA.

## 7 Performance of a gas-cooled reactor as a tritium production device for fusion reactors

Hideaki MATSUURA

Applied Quantum Physics and Nuclear Engineering, Kyushu University

744 Motoooka, Nishi-ku, Fukuoka 819-0395, Japan

e-mail: matsuura@kyudai.jp

To start up an initial fusion reactor and for technical tests for tritium circulation and blanket system, it is necessary to provide sufficient amount of tritium from an outside device. At this point, how to supply a sufficient amount of tritium for a future fusion DEMO and commercial reactors has not been clarified. We have proposed tritium production using a high temperature gas-cooled reactor (HTGR). In this paper, we introduce a HTGR system with a tritium production function for fusion reactors. Advantages of HTGRs for tritium production, performance of the typical HTGRs for tritium production, and current issues for development are discussed.

### 1. Introduction

To start up an initial fusion reactor and for technical test for tritium circulation and blanket system, it is necessary to provide a sufficient amount of tritium from an outside device. A required condition necessary for achieving self-sufficiency of deuterium-tritium (DT) fuel in a fusion reactor was investigated [1], and the uncertainties caused by nuclear data, calculation method, and system definition were revealed. Asaoka et al. [2] evaluated the tritium breeding ratio and the initial inventory required for the initial fusion power reactor with 2.28 GW thermal (~1GW electric) power as 1.10 and 27.6 kg respectively. In recent evaluations, amounts of tritium to be prepared for fusion reactor startup differ from 100 g to more than 10 kg [3-7]. The uncertainties of the amount of tritium-supply scenario still seem to be increasing. So far, the tritium for fusion reactors has been produced by using the  $D(n,\gamma)T$  reaction in the Canadian Deuterium Uranium (CANDU) reactors [8]. Since the cross section of the  $D(n,\gamma)T$  reaction has almost 6 orders smaller around the thermal-neutron energy range compared with the  ${}^6\text{Li}(n,\alpha)T$  reaction (see Fig. 1), the tritium production efficiency per year and per 1 GW electricity of CANDU reactor is smaller compared with other thermal fission reactors for tritium production using  ${}^6\text{Li}(n,\alpha)T$  reaction, i.e., 0.17-0.23 T kg/year/GWe. In Fig. 2 an annual change of the electricity produced and estimated tritium production by CANDU reactors in Canada, Korea, and Romania are plotted [9]. It is shown that these reactors have an ability of 2.2-3.0 kg/year tritium production in 2018. However, it is not clear whether these reactors can provide sufficient amount of tritium to fusion DEMO reactors after 20-30 years, because most of the reactors have already been operated over 30 years. To continue the development of fusion reactors, it is required a sure scenario of tritium supply at this point. We have proposed a tritium production method using high-temperature gas-cooled reactor [10,11].

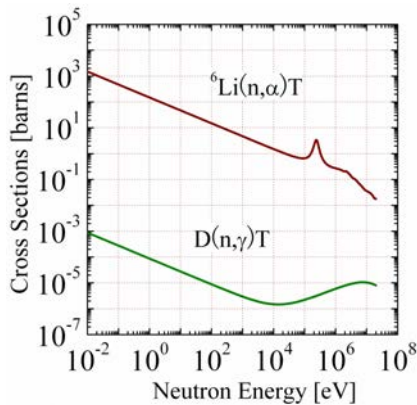


**Fig. 1** Cross sections of  ${}^6\text{Li}(n,\alpha)\text{T}$  and  $\text{D}(n,\gamma)\text{T}$  reactions (from JENDL-4.0).

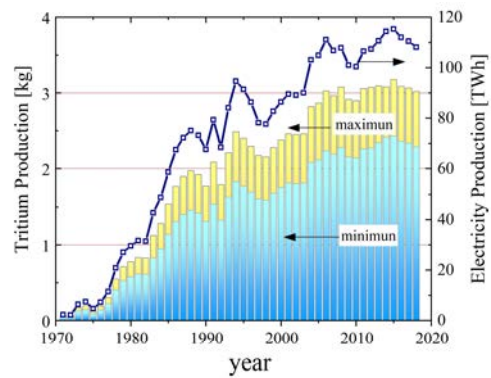


**Fig. 2** Tritium and electricity production by CANDU reactors. Yellow (blue) bars represent the maximum (minimum) estimation of tritium produced in each year.

## 2. Advantage of HTGR for tritium production

We consider the tritium production using the HTGR by inserting a Li compound as a burnable poison (BP) instead of a boron compound, i.e., an isotope as a neutron absorber is changed from  ${}^{10}\text{B}$  to  ${}^6\text{Li}$ . We intend to produce the tritium utilizing the nuclear reaction of  ${}^6\text{Li}(n,\alpha)\text{T}$ . The main core structure in the HTGR is graphite, which is chemically stable and does not react with the Li compound. Although the large core size of the HTGR is not attractive from the viewpoint of economy, it provides enough space for loading the Li compound without  ${}^6\text{Li}$  enrichment, along with structural materials to prevent the leakage of tritium. In the HTGR, the BP is usually used in a solid state (i.e., as  $\text{B}_4\text{C}$ ), and thus the Li compound can be loaded into the reactor's core without significantly changing the original structural design. The nuclear characteristics and fuel temperature were analyzed to confirm the nuclear and thermal feasibility of a lithium-loaded HTGR [12], and it was shown that the analysis results satisfied the design requirements and hence the nuclear and thermal feasibility was confirmed for a lithium-loaded HTGR that produces thermal energy and tritium [12].

Figure 3 presents the horizontal cross section of a gas turbine high-temperature reactor of 300 MWe nominal capacity (GTHTR300) core [13]. The core consists of 90 fuel columns arranged in an annular ring; 55 and 36 inner and outer removable reflector columns, respectively; 18 and 12 inner and outer control-rod guiding columns, respectively; and 8 outer fixed reflector sectors. Each fuel column is composed of 8 hexagonal graphite blocks, which are piled up in the vertical direction. The hexagonal fuel block is 407 mm wide across the flats (including 1-mm gaps at both sides) and 1000 mm high, with arrays of 57 fuel channels and 3 burnable poison (BP) insertion holes (Fig. 4). The fuel rod, which is placed in the fuel channel enclosed in a graphite block, is composed of fuel compacts and a graphite sleeve 26 mm in diameter. The diameter of each fuel channel in the fuel block is 39 mm, and helium gas flows in the space between walls of the fuel channel and the fuel rod as a coolant.

The horizontal cross section of the HTTR core is also shown in Fig. 5 (a) [14]. The core consists of 2 regions, i.e., actual core and reflector regions. The actual core consists of 30 fuel and 7 control-rod guide columns, each of which is composed of a stack of 5 fuel and 4 reflector blocks. The actual core is surrounded

by the reflector region, i.e., replaceable and permanent reflector blocks and 9 control-rod guide blocks. The core is 2.9 m in height and 2.3 m in diameter. Each hexagonal block is 360 mm wide across the flats and 580 mm high [see Fig. 5 (b)]. The fuel block contains 31 or 33 fuel channels and 3 BP insertion holes. 480 mm high Li rods with 15 mm Al<sub>2</sub>O<sub>3</sub> caps on both upper and bottom sides are loaded into the BP insertion holes.

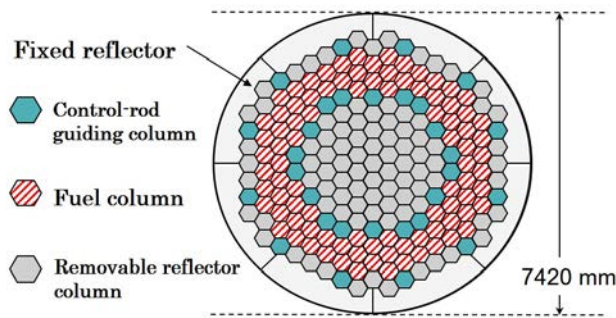


**Fig. 3** Horizontal cross-section of the GTHTR300 core.

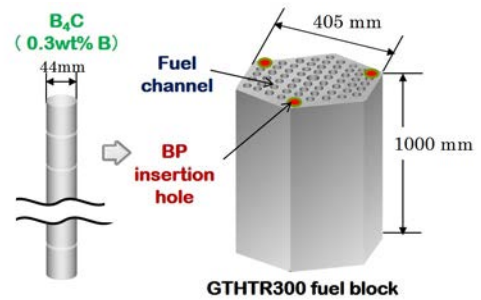


**Fig. 4** Fuel block with BP insertion holes and BP rod for GTHTR300.

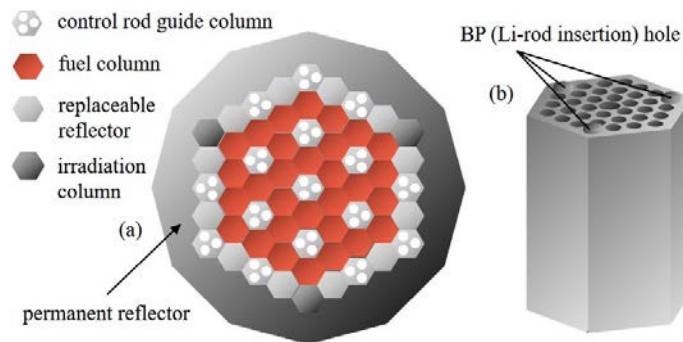


**Fig. 5** (a) Horizontal cross-section of the HTTR core, (b) Fuel block with Li-rod insertion holes.

### 3. Performance of HTGR for tritium production

The estimation of the amount of tritium produced and the effective multiplication factor during the GTHTR300 and HTTR 360-day operations was carried out using the continuous-energy Monte Carlo transport code MVP-BURN [15] using the whole core model. Throughout the calculations, nuclear data were taken from JENDL-3.3 [16] and JENDL-4.0 [17], and the results for each nuclear cross-section dataset are presented and compared in Figs. 6 and 7. The fuel region temperature was 1,100 °C and the Li-rod temperature was the same as the moderator (900 °C). In this study we assumed 360-day reactor operation period. All control rods were assumed to be pulled out. The time steps in the burn-up simulations were taken as 0, 1, 5, 30, 60, 120, 180 and 360 days. For each of the time steps, 6,000,000 neutrons were generated. The statistical errors of the effective multiplication factor and the reaction rate were less than 0.1% in all calculations, which is sufficient accuracy in our discussion.

In Figures 6 and 7, the effective multiplication factor  $k_{\text{eff}}$  keeps decreasing over the operation and reached the minimum value after the 360-day operation. On the contrary, the cumulative weight of the produced tritium is increasing over the time and reached the maximum value after the 360-day operation. In these simulations, as a typical value, a rod with a 44 mm diameter, a 6.4 (6.3) mm thick  $\text{Al}_2\text{O}_3$  layer, a 1 mm thick Zr layer, and a 2.4 (2.3) mm thick  $\text{LiAlO}_2$  layer are assumed when JENDL-4.0 (3.3) is used for GTHTR300. For HTTR, a rod with a 14 mm diameter, a 1.9 mm thick  $\text{Al}_2\text{O}_3$  layer, a 0.1 mm thick Zr layer, and a 2.4 (2.7) mm thick  $\text{LiAlO}_2$  layer are assumed when JENDL-4.0 (3.3) is assumed. In order to operate the reactor during 360 days, at least 1.02 of  $k_{\text{eff}}$  is required at the end of the operation. From Fig. 6 we can estimate that the possible weight of tritium produced in the GTHTR300 is roughly 800 g during 360-day operation. From Fig. 7 we can estimate that the possible weight of tritium produced in the HTTR is roughly 30 g during 360-day operation.

In JENDL-4.0 the neutron capture cross section of carbon is evaluated almost 10% larger compared with previous other cross section sets. It is well known that by using the JENDL-4.0 the effective multiplication factor in criticality is evaluated in smaller value, and the simulations become consistent with experimental observation in HTGRs [18]. When we use the JENDL-4.0 instead of 3.3, the effective multiplication factor is evaluated smaller, thus the amount of tritium produced in unit time is also decreased. As was explained before, the weight of Li loading into the core is adjusted so that the effective multiplication factor is the same value at the end of the operation (shown in Figs. 6 and 7). From the viewgraphs, we can find that the amount of tritium produced decreases by about several percentages when we adopted the JENDL-4.0.

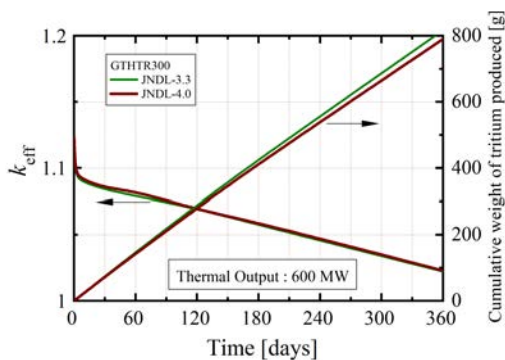


**Fig. 6** The effective multiplication factor and the amount of tritium produced for GTHTH300.

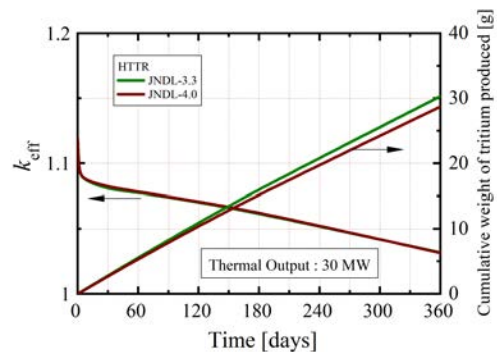


**Fig. 7** The effective multiplication factor and the amount of tritium produced for HTTR.

#### 4. Status of the development and current issues

During the operation, the amount of tritium flowing out from the Li rod into helium gas should be suppressed to a lower level as much as possible. Numerical simulations have predicted that if we could operate the HTGR in a low temperature range, keeping the rod temperature below 500 °C, the tritium leaking from the Li rod can be suppressed to almost 1% of the amount produced [19]. However, if we intended to operate the HTGR in a much higher temperature range (i.e., the rod temperature reaching 800-900 °C) so as to increase the electricity generation efficiency, the leakage of the tritium would rapidly increase. This is

because the hydrogen permeability of the  $\text{Al}_2\text{O}_3$  layer in the Li rod increases with the increase of the rod's temperature [20]. In order to reduce the leakage of tritium from the rod, we attempted to adopt Zr in the rod as a tritium absorption material to avoid increasing the inner tritium partial pressure [21-23]. To prevent the tritium absorption capability from decreasing due to oxidization via interacting with coexisting oxides (i.e.,  $\text{LiAlO}_2$  and  $\text{Al}_2\text{O}_3$ ), some kind of coating with an antioxidant material is necessary [21]; it is desirable to have a surface area of Zr is as large as possible. We propose the Li rod including Zr pebbles with Ni coating as shown in Fig. 8 [24].

We have experimentally measured the hydrogen absorption performance of Zr (i.e., hydrogen absorption speed) [24]. The performance is governed by concentration of hydrogen in Zr, surface area, H/Zr ratio, pressure and temperature of the circumstance [25, 26], in addition to the surface status, e.g., oxidization via interacting with coexisting oxides. On the basis of the measured data, we numerically simulated the tritium leakage from the Li rod during the reactor's operation and the correlation with the rod structure, assuming several patterns of the tritium absorption capability. The optimal size of each layer and the diameter of the pebble (e.g., x, y, and z in Fig. 8) should be clarified. At this point, we consider that a rod with a 14 mm diameter, a 1.9 mm thick  $\text{Al}_2\text{O}_3$  layer, a 0.1 mm thick Zr layer, and a 2.7 mm thick  $\text{LiAlO}_2$  layer, involving Zr pebbles with Ni coating and a 0.5 mm radius, is one of the most desirable structures of a Li-rod for an HTTR [24]. By using the presented rod, we estimate approximately 30 g of tritium can be produced in 360-day operation in HTTR, and the tritium flowout into He is less than 1% (when tritium absorption time is smaller than 1 hour [24]).

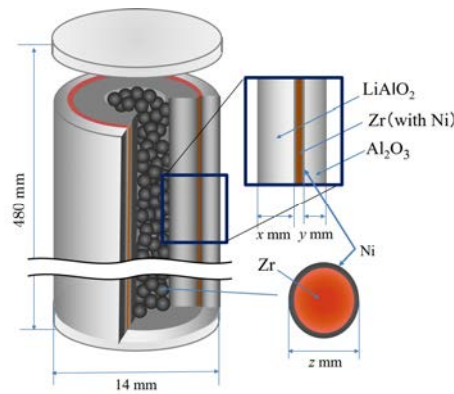


**Fig. 8** A schematic view of the Li-loading rod including Zr with Ni coating for HTTR.

## 5. Summary

To confirm the optimal Li-loading structure and to produce the tritium for fusion reactor stably, it is necessary to ascertain the performance of the Li-loading rod presented. We are now planning an irradiation test of the tritium production and containment. In order to complete the final design, the amount of tritium produced and leaked (i.e., the analysis model and the effective hydrogen absorption time of Zr) should be validated in a demonstration test in an HTTR.

## Acknowledgement

This work is supported by JSPS KAKENHI Grant-in-Aid for Scientific Research (B) JP18H1200 and cooperative program with BA (The Joint Implementation of the Broader Approach Activities in the Field of Fusion Energy Research) reactor design team in Japan. The author acknowledges the collaborators, Dr. K. Katayama, Dr. T. Otsuka, Dr. M. Goto, S. Nakagawa, Dr. E. Ishitsuka, Dr. S. Hamamoto, Dr. K. Tobita, Dr. R. Hiwatari, Dr. Y. Someya, Dr. Y. Sakamoto, and students Y. Koga, T. Sukanuma, and K. Nakagawa for many useful discussions.

## References

- [1] M. A. Abdou, et al., Fusion Technol., **9** (1986) 250.
- [2] Y. Asaoka, et al., Fusion Technol., **30** (1996) 853.
- [3] M. Nishikawa, Fusion Eng. Des., **87** (2012) 466.
- [4] R. Kasada, et al., Fusion Eng. Des., **98-99** (2015) 1804.
- [5] S. Kwon, et al., IEEE Tr. Fusion Sci. (2013).
- [6] S. Konishi, et al., Fusion Eng. Des., **121** (2017) 111.
- [7] R. Hiwatari, et al., J. Atomic Energy Society of Japan: ATOM  $\Sigma$ , **60** (2018) 488 ( in Japanese ).
- [8] P. Gierszewski, Fusion Eng. Des., **10** (1989) 399-403.
- [9] IAEA Web Site: <https://pris.iaea.org/PRIS/WorldStatistics/OperationalReactorsByRegion.aspx> (accessed 2019/12/22).
- [10] H. Matsuura, et al., Nucl. Eng. Des., **243** (2012) 95.
- [11] H. Matsuura, J. Plasma Fusion Res., **93** (2017) 457 ( in Japanese ).
- [12] M. Goto, et al., Fusion Eng. Des., **136** (2018) 357.
- [13] X. Yan, et al., Nucl. Eng. Des., **222** (2003) 247.
- [14] S. Saito, et al., JAERI 1332 (1994).
- [15] Y. Nagaya, et al., JAERI 1348 (2005).
- [16] K. Shibata, et. al., J. Nucl. Sci. Technol., **39** (2002) 1125.
- [17] K. Shibata, O. Iwamoto, T. Nakagawa, et al., J. Nucl. Sci. Tech., **48** (2011) 1.
- [18] M. Goto, et al., J. Nucl. Sci. Tech., **48** (2011) 965.
- [19] H. Nakaya, H. Matsuura, K. Katayama, et al., Nucl. Eng. Des., **292** (2015) 277.
- [20] K. Katayama, H. Ushida, H. Matsuura, et al., Fusion Sci. Tech., **68** (2015) 662.
- [21] K. A. Burn, E. F. Love, C. K. Thornhill, 2012.TTQP-1-015, **19**, PNNL-22086.
- [22] S. Nagasumi, H. Matsuura, K. Katayama, et al., Fusion Sci. Tech., **72** (2017) 753.
- [23] Y. Koga, H. Matsuura, Y. Ida, et al., Fusion Eng. Des., **136** (2018) 587.
- [24] H. Matsuura, et al., Fusion Eng. Des., **146** (2019) 1077.
- [25] E. Zuzek, et al., Bull. Alloy Phase Diag., **11** (1990) 385.
- [26] S. Yamanaka, et al., J. Nucl. Mater., **167** (1989) 231.

## 8 Research and development of an innovative transmutation system of LLFP by fast reactors

Satoshi CHIBA

Tokyo Institute of Technology

e-mail: chiba.s.ae@m.titech.ac.jp

A project on transmutation of LLFPs, supported by MEXT, is described. In this project, 6 LLFPs, namely,  $^{79}\text{Se}$ ,  $^{93}\text{Zr}$ ,  $^{99}\text{Tc}$ ,  $^{107}\text{Pd}$ ,  $^{129}\text{I}$  and  $^{135}\text{Cs}$ , were selected as target materials. We combine materials including these LLFPs with novel moderators  $\text{YH}_2$  and  $\text{YD}_2$  to soften neutron spectra of fast reactors to make transmutation rate larger. The ultimate goal is to make the support factor, which is defined as a ratio of amount of a specific LLFP transmuted and amount of the same LLFP populated in the core of fast reactors, to be larger than 1 so that we can actually reduce amount of LLFPs. We have shown that such a transmutation scheme is possible without performing isotopic separation nor even-odd separation of LLFPs.

### 1. Introduction

Disposal and proper treatment of radioactive wastes generated by nuclear power plants are considered to be important national problems, which is directly connected to acceptance of nuclear technology from the society. Partitioning and transmutation scenario is an efficient way to achieve reduction of radioactive wastes. Minor actinide is the major target of such a scheme. However, if we perform transmutation of MAs, they are destroyed by the fission reaction and hence enhancement of long-live fission products (LLFPs). We recognize that this problem reduces to the problem how to treat the LLFPs. On the other hand, LLFPs are the major source of dose level which general public may be exposed from deep geological repository site after several hundred thousands years, which makes construction of such site extremely difficult. Therefore, we aim to design a transmutation scheme for the LLFPs. Among 7 LLFPs, we try to propose a scheme to transmute 6 LLFPs, namely,  $^{79}\text{Se}$ ,  $^{93}\text{Zr}$ ,  $^{99}\text{Tc}$ ,  $^{107}\text{Pd}$ ,  $^{129}\text{I}$  and  $^{135}\text{Cs}$  by fast reactors.  $^{126}\text{Sn}$  was excluded since its neutron capture cross section is estimated to be very small, even though its uncertainty is quite large (there is no data).

At the beginning, we aimed to utilize MONJU experimental reactor for this transmutation. However, after 1 year of research, it was decided to shut down MONJU by the government, so we switched to utilize a small fast reactor equivalent to MONJU.

2. Outline of the research

We performed research in conceptual design of LLFP transmutation system which comprised reactor physics analysis, selection of target materials, thermal hydraulics, safety, retrieval and reprocessing of LLFPs, irradiation scheme, nuclear data, planning of irradiation test, feasibility of transmutation of LLFP by large FBR, and social scientific aspects of transmutation technology. These results were already published in Refs. [1-6] as well as press releases [7-10] and patent application [11], so we do not describe them in detail here. The basic concept is to irradiate materials including the target LLFPs in the blanket region of MONJU-like small fast reactors. The basic concept is shown in Fig. 1.

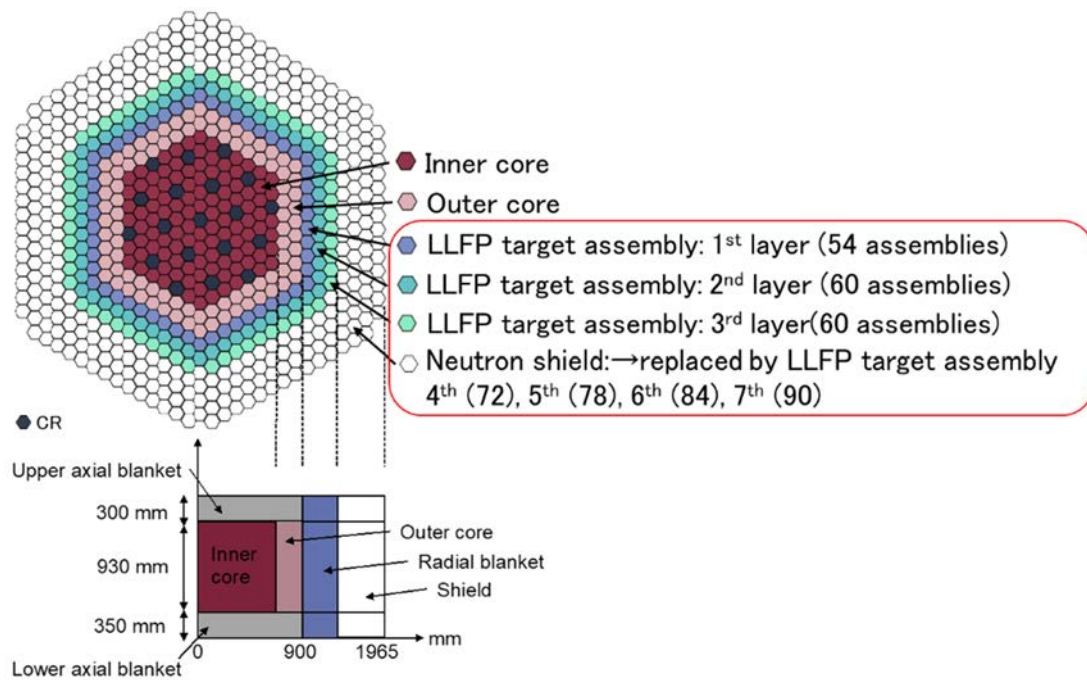


Fig. 1 Basic concept of LLFP transmutation considered in the present project.

We made several trial and error in analyses, then reached to the following 4 concepts:

1. A reactor containing 6 LLFPs simultaneously in the radial and axial blanket and even in some structural part of the reactor (Fig. 2)[3]
2. A system of 3 reactors, each transmuting 2 LLFPs (Fig. 3)
3. A system of 1 reactor containing 4 LLFPs  $^{99}\text{Se}$ ,  $^{99}\text{Tc}$ ,  $^{107}\text{Pd}$  and  $^{129}\text{I}$
4. A system of 2 reactors, 1 containing 3 LLFPs  $^{79}\text{Se}$ ,  $^{99}\text{Tc}$  and  $^{129}\text{I}$ , and 1 used for breeding of  $^{239}\text{Pu}$

These systems can be selected according to the needs of the society.

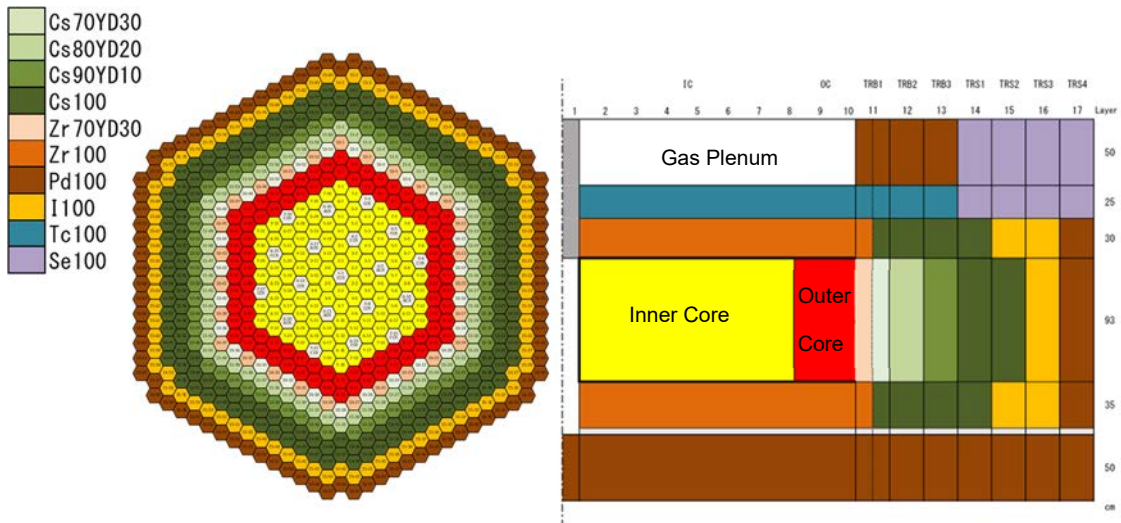


Fig. 2 A system for simultaneous transmutation of 6 LLFPs [3]

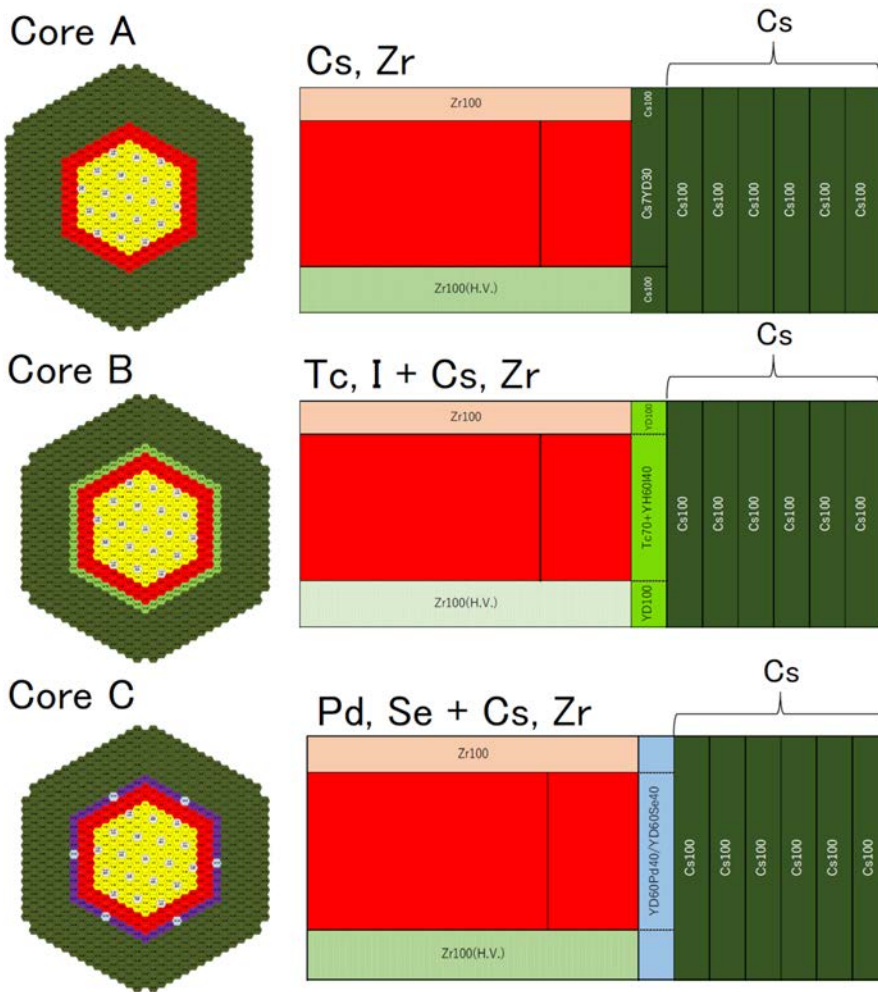


Fig. 3 A system of combination of 3 fast reactors, each transmuting different LLFPs

At the same time, researches on nuclear data have been performed, and the results were published as Ref. [2] and [5-6]. Especially, new fission yield data was generated, and it will be included in the next version of JENDL FPY data library.

We have found that the transmutation ratios of LLFPs in these systems have rather large uncertainty reflecting the fact that all of them are radioactive nuclei (so nuclear data is not accurate enough). It is high desirable to quantify uncertainty of nuclear data of these isotopes.

### 3. Summary

A project on transmutation of LLFPs by MONJU-like small fast reactors is described. The details can be found in the given references, and more papers are going to appear.

### Acknowledgement

This study comprises the results of “Research and development of an innovative transmutation system of LLFP by fast reactors” entrusted to the Tokyo Institute of Technology by the Ministry of Education, Culture, Sports, Science and Technology of Japan (MEXT).

### References

- [1] S.Chiba, T.Wakabayashi, Y.Tachi, N.Takaki, A.Terashima, S.Okumura and T.Yoshida, “Method to Reduce Long-lived Fission Products by Nuclear Transmutations with Fast Spectrum Reactors”, *Scientific Reports*, 7, 13961(2017).
- [2] M.D.Usang, F.A.Ivanyuk, C.Ishizuka and S.Chiba, “Correlated transitions in TKE and mass distributions of fission fragments described by 4-D Langevin equation”, *Scientific Reports*, 9, 1525(2019).
- [3] T.Wakabayashi, M.Takahashi, S.Chiba, N.Takaki, Y.Tachi and Y.Tahara, “Core concept of simultaneous transmutation of six LLFP nuclides using a fast reactor”, *Nucl. Eng. Design*, 352, 110208(2019).
- [4] T.Wakabayashi, Y.Tachi, M.Takahashi, S.Chiba and N.Takaki, “Study on method to achieve high transmutation of LLFP using fast reactor”, *Scientific Reports*, 9, 19156(2019).
- [5] C.Ishizuka, X.Zhang, M.D.Usang, F.A. Ivanyuk and S.Chiba, “The effect of the doubly magic shell closures in  $^{132}\text{Sn}$  and  $^{208}\text{Pb}$  on the fission fragments mass distributions of superheavy nuclei”, *Phys. Rev. C*, 101, 011601(R)(2020).
- [6] K.Tsubakihara, S.Okumura, C.Ishizuka, T.Yoshida, F.Minato and S.Chiba,

“Systematic Evaluation of Independent Yields Based on Nuclear Shell Correction and Boltzmann Weight” (to be submitted to J.N.S.T.).

- [7] Tokyo Tech. News, <https://www.titech.ac.jp/news/2017/039840.html> (accessed 2020/03/24).
- [8] Tokyo Tech. News, <https://www.titech.ac.jp/news/2019/043509.html> (accessed 2020/03/24).
- [9] Tokyo Tech. News, <https://www.titech.ac.jp/news/2020/046068.html> (accessed 2020/03/24).
- [10] Tokyo Tech. News, <https://www.titech.ac.jp/news/2020/046173.html> (accessed 2020/03/24).
- [11] Patent application 2020-046979, March 17, 2020 (Tokyo City University).

This is a blank page.

## 9 Nuclear Data Activities and Related Database Services at the IAEA Nuclear Data Section

Shin OKUMURA<sup>1</sup>

<sup>1</sup>International Atomic Energy Agency, 1400 Vienna, Austria  
e-mail:s.okumura@iaea.org

The Nuclear Data Section (NDS) of IAEA conducted the completeness assessment of fission product yield data in EXFOR database against two lists of articles that were used in ENDF/B-VI and UKFY3.0 library evaluations. We found that 194 articles were found to be relevant for new entry. The IAEA-NDS also launched a new online application, the Medical Isotope Browser, which allows professional users to calculate and predict the medical isotope production yield of any diagnostic, therapeutic or theranostic isotope with accelerators. We here review above two main activities.

### 1 Introduction

The Nuclear Data Section (NDS) of IAEA assembles, develops and disseminates nuclear data and related databases for basic science and nuclear applications. The IAEA-NDS develops nuclear data, nuclear structure and decay data libraries, disseminates them, and maintains databases, as well as organize the various meetings to produce outputs by encouraging collaboration worldwide.

The fission product yield (FPY) is important for many application fields because FPY determines the compositions of radioactive nuclear wastes, affect the safety-operation of nuclear power plants (because of delayed neutron emissions), design accelerator-driven systems (ADS) systems for transmutations of minor actinides, and so on [1]. The IAEA-NDS has extensively reviewed the user needs in these fields in the previous IAEA Coordinated Research Projects (CRPs) and meetings [1, 2, 3, 4].

In recent years, several theories and models have been developed to study nuclear fission phenomenon, such as microscopic theories [5, 6] and dynamical models [7]. Despite many theories and models have been developed, it is still a challenging problem to understand nuclear fission phenomenon, because nuclear fission is a very complex process that incorporates large-amplitude collective motion of nucleons. Besides theoretical and modelling approaches, the experimental observation of FPY is also still a challenging subject while various experimental fission techniques have been developed [8]. The current evaluated libraries, *i.e.* later than ENDF/B-VI [9], JENDL/FPY-2011 [10], and JEFF3.3 FPY library [11], comprise from the evaluation of the experimental data as well as some empirical models such as  $Z_P$  model from Wahl systematics [12]. Such evaluation works have been done about two decades ago and only a few additions have been applied [13]. Recent increase in interests on the FPY from many fields stresses the importance to develop the new evaluated FPY data libraries [3]. Under this circumstance, the IAEA-NDS will launch the new CRP in 2020 on “Updating Fission Product Yield Data for Applications” for independent and cumulative FPY important actinides. Prior to start the CRP, the IAEA-NDS investigated the completeness of FPY data in the experimental nuclear reaction (EXFOR) database [14, 15] against FPY datasets that were used in the evaluation of in ENDF-B/VI [16] and UKFY3.0 [17].

The IAEA-NDS also launched a new online application, the Medical Isotope Browser [18], which brings data directly to professionals in radiopharmaceutical research and industry. In this report, we review the result of completeness investigation of FPY data in EXFOR and the brief instruction of the Medical Isotope Browser.

## 2 FPY data assessment

The EXFOR database was established in 1960s originally exclusively neutron-induced reaction data and contains data for more than 22,000 experiments, resulting in more than 13,000,000 data points, and continue the effort to compile new and overlooked data, and to remove errors. Nevertheless, some of the FPY data have not been accessible due to the classification or dissertation. Prior to start new CRP on FPY evaluation, the IAEA-NDS conducted the completeness investigation of FPY data in EXFOR database to compare with the articles cited in the ENDF-B/VI [16] and UKFY3.0 [17] reports. The detail of the assessment procedure is described in Refs. [19, 20]. The complete list of articles reviewed in this assessment are listed in the Appendix of Ref. [21].

The ENDF/B-VI report cites 1,602 references, of which 924 references provide FPY data adopted, while the rest 678 references are not used for the evaluation because of superseded later publication. The UKFY3.0 evaluation summary cites 646 references. About 600 references are overlapped in both ENDF/B-VI and UKFY3.0 reports and about 1,200 references are unique. Table 1 shows the summary of this investigation. We reviewed all articles that possibly have experimental FPY data that is relevant to compile into EXFOR database. The articles were then categorized into (a) Already compiled, (b) not found in EXFOR and need to be compiled, (c) need to check further details, or (d) not relevant. The world wide collaboration, NRDC network, has started to compile (a) cases.

Table 1: The number of FPY references categorised during our assessment for those cited in evaluation summaries of ENDF/B-VI [16] and UKFY3.0 [17]. See Refs. [19, 20, 21] for details.

Source	Exist <sup>a</sup>	Create new entry <sup>b</sup>	Check <sup>c</sup>	Not relevant <sup>d</sup>	Total
ENDF/B-VI	618	154	36	116	924
UKFY3.0	409	139	32	64	645
Total <sup>e</sup>	720	194	54	167	1203

<sup>a</sup> Already compiled in EXFOR.

<sup>b</sup> Not found in EXFOR and need to create new entry.

<sup>c</sup> Need to check if all relevant data are compiled in EXFOR entry.

<sup>d</sup> Not FPY or not relevant for EXFOR or the original article cannot identify.

<sup>e</sup> Total after elimination of overlap.

Figure 1 shows the number of FPY entries that have been stored in EXFOR database with the publication year on the horizontal axis. The number of FPY entries in EXFOR is supposed to reflect the number of publications in a year. Based on this data, the first FPY measurement data was published in 1943. Until 1960s, FPY measurements are mostly dominated by the neutron induced fission of important actinides as targets, namely Th, U, Pu, and Cf isotopes. The experimental FPY data drastically increase in 1970s. After 1980s, variations of target isotopes, *e.g.* Np, Am or Cm, have increased while the majority of trend remains. Up to now, the majority of reactions are the neutron induced fission followed by the spontaneous fission, photon, and proton induced fission.

By comparing the number of FPY data in Fig. 1 extracted from EXFOR database on July 2019 and on December 2019, the number of entries has increased in wide range of published year as a result of compilation efforts of NRDC network.

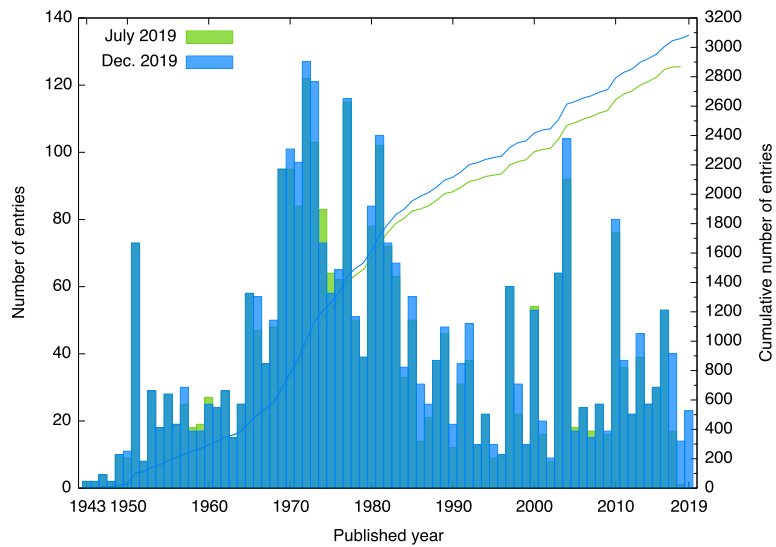


Figure 1: Number of FPY related entries extracted from EXFOR database on July 2019 (before starting compilations) and December 2019 (some FPY data from this assessment have been compiled.)

### 3 Medical Isotope Browser

The IAEA-NDS launch a new web application product for the prediction of medical isotope production yield of any diagnostic, therapeutic or theranostic isotope with accelerators. The isotope production yield can be calculated for any isotope production route for many targets, natural or enriched, reacting with incident protons, deuterons, tritons, helions or alpha particles. IAEA has evaluated cross sections in a series of IAEA research projects that started in 2005. The cross sections from IAEA-evaluated medical isotope data library [22, 23] for about 150 reaction channels are used for the calculation. For reactions or extended energy ranges (up to 200 MeV) not covered by IAEA-evaluated cross sections, TENDL-2017 library [24] are used. User can also use own cross section data as input. The radioactive decay from isotope to any other isotope is calculated based on the JEFF-3.3-RD decay data library [11].

The Medical Isotope Browser can be reached via IAEA-NDS web site (URL <https://nds.iaea.org/mib>). The essential fields in the form are Product, Projectile, Target, Thickness, Incident energy, and Irradiation time. On the left panel of Figure 2 shows the sample inputs for medical isotope production yield of  $^{44}\text{Sc}$  from  $^{44}\text{Ca}+p$  reaction with 20 MeV incident energy and  $1\ \mu\text{A}$  current for 1 day irradiation followed by 12 hour elapsed time after irradiation. The cross section used in the calculation can be plotted compared with available experimental data as shown in the right panel of Fig. 2. As above example shows, the Medical Isotope Browser gives a first guess to users who aim to find a new production route, an optimal incident energy, and so on. The IAEA-NDS acknowledges for any feedback to make the product better.

### 4 Conclusion

The IAEA-NDS investigated the completeness of the FPY data in the EXFOR database by crosschecking against the articles listed in the ENDF-B/VI and UKFY3.0 evaluation reports. It was found that approximately 194 references are relevant to create new entry in EXFOR database, and about 54 references must be checked with the existing EXFOR entries to ensure that the all experimental FPY data are properly compiled. The compilation has been started by data centers of NRDC network.



Figure 2: Screenshots of Medical Isotope Browser. (Left) Sample isotope yield calculation of  $^{44}\text{Sc}$  from  $^{44}\text{Ca} + p$  at 20 MeV incident energy. (Right) Cross section view used in the calculation showing together with some experimental data.

The new web application, the Medical Isotope Browser, has been released. The isotope production yield can be calculated for any isotope production route for many targets, natural or enriched, reacting with incident protons, deuterons, tritons, helions or alpha particles.

## References

- [1] International Atomic Energy Agency. CRP on Compilation and evaluation of fission yield nuclear data (1991-1996). International Atomic Energy Agency; 2000. IAEA-TECDOC-1168.
- [2] CRP on Fission Product Yield Data for the Transmutation of Minor Actinide Nuclear Waste (1997-2002). International Atomic Energy Agency; 2008. STI/PUB/1286.
- [3] Dimitriou P, Hamsch FJ, Pomp S (eds.). Fission Yields: current status and perspective in measurements, theory and evaluations. International Atomic Energy Agency; 2016. INDC(NDS)-0713.
- [4] Minato F, Okumura S, Koning A, Kawano T. Implementation of the Hauser-Feshbach theory for Fission Product Yield Evaluation and Fission Modelling. International Atomic Energy Agency; 2019. IAEA-NDS-230. <https://www-nds.iaea.org/publications/nds/iaea-nds-0230/> (accessed 2020/3/24).
- [5] Bertsch GF, Loveland W, Nazarewicz W, Talou P. Benchmarking nuclear fission theory. 2015 may;42(7):077001.
- [6] Schunck N, Robledo LM. Microscopic theory of nuclear fission: a review. Reports on Progress in Physics. 2016 oct;79(11):116301.
- [7] Ishizuka C, Usang MD, Ivanyuk FA, Maruhn JA, Nishio K, Chiba S. Four-dimensional Langevin approach to low-energy nuclear fission of  $^{236}\text{U}$ . Phys Rev C. 2017;96:064616.
- [8] Andreyev AN, Nishio K, Schmidt KH. Nuclear fission: a review of experimental advances and phenomenology. Reports on Progress in Physics. 2017 nov;81(1):016301.

- [9] Brown DA, Chadwick MB, Capote R, Kahler AC, Trkov A, Herman MW, et al. ENDF/B-VIII.0: The 8th Major Release of the Nuclear Reaction Data Library with CIELO-project Cross Sections, New Standards and Thermal Scattering Data. Nuclear Data Sheets. 2018;148:1 – 142. Special Issue on Nuclear Reaction Data.
- [10] Katakura J. JENDL FP Decay Data File 2011 and Fission Yields Data File 2011. Japan Atomic Energy Agency; 2012. JAEA-Data/Code 2011-025.
- [11] Kellett MA, Bersillon O, Mills RW. The JEFF-3.1/-3.1.1 radioactive decay data and fission yields sub-libraries. OECD NEA; 2009. JEFF Report 20 OECD NEA.
- [12] Wahl AC. Systematics of Fission-Product Yields. Los Alamos National Laboratory; 2002. LA-13928.
- [13] Kawano T, Chadwick MB. Estimation of  $^{239}\text{Pu}$  independent and cumulative fission product yields from the chain yield data using a Bayesian technique. Journal of Nuclear Science and Technology. 2013;50(10):1034-1042.
- [14] Otuka N, Dupont E, Semkova V, Pritychenko B, Blokhin AI, Aikawa M, et al. Towards a More Complete and Accurate Experimental Nuclear Reaction Data Library (EXFOR): International Collaboration Between Nuclear Reaction Data Centres (NRDC). Nuclear Data Sheets. 2014;120:272 – 276.
- [15] Zerkin VV, Pritychenko B. The experimental nuclear reaction data (EXFOR): Extended computer database and Web retrieval system. Nuclear Instruments and Methods in Physics Research Section A: Accelerators, Spectrometers, Detectors and Associated Equipment. 2018;888:31-43.
- [16] England TR, Rider BF. Evaluation and compilation of fission product yields. Los Alamos National Laboratory; 1994. ENDF-349, LA-UR-94-3106.
- [17] Mills RW. Fission product yield evaluation: Appendix 5. University of Birmingham; 1995.
- [18] Medical Isotope Browser;. <https://nds.iaea.org/mib> (accessed 2020/3/24).
- [19] Okumura S. Experimental fission product yields adopted in ENDF and UKFY evaluation but missing in EXFOR (A29). 2019;NRDC Meeting 2019.
- [20] Okumura S. Experimental fission product yields missing in EXFOR. NRDC Memo CP-D/979. 2019.
- [21] Fleming M, Kawano T, Otuka (eds ) N. Fission Product Yield Experimental Database. International Atomic Energy Agency; 2019. INDC(NDS)-793.
- [22] Tárkányi FT, Ignatyuk AV, Hermanne A, Capote R, Carlson BV, Engle JW, et al. Recommended nuclear data for medical radioisotope production: diagnostic positron emitters. Journal of Radioanalytical and Nuclear Chemistry. 2019;319(2):533–666.
- [23] Engle JW, Ignatyuk AV, Capote R, Carlson BV, Hermanne A, Kellett MA, et al. Recommended Nuclear Data for the Production of Selected Therapeutic Radionuclides. Nuclear Data Sheets. 2019;155:56 – 74. Special Issue on Nuclear Reaction Data.
- [24] Koning AJ, Rochman D, Sublet JC, Dzysiuk N, Fleming M, van der Marck S. TENDL: Complete Nuclear Data Library for Innovative Nuclear Science and Technology. Nuclear Data Sheets. 2019;155:1 – 55. Special Issue on Nuclear Reaction Data.

This is a blank page.

## **10 Status of the Nuclear Energy Agency Data Bank – Services for Nuclear Data and Computer Programs**

Kenya SUYAMA, Franco MICHEL-SENDIS, Alice DUFRESNE and Maria-Eleni RAGOUSI

Nuclear Energy Agency (NEA) Data Bank  
Organisation for Economic Cooperation and Development (OECD)  
2, rue André Pascal, 75775 Paris Cedex 16, France  
e-mail: kenya.suyama@oecd-nea.org

The Nuclear Energy Agency (NEA) Data Bank is responsible for the coordination of the Joint Evaluated Fission and Fusion (JEFF) Nuclear Data Library project, which is a collaboration between NEA Data Bank participating countries. The JEFF library combines the efforts of its participating institutions to produce sets of evaluated nuclear data, for fission and fusion applications. This evaluated nuclear data library is a reference for many European countries, and in particular for the French nuclear industry. In addition to the Nuclear Data Services (NDS), the Data Bank Computer Program Services (CPS) is in charge of providing direct services to end users by collecting and disseminating computer programs in the Data Bank participating countries and organising training courses on the most widely used codes. The Data Bank also supports other NEA standing technical committees (STCs). For example, the Data Bank has been developing the Thermochemical Database (TDB) Project since 1984, following recommendations by the NEA Radioactive Waste Management Committee (RWMC) concerning the need for a database of high-quality thermochemical data for species relevant to performance assessments of deep geological repositories.

### **1. Introduction**

With the consolidation of the Computer Program Library (CPL) and the Neutron Data Compilation Centre (CCDN) – established in Ispra (Italy) and Saclay (France), respectively in 1964 as common service providers for the European Nuclear Energy Agency (ENEA) – the Data Bank of the Nuclear Energy Agency was founded in 1978. Since then, the NEA Data Bank has been providing computer codes and nuclear data to end users of its participating countries and a platform to exchange information in these technical fields.

It is widely known that the main activity of the Data bank is its: i) Computer Program Services (CPS); and ii) Nuclear Data Service (NDS) to disseminate computer codes and nuclear data. Since the end of 1980s, however, the Data Bank has been supporting the activities of NEA standing technical committees (STCs), which has in fact become one of the most important activities of the Data Bank today. Indeed, the Data Bank is also overseeing the controlled distribution of integral experimental data and databases, and of joint-project outcomes, in addition to preserving all scientific content. Therefore, the activity and the role of the Data Bank in terms of knowledge preservation and management has been increasing in importance and is now referred to as “Knowledge Preservation and Management” (KPM).

This article provides end users of the Data Bank not only with an outline of current Data Bank activities, i.e. NDS, CPS and KPM, but also with some strategic directions for the future.

### **2. Nuclear Data Services [1]**

The Nuclear Data Services (NDS) of the Data Bank overlooks all nuclear data related activities carried out within the framework of the Data Bank. These activities include: the co-ordination of the JEFF Nuclear Data Library project; the compilation of experimental data (EXFOR) by agreement with the network of international Nuclear Reaction Data Centres (NRDC); and, in recent years, the definition and implementation of verification

and benchmarking processes for nuclear data, under the scope of the nuclear data validation mission of the Data Bank. A brief description of these activities is given below:

As co-ordinator and secretariat to the JEFF Nuclear Data Library Project, the NDS organises the “Nuclear Data Week” twice a year with the aim of gathering experimentalists, evaluators and end users belonging to the JEFF community, along with other representatives of Nuclear Data projects carried out under the NEA auspices (WPEC) or in other NEA member countries (in particular, the European Commission). This project is a mandated activity of the Data Bank. The current mandate of the JEFF project is aimed at preparing and releasing the next update of the library, JEFF-4, by 2024. This release would follow the latest JEFF-3.3 library release, dating from the end of 2017.

Another main activity of the NDS is the coordination of the Data Bank contribution to the Nuclear Reaction Data Centres (NRDC) Network of the International Atomic Energy Agency (IAEA), which oversees the compilation of experimental nuclear reaction data (EXFOR) database. The Data Bank is responsible for the compilation of reaction data in the EXFOR database that has been obtained from Data Bank participating countries.

The NDS also carries out technical developments in the area of nuclear data visualisation, verification and validation for end users of the nuclear data library, with the development of tools such as JANIS for the visualisation of nuclear data and the implementation of verification and validation (V&V) sequences such as the Nuclear Data Evaluation Cycle (NDEC) for the benchmarking and validation of nuclear data. This work also provides an important infrastructure that is routinely used by the JEFF project.

### **3. Computer Program Services [2]**

The Computer Program Services (CPS) collects computer codes, integral experimental data and other related documents and disseminates them to end users. The CPS also verifies deposited computer programs to ensure that they can easily be installed and used by those who will receive them. With more than 55 years of experience, the CPS distributes approximately 3 500 packages of computer code and integral experimental data every year, with a careful screening of the requests to comply with the corresponding restrictions. This distribution also includes the outcomes of joint projects conducted by NEA STCs.

The CPS acts as an important hub in the field of exchanging nuclear related computer codes around the world. The Data Bank has an agreement, in particular, with the Radiation Safety Information Computational Centre (RSICC) for the exchange of computer programs between Data Bank participating countries and the RSICC service area (i.e. in the United States and Canada). The Data Bank also exchanges computer codes with non-OECD countries according to an arrangement with the International Atomic Energy Agency (IAEA). This service to non-OECD countries is carried out in compliance with the procedures set out by NEA Data Bank countries, which developed the requested code.

The CPS also organises approximately 10+ training courses every year on the most popular computer codes, where code developers are leading the course. In recent years, this activity has been recognised as key to sustaining the technical knowledge of nuclear technology with its vast contribution to the education of nuclear professionals.

For the past two years, the CPS has been attempting to change the licensing framework for its computer codes catalogue so as to comply with requests from Data Bank participating countries and trends in the licensing of codes with applications in the nuclear science and technology domain. Currently, two main licence types co-exist, the “single site” versus “single user” licences. The “single site” licence, which allows the designated establishment to share codes among all staff members, will disappear upon the introduction of the generic “single user licence”, expected to enter into force during 2020.

### **4. Knowledge Preservation and Management and NEA standing technical committees**

In addition to the CPS and NDS, the Data Bank has another important function, which is to collaborate with and offer support to NEA STCs in the area of knowledge preservation and management (KPM) by supporting the development and dissemination of databases.

For example, the International Criticality Safety Benchmark Evaluation Project (ICSBEP) and international Reactor Physics Experiment Evaluation (IRPhE) Project are evaluated and revised under the working parties of the NEA Nuclear Science Committee (NSC). It is the CPS, however, that receives and handles the

requests for these two projects. The Data Bank also supports the development and maintenance of databases such as the Code Validation Matrix (CCVM), Information System on Occupational Exposure (ISOE), International Fuel Performance Experiments (IFPE) and SINBAD, all of which are under the auspices of the NEA Committee on the Safety of Nuclear Installations (CSNI).

The Data Bank directly manages the Thermochemical Database (TDB) project [3], which started in 1984 following a recommendation by the NEA Radioactive Waste Management Committee (RWMC). The TDB is a database of evaluated and qualified thermochemical data, which is required for the safety evaluation of radioactive waste disposal facilities. The TDB project is carried out through separate funds from 12 countries, and the data is used as an international reference.

Because of the increased importance of peer-reviewed and internationally recognised experimental data, for example the validation of computer simulation systems, the share of integral experimental data in the total dispatch number of the CPS has been increasing, particularly in recent years. Assembling, preserving and managing data obtained through past and current research and development (R&D) activities is the first step in contributing to the effective use of resources invested in R&D programmes.

NEA Data Bank experience in the area of KPM has thus become a strength to build upon, and the Data Bank now considers databases as a key pillar to this strategy. The idea is therefore to transition from Computer Program Services to Computer Program and Database Services, which will centralise NEA wide efforts, including those involving STCs, so as to preserve, evaluate and distribute data in support of V&V activities for NEA member countries. This idea was presented to the Data Bank management committee, the Management Board for the Development, Application and Validation of Nuclear Data and Codes (MBDAV), at its 2019 meeting, and will be further discussed at the MBDAV meeting in 2020.

## 5. Joint CPS-NDS initiative for a nuclear data and code performance comparison

Aligned with the objective of better data preservation and evaluation, the NDS and CPS are currently joining efforts to provide better services with regard to the benchmarking of nuclear data in conjunction with computer programs, from nuclear data processing to transport codes. The aim is to leverage the unique position of the NEA Data Bank – as a central point for both nuclear data and computer programs – to share quality-assured input data for integral experimental benchmark evaluations. This initiative will be carried out using a down-selection of both internationally recognised test cases and of computer codes, while promoting the inclusion of the code suites used in the Data Bank participating countries. This new initiative is now being actively discussed within the Data Bank and will be debated in more depth by MBDAV members in 2020.

## 6. Conclusion

The NEA Data Bank has been a centre of excellence for computer codes and nuclear data for over 50 years. Based on this unique experience, the Data Bank is striving to improve its activities through live and direct communication with end users from all its participating countries.

Each activity at the NEA Data Bank, including those involving Computer Program Services (CPS), Nuclear Data Services (NDS) and Knowledge Preservation and Management (KPM), can entail a substantial technical contribution from end users and for end users, and this activity must keep evolving to ensure better services for end users. This evolution includes not only a change of the framework of our service, such as the transformation of user licensing, but also new technical proposals related to database development for nuclear data and computer code validation. Activities related to database development are key to the future of the Data Bank as these offer real benefits to Data Bank participating countries.

The NEA Data Bank sees the needs of its end users as of utmost importance, and it highly appreciates, and welcomes, any comments and suggestions from end users.

*The opinions expressed and arguments employed herein are those of the authors and do not necessarily reflect the official views of the OECD, the NEA or of the governments of their member countries.*

## References

- [1] F. Michel-Sendis, L. Fiorito and M. Fleming (2018), “Perspectives on nuclear data activities at the Data Bank: Enhancing the validation function,” NEA News, Vol. 36.2, pp.4-8.
- [2] A. Dufresne, E. Poplavskaia, and K. Suyama (2019), “Overview of the Activities of the OECD Nuclear Energy Agency Data Bank Computer Program Services,” Proceedings of the International Conference on Mathematics and Computational Methods Applied to Nuclear Science and Engineering (M&C 2019), 25-29 August 2019, Portland, Oregon, United States.
- [3] M.E. Ragoussi and D. Costa, (2019) “Fundamentals of the NEA Thermochemical Database and its influence over national nuclear programs on the performance assessment of deep geological repositories”, J. Environ. Radioact. 2019, Vol. 196, p. 225.

## 11 From the resonance theory to the statistical model

Toshihiko KAWANO

Los Alamos National Laboratory, Los Alamos, NM 87545, USA

Email: kawano@lanl.gov

We present a brief introduction to the  $R$ -matrix theory for the compound nuclear reaction, and explain its relation to the energy-average cross section in the unresolved resonance region. To bridge these two representations of the compound reaction cross section, we utilize the Gaussian Orthogonal Ensemble (GOE) embedded in the scattering matrix to calculate the average cross sections, and demonstrate calculation of the decay width from a transmission coefficient that is a model input.

### 1. Introduction

When a slow neutron interacts with a nucleus, the reaction cross section shows a distinct resonating structure, in which each of the peak location corresponds to an eigenstate of the compound system just above the neutron separation energy. In the case of a fast-energy neutron (in the keV to MeV region), the reaction cross section no longer shows sharp resonances because the compound states strongly overlap each other. Under this circumstance, each of the resonances cannot be resolved, and an energy-average cross section is only meaningful. The average cross section can be related to statistical properties of resolved resonances, namely the average resonance spacing  $D$  and decay widths  $\langle\Gamma\rangle$ . These statistical properties are often studied by applying the Gaussian Orthogonal Ensemble (GOE) implemented in the  $S$  and  $K$ -matrices. Although this is an old problem, our recent development on the GOE Monte Carlo technique [1, 2] sheds a new light on some long standing compound nuclear reaction problems.

Figure 1 shows the neutron radiative capture cross section of  $^{157}\text{Gd}$  in JENDL-4.0 at low energies, where the fluctuation suddenly disappears beyond 300 eV.

This is because the representation of cross section changes at this boundary energy. Above

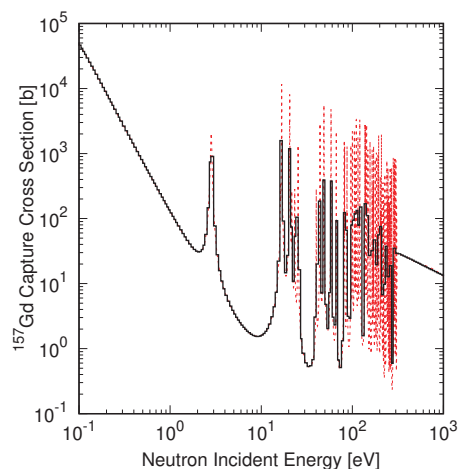


Fig. 1: Evaluated  $^{157}\text{Gd}$  capture cross section from the thermal to the fast energy. The thin dotted curve is for the 0 K cross section reconstructed from the resolved resonance parameters. The thick histogram is a grouped cross section in the SAND-II 640 energy group structure.

300 eV, the cross sections are energy-averaged, while they are not below that energy. This can be seen when we calculate a group cross section shown by the thick histogram; the cross section shape in the 100 - 300 eV region is converging to the smooth straight line at higher energies.

## 2. Compound Nuclear Reaction

### 2.1 $R$ -matrix theory

We still base an interpretation of compound nuclear reaction upon Bohr's Hypothesis; (i) an incident particle shares its energy with the target nucleons, (ii) a compound nucleus (CN) attains statistical equilibrium, and (iii) the decay modes of CN are independent of formation. Several theories were formulated to characterize the resonances in CN, which are by Breit and Wigner [3], Kapur and Peierls [4], and the most commonly quoted one is the  $R$ -matrix theory of Wigner and Eisenbud [5].  $R$ -matrix is defined by the energy of  $\lambda$ -th resonance  $E_\lambda$ , and the decay amplitude  $\gamma_{\lambda c}$  into the channel  $c$ ,

$$R_{cc'} = \sum_{\lambda} \frac{\gamma_{\lambda c} \gamma_{\lambda c'}}{E_{\lambda} - E}, \quad (1)$$

which yields the scattering matrix  $S$  [6]. Instead of  $\gamma_{\lambda c}$ , the decay width  $\Gamma_{\lambda c} = 2P_c \gamma_{\lambda c}^2$  is often used, where  $P_c$  is a penetration factor [6]. These parameters are determined by fitting calculated quantities to available experimental data, and in this sense the  $R$ -matrix formula is not a predictive theory, nevertheless no approximation was made to derive the equation. The resonance energy  $E_\lambda$  can be estimated from the nuclear excited state in CN when the nuclear structure is known. In Fig. 2, resonances for neutron-induced reaction on  $^{12}\text{C}$  are depicted on the right, and the excited state in  $^{13}\text{C}$  corresponding to each resonance is shown on the left. The first resonance occurs at 2.077 MeV, while the 6.864 MeV  $(5/2)^+$  level corresponds to this resonance.

One of the significant features of the  $R$ -matrix theory is the  $S$ -matrix unitarity,  $S^\dagger S = 1$ , which ensures the flux conservation. Because of this one can estimate some experimentally unknown cross section by inverse reactions, *e.g.*, prediction of  $(n, \alpha)$  by  $(\alpha, n)$  data.

### 2.2 Approximations to $R$ -matrix theory

Although the  $R$ -matrix theory is exact, a downside is that it requires enough experimental data to determine all the channels. This situation becomes more severe when the radiative capture

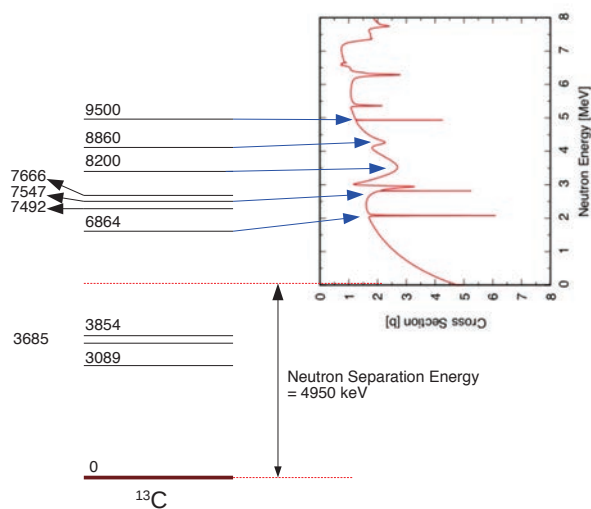


Fig. 2: The  $^{12}\text{C}$  total cross section is shown on the right side, and the left side is nuclear structure of  $^{13}\text{C}$  and some of the excited states that correspond to the resonances.

channel has a lot of final states. This is one of the main reasons why the full  $R$ -matrix analysis is limited to light elements.

In the case of resonance reactions on medium to heavy nuclei, there are many small photon channels  $\gamma_{\lambda c}$ , and their sign is random. When all the photon emission channels are lumped into a single capture channel  $\Gamma_\gamma$ , as an approximation often made in the single-level (SLBW) or multi-level Breit-Wigner (MLBW) formulae [7], interference between resonances will have some issues. The Reich-Moore (RM) approximation [8], which eliminates all the photon emission channels and lumps them into one capture channel, has better treatment of resonance interference. The RM  $R$ -matrix reads

$$R_{cc'}^{\text{RM}} = \sum_{\lambda} \frac{\gamma_c \gamma_{c'}}{E_{\lambda} - E - i\Gamma_\gamma/2}. \quad (2)$$

When these approximations are applied, the  $S$ -matrix is no longer unitary, and the flux

deficit depends on the size of capture width. Figure 3 demonstrates the  $S$ -matrix elements of  $^{184}\text{W}$  for the elastic channel calculated from the RM resonance parameters in JENDL-4. The incident neutron energy changes from zero at the bottom plane to 1.5 keV at the top. At each resonance, the  $S$ -matrix draws a circle in the complex plane, and smaller circles correspond to the large capture cross section case, where the unitary deficit is also large.

Although RM and MLBW  $S$ -matrices are not unitary, one can still calculate angular distributions of elastically scattered neutrons by applying the Blatt-Biedenharn formula [9]. This is particularly important for nuclides near the magic numbers, where non-statistical behavior of the resonance distribution sometimes enhances the neutron scattering in the forward and backward angles. Such scattering angular distributions are very different from predictions by the optical model that often gives a very small  $p$ -wave contribution in the resonance range [10]. Neutron leakage is enhanced when more neutrons are scattered in the forward angles, while larger backward scattering increases an effective neutron multiplicity  $k_{\text{eff}}$ .

### 2.3 Random matrix approach in unresolved resonance region

Since individual resonances cannot be resolved anymore above the resolved resonance region, energy-average cross sections and/or average resonance parameters ( $\langle \Gamma_c \rangle$  and  $D$ ) are given in evaluated nuclear data files. The channel degree-of-freedom  $\nu_c$  of the  $\chi^2$ -distribution for  $\Gamma_c$  also characterizes the distribution of cross sections. When  $\nu_c = 1$ , the width distribution is reduced to the well-know Porter-Thomas distribution. The resonance spacing is also known to

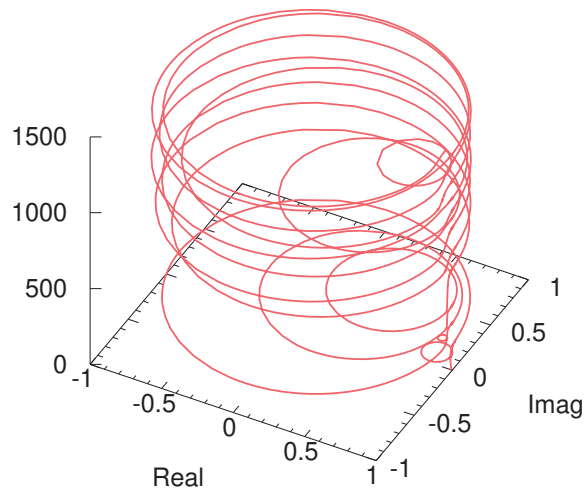


Fig. 3:  $S$ -matrix elements (elastic channel) on the complex plane for neutron induced reaction on  $^{184}\text{W}$  with the Reich-Moore approximation. The vertical axis is the neutron incident energy in eV.

form the Wigner distribution. Sometimes it is claimed that these distributions are obtained by applying GOE to the compound nuclear reaction. However, they are not directly connected but inspired [7]. A realistic implementation of GOE in the scattering matrix  $S$  was first proposed by Verbaarschot *et al.* [11], and ensemble average of the calculated cross sections was performed by the Grassmann integration technique.

The energy-average compound reaction cross section from channel  $a$  to  $b$  can be defined by the average decay width

$$\sigma_{ab}^{\text{CN}} = \frac{2\pi}{D} \left\langle \frac{\Gamma_a \Gamma_b}{\sum_c \Gamma_c} \right\rangle = \frac{2\pi}{D} \frac{\langle \Gamma_a \rangle \langle \Gamma_b \rangle}{\sum_c \langle \Gamma_c \rangle} W_{ab} = \frac{T_a T_b}{\sum_c T_c} W_{ab}, \quad (3)$$

where  $W_{ab}$  is the width fluctuation correction factor [12], and  $T_c$  is the particle transmission coefficient. In Eq. (3), a weak-coupling limit approximation  $T_c \simeq 2\pi \langle \Gamma_c \rangle / D$  is used. This was examined in the strong-coupling regime [13] by applying the GOE model [1].

Defining the compound cross section by  $\Gamma_c$  is somewhat ambiguous, nevertheless the statistical model has been developed in such a way. In fact the partial decay amplitude  $\gamma_c$  in the GOE model can be defined by two matrices,  $S$  and  $K$ . When the random matrix  $H^{\text{GOE}}$  is first diagonalized, the  $K$ -matrix that has a similar form to  $R$  includes the partial decay amplitude in the numerator,

$$K = \pi W^T \frac{1}{E - H^{\text{GOE}}} W, \quad K_{cc'} = \frac{1}{2} \sum_{\lambda} \frac{\tilde{\gamma}_{\lambda c} \tilde{\gamma}_{\lambda c'}}{E - E_{\lambda}}, \quad (4)$$

where  $W$  is the coupling matrix [1]. The average width  $\langle \Gamma_c \rangle$  can be evaluated by an ensemble average of  $\tilde{\gamma}_{\lambda c}^2$ . On the other hand, a pole-expansion form of the  $S$ -matrix gives another decay width [6].

$$S_{cc'} = \delta_{cc'} - i \sum_{\nu} \frac{\gamma_{\nu c} \gamma_{\nu c}^*}{E - E_{\nu} + i\Gamma_{\nu}/2}. \quad (5)$$

The top panels in Fig. 4 show an example of GOE realizations for a two-channel case (elastic and inelastic scattering only). The left panel is for the weak-coupling case ( $T_c = 0.1$ ), and the right panel is for the strong-coupling case ( $T_c = 0.9$ ). The bottom panels are the normalized average width  $\pi \langle \Gamma_a \rangle / D$  plotted at each resonance energy  $E_{\lambda}$ . In the small  $T_a$  case, both the  $K$  and  $S$ -matrices give very similar decay width, while they differ in the strong absorption case. This situation becomes more complicated when we calculate  $\langle \Gamma_a \Gamma_b / \sum \Gamma_c \rangle$  or  $\langle \Gamma_a \rangle \langle \Gamma_b \rangle / \sum \langle \Gamma_c \rangle$  by the GOE model, hence definition of the cross section by the decay width would be open to argument. We are investigating the equality in Eq. (3) by performing the Monte Carlo calculation for  $\langle \Gamma_a \Gamma_b / \sum \Gamma_c \rangle$  and  $\langle \Gamma_a \rangle \langle \Gamma_b \rangle / \sum \langle \Gamma_c \rangle$ . However, so far what we can conclude is that the last term of  $T_a T_b / \sum T_c W_{ab}$  is the most accurate expression for the compound nuclear reaction.

### 3. Conclusion

A brief introduction to the  $R$ -matrix theory for the compound nuclear reaction is given, and its relation to the energy-average cross section in the unresolved resonance region was summarized.

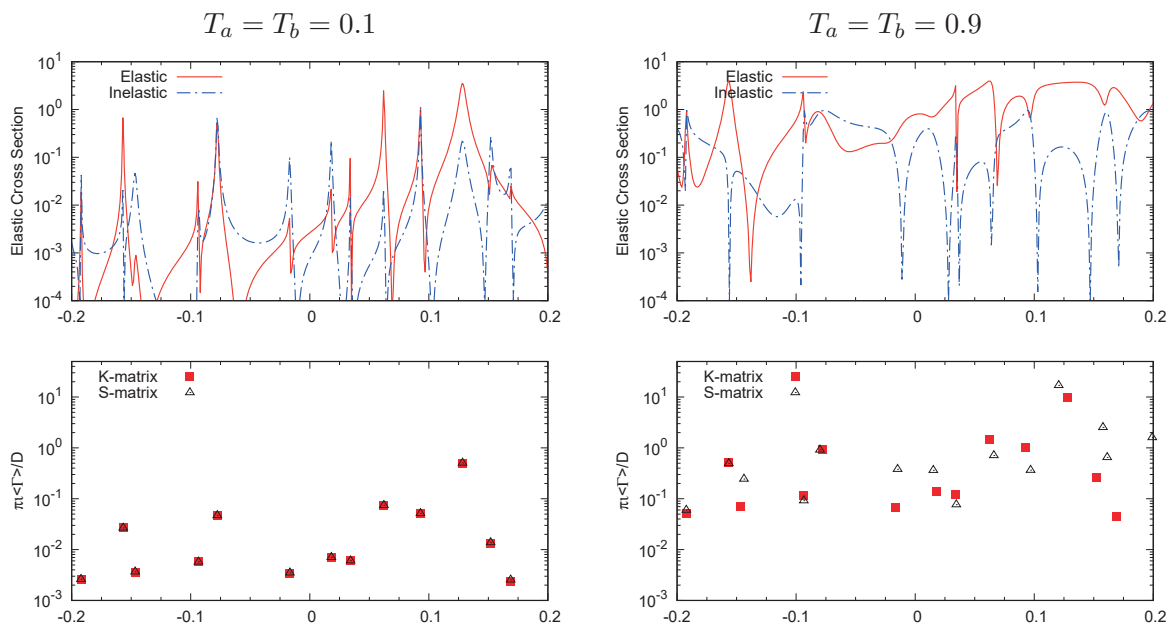


Fig. 4: An example of GOE model realization. The top panels are the calculated cross sections for the weak and strong coupling cases, where the same random number sequence was used. The bottom panels are the calculated resonance decay width by  $K$  and  $S$  matrices.

We utilized the Gaussian Orthogonal Ensemble (GOE), which is embedded in the scattering matrix, to calculate the energy-average cross section by a given transmission coefficient. It was shown that defining compound reaction cross sections in terms of the decay width might be somewhat ambiguous.

## Acknowledgment

This work was carried out under the auspices of the National Nuclear Security Administration of the U.S. Department of Energy at Los Alamos National Laboratory under Contract No. 89233218CNA000001.

## References

- [1] T. Kawano, P. Talou, and H. A. Weidenmüller, *Phys. Rev. C*, **92**, 044617 (2015).
- [2] T. Kawano, R. Capote, S. Hilaire, and P. Chau Huu-Tai, *Phys. Rev. C*, **94**, 014612 (2016).
- [3] G. Breit and E. Wigner, *Phys. Rev.*, **49**, 519 (1936).
- [4] P. L. Kapur and R. Peierls, *Proc. Royal Society A*, **166**, 277 (1938).
- [5] E. P. Wigner and L. Eisenbud, *Phys. Rev.*, **72**, 29 (1947).
- [6] A. M. Lane and R. G. Thomas, *Rev. Mod. Phys.*, **30**, 257 (1958).

- [7] F.H. Fröhner, “Evaluation and analysis of nuclear resonance data,” JEFF Report **18**, Nuclear Energy Agency Data Bank (2000).
- [8] C. W. Reich and M. S. Moore, Phys. Rev., **111** 929 (1958).
- [9] J. M. Blatt and L. C. Biedenharn, Rev. Mod. Phys., **24**, 258 (1952).
- [10] T. Kawano and D. A. Brown, J. Nucl. Sci. Technol., **52** 274 (2015).
- [11] J. J. M. Verbaarschot, H. A. Weidenmüller, and M. R. Zirnbauer, Phy. Rep., **129** 367 (1985).
- [12] P. A. Moldauer, Nucl. Phys. A, **344** 185 (1980).
- [13] Y. Alhassid, G. F. Bertsch, P. Fanto, and T. Kawano, Phys. Rev. C, **99** 024621 (2019).

## 12 Current status of search for element 119

Satoshi SAKAGUCHI<sup>1,2,3</sup> for nSHE collaboration and for Research Center for Superheavy Elements

1 Department of Physics, Kyushu University, Motoooka 744, Nishi, Fukuoka, 819-0395 Japan

2 Research Center for Superheavy Elements, Kyushu University

3 RIKEN Nishina Center for Accelerator-Based Science

e-mail: sakaguchi@phys.kyushu-u.ac.jp

Search for the new element 119 is ongoing at RIKEN by the nSHE collaboration. Current status of the experiment is briefly described. Research Center for Superheavy Elements was recently founded at Kyushu University. Experimental and theoretical research activities at the center are also explained.

### 1. Introduction

Search for new elements is a part of an attempt to find the limits of existence of the elements and atomic nuclei. In addition, new elements may have unique chemical properties which could open up new possibilities of application. Up to present, 118 elements have been found and named. Those heaviest elements were artificially synthesized by using the fusion reaction, and the 7<sup>th</sup> row of the periodic table has been completed. To extend our knowledge on the physical and chemical properties of heavy elements and nuclei, further search for the element 119, a new element in the 8<sup>th</sup> period, was started at RIKEN in 2018 by an international nSHE collaboration composed of more than ten institutes. Around the same time, Kyushu University founded a new research center, Research Center for Superheavy Elements, to reinforce the research activities on the science of superheavy elements in Japan.

### 2. Current status of search for element 119

For the efficient synthesis of element 119, a hot fusion method was adopted since it is expected to have a higher production cross section than the cold fusion which was used to synthesize the element 113, nihonium [1]. It is well known that the cross section increases as the system becomes more “asymmetric”, i.e. when the atomic number ( $Z$ ) of the beam nucleus becomes lower and that of the target nucleus higher. On the other hand, the amount of high- $Z$  target material is severely limited since it has to be artificially produced in a nuclear reactor making use of its high-flux neutron environment. For the nSHE experiment,  $^{248}\text{Cm}$  material is supplied from Oak Ridge National Laboratory (ORNL). The material is processed and prepared as a rotating target at RIKEN. In addition to the  $^{248}\text{Cm}$  target, one needs a  $^{51}\text{V}$  beam, a separator, and a detection system. A new separator, GARIS-II was newly constructed [2] aimed at enlarging the angular acceptance for a higher collection efficiency for hot-fusion products and also at decreasing the background-event rate. The GARIS-II was installed at the RIKEN Ring Cyclotron (RRC) facility in 2017. The search for

element 119 was initiated in January 2018 with a  $^{51}\text{V}$  beam accelerated by the RRC [3]. From 2018 to 2019, the nSHE experiment has been performed intermittently. The detection system, consisting of MCP-ToF detectors and DSSDs, has been continuously upgraded.

In parallel with the nSHE experiment at the RRC facility, the RILAC facility has been upgraded to increase the beam intensity by 5–10 times. A 28 GHz superconducting ECR ion source and a superconducting quarter-wavelength resonator are being installed. To perform the nSHE experiment at the upgraded RILAC facility, a new separator GARIS-III is under construction. The nSHE experiment will soon be started with these new devices at the RILAC facility.

### 3. Research Center for Superheavy Elements at Kyushu University

Research Center for Superheavy Elements (RCSHE) was founded in 2018 at Kyushu University. Activities related to the nSHE experiment are ongoing as below. (1) A beamline dedicated for SHE research was constructed at the Center for Accelerator and Beam Applied Science (CABAS) at Kyushu University. (2) Reaction studies such as measurement of quasi-elastic barrier distribution has been carried out using a tandem accelerator. (3) An analysis group of nSHE data has been launched independently of the RIKEN group to secure complementarity and objectivity of the interpretation of the data. (4) Basic development of the detectors (MCP-ToF detector for nSHE experiment and new type of an implantation detector utilizing the inorganic scintillator) has been started.

Related to the superheavy element physics, theoretical studies on fusion and fission processes are being carried out. Collective inertia of  $^{240}\text{Pu}$  was calculated along the fission path by the density functional theory [4]. Development of computer code for estimating evaporation-residue cross sections is planned.

Experimental studies of structures of heavy nuclei are also ongoing at JAEA. Decay spectroscopy of n-deficient Am isotopes was done in FY2019. Through EC decay of  $^{234}\text{Am}$ , excited states in  $^{234}\text{Pu}$  are investigated by the method of gamma-ray spectroscopy at JAEA-ISOL [5]. Isomer spectroscopy using multi-nucleon transfer reaction on actinides targets will also be performed in near future.

### References

- [1] K. Morita et al., New result in the production and decay of an isotope,  $^{278}113$ , of the 113th element, J. Phys. Soc. Jpn., **81**, 103201 (2012).
- [2] K. Morita et al., Discovery of new element, nihonium, and perspectives, Prog. Nucl. Sci. Technol., **5**, **8** (2018).
- [3] H. Haba, A new period in superheavy-element hunting, Nat. Chem., **11**, 10 (2019).
- [4] Private Communication
- [5] Private Communication

## 13 Application of CDCC to many-body breakup reaction

Takuma MATSUMOTO

Department of Physics, Kyushu University, Fukuoka 819-0395, Japan

email: matsumoto@phys.kyushu-u.ac.jp

The continuum-discretized coupled-channels method (CDCC) has been successful in analyzing breakup reactions involving many-body projectiles. The many-body breakup reactions are important for not only nuclear physics but also nuclear engineering studies. In this article, we give some results of CDCC analyses for studies of unstable nuclei and nuclear data evaluations.

### 1 Introduction

Breakup reactions have played a key role in investigating the exotic properties of unstable nuclei. The observables such as breakup and neutron removal cross sections include properties of the ground and resonant states. In order to exclude such exotic properties from the observables, an accurate analysis of breakup reactions is highly required.

As one of the most reliable methods for treating breakup processes, the continuum-discretized coupled-channels method (CDCC) [1, 2, 3] has been proposed. At first, CDCC has been applied to analyses of three-body scattering problems, in which a projectile breaks up into two constituents. Recently, we have developed CDCC as a method of treating four-body scattering with a three-body projectile. This new version of CDCC is called four-body CDCC [4, 5, 6, 7]. In the four-body CDCC, breakup continuum states of a projectile are calculated by the pseudo-state method, in which an internal model Hamiltonian of the projectile is diagonalized in a space spanned by a finite number of  $L^2$ -type basis functions. The advantage of the pseudo-state method is applicable to analyses of more than four-body breakup system. As another development of CDCC, the eikonal reaction theory (ERT) [8] has been proposed. In ERT, we can calculate inclusive breakup cross sections such as neutron removal cross sections, in which Coulomb breakup processes are consistently described by CDCC without making the adiabatic approximation used in the Glauber model.

In this workshop, we reviewed recent studies of CDCC for analyses of various reactions involving unstable nuclei and application to nuclear engineering. This presentation is based on the review paper of CDCC [3] and Ref. [9].

### 2 Borromean Feshbach resonance of $^{11}\text{Li}$

In this section, we introduce the study of a resonance of  $^{11}\text{Li}$  via CDCC analysis of the  $^{11}\text{Li}(p, p')$  reaction. The existence of a resonance of  $^{11}\text{Li}$  is a long-standing open question. Very recently, a measurement of the  $^{11}\text{Li}(p, p')$  reaction at 6 MeV/nucleon [10] with high statistics and high

resolution has been performed, and a low-lying excited state of  $^{11}\text{Li}$  has clearly been identified. To clarify the low-lying state, we analyze the  $^{11}\text{Li}(p, p')$  reaction with CDCC.

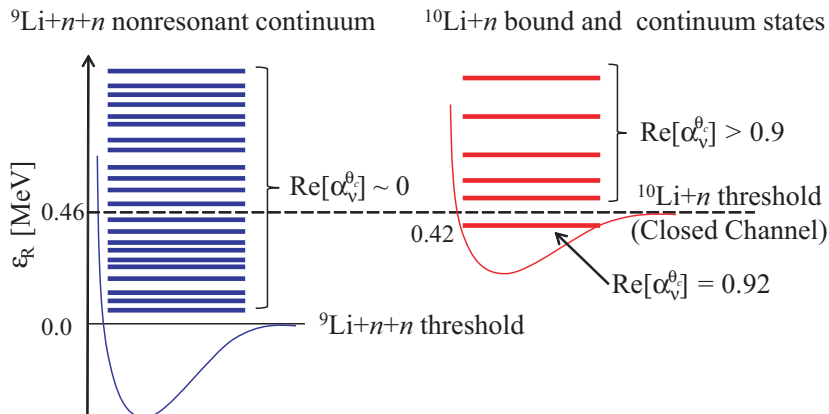


Figure 1: A schematic representation of complex-scaled states of  $^{11}\text{Li}$  for  $I^\pi = 1^-$  is shown.

In CDCC analysis, we adopt a  $^9\text{Li} + n + n$  three-body model for  $^{11}\text{Li}$ , assuming for simplicity that  $^9\text{Li}$  is a spinless and inert particle. This simplified model has been applied to analyses of some reactions of  $^{11}\text{Li}$ , and the details of the calculation are shown in Ref. [9]. In this model of  $^{11}\text{Li}$ , we found the resonance state for  $I^\pi = 1^-$  with the resonance energy (decay width) 0.42 MeV (0.14 MeV). Furthermore, we concluded that the resonance is interpreted as a bound state of a valence neutron with respect to  $^{10}\text{Li}$ , which is a resonance state for the  $n + ^9\text{Li}$  system with a resonance energy (decay width) of 0.46 MeV (0.36 MeV). This type of resonance, which is regarded as a bound state embedded in continuum, is referred to as a Feshbach resonance. We thus refer to this resonance of  $^{11}\text{Li}$  as a Borromean Feshbach resonance. In Fig. 1, properties of the low-lying states in  $^{11}\text{Li}$  are summarized.

Using the bound, resonant and continuum states of  $^{11}\text{Li}$  calculated above, we analyzed the  $^{11}\text{Li}(p, p')$  reaction with CDCC. In the CDCC calculation, we adopt the folding potential between  $^{11}\text{Li}$  and  $p$  with the JLM effective interaction [11], and introduce the adjustable parameter  $\lambda_I$  that is a normalization factor of the imaginary part of the folding potential. The details of the calculation are shown in Ref. [9]. Figure 2 shows the breakup cross section with respect to the three-body energy  $\varepsilon$  after breakup. Here the energy resolution of the experimental data are taken into account. One sees that the contribution from the dipole resonance of  $^{11}\text{Li}$  shown by the thin solid line dominates the low-lying peak. Up to  $\varepsilon \sim 1.0$  MeV, it can be concluded that the low-lying continuum structure of  $^{11}\text{Li}$  including the resonance is consistent with the measured cross sections. On the other hand, the calculated cross section undershoots the data for  $\varepsilon \gtrsim 1.0$  MeV, which will be due to some other degrees of freedom that are not taken into account in the present calculation, e.g., a transition to higher spin states and a core excitation in  $^9\text{Li}$ . In order to clarify properties of the continuum structure of  $^{11}\text{Li}$  including the higher excited states, we require more reliable calculations of  $^{11}\text{Li}$  with the core excitation in  $^9\text{Li}$ .

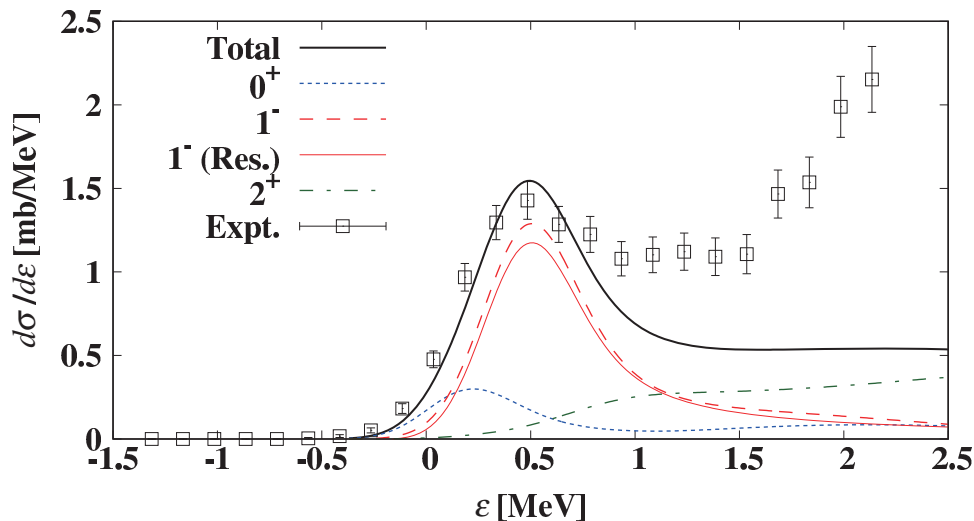


Figure 2: The breakup cross section as a function of the three-body breakup energy  $\varepsilon$  of  $^{11}\text{Li}$  in the  $^{11}\text{Li}(p, p')$  reaction [10]. The cross section is integrated over  $\theta_{\text{c.m.}}$  from  $115^\circ$  to  $124^\circ$ . The dotted, dashed, and dot-dashed lines represent calculated cross sections to the  $0^+$ ,  $1^-$ , and  $2^+$  breakup states, respectively, and the sum of them is shown by the thick solid line. The thin solid line shows the contribution of the three-body resonance of  $^{11}\text{Li}$ .

### 3 Application of CDCC to nuclear engineering

Next we show results of an application of CDCC to evaluating of nuclear data. Since CDCC is a fully quantum-mechanical method, it is applicable to reactions at low incident energies, which are important for nuclear engineering. Recently, accurate nuclear data of nucleon induced reactions on  $^6,^7\text{Li}$  that is important material for  $DT$  fusion reactor are highly required. In Ref. [12], we analyzed  $n + ^6\text{Li}$  scattering by the three-body CDCC method, in which  $^6\text{Li}$  is described as a  $d + \alpha$  system. In this analysis, we calculate diagonal and coupling potentials between  $n$  and  $^6\text{Li}$  by using the folding model with the JLM effective interaction [11] with  $\lambda_w$  that is optimized to reproduce the elastic cross sections. Details of the calculation are shown in Ref. [12].

Figure 3 shows the differential elastic cross sections of  $n + ^6\text{Li}$  for incident energies between 7.47 and 24.0 MeV. One sees that the results calculated by CDCC (the solid lines) are in good agreement with the experimental data. The dashed lines represent the results of a single-channel calculation without couplings to the breakup states of  $^6\text{Li}$ . For all incident energies, we take  $\lambda_w = 0.1$  to reproduce the data. It should be noted that the single-channel calculation cannot reproduce the experimental data with any values of  $\lambda_w$ . Thus breakup effects are significant to reproduce the angular distributions of the elastic scattering. Very recently we also applied CDCC to scattering of  $^7\text{Li}$  and the results are summarized in Ref. [16].

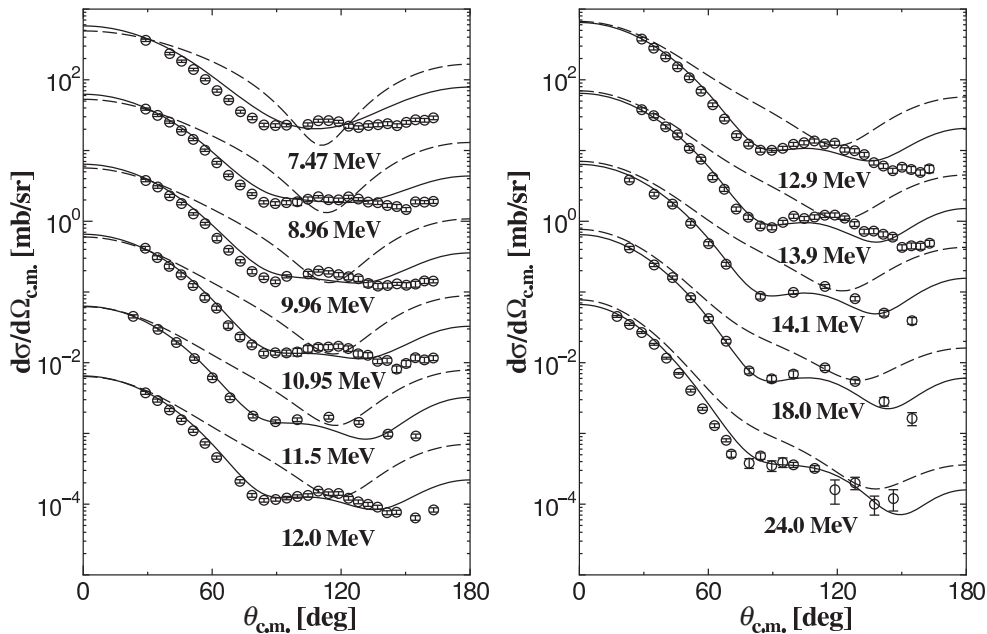


Figure 3: Angular distribution of the elastic differential cross section of  $n + {}^6\text{Li}$  scattering for incident energies between 7.47 and 24.0 MeV. This figure is taken from Ref. [12]. The solid and dashed lines correspond to the result with and without couplings to breakup states of  ${}^6\text{Li}$ , respectively. Experimental data are taken from Refs. [13, 14, 15].

## 4 Summary

Many-body breakup reactions are important for not only nuclear physics but also nuclear engineering studies. CDCC is more reliable method to describe many-body breakup processes accurately. Recently, we analysed the the  ${}^{11}\text{Li}(p, p')$  reaction with CDCC. In the analysis, we found that  ${}^{11}\text{Li}$  might have a resonance in the low-lying structure, and the resonance is regarded as a Feshbach type resonance. The resonance of  ${}^{11}\text{Li}$  is referred to as Borromean Feshbach resonance. Furthermore, we also applied CDCC to analyses of  ${}^6\text{Li}(n, n')$  and  ${}^7\text{Li}(n, n')$  reactions, which are important for nuclear data evaluations. In the analyses, CDCC well reproduces both the elastic and inelastic cross sections, and we then expect that CDCC can predict the cross sections if the experiment data do not exist. Thus CDCC is indispensable for not only study of unstable nuclei but also nuclear data evaluations.

## Acknowledgements

The author is grateful to K. Ogata and J. Tanaka for helpful discussion. Furthermore I wish to thank to members of JCPRG in Hokkaido University and Y. Watanabe and H. Guo for the discussion of

nuclear data evaluation. This work was supported in part by a Grant-in-Aid for Scientific Research (No. JP18K03650) from the Japan Society for the Promotion of Science (JSPS).

## References

- [1] M. Kamimura *et al.*, “Chapter I. Projectile Breakup Processes in Nuclear Reactions”, Prog. Theor. Phys. Suppl. **89** (1986), 1.
- [2] N. Austern *et al.*, “Continuum-discretized coupled-channels calculations for three-body models of deuteron-nucleus reactions”, Phys. Rep. **154** (1987), 125.
- [3] M. Yahiro *et al.*, “The continuum discretized coupled-channels method and its applications”, Prog. Theor. Exp. Phys. **01A206** (2012).
- [4] T. Matsumoto *et al.*, “Continuum-discretized coupled-channels method for four-body nuclear breakup in  ${}^6\text{He}+{}^{12}\text{C}$  scattering”, Phys. Rev. C **70** (2004), 061601(R).
- [5] M. Rodríguez-Gallardo *et al.*, “Three-body continuum discretization in a basis of transformed harmonic oscillator states”, Phys. Rev. C **72** (2005), 024007.
- [6] T. Matsumoto *et al.*, “Coulomb breakup effects on the elastic cross section of  ${}^6\text{He}+{}^{209}\text{Bi}$  scattering near Coulomb barrier energies”, Phys. Rev. C **73** (2006), 051602(R).
- [7] M. Rodríguez-Gallardo *et al.*, “Four-body continuum-discretized coupled-channels calculations”, Phys. Rev. C **80** (2009), 051601(R).
- [8] M. Yahiro, K. Ogata, and K. Minomo, “Eikonal Reaction Theory for Neutron Removal Reaction”, Prog. Theor. Phys. **126** (2011), 167.
- [9] T. Matsumoto, J. Tanaka, and K. Ogata, “Borromean Feshbach resonance in  ${}^{11}\text{Li}$  studied via  ${}^{11}\text{Li}(p, p')$ ”, Prog. Theor. Exp. Phys. **123D02** (2019).
- [10] J. Tanaka *et al.*, “Halo-induced large enhancement of soft dipole excitation of  ${}^{11}\text{Li}$  observed via proton inelastic scattering”, Phys. Lett. B **774** (2017), 268.
- [11] J.-P. Jeukenne, A. Lejeune, and C. Mahaux, “Optical-model potential in finite nuclei from Reid’s hard core interaction”, Phys. Rev. C **16** (1977), 80.
- [12] T. Matsumoto *et al.*, “Systematic description of the  ${}^6\text{Li}(n, n'){}^6\text{Li}^* \rightarrow d + \alpha$  reactions with the microscopic coupled-channels method”, Phys. Rev. C **83** (2011), 064611.
- [13] S. Chiba *et al.*, “Measurement and theoretical analysis of neutron elastic scattering and inelastic reactions leading to a three-body final state for  ${}^6\text{Li}$  at 10 to 20 MeV”, Phys. Rev. C **58** (1998), 2205.
- [14] H. Hogue *et al.*, “Elastic and Inelastic Scattering of 7- to 14-MeV Neutrons from Lithium-6 and Lithium-7”, Nucl. Sci. Eng. **69** (1979), 22.
- [15] L. Hansen *et al.*, “Proton and neutron transition densities in  ${}^{6,7}\text{Li}$  from low energy neutron and proton scattering”, Phys. Rev. C **38** (1988), 525.
- [16] H. Guo *et al.*, “Analysis of nucleon and triton emissions from nucleon- ${}^7\text{Li}$  collisions below 20 MeV”, Phys. Rev. C **99** (2019), 034602.

This is a blank page.

## 14 Topics from Radiation Safety Design of J-PARC

Hiroshi NAKASHIMA

Japan Atomic Energy Agency

Tokai-mura, Naka-gun, Ibaraki-ken 319-1195 Japan

e-mail: nakashima.hiroshi@jaea.go.jp

J-PARC (Japan Proton Accelerator Research Complex) is a high-energy proton accelerator complex of the world's highest beam power. Because of its very high beam power and its high energy as well as the large-scale accelerator complex, we encountered some very difficult problems on radiation safety design. Various examinations and countermeasures were considered in order to overcome the difficulty. This paper introduces some of them. In addition, some new knowledges obtained during 10 years after completion are described.

### 1. Introduction

J-PARC is a complex of GeV class high energy accelerator facilities with the world's largest beam power, jointly organized by JAEA (Japan Atomic Energy Agency) and KEK (High-energy accelerator laboratory).[1] The accelerator consists of 400MeV LINAC, 3GeV synchrotron and a main ring (currently 30GeV). These accelerator facilities include the Materials and Life Science Experimental Facility, the Hadron Experimental Facility, and the Neutrino Experimental Facility. The experimental facilities are conducting research in various fields. In the future, a transmutation experiment facility will be also built.

This paper summarizes J-PARC's topics related to radiation safety design, including measures at the time of design and new knowledges obtained 10 years after the completion of the facility.

### 2. Basic concept in radiation safety design[2]

J-PARC has many problems to be overcome from the viewpoint of radiation safety as the followings.

- 1) It is necessary to conduct a large-scale radiation safety estimation integrally.
- 2) Radiation shielding design is needed to be performed effectively and economically.
- 3) It is necessary to take measures for activation on structures, equipment, air, cooling water, etc.

Therefore, radiation safety design was performed based on the following concept.

- 1) Use a design method system that combines the simple methods and the detailed calculation methods.
- 2) Accelerator facilities are basically installed underground.
- 3) Air and cooling water are circulated in a closed loop during operation, and after shutdown, monitoring is performed to control the activities. Low activation materials are used for buildings and equipment.
- 4) Monitor and limit the beam loss to keep radiation source condition on safety.

### 3. Topics from radiation safety design

#### 3.1 Radiation source condition

It is the most important in a radiation safety design to determine the radiation source conditions. In accelerator facilities, the source condition is proportional to the beam loss at each loss points. Therefore, we determined the beam loss amount at the initial design stage for the entire facility.

Beam losses of targets and beam dumps in each facility were determined by the facility plan, and those of injections of accelerators are determined by the device performance. On the other hand, it is very difficult to

assume those of the accelerators itself. Beam loss of 1W/m was adopted based on reports of the ICFA (International Committee on Future Accelerators) and KEK.[3] The effective dose caused by the beam loss in working environment makes possible hands-on-maintenance after shutdown. The assumption has been verified by estimation on the effective doses caused by the beam loss.[4] During operation, the beam losses are measured by a real-time monitor along all accelerators.

### 3.2 Design method

Semi-empirical formulas and/or simplified methods were applied for the overall design. On the other hand, detailed design methods such as Monte Carlo methods were used for high beam loss points and complicated structures such as targets and injectors.[2]

As for the simplified methods on deep penetration, the Moyer's Model [5] was used in the proton energy region above 1 GeV, while the Tesch's equation [6] was used below 1 GeV. In the calculation the KEK parameter was adopted as the attenuation coefficient. After the design, it has been confirmed that the attenuation coefficient has been evaluated more safely by experiments at BNL (the Brookhaven National Laboratory) and FNAL (the Fermi National Accelerator Laboratory).[7, 8] For streaming in mazes and ducts, DUCT-III [9] was applied and the results were validated by experimental data at TIARA (Takasaki Ion Accelerators for Advanced Radiation Application)[10]. As for skyshine, calculations using Stapleton's equation [11] were performed to estimate the doses at the site boundary. The accuracy was verified by comparing it with calculation using the Monte Carlo method and SHINE3 [12], because no experiment existed on the high energy accelerator facility. It is expected that benchmark experiments will be conducted.

An integrated calculation system: SSCAT (Simplified Shielding Calculation Table System) [13] was developed to comprehensively calculate the dose of all facilities on bulk shielding and skyshine. As for the dose at the site boundary, the dose calculated by the Monte Carlo methods in some facilities is also added to the dose calculated by this system.

In the detailed calculation system, Monte Carlo codes: PHITS [14], MCNPX [15] and MARS [16] were used for high-energy particle transport, as shown in figure 1. They were used differently according to facilities and their conditions, because each code has its own characteristics. DCHAIN-SP [17] was used as a radioactivity calculation code, and QAD-CGGP2 [18] was used for radiation generated by radioactivity.

The results by each code show a difference among them. Therefore, the difference was validated based on shielding experiments[19]. The benchmarking was carried out for the following shielding items:1) Thick Target Neutron Yield, 2) Beam dump, 3) Deep penetration, 4) Streaming and 5) Skyshine. All are based on experiments except for skyshine. A safety factor of 2 was obtained from the benchmarking. By using the safety factor, estimation values were obtained for licensing. A report summarizing the results has been submitted as a reference for licensing. Even after the benchmarking was conducted, benchmark experiments have been conducted using RCNP [20], FNAL [8], and so on. Some of the experimental results have been compiled as an experiment database: SINBAD [21] in OECD / NEA (the Organization for Economic Co-operation and Development / the Nuclear Energy Agency).

At J-PARC, the accuracy was systematically verified. However, an accuracy verification system for shielding calculation codes has not been established in Japan as a whole. As a result, old-fashioned shielding codes are still used.[22] In order to apply the newest knowledges on shielding to licensing, it is desirable to build an authorized protocol that apply newly developed data and codes in licensing.

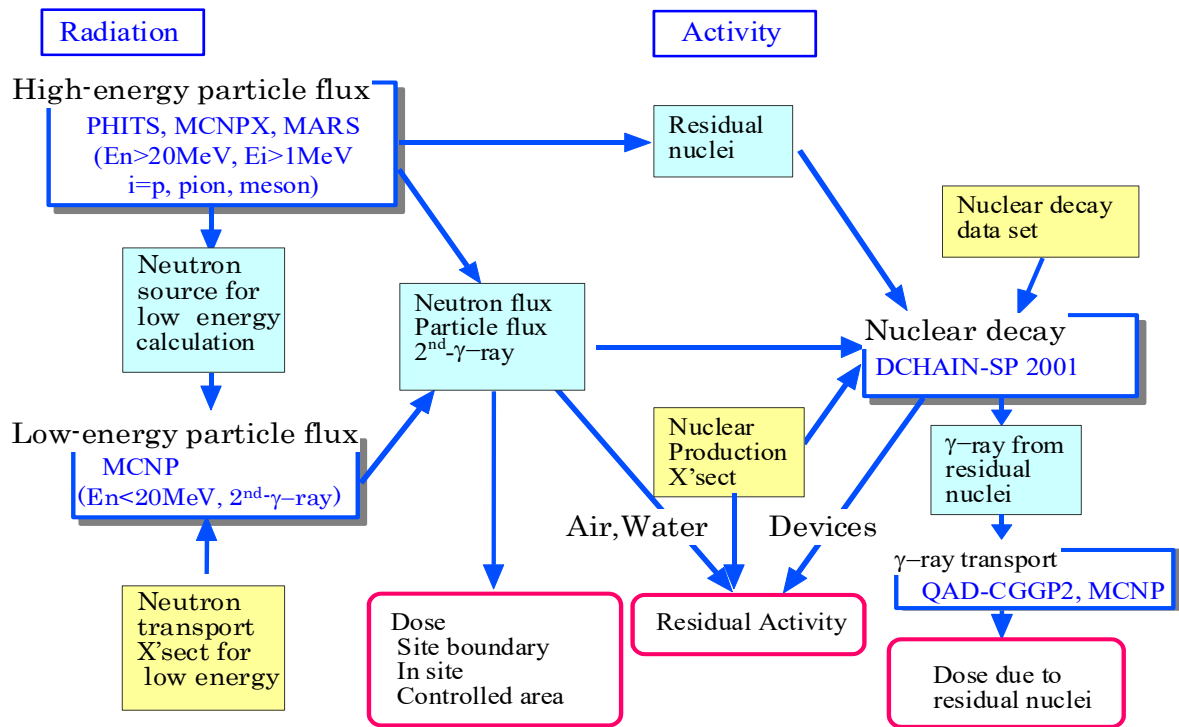


Figure 1 Calculation flow of radiation and activity for J-PARC.[2]

### 3.3 Radiation confinement system

The high-energy radiation produced by the beam loss causes a nuclear reaction with surrounding air and cooling water, and generates various radioactivity. It is very difficult to evaluate the produced radioactivity accurately, because the energy range is very wide, up to GeV, and many kinds of reaction channels open. However, the reactions at high energy generate unstable nuclides such as  $^{13}\text{N}$  ( $T_{1/2}$  9.97 minutes) and  $^{15}\text{O}$  ( $T_{1/2}$  2.04 minutes) having a half-life of several minutes or less. Therefore, those that affect the environment are confined and released to the outside after confirming the activity concentration by monitoring them.

A conceptual diagram is shown in figure 2.[2] A buffer region, that is a controlled area, is placed between the accelerator room: controlled area, and the outside uncontrolled area. During operation, air is circulated in the accelerator room for air conditioning. The accelerator room is maintained at a negative pressure compared to the buffer region, and the air in the buffer region is monitored. If this monitor is abnormal, the accelerator is stopped immediately. After the operation and the cooling time, it is possible to access to the accelerator room with confirming safety by monitoring the concentration in air. During exhaust,  $^7\text{Be}$  is removed by using a HEPA filter.

Cooling water is also stored once in disposal tanks. After removing  $^7\text{Be}$  using an ion exchange resin and monitoring the concentration, the water is drained to the outside.

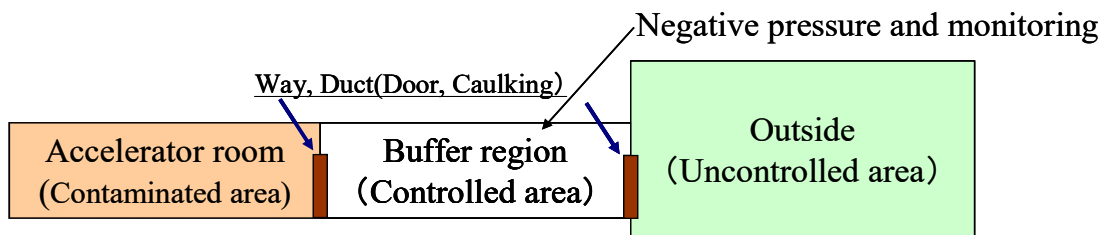


Figure 2 Conceptual view of air confinement system

### 3.4 Low-activation concrete

The high-energy radiation generated by the beam loss also activates concrete on the accelerator room wall. The radioactivity makes increase the irradiation dose to workers in the accelerator room during maintenance. Therefore, low-activation concrete was adopted to reduce the dose.

There are two types of low-activation concrete depending on the purpose. One is to reduce the environmental burden at decommissioning, and the other is to improve the working environment as this case. In the former case, the long-lived  $^{60}\text{Co}$  and  $^{152, 154}\text{Eu}$  are the nuclides of interest. On the other hand, in the latter case,  $^{24}\text{Na}$  is the nuclide of interest, which makes increase the dose in working environment several days after the shutdown. Therefore, J-PARC has adopted criteria for  $^{24}\text{Na}$ . [23]

In concrete,  $^{24}\text{Na}$  is mainly produced by the reaction of  $^{23}\text{Na}(n, \gamma)^{24}\text{Na}$ ,  $^{24}\text{Mg}(n, p)^{24}\text{Na}$ ,  $^{27}\text{Al}(n, \alpha)^{24}\text{Na}$ , and  $^{28}\text{Si}(n, X)^{24}\text{Na}$ . Although the production rate is precisely calculated by the neutron flux and each reaction cross section, it is very difficult to do so. Thus, the  $^{24}\text{Na}$  production ratio has been set as follows by their cross sections approximately:  $^{23}\text{Na} = 1$ ,  $^{24}\text{Mg} = 0.02$ ,  $^{27}\text{Al} = 0.01$  and  $^{28}\text{Si} = 0.002$ . The  $^{24}\text{Na}$ -equivalent is defined by the following formula with weight percent of the concrete composition.

$$^{24}\text{Na}\text{-equivalent (g/m}^3\text{)} = \sum ^{24}\text{Na production ratio (\%)} \times \frac{\text{weight of origin nuclei on } ^{24}\text{Na (g/m}^3\text{)}}{\text{(Natural abundance \%)}}$$

Resultantly, limestone was selected as a concrete aggregate for low activation concrete, and the residual dose in the concrete was reduced by an order of magnitude. It should be noted here that the quality of limestone must be well managed during construction to keep the criteria.

### 3.5 Activation by muon

A series of experimental study on shielding and radiation effects at FNAL have been carried out under collaboration between FNAL and Japan. [8] The purposes of the experiments were mainly measurement of particle flux and residual activity inside and around shields at Pbar station (anti-proton target station) and NuMI beamline (beamline for neutrino oscillation experiment) with 120GeV protons. In the study a new result related with J-PARC was obtained by Prof. Matsumura, et. al, that was activation caused by muon interaction with matters. [24]

At NuMI, as neutrino experimental facility in J-PARC, proton beam strikes a carbon target and produce pions in the forward direction. The pions decay into neutrinos and muons at the decay volume, and the neutrinos are used for neutrino experiments. Most of the muons are absorbed by the iron shield located at downstream of the decay volume.

In this experiment, the distributions of neutron fluxes and of generated radioactivity were measured by the activation foil method in the tunnel downstream of the iron shield. The mass distributions produced in the copper foil were measured, and the dependency on the incident particles was identified. As a result, it was founded that the dependency was similar to that of the photonuclear reaction. Only a few photons are measured in the tunnel and it is known that a pseudo-photonuclear reaction occurs in the muon nuclear reaction. Therefore, it is confirmed that the reaction is caused by muon.

It is necessary to confirm the muon effect on activation, because the muon reaction is not considered in the radiation safety design of J-PARC.

### 3.6 Effects of $\Lambda$ and $\Sigma$ on neutron transmission

International comparisons among codes developed by research institutes around the world has been

conducted at SATIF (the task- force on Shielding aspects of Accelerators, Targets and Irradiation Facilities) of OECD/NEA for more than 20 years, in order to compare the accuracy of high-energy particle transport calculation codes. In the SATIF-10, the neutron dose distribution, neutron energy spectrum and attenuation coefficient in iron and concrete bulk shields under the conditions of 0.1 to 100 GeV proton injection were compared.[25]

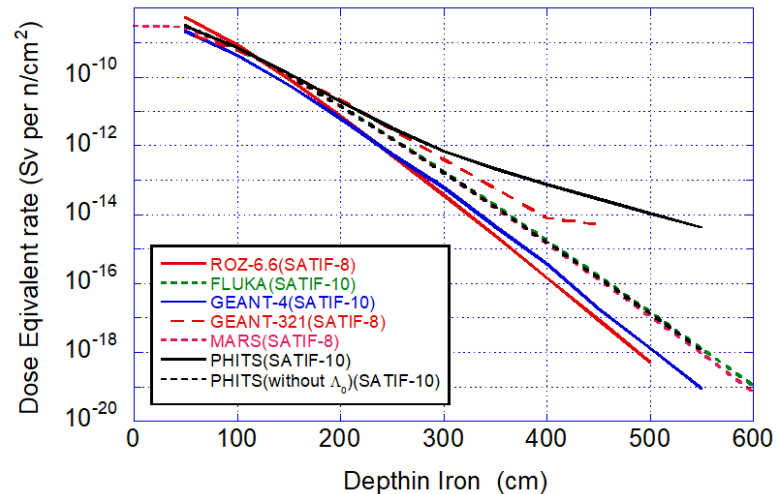


Figure 3 Comparison of dose equivalent rate in iron for incident of 10 GeV protons.

The neutron dose distribution in a 10 GeV incident iron shield are compared in figure 3. The comparison shows that the calculation by PHITS became larger as compared with calculations by other codes. This seemed to come from the fact that PHITS considers transport of baryons such as  $\Lambda$  and  $\Sigma$ . Because baryons have a higher mass than neutrons and protons, more energy is carried forward. When  $\Lambda$  and  $\Sigma$  decays, neutrons and protons are generated. Further,  $\Lambda$  and  $\Sigma$  have a higher generation ratio in this energy region than those of  $\Xi$  and  $\Omega$ . As a result, it is considered that  $\Lambda$  and  $\Sigma$  increase the neutron dose. The phenomenon has not been calculated by other codes, and it is uncertain whether other codes calculate baryon production.

This may affect to neutron dose downstream of the hadron experimental facility at J-PARC. It is necessary to verify the phenomenon experimentally.

#### 4. Summary

J-PARC is a high-energy proton accelerator complex of the world's highest beam power, and its characteristics caused many difficulties on radiological safety. In order to overcome the difficulties and secure safety, various countermeasures are adopted and many shielding design methods were also applied. The design and construction of J-PARC have affected to improve radiation safety of other facilities. After completion, many kinds of newly knowledges have been obtained. Based on the knowledges, the radiological safety of J-PARC and other high energy accelerator facilities may be the time to be reconfirmed.

#### References

- [1] S. Nagamiya, J. of Nucl. Materials, 343, 1 (2005).
- [2] H. Nakashima, et al., "Radiation Shielding Design for the J-PARC Project", Proc. on shielding aspects of accelerators, targets and irradiation facilities - SATIF 8 (2006), NEA/NSC/DOC(2010)6, 79-87 (2010).
- [3] I. Yamane, "Radiation Protection Measures for the Maintenance Service of JHF 3-GeV Ring", KEK Internal Report, 98-7 (1998).

- [4] H. Nakashima, et al., “Estimation of activity and dose distributions around a proton linac induced by beam spill”, *J. Nucl. Sci. Technol.*, Suppl.1, 870-874 (2000).
- [5] B. J. Moyer, “Method of Calculation of the Shielding Enclosure for the Berkley Bevatron”, *Proc. on 1st Int. Conf. Shielding around High Energy Accelerators*, Presses Universitaires de France, Paris, 65 (1962).
- [6] K. Tesch, “A Simple Estimation of the Lateral Shielding for Proton Accelerators in the Energy Range 50 to 1000 MeV”, *Radiat. Prot. Dosim.*, 11, 165 (1985).
- [7] H. Nakashima, et al., “Current Status of the AGS Spallation Target Experiment”, *Proc. on shielding aspects of accelerators, targets and irradiation facilities - SATIF 6* (2002), OECD/NEA No.3828, 27-36 (2004).
- [8] H. Nakashima, et al., “Research activities on JASMIN: Japanese and American Study of Muon Interaction and Neutron detection”, *J. Nucl. Sci. Technol.*, Suppl. 4, 191 (2014).
- [9] R. Tayama, et al., “DUCT-III: A Simple Design Code for Duct-Streaming Radiations”, *KEK Internal*, 2001-8, (2001).
- [10] F. Masukawa, et al., “Analyses of Streamed Neutron Spectra at TIARA Using DUCT-III”, *J. Nucl. Sci. Technol.*, Suppl. 4, 46 (2004).
- [11] G. B. Stapleton, “Accelerator Skyshine: Tyger, Tyger, Burning Bright”, *Particle Accelerators*, 44, 1 (1994).
- [12] T. Tsukiyama, et al., “Simple Code for Skyshine Dose Calculation up to 3 GeV Neutrons”, *J. Nucl. Sci. Technol.*, Suppl. 1, 640 (2000).
- [13] T. Oguri, et al., “Revised Version of SSCAT: Simplified Shielding Calculation System for High Energy Proton Accelerator Facilities”, *JAEA-Data/Code 2011-026* (2012).
- [14] T. Sato, et al., “Particle and Heavy Ion Transport code System, PHITS, version 2.52”, *J. Nucl. Sci. Technol.*, 50[9], 913 (2013).
- [15] N. V. Mokhov, “The Mars Code System User's Guide,” *Fermilab-FN-628* (1995), N. V. Mokhov and O. E. Krivosheev, “MARS Code Status”, *Fermilab-Conf-00/181* (2000).
- [16] L. S. Waters (Ed.), “MCNPX Users Manual – Version 2.1.5”, *TPO-E83-G-UG-X-00001*, LANL (1999).
- [17] T. Kai, et al., “DCHAIN-SP 2001: High Energy Particle Induced Radioactivity Calculation Code”, *JAERI-Data/Code 2001-016*, JAERI (2001) (in Japanese).
- [18] K.A. Litwin, et al., “Improvements to the Point Kernel Code QAD- CGGP: A Code Validation and User's Manual”, *RC-1214, COG-94-65*, AECL Research (US) (1994).
- [19] N. Matsuda, et al., “Analyses of Shielding Benchmark Problems for the Shielding Design of the High Intensity Proton Accelerator Facilities”, *JAEA-Technology 2008-030* (2008).
- [20] T. Matsumoto, et al., “Shielding experiments of concrete and iron for the 244 MeV and 387 MeV quasi-mono energetic neutrons using a Bonner sphere spectrometer”, *Les Ulis 153 EDP Sciences*, (2017).
- [21] I. Kodeli, et al., “20 Years of SINBAD (Shielding Integral Benchmark Archive and Database)”, *J. Nucl. Sci. Technol.*, Suppl. 4, 308 (2014).
- [22] H. Nakashima, et al., “Old-fashioned system on development of radiation transport calculation codes in Japan”, *Isotope News*, 745, 11 (2016) (in Japanese).
- [23] N. Matsuda, et al., “A study on induced radioactivity in a low-activationized concrete for J-PARC”, *J. Nucl. Sci. Technol.*, Suppl. 4, 74 (2004).
- [24] H. Matsumura, et al., “Shielding Experiments under JASMIN Collaboration at FERMILAB (III) Measurement of High-Energy Neutrons Penetrating a Thick Iron Shield from the Antiproton Production Target by Au Activation Method”, *Journal of the Korean Physical Society*, 59[2], 2059 (2011).
- [25] H. Hirayama, “Inter-comparison of Medium-Energy Neutron Attenuation in Iron and Concrete (7)”, *Proc. on shielding aspects of accelerators, targets and irradiation facilities – SATIF9* (2010), *NEA/NSC/DOC(2010)7*, 261-274 (2010).

# 15 Production cross sections of $^{45}\text{Ti}$ via deuteron-induced reaction on $^{45}\text{Sc}$

Tsoodol ZOLBADRAL<sup>1,2\*</sup>, Masayuki AIKAWA<sup>1,3</sup>, Dagvadorj ICHINKHORLOO<sup>2,3</sup>, Khishigjargal TEGSHJARGAL<sup>4</sup>, Yukiko KOMORI<sup>5</sup>, Hiromitsu HABA<sup>5</sup>, Sándor TAKÁCS<sup>6</sup>, Ferenc DITRÓI<sup>6</sup>, Zoltán SZÜCS<sup>6</sup>

<sup>1</sup> Graduate School of Biomedical Science and Engineering, Hokkaido University, Sapporo 060-8638, Japan

<sup>2</sup> Nuclear Research Center, National University of Mongolia, Ulaanbaatar 13330, Mongolia

<sup>3</sup> Faculty of Science, Hokkaido University, Sapporo 060-0810, Japan

<sup>4</sup> School of Engineering and Applied Sciences, National University of Mongolia, Ulaanbaatar 14201, Mongolia

<sup>5</sup> Nishina Center for Accelerator-Based Science, RIKEN, Wako 351-0198, Japan

<sup>6</sup> Institute for Nuclear Research (ATOMKI), 4026 Debrecen, Hungary

\*E-mail: zolbadral@nds.sci.hokudai.ac.jp

Production cross sections of the medical radionuclide  $^{45}\text{Ti}$  with the deuteron-induced reactions on  $^{45}\text{Sc}$  were investigated. The stacked foil activation method and  $\gamma$ -ray spectrometry were used. The physical yield of  $^{45}\text{Ti}$  was deduced from the measured cross sections. Our results are consistent with previous experimental data.

## 1. Introduction

The radionuclide  $^{45}\text{Ti}$  has a half-life of 184.8 min and is a positron emitter ( $E_{max} = 1040$  keV,  $E_{ave} = 439$  keV,  $I_{\beta^+} = 84.8\%$ ) [1]. The emitted positrons followed its decay are suitable for positron emission tomography (PET) [2]. The deuteron-induced reaction on a  $^{45}\text{Sc}$  target is a possible route to produce this radionuclide at cyclotrons. However, only one experimental study [3] on the cross sections of the  $^{45}\text{Sc}(d,2n)^{45}\text{Ti}$  reaction is available in the literature. Therefore, we measured the cross sections of the  $^{45}\text{Sc}(d,2n)^{45}\text{Ti}$  reaction.

## 2. Experimental methods

The experiment was performed at the AVF cyclotron of the RIKEN RI Beam Factory. The stacked-foil activation technique and  $\gamma$ -ray spectrometry were adopted to measure the cross sections.

The stacked target consisted of metallic foils of  $^{45}\text{Sc}$  (25  $\mu\text{m}$  thick, 99.0% purity, Nilaco Corp., Japan and 250  $\mu\text{m}$  thick, 99.9% purity, Johnson Matthey Alfa Products company, USA),  $^{27}\text{Al}$  (99.6% purity, Nilaco Corp., Japan) and  $^{nat}\text{Ti}$  (99.6% purity, Nilaco Corp., Japan). The size and weight of the foils were measured to determine the average thicknesses of the foils. The derived thicknesses were 7.71 and 76.0  $\text{mg}/\text{cm}^2$  for

$^{45}\text{Sc}$ , 4.99 mg/cm<sup>2</sup> for  $^{27}\text{Al}$  and 9.13 mg/cm<sup>2</sup> for  $^{\text{nat}}\text{Ti}$ , respectively. The foils were cut for the size of 8×8 mm to fit a target holder served also as a Faraday cup.

The target was irradiated for 30 min with a 24-MeV deuteron beam. The incident beam energy was measured by the time-of-flight method [4]. The energy degradation in the stacked target was calculated by the SRIM code [5]. The beam intensity was determined by collecting the charge in the Faraday cup.  $\gamma$ -rays were measured for each irradiated foil by a high-resolution HPGe detector. The detector was calibrated by a mixed standard  $\gamma$ -ray point source. The dead time was kept less than 7% in the measurements.

The cross sections of the  $^{\text{nat}}\text{Ti}(d,x)^{48}\text{V}$  monitor reaction were used to assess the beam parameters. The cross sections were derived from measurements of the 983.5-keV  $\gamma$ -ray ( $I_\gamma = 99.98\%$ ) emitted with the  $^{48}\text{V}$  decay ( $T_{1/2} = 15.9735$  d), and the result was compared with the IAEA recommended values [6]. The beam intensity measured by the Faraday-cup was decreased by 3.0 % to have good agreement among the derived and the recommended excitation function of the  $^{\text{nat}}\text{Ti}(d,x)^{48}\text{V}$  reaction (Fig. 1). The corrected beam intensity (175.2 nA) was adopted in the data assessment for the cross sections.

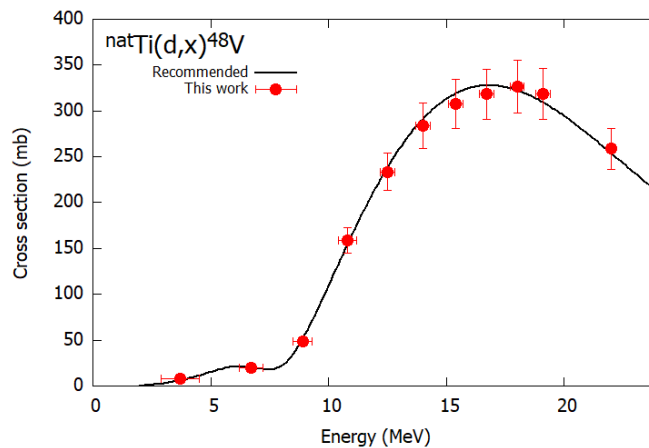


Fig. 1. The excitation function of the  $^{\text{nat}}\text{Ti}(d,x)^{48}\text{V}$  monitor reaction compared with the recommended values [6].

### 3. Results and Discussion

The cross sections of the  $^{45}\text{Sc}(d,2n)^{45}\text{Ti}$  reaction were derived from the measurement of the 719.6-keV  $\gamma$ -ray ( $I_\gamma = 0.154\%$ ) emitted in the decay of  $^{45}\text{Ti}$ , and are shown in Fig. 2 in comparison with the previous data [3] and the theoretical estimation of TENDL-2017 [7]. Our result is consistent with the previous data. The peak position of the TENDL-2017 data [7] is slightly shifted to the lower energy than those of the two experimental datasets.

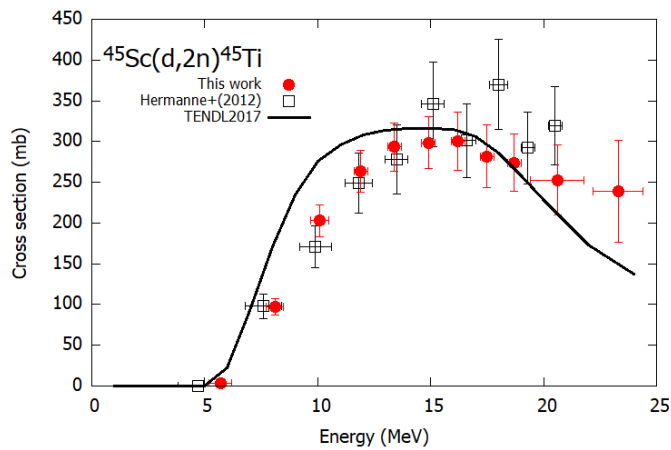


Fig. 2. Excitation function of the  $^{45}\text{Sc}(d,2n)^{45}\text{Ti}$  reaction.

The physical yield of  $^{45}\text{Ti}$  was deduced from a spline fitted curve of the measured excitation function and stopping power calculated using the SRIM code [5]. The derived yield is shown in Fig. 3 in comparison with the only experimental data [8]. The present yield curve of  $^{45}\text{Ti}$  is slightly larger than the experimental data at 22 MeV [8].

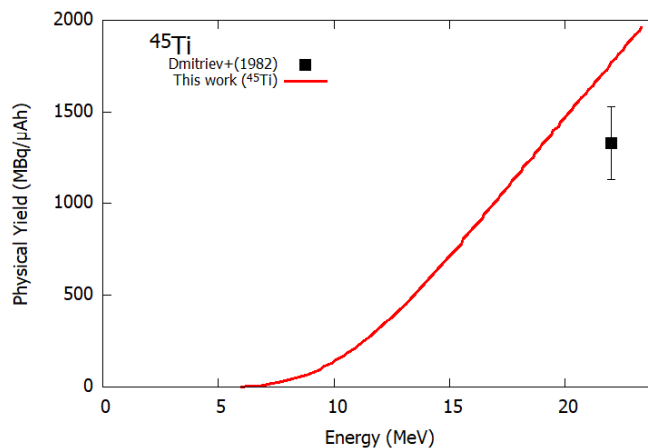


Fig. 3. Physical yield of  $^{45}\text{Ti}$  via the deuteron-induced reactions on  $^{45}\text{Sc}$ .

There are no isotopic impurities produced below 15.3 MeV, which is the threshold energy of the  $^{45}\text{Sc}(d,3n)^{44}\text{Ti}$  reaction. Production of  $^{45}\text{Ti}$  without radio-contamination is possible by using the  $^{45}\text{Sc}(d,2n)^{45}\text{Ti}$  reaction in the energy range from 15 to 5 MeV. Only the stable  $^{46}\text{Ti}$  is co-produced in the (d,n) reaction in comparable quantity by the prediction based on the cross section of the (d,n) reaction taken from the TENDL-2017 data library.

#### 4. Conclusion

The excitation function of the  $^{45}\text{Sc}(d,2n)^{45}\text{Ti}$  reaction was measured up to 24 MeV. The stacked-foil activation technique and the high-resolution  $\gamma$ -ray spectrometry were used for the cross section measurements.

The obtained data were compared with the previous experimental data and the TENDL-2017 data. The derived excitation function of the  $^{45}\text{Sc}(d,2n)^{45}\text{Ti}$  reaction is consistent with the data of Hermanne et al. (2012). The physical yield deduced from measured cross sections is slightly larger than the experimental data of Dmitriev et al. (1983). The production of radioactive-contamination-free  $^{45}\text{Ti}$  can be obtained via the  $^{45}\text{Sc}(d,2n)^{45}\text{Ti}$  reaction using cyclotrons in the energy region below 15 MeV.

### Acknowledgements

The experiment was carried out at RI Beam Factory operated by RIKEN Nishina Center and CNS, University of Tokyo, Japan. This work is supported by JSPS KAKENHI Grant Number 17K07004. Ts.Z was granted a scholarship by the M-JEED project (Mongolian-Japan Engineering Education Development Program, J11B16).

### References

- [1] National Nuclear Data Center, Nuclear structure and decay data on-line library, Nudat 2.7 [Internet]. 2017. Available from: <http://www.nndc.bnl.gov/nudat2/>
- [2] Vavere AL, Laforest R, Welch MJ. Production, processing and small animal PET imaging of titanium-45. *Nucl. Med. Biol.*, 2005, 32, 117–122.
- [3] Hermanne A, Adam Rebeles R, Tarkanyi F, et al., Cross sections of deuteron induced reactions on  $^{45}\text{Sc}$  up to 50 MeV: Experiments and comparison with theoretical codes, *Nucl. Instruments Methods Phys. Res. Sect. B Beam Interact. with Mater. Atoms*, 2012, 270, 106–115.
- [4] Watanabe T, Fujimaki M, Fukunishi N, et al., Beam energy and longitudinal beam profile measurement system at the RIBF, *Proc. 5th Int. Part. Accel. Conf. (IPAC 2014)*, 2014, 3566–3568.
- [5] Ziegler JF, Ziegler MD, Biersack JP, *SRIM - The stopping and range of ions in matter (2010)*, *Nucl. Instruments Methods Phys. Res. Sect. B Beam Interact. with Mater. Atoms*, 2010, 268, 1818–1823.
- [6] Hermanne A, Ignatyuk A V., Capote R, et al., Reference Cross Sections for Charged-particle Monitor Reactions, *Nucl. Data Sheets*, 2018, 148, 338–382.
- [7] Koning AJ, Rochman D, Sublet JC, et al., TENDL: Complete Nuclear Data Library for Innovative Nuclear Science and Technology, *Nucl. Data Sheets*, 2019, 155, 1–55.
- [8] Dmitriev PP, Krasnov NN, Molin GA, Yields of radioactive nuclides formed by bombardment of a thick target with 22-MeV deuterons, *INDC(CCP)-210*, 1983, 1–8.

## 16 Production of $^{169}\text{Yb}$ by the proton-induced reaction on $^{169}\text{Tm}$

Moemi SAITO<sup>1</sup>, Masayuki AIKAWA<sup>1,2\*</sup>, Tomohiro MURATA<sup>1</sup>, Yukiko KOMORI<sup>3</sup>, Hiromitsu HABA<sup>3</sup>,  
Sándor TAKÁCS<sup>4</sup>, Ferenc DITORÓI<sup>4</sup> and Zoltán SZÜCS<sup>4</sup>

<sup>1</sup> Graduate School of Biomedical Science and Engineering, Hokkaido University, Sapporo 060-8638, Japan

<sup>2</sup> Faculty of Science, Hokkaido University, Sapporo 060-0810, Japan

<sup>3</sup> Nishina Center for Accelerator-Based Science, RIKEN, Wako 351-0198, Japan

<sup>4</sup> Institute for Nuclear Research (ATOMKI), 4026 Debrecen, Hungary

\*e-mail: aikawa@sci.hokudai.ac.jp

Activation cross sections of the  $^{169}\text{Tm}(p,n)^{169}\text{Yb}$  reaction were measured using the MGC-20E cyclotron at Institute for Nuclear Research (ATOMKI), Hungary. The stacked-foil activation technique and the high-resolution gamma-ray spectrometry were adopted to derive the cross sections. The preliminary cross sections were compared with experimental data studied earlier and with theoretical model calculation.

### 1. Introduction

The radionuclide  $^{169}\text{Yb}$  ( $T_{1/2} = 32.018$  d) decays with emissions of Auger electrons and X-rays. These properties of  $^{169}\text{Yb}$  are appropriate for brachytherapy [1]. For such practical use, the best reaction for its production should be selected among all possible reactions. One of them is the neutron capture reaction on  $^{168}\text{Yb}$ , of which the isotopic ratio is only 0.123%. Another route is a reaction using charged particles, such as proton, deuteron and alpha particles. We have systematically investigated the production reactions of  $^{169}\text{Yb}$  with a focus on the charged-particle induced reactions. The experiments on deuteron- [2] and alpha-induced reactions on  $^{169}\text{Tm}$ , and alpha-induced reactions on  $^{nat}\text{Er}$  [3] have already been performed. Therefore, we carried out an experiment of the proton-induced reaction on  $^{169}\text{Tm}$ . In this paper, we report the preliminary result of this experiment.

### 2. Experimental

The experiment was performed using the MGC-20E cyclotron at Institute for Nuclear Research (ATOMKI), Hungary. The stacked-foil activation technique and the high-resolution gamma-ray spectrometry were adopted to derive cross sections.

The target consisted of metallic foils of  $^{169}\text{Tm}$  (99.0% purity) and  $^{nat}\text{Ti}$  (99.6% purity). The sizes and weights of the foils were measured for determining the average thicknesses of the Tm and Ti foils. The thicknesses were found to be 21.0 and 9.1 mg/cm<sup>2</sup>, respectively. The foils were cut into small pieces of 6 × 6 mm<sup>2</sup> and stacked into a target holder, which was also served as a Faraday cup. The target was irradiated for 30 min with an 18 MeV proton beam. Energy degradation in the target was calculated using the SRIM code

[4]. The average beam intensity was 210 nA, which was measured by the Faraday cup. Gamma rays emitted from each irradiated foil were measured by an HPGe detector without chemical separation. Nuclear data required to derive cross sections were obtained from NuDat 2.7 [5] and QCalc [6] and summarized in Table 1.

Table 1. Reaction and decay data for  $^{169}\text{Yb}$  production

Nuclide	Half-life	Decay mode (%)	$E_\gamma$ (keV)	$I_\gamma$ (%)	Contributing reaction	Q-value (MeV)
$^{169}\text{Yb}$	32.018 d	EC (100)	177.21	22.28(11)	$^{169}\text{Tm}(p,n)$	-1.7

### 3. Results

The 177.21-keV gamma rays ( $I_\gamma = 22.28\%$ ) emitted with the  $^{169}\text{Yb}$  decay ( $T_{1/2} = 32.018$  d) were measured after a cooling time of about 4 days. The cross sections of the  $^{169}\text{Tm}(p,n)^{169}\text{Yb}$  reaction were derived from the measurements and the nuclear data in Table 1. The preliminary result is shown in Fig. 1 in comparison with the previous experimental data [7–9] and the TENDL-2017 data [10]. The peak amplitude of the data of Birattari et al. (1973) [7] is almost consistent with our result. However, the data of Spahn et al. (2005) [8] shows two times larger amplitude than ours. The peak of the TENDL-2017 data shows the similar amplitude with ours, however smaller width and lower energy position than ours.

### 4. Summary

We measured activation cross sections of the  $^{169}\text{Tm}(p,n)^{169}\text{Yb}$  reaction up to 18 MeV. The experiment was performed using the cyclotron at ATOMKI. The well-established methods, the stacked-foil activation method and the gamma-ray spectrometry, were adopted. The preliminary result of the cross sections was compared with previous experimental data and theoretical model calculation. The further analysis is being performed.

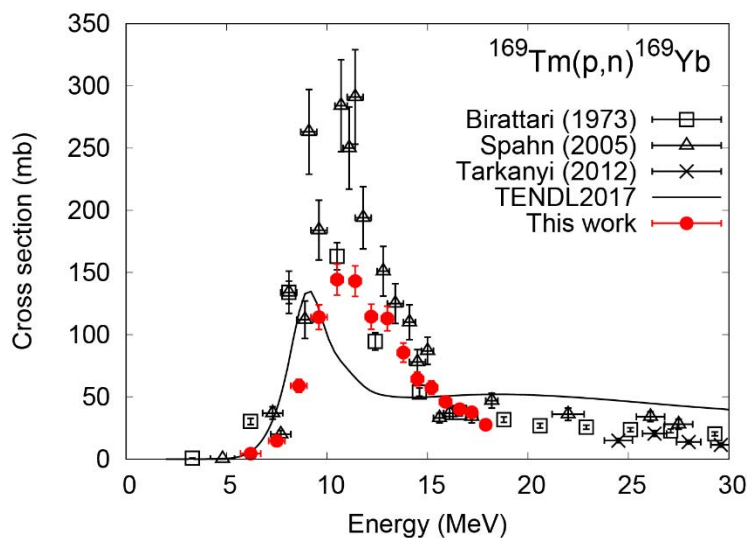


Fig. 1. Excitation function of the  $^{169}\text{Tm}(p,n)^{169}\text{Yb}$  reaction with the previous data [7–9] and the TENDL-2017 data [10].

## Acknowledgements

This work was carried out at Institute for Nuclear Research (ATOMKI), Hungary. This work was partly supported by “Optimization of accelerator production routes of the new theranostic radioisotopes Sc-47 and Cu-67 (FY2019-2020)”, under the Japan - Hungary Research Cooperative Program, JSPS and HAS and JSPS KAKENHI Grant Number 17K07004.

## References

- [1] Leonard KL, DiPetrillo TA, Munro JJ, et al., A novel ytterbium-169 brachytherapy source and delivery system for use in conjunction with minimally invasive wedge resection of early-stage lung cancer, *Brachytherapy*, 2011, 10, 163–169.
- [2] Saito M, Aikawa M, Komori Y, et al., Production cross sections of  $^{169}\text{Yb}$  and Tm isotopes in deuteron-induced reactions on  $^{169}\text{Tm}$ , *Appl. Radiat. Isot.* [Internet], 2017, 125, 23–26, Available from: <http://dx.doi.org/10.1016/j.apradiso.2017.04.010> (accessed 2020/03/24).
- [3] Saito M, Aikawa M, Sakaguchi M, et al., Production cross sections of ytterbium and thulium radioisotopes in alpha-induced nuclear reactions on natural erbium, *Appl. Radiat. Isot.* [Internet], 2019, 154, 108874, Available from: <https://doi.org/10.1016/j.apradiso.2019.108874> (accessed 2020/03/24).
- [4] Ziegler JF, Biersack JP, Ziegler MD, SRIM: the Stopping and Range of Ions in Matter [Internet], 2008, Available from: <http://www.srim.org> (accessed 2020/03/24).
- [5] National Nuclear Data Center, Nuclear structure and decay data on-line library, Nudat 2.7 [Internet], 2017, Available from: <http://www.nndc.bnl.gov/nudat2/> (accessed 2020/03/24).
- [6] Pritychenko B, Sonzogni A, Q-value Calculator (QCalc) [Internet], 2003, Available from: <http://www.nndc.bnl.gov/qcalc/> (accessed 2020/03/24).
- [7] Birattari C, Gadioli E, Gadioli Erba E, et al., PRE-EQUILIBRIUM PROCESSES IN (p,n) REACTIONS, *Nucl. Phys. A*, 1973, 201, 579–592.
- [8] Spahn I, Takács S, Shubin YN, et al., Cross-section measurement of the  $^{169}\text{Tm}(p,n)$  reaction for the production of the therapeutic radionuclide  $^{169}\text{Yb}$  and comparison with its reactor-based generation, *Appl. Radiat. Isot.*, 2005, 63, 235–239.
- [9] Tárkányi F, Hermanne A, Takács S, et al., Activation cross-sections of proton induced nuclear reactions on thulium in the 20-45MeV energy range, *Appl. Radiat. Isot.*, 2012, 70, 309–314.
- [10] Koning AJ, Rochman D, Sublet J-C, et al., TENDL: Complete Nuclear Data Library for Innovative Nuclear Science and Technology, *Nucl. Data Sheets*, 2019, 155, 1–55.

This is a blank page.

## 17 Measurements of nuclear cross section data for proton-induced reactions on Bi and Pb targets at intermediate energy

M. BAKHTIARI<sup>1</sup>, L. Mokhtari ORANJ<sup>2</sup>, N. S. JUNG<sup>2</sup>, A. LEE<sup>2</sup>, H. S LEE<sup>1,2\*</sup>

<sup>1</sup>*Division of Advanced Nuclear Engineering (DANE), POSTECH, Korea*

<sup>2</sup>*Pohang Accelerator Laboratory (PAL), POSTECH, Korea*

\* Email: lee@postech.ac.kr

Nuclear cross sections data of  $^{209}\text{Bi}(p, xn)^{207,206,205,204,203}\text{Po}$ ,  $^{209}\text{Bi}(p, pxn)^{207,206,205,204,203,202}\text{Bi}$ , and  $^{\text{nat}}\text{Pb}(p, xn)^{206,205,204,203,202,201}\text{Bi}$  reactions were measured using the stack-foil activation technique and gamma-ray spectrometry over the 40 to 100 MeV proton energy range. The targets were arranged in different stacks consisting of Bi, Pb, Al, Au foils and Pb plates. The proton beam intensity was determined by activation analysis method using  $^{27}\text{Al}$  and  $^{197}\text{Au}$  foils. Furthermore, excitation functions of the mentioned reactions were calculated by using the theoretical models based on the TALYS code and compared to the measured data in this work as well as with other data in the literature. Combinations of the nuclear input parameters of different level density models, optical model potentials, and  $\gamma$ -ray strength functions were considered. It was concluded that the level density models influenced the reaction cross sections significantly.

### I. Introduction

Production cross sections of radionuclide via proton-induced reactions play an important role in different applied physics fields [1]. A literature review showed that there is a lack of the production cross sections on bismuth and lead in the energy range of 40 to 100 MeV. In a series of the experiments, the production cross sections of  $^{209}\text{Bi}(p, xn)^{207,206,205,204,203}\text{Po}$ ,  $^{209}\text{Bi}(p, pxn)^{207,206,205,204,203,202}\text{Bi}$ , and  $^{\text{nat}}\text{Pb}(p, xn)^{206,205,204,203,202,201}\text{Bi}$  were measured [2–4]. Here a part of the measured data are reported. In addition, theoretical calculations were performed using the TALYS code [5] to understand the capability of the nuclear model calculations in the reaction cross sections estimation.

### II. Methods

#### A. Experiment

The cross sections of the proton-induced reactions on Bi and Pb were measured in four rounds of experiment. The targets were arranged in stacks and were irradiated with 100-MeV protons (two rounds) and 69-MeV protons (two rounds). Five  $^{209}\text{Bi}$  foils (purity: 99.97%, thickness: 50  $\mu\text{m}$ , density: 9.8  $\text{gcm}^{-3}$ ) were stacked and irradiated by 100-MeV (irradiation time: 120 s) and 69-MeV (irradiation time: 240 s and 25 s) protons. In addition, five  $^{\text{nat}}\text{Pb}$  foils (purity: 99.99%, thickness: 50  $\mu\text{m}$ , density: 11.35  $\text{gcm}^{-3}$ ) were used as target and irradiated by 100-MeV protons for 204 s. Au (purity: 99.95%, thickness: 30  $\mu\text{m}$ , density: 19.3  $\text{gcm}^{-3}$ ) and Al (purity:

99.999%, thickness: 100  $\mu\text{m}$ , density: 2.69  $\text{gcm}^{-3}$ ) foils were stacked in the target to monitor the proton beam intensities via  $^{197}\text{Au}(p, x)^{196,194}\text{Au}$  and  $^{27}\text{Al}(p, 3pn)^{24}\text{Na}$  reactions, respectively. Figure 1 shows the schematic view of the target stack. Proton energy distribution on each foil was determined using the Monte Carlo code FLUKA [6]. The experiments were conducted at Korea Multi-purpose Accelerator Complex (KOMAC). The detail information of the experimental set-up is explained in Refs. [2–4].

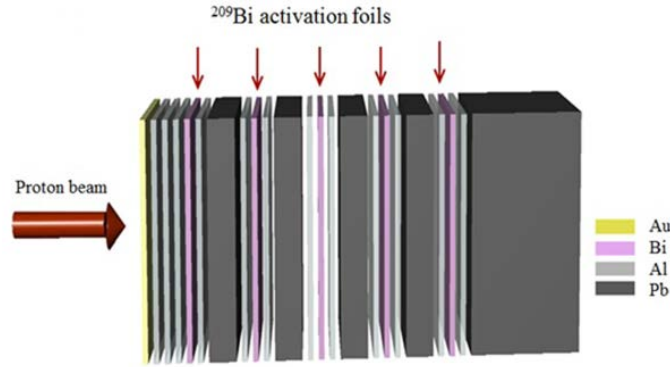


Fig 1. Schematic view of the target stack.

## B. Data analysis

Measurement of  $\gamma$ -ray spectra on each activation foil was performed using a high-resolution HPGe detector. The intense characteristic  $\gamma$  rays of each radionuclide were selected to identify the interested radionuclide [3]. The distance between the detector and activation foils was decided to keep the dead time low enough. The decay data of all radionuclides were taken from Ref. [7].

The production cross sections of the investigated radionuclides were determined by the following equation in case, the radionuclide is generated via only nuclear reaction of (p, xn):

$$\sigma = \frac{\lambda N_p}{\varepsilon_\gamma I_\gamma N_o \phi (1 - e^{-\lambda t_m}) e^{-\lambda t_c} (1 - e^{-\lambda t_i})}, \quad (1)$$

where  $N_p$  is net area of a full energy peak related to  $\gamma$ -ray transition of a nuclide,  $\lambda$  is the decay constant of the nuclide ( $\text{s}^{-1}$ ),  $\varepsilon_\gamma$  and  $I_\gamma$  are the efficiency of detector and absolute  $\gamma$ -ray intensity, respectively. The  $t_m$  and  $t_c$  denote the cooling time and measuring time (s), respectively.  $N_o$  is the number of target nuclei (atoms) and  $\Phi$  is the proton flux (protons/ $\text{cm}^2/\text{s}$ ). A radionuclide could be generated by a nuclear reaction as well as by the decay of a mother radionuclide. In such a case, the contribution of the precursor needs to be taken into account and the production cross section of the daughter radionuclide is determined using Eq. (2) for (p, pxn) reactions:

$$\sigma_d = \frac{\lambda_d (N_p)_d}{(\varepsilon_\gamma)_d (I_\gamma)_d N_o \phi F_d} + P \sigma_m \frac{\lambda_m}{\lambda_d - \lambda_m} \left( 1 - \frac{\lambda_d^2}{\lambda_m^2} \frac{F_m}{F_d} \right), \quad (2)$$

where the factor  $F_k$  ( $k = m, d$ ) is related to the time condition as follows:

$$F_k = (1 - e^{-\lambda_k t_i}) e^{-\lambda_k t_c} (1 - e^{-\lambda_k t_m}), \quad (3)$$

where  $\sigma_d$  and  $\sigma_m$  are the cross sections for formation of daughter and mother radionuclei ( $\text{cm}^2$ ),  $\lambda_d$  and  $\lambda_m$  are the decay constant of daughter and mother radionuclei, respectively.  $P$  is the branching fraction of mother nuclei decay to daughter,  $t_i$  is the irradiation time (s). The results of  $^{209}\text{Bi}(p, xn)^{206,205}\text{Po}$ ,  $^{209}\text{Bi}(p, pxn)^{204}\text{Bi}$  and  $^{\text{nat}}\text{Pb}(p, xn)^{204}\text{Bi}$  are presented.

### C. Nuclear model calculations

Reaction cross sections of the assessed radionuclei were calculated using the nuclear model calculations based on the TALYS [5] code and were compared to the measured experimental data. TALYS is a nuclear model code that uses protons, neutrons, photons,  $^3\text{He}$  and  $^4\text{He}$  as projectiles in the energy range of 1 keV to 200 MeV. The calculations were performed using different nuclear ingredients to consider their effects on the reaction cross sections. Nuclear level densities (NLDs), optical model potentials (OMPs) and  $\gamma$ -ray strength functions ( $\gamma$ SFs) with all 768 possible combinations were used in the calculations. The detail information of the models and their definitions can be found in Refs. [2,5]. In the figures, the shaded areas indicate the variation of the cross sections by using different combinations.

## III. Results

$^{206}\text{Po}$  ( $T_{1/2} = 8.8$  d; EC, 94.55%; and  $\alpha$ , 5.45%) can be produced through  $^{209}\text{Bi}(p, xn)^{206}\text{Po}$  reaction. The activities of this radionuclide were measured using 286.4-, 522.5-, 807.4- and 980.2-keV  $\gamma$  rays. The measured cross sections are shown in Fig. 2(a) and are compared with other experimental data together with theoretical calculations. Generally, our measured data are in agreement with other experimental data in the literature. As it is seen from the figure, experimental and theoretical results show two different peaks at 40 MeV. The TALYS calculations using different model combinations showed that by changing the type of the NLD, the cross section values are changed significantly. TALYS calculations predict the reaction threshold well.

The  $^{205}\text{Po}$  ( $T_{1/2} = 1.74$  h; EC, 99.96%; and  $\alpha$ , 0.04%) production cross sections were measured using 836.8-, 849.8- and 872.4-keV  $\gamma$  rays in the energy range of 40 to 100 MeV and are shown in Fig. 2(b). Measured cross sections are on a similar trend to experimental data in the literature. The TALYS calculation predicts the maximum cross section of 890 mb at 45 MeV, while the measured cross section is 875.8 mb at 51 MeV. It seems that TALYS is indicating a lower energy threshold than the experimental data.

$^{204}\text{Bi}$  has a ground state with a half-life of 11.22 h and two short-lived metastable states with half-lives of 13 and 1.07 ms which decay to the ground state with branching ratios of 100%. The  $^{209}\text{Bi}(p, p5n)^{204}\text{Bi}$  reaction and  $^{204}\text{Po}$  ( $T_{1/2} = 3.519$  h) decay could lead to the production of  $^{204}\text{Bi}$ . The production yield of  $^{204}\text{Bi}$  was measured using 374.76-keV  $\gamma$  ray in the spectrum. The measured independent cross sections are illustrated in Fig. 2(c). Our measured data in two are newly measured cross sections. Nuclear model calculations predict the reaction threshold energy well. Theoretical calculations vary significantly with level density models, indicating

the effectiveness of the NLDs on the reaction cross sections. The reaction cross sections did not change significantly by changing the type of OMP and  $\gamma$ SF [2].

$^{204}\text{Bi}$  production cross sections on  $^{\text{nat}}\text{Pb}$  target were also measured and compared to the measured data in the literature as well as the TALYS calculations as shown in Fig. 2(d). Measured cross sections in this work are in agreement with other experimental data. TALYS default calculations seem to predict the maximum measured cross sections quite well. On the other hand, microscopic NLDs show lower cross sections values. The reaction cross sections did not change significantly by changing the type of OMP and  $\gamma$ SF. All nuclear model calculations underestimate the experimental data after 60 MeV.

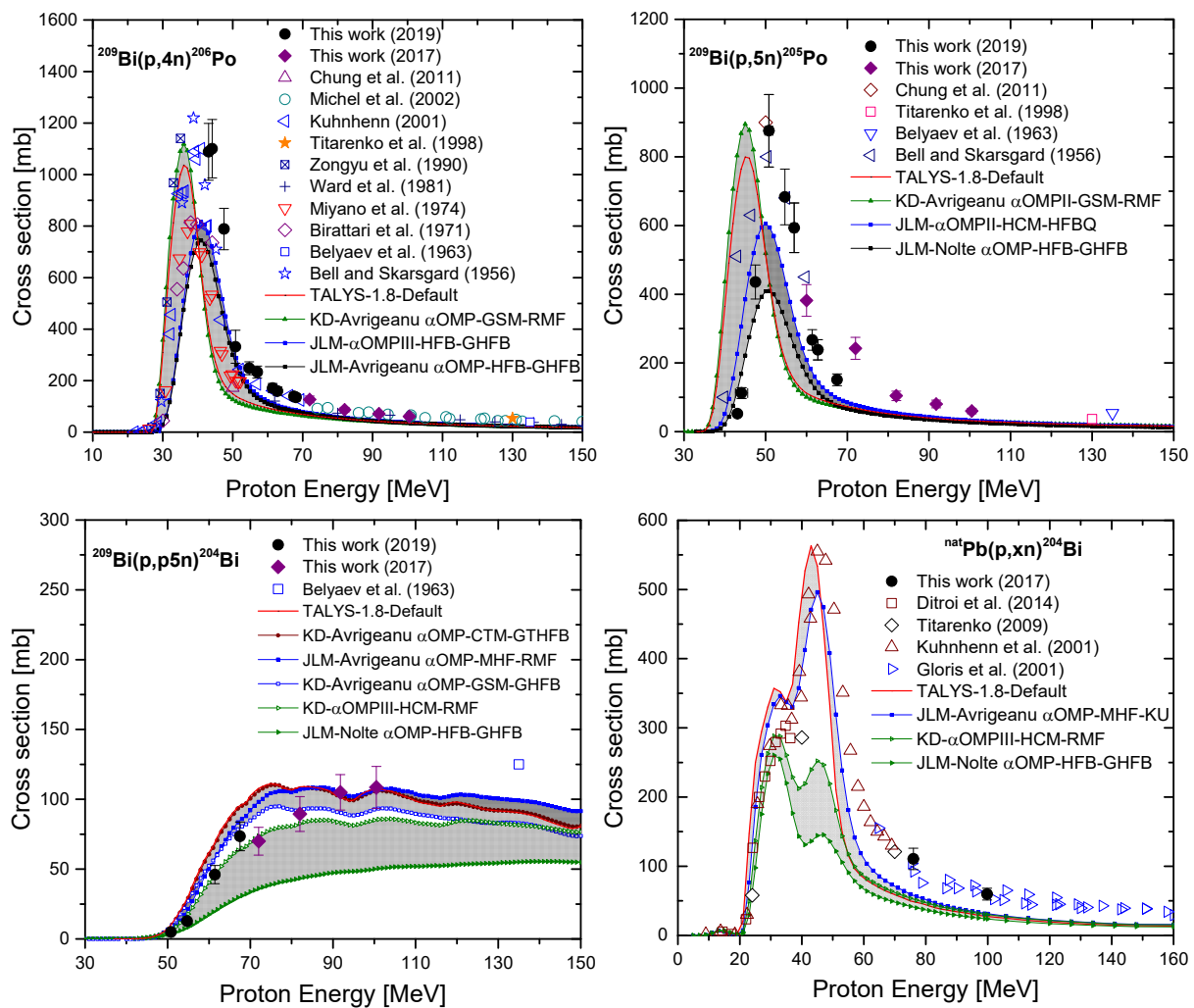


Fig 2. Measured independent cross sections for the (a)  $^{209}\text{Bi}(p,4n)^{206}\text{Po}$ , and (b)  $^{209}\text{Bi}(p,5n)^{205}\text{Po}$ , (c)  $^{209}\text{Bi}(p,p5n)^{204}\text{Bi}$ , and (d)  $^{\text{nat}}\text{Pb}(p,xn)^{204}\text{Bi}$  reactions compared with the previously published data together with theoretical calculations using the TALYS code. Our measured data are published in Refs. [2,3]. Other experimental data are taken from EXFOR [8].

## IV. Conclusions

Production cross sections of proton-induced reactions on  $^{209}\text{Bi}$  and  $^{\text{nat}}\text{Pb}$  were measured using over the energy range of 40 to 100 MeV. The results of  $^{209}\text{Bi}(p, xn)^{206,205}\text{Po}$ ,  $^{209}\text{Bi}(p, pxn)^{204}\text{Bi}$  and  $^{\text{nat}}\text{Pb}(p, xn)^{204}\text{Bi}$  are presented. Our measured data were in agreement with the other experimental data reported in the literature. Theoretical calculations were performed using the TALYS code by applying different nuclear ingredients of NLDs, OMPs and  $\gamma$ SFs and were compared to the theoretical calculations. It was concluded that the most effective models were NLDs rather than OMPs and  $\gamma$ SFs for the investigated nuclear reactions between 40 and 100 MeV.

## Acknowledgement

The authors thank the KOMAC team for their support during the experiment. This work is supported by the Nuclear Safety Research Program through the Korea Foundation Of Nuclear Safety (KOFONS), granted financial resources from the Nuclear Safety and Security Commission (NSSC) of Republic of Korea (Grants No.1303026 and No. 1603005).

## References

- [1] Gloris M, Michel R, Herpers U, Sudbrock F, Filges D. Production of residual nuclei from irradiation of thin Pb-targets with protons up to 1.6 GeV. Nucl. Instruments Methods Phys. Res. Sect. B Beam Interact. with Mater. Atoms. 1996;113:429–433.
- [2] Mokhtari Oranj L, Jung NS, Bakhtiari M, Lee A, Lee HS. Cross sections of proton-induced nuclear reactions on bismuth and lead up to 100 MeV. Phys. Rev. C. 2017;95:1–15.
- [3] Mokhtari Oranj L, Bakhtiari M, Jung NS, Lee A, Lee HS. Extension of excitation functions of proton-induced reactions on bismuth. Phys. Rev. C. 2020;101:14602.
- [4] Mokhtari Oranj L, Bakhtiari M, Kye YU, Jung NS, Lee A, Lee HS. Benchmarking FLUKA, PHITS, MCNPX, and MARS15 codes with product yields of  $^{209}\text{Bi}(p, x)$  reactions. Nucl. Instruments Methods Phys. Res. Sect. B Beam Interact. with Mater. Atoms. 2020;462:154–162.
- [5] Koning AJ, Hilaire S, Duijvestijn MC. TALYS-1.0. ND2007. Les Ulis, France: EDP Sciences; 2007. Available from: <http://www.talys.eu/> (accessed 2020/03/24).
- [6] Fasso A, Ferrari A, Ranft J, Sala PR. FLUKA: a multi-particle transport code [Internet]. CERN-2005-10, INFN/TC\_05/11, SLAC-R-773; 2005. Available from: <http://www.fluka.org/> (accessed 2020/03/24).
- [7] ENSDF database [Internet]. Available from: <http://www.nndc.bnl.gov/ensarchivals/> (accessed 2020/03/24).
- [8] Zerkin VV, Pritychenko B. The experimental nuclear reaction data (EXFOR): Extended computer database and Web retrieval system. Nucl. Instruments Methods Phys. Res. Sect. A Accel. Spectrometers, Detect. Assoc. Equip. 2018;888:31–43.

This is a blank page.

## 18 Measurement of nuclide production cross sections for $Z = 26-30$ elements irradiated with 0.4 - 3.0 GeV proton in J-PARC

Hiroki MATSUDA<sup>1</sup>, Hayato TAKESHITA<sup>2</sup>, Hiroki IWAMOTO<sup>1</sup>, and Shin-ichiro MEIGO<sup>1</sup>

<sup>1</sup> J-PARC Center, Japan Atomic Energy Agency, 2-4 Tokai-mura, Ibaraki 319-1195, Japan

<sup>2</sup> Department of Advanced Energy Engineering Science, Kyushu University, Kasuga, Fukuoka 816-8580, Japan

email: matsuda.hiroki@jaea.go.jp

For the design of Accelerator-Driven nuclear transmutation System (ADS), accurate cross section data are required to estimate the number of radioactive nuclides for treating radioactive wastes in the ADS plant. Although much effort has been devoted to obtaining the nuclide production cross section irradiated by protons in the energy region utilized for the ADS at several facilities so far, data with systematic uncertainties of  $\sim 10\%$  exist. Furthermore, no experimental data still exist around for protons in a few GeV region. In order to validate the calculation code and the evaluated data utilized for the ADS, we started the experiment to obtain the cross section at 3-GeV synchrotron in J-PARC. In this study, we obtained nuclide production cross section for targets with  $Z$  numbers from 26 to 30 (i.e.,  $^{nat}\text{Fe}$ ,  $^{nat}\text{Ni}$ , and  $^{nat}\text{Zn}$ ), which are important regions for the estimation of the radioactivity of the ADS structural materials. Furthermore, we investigated the incident energy dependency on the cross section from several hundred MeV to 3 GeV using the present and the previous experimental data, comparing with different intra-nuclear cascade and evaporation models of INCL4.6/GEM, INCL++/ABLA07, and Bertini/GEM, and evaluated nuclear data of JENDL-HE2007.

### 1. Introduction

Accelerator-Driven nuclear transmutation System (ADS) transmutes minor actinides (MA) by supplying neutrons continuously. Neutrons are supplied by a spallation reaction of lead-bismuth eutectic (LBE) irradiated by 1.5 GeV energy protons, which is also utilized as coolant. For the estimation of the radioactive nuclides to treat wastes and evaluate the chemical effect of spallation products in the LBE, accurate cross section data are required. Although much effort has been devoted to conducting nuclide production cross section measurements at several facilities since the 1950s, the uncertainties of data, being typically about 10%, are not good enough to validate the calculation model. Furthermore, data around in a few GeV region, which are candidates for projectile energies of the ADS, have larger uncertainty than other regions. Thus, the experiment was performed in J-PARC. In this study, we obtained nuclide production cross section for targets with  $Z$  numbers from 26 to 30 (i.e.,  $^{nat}\text{Fe}$ ,  $^{nat}\text{Ni}$ , and  $^{nat}\text{Zn}$ ), which are important regions for the estimation of the radioactivity of the ADS structural materials. They were irradiated by proton

beams having different energies of 0.4, 1.3, 2.2, and 3.0 GeV. A comparison between the experimental data and the calculations were demonstrated. In this paper, the details of the experiment and analysis procedure for Zn target are described. The results of Fe and Ti have been already reported [1,2].

## 2. Experiment

### 2.1 Setup

The basic experiment setup was the same as Ref. [3]. The experiment was carried out at the beam transport line from the RCS [4] to the Materials and Life Science Experimental Facility (MLF), which is called as 3NBT. Thin square foils of Fe, Ni, and Zn, 0.1 mm thick and 25mm long, were sandwiched with thin aluminum foil with 0.1mm thick to evaluate the number of recoil nuclides. Four sets of this sample were placed at the head of each linear stage guide. They were placed in the vacuum chamber that was installed in the beam dump line. A linear stage guide was controlled remotely to insert and extract samples.

### 2.2 Irradiation

Each sample set was irradiated by 0.4, 1.3, 2.2, and 3.0 GeV protons, respectively. The 0.4 GeV beam was transported from the LINAC without acceleration. The other energies were obtained by changing the extraction timing of the kicker magnet at RCS. The beam width and position were measured with the multi-wire profile monitor (MWPM) installed in the beamline. The number of protons in the beam was monitored by the current transformer (CT). Beam profile measurement using an imaging plate (IP) was performed after irradiation to improve the accuracy of the beam position on the samples. Repetition of shots was set to 0.4 Hz to avoid melting of samples. In total, 40 shots, i.e.,  $2.32 \times 10^{14}$  protons, were irradiated for each target. After irradiation, the linear stage guides were removed from the chamber. The cooling time, which is the time interval between the end of the irradiation to the beginning of the measurement, was approximately six to nine hours.

### 2.3 Analysis

Decay gamma-rays from irradiated samples were measured by the high pure germanium detector (HPGe, Mirion Technologies GC2018). The list of activation products analyzed in this paper was summarized in Table 1.

The samples were mounted on the acrylic spacer apart from the head of HPGe by about 5 cm or 25 cm to keep detector-to-sample geometry rigidly. The production cross section of specified nuclei  $\sigma$  was written as

$$\sigma = \frac{C}{t_l \epsilon I \gamma \mu} \times \frac{t_r}{1 - \exp(-\lambda t_r)} \times \frac{\exp(\lambda t_c)}{N_p n} \dots (1)$$

where  $C$  is the number of count of a peak,  $t_l$  is so-called live-time which includes deadtime

correction during measurement,  $\epsilon$  is the efficiency at the peak energy,  $I_\gamma$  is the absolute gamma-ray intensity,  $\mu$  is the self-absorption correction,  $t_r$  is so-called real-time,  $\lambda$  is the decay constant of the nuclide,  $N_p$  is the number of protons irradiated, and  $n$  is the number density of the sample.

**Table 1 The list of nuclides analyzed.**

Nuclide	Half-life
<sup>7</sup> Be	53.22 d
<sup>22</sup> Na	2.6018 y
<sup>48</sup> Cr	21.56 h
<sup>54</sup> Mn	312.20 d
<sup>52</sup> Fe	8.275 h
<sup>55</sup> Co	17.53 h
<sup>58</sup> Co	70.86 d
<sup>57</sup> Ni	35.60 h
<sup>61</sup> Cu	3.389 h
<sup>64</sup> Cu	12.701 h
<sup>62</sup> Zn	9.193 h
<sup>65</sup> Zn	243.93 d

Here the correction during irradiation was not applied since the irradiation time was considerably shorter than the half-life of products. The recoil particles could be trapped by the forward and backward aluminum foils. They were observed in the actual aluminum foil. However, the activity of them was evaluated as a negligible amount. Thus, this correction was not applied in this experiment. The effects of secondary particles affecting the backward samples were also estimated by the simulation. Since very thin samples were employed in this experiment, the number of secondary particles was lower than the irradiated protons in the order of three or four digits. Hence, this effect

was not considered in this analysis. The number density of the sample  $n$  is derived by

$$n = \frac{m}{MS} N_A \dots (2)$$

where  $m$  is the sample mass that is measured by the electric scale,  $S$  is the surface area of the sample,  $M$  is the atomic weight of the sample, and  $N_A$  is Avogadro constant. The self-absorption correction  $\mu$  is calculated by

$$\mu = \frac{1 - \exp(-\mu_{att}\rho t)}{\mu_{att}\rho t} \dots (3)$$

where  $\mu_{att}$  is the attenuation coefficient,  $\rho$  is the sample density, and  $t$  is the thickness of the sample. Detector efficiency of the HPGe was evaluated by using <sup>241</sup>Am, <sup>152</sup>Eu, <sup>60</sup>Co, and <sup>137</sup>Cs standard gamma-ray sources, which were put at the same position as the samples. Sum-peak corrections for multi gamma-ray sources were applied [5].

The number of protons and beam profile (width and position) were measured precisely by the CT and the MWPM, respectively. Beam profile measurement using an IP (FUJI-FILM BAS-SR2040) was also performed to improve the accuracy of the beam profile. The irradiated samples were placed onto the IP to expose. After exposure, the IP was scanned by the image processor (GE healthcare Typhoon FLA 7000). Scanned images were fit by a two-dimensional Gaussian to evaluate the width and position of the beam. Here the Gaussian shape was guaranteed by the measurement of the MWPM. Finally, the fractions of the proton beam on the sample foils were

derived by integrating the function over the sample area. As a result, the fractions ranged from 0.98 to 1.00. This fraction was used for the final correction.

The sample surface area was measured by a typical image scanner (EPSON GT-S650).

### 2.4 Uncertainty estimation

**Table 2** Table of uncertainties.

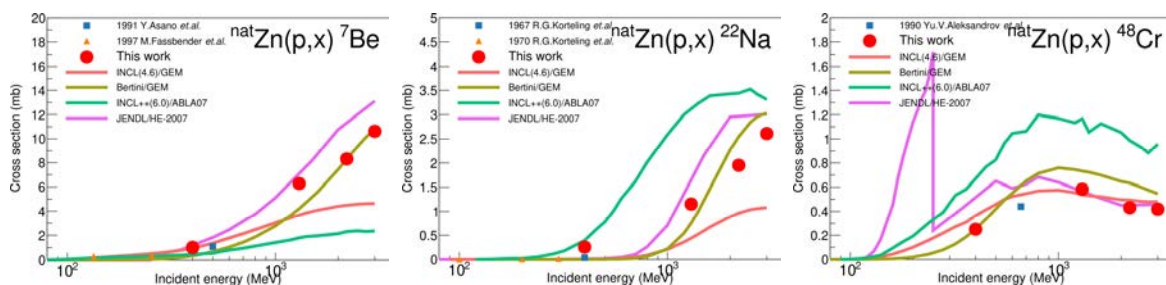
Description	Estimated uncertainty %
Statistics of gamma-ray count	<0.1 – 10
Detector efficiency	1.0
Sample weight	<0.1
Sample surface area	1.4
Time	<0.1
Self-absorption	0.1
The number of protons	1
Imaging plate	<0.1
Branching ratio	<0.1 – 30
In total	2.0 – 31.7

The list of uncertainties concerned is shown in Table 2. The uncertainty of the detector efficiency was the standard deviation of differences between measured points and calculated ones. Imaging plate uncertainty, namely the uncertainty of irradiated proton fraction, was evaluated as the standard deviation of proton fraction of all samples at the same energy. The

reading uncertainty of scanning of 1mm scale with 800 dots/inch, i.e., 314.96 dots/mm, was 1 dot. In addition, an ambiguity for an edge detection could be estimated as 2 dots. Thus, the uncertainty of the sample surface was evaluated as 1.4% by a square root of the sum of the square of 3/314.96.

### 3. Results and observations

The PHITS code [6] was employed to calculate the production cross sections with two intranuclear cascade models (Bertini and INCL4.6 [7]) and generalized evaporation model (GEM [8]). The calculation by using the INCL++ code [9] with INCL++v6.0.1 and ABLA07 [10] models was also performed. The number of histories was sufficiently large, so that calculation uncertainties were negligible. In Fig. 1, the measured, the calculated, and the evaluated cross sections of JENDL-HE/2007 [11] for each production cross sections of zinc were shown. The other experimental data were taken from EXFOR [12].



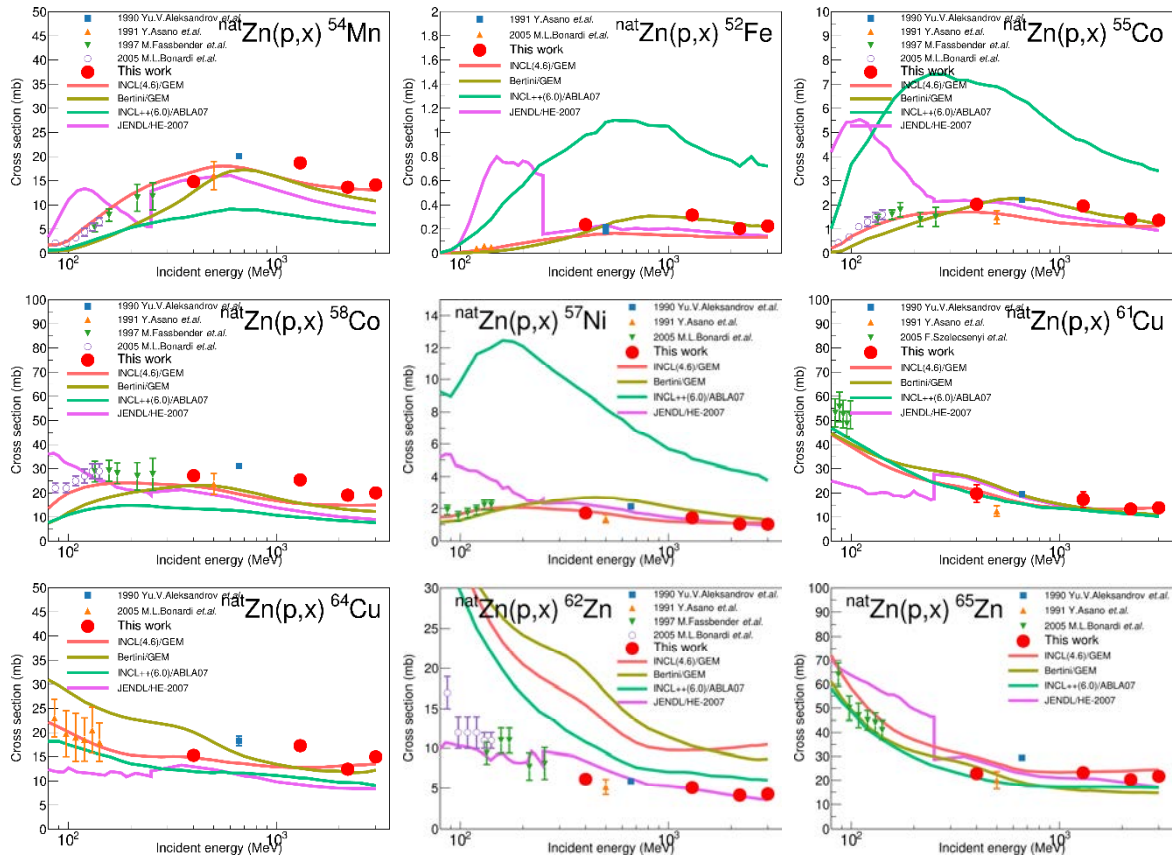


**Figure 1** Production cross sections of  ${}^7\text{Be}$ ,  ${}^{22}\text{Na}$ ,  ${}^{48}\text{Cr}$ ,  ${}^{54}\text{Mn}$ ,  ${}^{52}\text{Fe}$ ,  ${}^{55}\text{Co}$ ,  ${}^{58}\text{Co}$ ,  ${}^{57}\text{Ni}$ ,  ${}^{61}\text{Cu}$ ,  ${}^{64}\text{Cu}$ ,  ${}^{62}\text{Zn}$ , and  ${}^{65}\text{Zn}$  from  $\text{natZn}$ . This works (red filled circle), other experiments (colored other symbols) taken from EXFOR, calculations (colored solid lines), and the evaluated data (magenta solid line) are plotted.

For all production cross sections shown in this paper, PHITS calculations agreed with the experimental data. In the light nuclide productions such as  ${}^7\text{Be}$  and  ${}^{22}\text{Na}$ , Bertini model gave better agreement than INCL4.6. INCL4.6 calculations agreed with heavier nuclide productions, i.e., less than 10 nucleons emission reactions. In contrast, INCL++ code overestimated or underestimated for almost all productions. This tendency was also observed in the cross section with Fe and Ni targets [1,2]. JENDL-HE/2007 agreed with the experimental data for all cross sections though it showed strange behavior below 150 – 250 MeV, in which the evaluation method was changed from the GNASH code [13] to a microscopic simulation code (either JAM [14] or JQMD [15]).

#### 4. Summary

The production cross sections from Zn with 0.4, 1.3, 2.2, and 3.0 GeV protons were measured at J-PARC. In total, nearly 50 cross sections were obtained with higher accuracy than other experimental data in the past thanks to quite stable J-PARC beam and monitoring systems. The present results were compared with the calculations and the evaluated nuclear data. The present

experimental data suggested that further improvement of models is mandatory in the GeV energy region. The evaluated data was in good agreement with the experimental data.

### Acknowledgment

The authors are grateful to Mrs. Nishikawa and Hirano, and the members of Nippon Advanced Technology (NAT) for technical assistance with the experiments and to Drs. Saha, Hotchi, and Harada for tuning of the RCS.

### References

- [1] H. Matsuda, *et al.*, Atomic Energy Society of Japan, 2019 Spring Meeting, Mar. 2019 (in Japanese).
- [2] H. Takeshita, *et al.*, Atomic Energy Society of Japan, 2019 Fall Meeting, Sep. 2019 (in Japanese).
- [3] H. Matsuda, S. Meigo, H. Iwamoto, *J. Nucl. Sci. Technol.* **55**, 8 (2018).
- [4] S. Meigo, F. Noda, S. Ishikura, *et al.*, *Nucl. Instrum. Meth. A* **562**, 569 (2006).
- [5] E. Tomarchio, S. Rizzo, *Radiat. Phys. Chem.* **80**, 318 (2011).
- [6] T. Sato, Y. Iwamoto, S. Hashimoto, *et al.*, *J. Nucl. Sci. Technol.* **55**, 6 (2018).
- [7] A. Boudard, J. Cugnon, J.C. David, *et al.*, *Phys. Rev. C* **87**, 014606 (2013).
- [8] S. Furihata, *Nucl. Instrum. Meth. B* **171**, 3 (2000).
- [9] D. Mancusi, A. Boudard, J. Cugnon, *et al.*, *Phys. Rev. C* **90**, 054602 (2014).
- [10] A. Kelic, M.V. Ricciardi, K.H. Schmidt (2009), arxiv:0906.4193.
- [11] Y. Watanabe, K. Kosako, S. Kunieda, *et al.*, *J. Korean Phys. Soc.* **59**, 1040 (2011).
- [12] V. Zerkin, B. Pritychenko, *Nucl. Instrum. Meth. A* **888**, 31 (2018).
- [13] P. G. Young, E. D. Arthur, M. B. Chadwick, LA-12343-MS, LANL (1992).
- [14] Y. Nara, N. Otuka, A. Ohnishi, *et al.*, *Phys. Rev. C* **61**, 024901 (1999).
- [15] K. Niita, S. Chiba, T. Maruyama, *et al.*, *Phys. Rev. C* **52**, 2620 (1995).

# 19 Study of an angular correlation of $\gamma$ -rays emitted by $^{117}\text{Sn}(n,\gamma)$ reactions for T-violation search

Jun KOGA<sup>1</sup>, Shunsuke ENDO<sup>2</sup>, Hiroyuki FUJIOKA<sup>3</sup>, Katsuya HIROTA<sup>4</sup>, Kohei ISHIZAKI<sup>4</sup>,  
 Atsushi KIMURA<sup>2</sup>, Masaaki KITAGUCHI<sup>4</sup>,  
 So MAKISE<sup>1</sup>, Yudai NIINOMI<sup>4</sup>, Takuya OKUDAIRA<sup>2</sup>, Kenji SAKAI<sup>2</sup>, Tatsushi SHIMA<sup>5</sup>, Hirohiko  
 M. SHIMIZU<sup>4</sup>, Sshusuke TAKADA<sup>1</sup>, Yuika TANI<sup>3</sup>, Tomoki YAMAMOTO<sup>4</sup>, Hiromoto YOSHIKAWA<sup>5</sup>,  
 and Tamaki YOSHIOKA<sup>1</sup>

<sup>1</sup>*Kyushu University, 744 Motoooka, Nishi-ku, Fukuoka 819-0395, Japan*

<sup>2</sup>*Japan Atomic Energy Agency, 2-4 Shirakata, Tokai 319-1195, Japan*

<sup>3</sup>*Tokyo Institute of Technology, 2-12-1 Ookayama Meguro-ku, Tokyo 152-8550, Japan*

<sup>4</sup>*Nagoya University, Furo-cho, Chikusa-ku, Nagoya 464-8601, Japan*

<sup>5</sup>*Research Center for Nuclear Physics, Osaka University, 10-1 Mihogaoka, Ibaraki 567-0047, Japan*

*E-mail: j.koga@epp.phys.kyushu-u.ac.jp*

A discovery of violation of time-reversal symmetry (T-violation) can lead to a solution for an asymmetry between matter and antimatter in the current universe, which is one of the important problems in particle physics and astrophysics. An enhancement of T-violation is theoretically proposed in several compound nuclear reactions. The experimental sensitivity to find a T-violating effect depends on a spin factor  $\kappa(J)$  which is different from each nuclide. It can be determined from an angular dependence of a differential cross section of neutron-nucleus reaction, and the experiments to measure this angular correlation have conducted at J-PARC. In this paper, the measurement result and the analysis status of experiments using the target nucleus  $^{117}\text{Sn}$  are reported.

## 1. Introduction

An asymmetry between the number of matter and antimatter in the current universe is one of the important problems which should be solved in particle physics and astrophysics. A. Sakharov proposed that violation of charge conjugation and parity symmetry (CP-violation) stronger than expected within the Standard Model of particle physics is necessary to explain this asymmetry [1].

Compound nuclear reactions are expected as one of CP-violation search beyond the Standard Model under the assumption that the CPT theorem, which means that CP-violation is equal to the violation of time-reversal symmetry (T-violation), is correct. In several compound nuclear reactions, the violation of parity symmetry (P-violation) is observed with an enhancement factor of  $10^6$  compared to the proton-proton scattering [2]. This enhancement is theoretically explained as a *sp*-mixing model describing an interference between amplitudes of s-wave resonances and p-wave resonances. It is theoretically suggested that T-violation is enhanced by a similar mechanism in several nuclear reactions [3]. In addition, this theory proposes that an experimental sensitivity depends on each nuclides. One of the key parameters allowing to become good candidate nuclei is a spin factor  $\kappa(J)$ . Thus, there is a possibility that the magnitude of T-violating effect is enhanced if the value of  $\kappa(J)$  is not small. The  $\kappa(J)$  is related to neutron resonance partial widths via a mixing angle  $\phi$  describing a superposition of different spin components. So far only  $^{139}\text{La}$  has been determined the value of  $\kappa(J)$  by Okudaira et al. [4]. To identify further candidates for T-violation search, other nuclei must be measured.

The mixing angle  $\phi$  can be determined by measuring an angular correlation of prompt  $\gamma$ -rays emitted from compound nucleus with respect to a direction of incident neutrons. According to Flambaum [5],

the differential cross section for unpolarized neutrons is described as follows:

$$\frac{d\sigma}{d\Omega} = \frac{1}{2} \left\{ a_0 + a_1 \cos \theta_\gamma + a_3 \left( \cos^2 \theta_\gamma - \frac{1}{3} \right) \right\}, \quad (1)$$

where  $\theta_\gamma$  is an angle between the flight directions of the emitted  $\gamma$ -rays and the incident neutrons. The  $a_0$  term corresponds to the Briet-Wigner formula, while the  $a_1$  and  $a_3$  terms include the mixing angle  $\phi$  [5]. Equation (1) indicates the shape of p-wave resonance depends on the direction of emitted  $\gamma$ -rays with respect to the incident neutrons due to their terms. We can verify the  $sp$ -mixing model by measuring this angular dependence of p-wave resonance.

The isotope  $^{117}\text{Sn}$  is one of the candidates for T-violation search. In this paper, the results of measurements of angular dependence of  $\gamma$ -ray emission around the 1.33 eV p-wave resonance, resonance parameters, and branching ratio of each resonance, which are essential values to calculate precisely the Eq. (1), is reported.

## 2. Experiment

### 2.1 Experimental setup

Our experiments were carried out with Accurate Neutron-Nucleus Measurement Instrument (ANNRI) in the Material and Life science experimental Facility (MLF) of the Japan Proton Accelerator Research Complex (J-PARC). ANNRI is installed at the neutron beam line BL04 to accept the pulsed neutron beam from spallation source of J-PARC MLF. Produced neutron beam was moderated by a liquid hydrogen moderator and supplied to the beam line at a repetition rate 25 Hz. The position of nuclear target is placed at 21.5 m from the moderator surface. Lead plates (in total 37.5 mm thickness) were installed at upstream to suppress background events stemmed from fast neutrons and  $\gamma$ -rays produced by spallation reactions. The disk choppers were operated synchronously with the proton-beam injection to avoid frame overlap due to low-energy neutrons.

ANNRI has a germanium detector assembly shown in Fig. 1. It consists of two types of detector units: type-A and type-B. The type-A is an assembly of 7 germanium crystals, while the type-B has a germanium crystal, and it has 22 crystals in total. Each crystal is installed at 36.0, 70.9, 72.0, 90.0, 108.0, 109.1, and 144.0 degrees with respect to the neutron beam direction, respectively. This detector assembly enables us to measure the deposit energy and the detection time of  $\gamma$ -rays in each germanium crystal. When we focus on the prompt  $\gamma$ -rays from the nucleus target by (n, $\gamma$ ) reaction, the detection time can be regarded as time-of-flight (TOF) of neutrons from moderator surface to the target position because the time difference between neutron capture and the emission of a prompt  $\gamma$ -ray is negligible. The incident neutron energy is calculated from the TOF of the neutrons.

### 2.2 Measured data set

We have conducted three experiments to measure (i) the angular dependence of the shape of p-wave resonance, (ii) resonance parameters, and (iii) branching ratio of each resonance. Here, the branching ratio means the transition ratio that the compound state decays to a final state of a specific energy level, which corresponds to the partial gamma width. Table I shows that each experimental condition. Target and measurement time are different in order to achieve each purpose.

**Table I.** Each experimental condition. Target and measurement time are different for each purpose. Proton beam power also depends on the date conducted in each experiment.

Purpose	Target	Size	Beam power	Measurement time
Angular dependence	$^{nat}\text{Sn}$	40×40×4 mm <sup>3</sup>	150 kW	65 hours
Resonance paramter	$^{117}\text{Sn}$ (86% enrich)	ϕ5 mm×6 mm	525 kW	6 hours
Branching ratio	$^{nat}\text{Sn}$	40×40×1 mm <sup>3</sup>	525 kW	100 hours

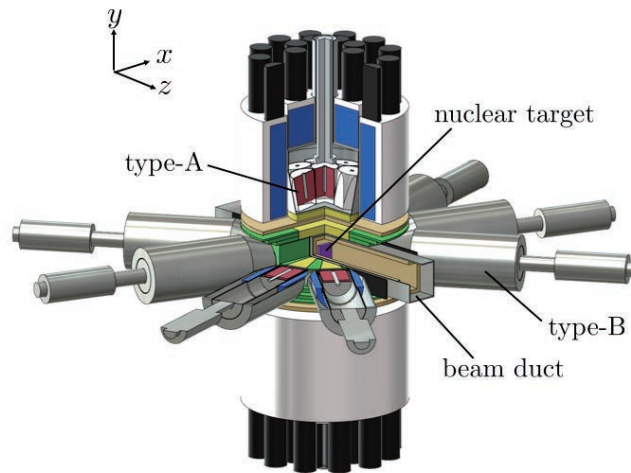


**Fig. 1.** Configuration of the germanium detector assembly in ANNRI.

Figure 2 shows the spectrum of the energy deposit of  $\gamma$ -rays in all germanium detectors in the experiment (i). The  $\gamma$ -transition in the nucleus  $^{118}\text{Sn}$  with an energy of 9327 keV and its single- and double-escape peaks can be observed clearly. It is known that the compound state in the p-wave resonance decays to the ground state of  $^{118}\text{Sn}$  directly. Therefore, we focused the peak with 9327 keV and its single- and double-escape peaks for our analysis to examine the angular dependence of the shape of p-wave resonance and to determine the branching ratio that the compound state of  $^{117}\text{Sn} + n$  system decays to the ground state of  $^{118}\text{Sn}$ .

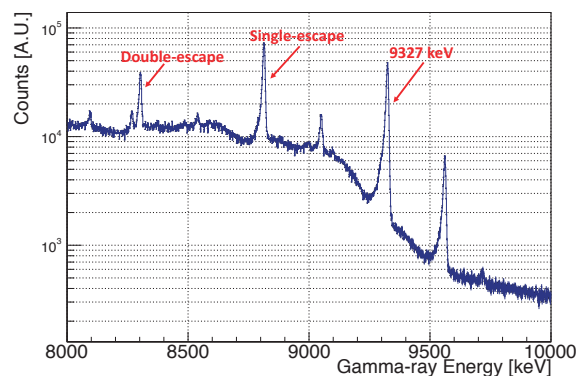


**Fig. 2.** Gamma-ray spectrum by neutron capture reactions in the experiment (i) at the range of 8 - 10 MeV. The peak with an energy deposit of 9327 keV and its single- and double-escape peaks due to  $^{117}\text{Sn}(n,\gamma)$  reactions in the target can be observed clearly.

### 3. Analysis

#### 3.1 Background subtraction and beam intensity normalization

The neutron energy spectrum gated with events from signal regions (9327 keV, its single- and double-escape peaks) includes background events from other sources. There are two kinds of background events.

One is caused by the Compton scattering of the 9563 keV  $\gamma$ -rays emitted from the compound state of  $^{116}\text{Sn}$ . The other stems from pileup events due to simultaneous detection of multi  $\gamma$ -rays. These background events must be subtracted. First, the number of background events in the signal regions was estimated using a GEANT4 simulation [6], which enables us to obtain a spectrum convoluted a response function of the germanium detector for monoenergetic  $\gamma$ -rays [7]. Spectra gated with the background regions (9563 keV peak and energies higher than 9600 keV) were scaled that number of events matched that of GEANT4 calculated ones. After that, they were subtracted from spectra gated with the signal regions. The procedure of this subtraction was conducted for the analysis of the experiment (i) and (iii). On the other hand, this was not conducted for the analysis of the experiment (ii) because the spectrum for determining resonance parameters was not gated with the energies of  $\gamma$ -rays.

In the energy region of epithermal neutrons, the intensity of neutron beam increases for lower neutron energies as a result of moderation. The energy spectrum of neutrons captured by the target must be normalized in order to compare the measured spectrum and the calculated cross section. We used the spectrum gated with the 477.6 keV  $\gamma$ -rays from  $^{10}\text{B}(n,\alpha\gamma)^7\text{Li}$  reactions because the cross section of this reaction has no resonance at the epithermal energy region [8]. This normalization was conducted for all analysis, and the beam intensity was measured in each experiment.

### 3.2 Angular dependence

Figure 3 shows spectra of the neutron energy dependent on the angle of the  $\gamma$ -rays emitted from the compound states of  $^{118}\text{Sn}$ . An angular dependence of the shape of the p-wave resonance has clearly been observed. To evaluate quantitatively, we defined an asymmetry value  $A_{\text{LH}}$  as

$$A_{\text{LH}} = \frac{N_{\text{L}} - N_{\text{H}}}{N_{\text{L}} + N_{\text{H}}}, \quad (2)$$

where  $N_{\text{L}}$  and  $N_{\text{H}}$  are the integrated values in a lower (L) and a higher (H) energy region of the p-wave resonance, respectively. The integral regions were defined using the p-wave resonance energy  $E_{\text{p}}$  and the resonance width  $\Gamma_{\text{p}}$  as follows:  $E_{\text{p}} - 2\Gamma_{\text{p}} < E_{\text{n}} < E_{\text{p}}$  for  $N_{\text{L}}$  and  $E_{\text{p}} < E_{\text{n}} < E_{\text{p}} + 2\Gamma_{\text{p}}$  for  $N_{\text{H}}$ . The value of  $A_{\text{LH}}$  in each angle is plotted in Fig. 4. Based on the Flambaum's formalism, the angular dependence can be written as

$$A_{\text{LH}} = A \cos \theta_{\gamma} + B, \quad (3)$$

The expression was fitted to the experimental data, with the result:

$$A = 0.494 \pm 0.043, B = 0.040 \pm 0.018. \quad (4)$$

### 3.3 Resonance parameters and branching ratios

Resonance parameters are determined by fitting to the neutron energy spectrum gated with  $\gamma$ -rays of more than 2 MeV to suppress background events in low  $\gamma$ -rays' energy region. Fitting function is the Briet-Wigner formula convoluted the doppler broadening effect [9] and a time structure of pulsed beam [10]. Figure 5 shows the neutron energy spectrum around the p-wave resonance and fitting result. The resonance parameters in this p-wave resonance were determined as

$$E_{\text{p}} = 1.331 \pm 0.002 [\text{eV}], \Gamma_{\text{p}}^{\gamma} = 133 \pm 5 [\text{meV}]. \quad (5)$$

In s-wave resonances, an influence of self-shielding can be considered. In general, the cross sections of s-wave resonances is very larger than those of p-wave resonances, so that neutron beam cannot reach deeply inside the target. This causes a shortage of the number of neutrons which interact with nuclei. As this result, the shapes of resonances can be changed, and this effect must be considered. At the moment, the estimation of this effect by a Monte Carlo simulation is ongoing.

Branching ratio of each resonance can be determined by fitting like the determination of resonance parameters. In this analysis, the spectrum which should be fitted must be gated with the signal regions. In this case, a fitting function has a branching ratio as an only free parameter, while other parameters

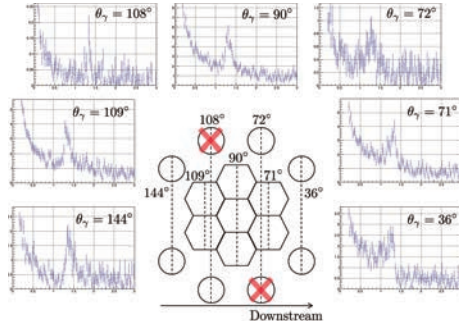


**Fig. 3.** Capture yields as a function of neutron energy around the 1.33 eV p-wave resonance, for variable angles accessible at ANNRI. The central figure shows the placement and the shape of each crystal. Two detectors marked by crosses were not available for the experiment (i).

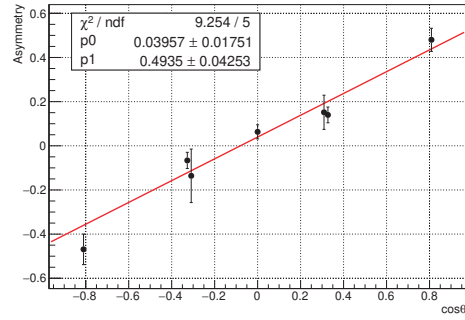


**Fig. 4.** The angular dependence of  $A_{LH}$ . The solid line shows the fitting result using the function of Eq. (3).

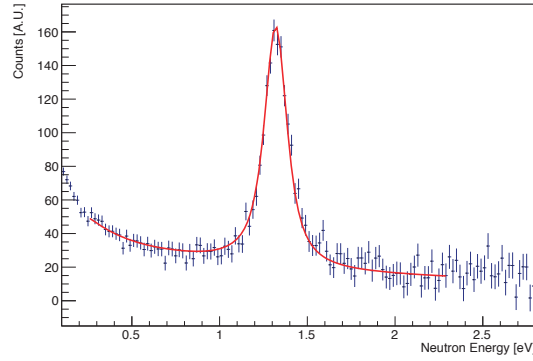


**Fig. 5.** Capture yields as a function of neutron energy gated with an  $\gamma$ -rays' energy regions of more than 2 MeV around p-wave resonance in the experiment (ii). The solid line shows the best fit line.

are fixed as follows:  $f(E_n) = C\sigma(E_n)$ , where  $\sigma(E_n)$  is the Briet-Wigner formula with fixed resonance parameters and  $C$  is the free parameter corresponding to the branching ratio of its resonance. Thus, branching ratios are able to be determined after the determination of their resonance parameters. In the near future, branching ratio of each resonance will be determined.

#### 4. Summary

CP-violation (T-violation) is one of the essential contents to explain the dominance of matter over antimatter in the current universe. For the preparation of T-violation search using compound nuclei, one has to determine the spin factor  $\kappa(J)$  which directly relates to the experimental sensitivity. The angular correlation of  $\gamma$ -rays emitted from the compound states of  $^{118}\text{Sn}$  in the p-wave resonance can be clearly observed by the measurement at ANNRI in J-PARC MLF. In addition, the experiments to measure the resonance parameters and the branching ratios have been conducted and the analysis is ongoing. In the near future, the mixing angle  $\phi$ , and hence the value of  $\kappa(J)$  will be determined.

**References**

- [1] A. Sakharov, JETP **5**, 24 (1967).
- [2] G. Mitchell et al., Phys. Rep. **354**, 157 (2001).
- [3] V. Gudkov, Phys. Rep. **212**, 77 (1992).
- [4] T. Okudaira et al., Phys. Rev. C, **97**, 034622 (2018).
- [5] V. V. Flambaum, O. P. Sushkov, Nucl. Phys. A **435**, 352 (1985).
- [6] Website of GEANT4, Available from: <https://geant4.web.cern.ch/>, accessed 2020/01/06.
- [7] S. Takada et al., JINST **13** P02018 (2018).
- [8] Website of JENDL-4.0, Available from: <https://wwwndc.jaea.go.jp/jendl/j40/j40.html>, accessed 2020/01/06.
- [9] H. A. Bethe, Nucl. Phys. b **9**, 69 (1937).
- [10] K. Kino et al., Nucl. Instr. and Meth. A **736**, 66 (2014).

## 20 Measurement of the photon strength function in $^{115}\text{In}$ at the $\gamma\text{ELBE}$ facility

A. MAKINAGA<sup>1,2,3</sup>, R. SCHWENGER<sup>4</sup>, R. BEYER<sup>4</sup>, M. GRIEGER<sup>4</sup>, S. HAMMER<sup>4</sup>,  
T. HENSEL<sup>4</sup>, A. R. JUNGHANS<sup>4</sup>, F. LUDWIG<sup>4</sup>, T. T. TRINH<sup>4</sup>, S. TURKAT<sup>4</sup>

<sup>1</sup>Department of Radiological Technology, Teikyo, University 6-22, Misaki-machi,  
836-8505 Omuta, Japan

<sup>2</sup>Jein Institute for Fundamental Science, 606-8317, Kyoto, Japan

<sup>3</sup>Graduate School of Medicine, Hokkaido University, Kita 15 Nishi 7, Kita-ku,  
060-8638, Sapporo, Japan

<sup>4</sup>Helmholtz-Zentrum Dresden-Rossendorf, 01328 Dresden, Germany

\*E-mail: makinaga@fmt.teikyo-u.ac.jp

The photon strength function (PSF) in  $^{115}\text{In}$  is an important parameter for the estimate of the neutron capture cross section on  $^{114}\text{In}$  in the field of astrophysics and nuclear engineering. Until now, the so-called PSF method for  $^{115}\text{In}$  was applied only above the neutron-separation energy ( $S_n$ ), and the evaluated  $^{114}\text{In}(n,\gamma)$  cross section has uncertainties caused by the lack of the PSF below  $S_n$ . We studied the dipole strength distribution of  $^{115}\text{In}$  with a photon-scattering experiment using bremsstrahlung produced by an electron beam of an energy of 10.3 MeV at the linear accelerator ELBE at HZDR.

### 1 Introduction

The nuclei heavier than iron are mainly produced via s-, r- or p- processes. The origin of p-nuclei is assumed from photodisintegration in the O/Ne layers of core-collapse of massive stars, of type I or II supernovae explosions, or/and s-, r- processes [1]. However, the production abundance of one of the p-nuclei,  $^{115}\text{Sn}$ , still cannot be explained [2-3]. Recently, an s-process contribution is tried to explain the neutron capture reaction and  $\beta$ -decay at  $^{113}\text{Cd}^m$  as competing reactions, i.e.  $^{112}\text{Cd}(n,\gamma)^{113}\text{Cd}^m(\beta^-)^{113}\text{In}(n,\gamma)^{114}\text{In}(\beta^-)^{114}\text{Sn}(n,\gamma)^{115}\text{Sn}$  (see Figure 1).  $\gamma$ -rays were measured following neutron captures on  $^{112}\text{Cd}$  at the MLF in J-PARC and it was found that the s-process contribution from  $^{113}\text{Cd}^m$  is not big enough to explain the production problem of  $^{115}\text{Sn}$  [4]. So, origin of  $^{115}\text{Sn}$  is still open question.

In this study, we will shift the viewpoint to  $^{115}\text{In}$ , which is produced via the main s-process. In the p- or/and r- process environment ( $T > 2 - 3 \times 10^9$  K),  $^{115}\text{In}$  has 3 possible reactions such as

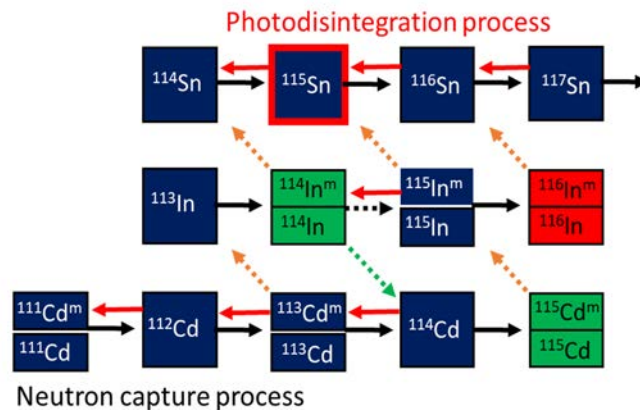


Figure 1. Nuclear reaction path to produce  $^{115}\text{Sn}$ .

photodisintegration, neutron capture and  $\beta$ -decay. While the effective  $\beta$ -decay rate for  $^{115}\text{In}$  is the order of  $10^{-5} \text{ s}^{-1}$  at the temperature higher than  $3 \times 10^9 \text{ K}$  [5], the stellar reaction rate of photodisintegration of  $^{115}\text{In}$  calculated using the TALYS code [6] is around  $10^7$  to  $10^8 \text{ s}^{-1}$  and the neutron-capture rate for  $^{115}\text{In}$  is around  $10^8$ - $10^7 \text{ s}^{-1}$  at a temperature of  $3.5$  -  $4.0 \times 10^9 \text{ K}$ , respectively.

In addition, the neutron capture rate of  $^{114}\text{In}$  is around  $10^8 \text{ s}^{-1}$ . It means that the production process of  $^{115}\text{In} (\gamma, n) \rightleftharpoons (n, \gamma) ^{114}\text{In} (\beta^-) ^{114}\text{Sn} (\gamma, n) \rightleftharpoons (n, \gamma) ^{115}\text{Sn}$  may contribute to produce  $^{115}\text{Sn}$ . This story is also mentioned shortly in Ref. [3]. However, both the photodisintegration rate for  $^{115}\text{In}$  and the neutron capture rate for  $^{114}\text{In}$  have not well been known experimentally, so they could not be discussed quantitatively.

From the view point of nuclear physics, photo-neutron cross sections have been measured above Sn [7-10]. However, precise measurements have not been performed (see Figure 2). The PSF below Sn was measured using the Nuclear Resonance Fluorescence (NRF) in the energy range between 2-5 MeV at Darmstadt [11]. A photoactivation yield measurement on  $^{115}\text{In}$  performed at the ELSA facility reported the possibility of an extra enhancement of the PSF in  $^{115}\text{In}$  below Sn [12]. On the other hand, neutron capture cross sections for  $^{114}\text{In}$  have not been measured because of the unstable isotope. A possible way to estimate cross sections for  $^{114}\text{In} (n, \gamma)$  is to use the inverse-reaction method, which means the measurement of the PSF in  $^{115}\text{In}$  below Sn. Therefore, we have performed the measurement of the PSF in  $^{115}\text{In}$  below Sn using the NRF method at the  $\gamma$ ELBE facility.

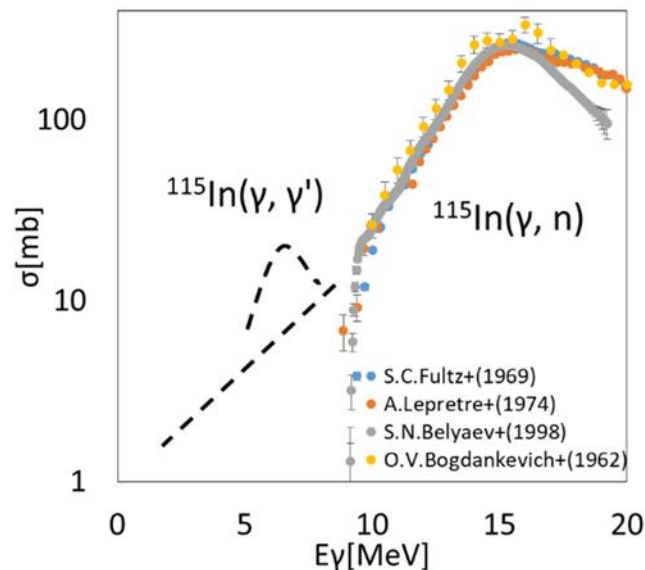


Figure 2. Current status of photo absorption cross sections of  $^{115}\text{In}$ .  
Dashed line shows image of typical behavior below Sn.  
No experimental data exists in this region.

## 2 Experimental methods and results

The photon-scattering cross section  $\sigma_{\gamma f}(E_R)$  can be measured via the  $\gamma$ -ray transition from a given excited level  $E_R$  and deexcitation to a level  $E_f$  in the target. In case of non-overlapping resonances, photon scattering is described to process via a compound nucleus reaction with uncorrelated channels  $f$  characterized by the partial width  $\Gamma_f$ , so the photon-scattering cross section  $\sigma_{\gamma f}(E_R)$  can be described as:

$$\sigma_{\gamma f}(E_R) = \sigma_{\gamma}(E_R) \frac{\Gamma_f}{\Gamma} \quad (1)$$

Here, all partial widths contribute to the total level width  $\Gamma = \sum \Gamma_f$ .

$$I_S = \int_0^{\infty} \sigma_{\gamma\gamma}(E) dE = \frac{2J_R+1}{2J_0+1} \left( \frac{\pi \hbar c}{E_R} \right)^2 \Gamma_0 \frac{\Gamma_f}{\Gamma} \quad (2)$$

$I_S$  is the integral over the scattering cross section for the level R and  $\Gamma_f$  is the partial width for a transition from R to a level f. The measured intensity of  $\gamma$ -rays emitted to the ground state at  $E_{\gamma} = E_R$  at an angle  $\theta$  can be expressed as,

$$I_{\gamma}(E_{\gamma}, \theta) = I_S(E_R) \Phi(E_R) \varepsilon(E_{\gamma}) N_{at} W(\theta) \frac{\Delta\Omega}{4\pi} \quad (3)$$

Here,  $N_{at}$  is number of the target nuclei per area unit,  $\varepsilon(E_{\gamma})$  is the absolute full-energy peak efficiency at  $E_{\gamma}$ ,  $\Phi(E_R)$  is the absolute photon flux at  $E_R$ ,  $W(\theta)$  is the angular correlation of this transition, and  $\Delta\Omega$  is solid angle of the detector.

If the electron energy is high enough above a particular level, the experiments with bremsstrahlung lead to the possibility of the population of a level by a feeding transition from a higher-lying level. Such feeding increases the intensity of the transition to the ground state from the considered resonance R. The intensity of the transition to the ground state becomes a superposition of the rate of elastic scattering and the intensity of the transitions feeding level R. The cross-section integral  $I_{s+f}$  can be expressed as:

$$\begin{aligned} I_{s+f} &= \int_0^{\infty} \sigma_{\gamma\gamma}(E) dE + \sum_{i>R} \sigma_{\gamma i} \frac{\Gamma_0}{\Gamma} dE \\ &= \frac{2J_R+1}{2J_0+1} \left( \frac{\pi \hbar c}{E_R} \right)^2 \frac{\Gamma_0^2}{\Gamma} + \sum_{i>R} \frac{\Phi(E_i)}{\Phi(E_R)} \frac{2J_i+1}{2J_0+1} \left( \frac{\pi \hbar c}{E_i} \right)^2 \Gamma_0^i \frac{\Gamma_R^i}{\Gamma^i} \frac{\Gamma_0}{\Gamma} \end{aligned} \quad (4)$$

Here, the summation over  $i>R$  means that the energy  $E_i$  of a level which feeds the considered resonance R is higher than the energy  $E_R$  of this resonance.  $\Gamma_i$ ,  $\Gamma_{i0}$ , and  $\Gamma_R^i$  are the total widths of the level  $E_i$ , the partial width of the transition to the ground state and the partial width of the transition to the level R, respectively. Details of the experimental method are given in Refs. [13-20].

The photon-scattering cross section measurement on  $^{115}\text{In}$  was performed at the superconducting electron accelerator ELBE of the Research Center Dresden - Rossendorf. Bremsstrahlung was produced by hitting 7  $\mu\text{m}$  niobium radiator with an electron beam of 10.3 MeV electron kinetic energy and an average current of 490  $\mu\text{A}$ . The produced bremsstrahlung was collimated by an Al collimator with a length of 2.6 m and an opening angle of 5 mrad. A cylindrical Al absorber of 10 cm length was placed between the radiator and the collimator to reduce the low-energy part of the bremsstrahlung spectrum. The scattered photons were measured with four 100% HPGe detectors surrounded by BGO escape-suppression shields. Two Ge detectors were placed at 90 degrees relative to the photon-beam direction. The other two HPGe detectors placed at 127 degrees were used to deduce angular distributions of the  $\gamma$  rays. To reduce the intensity of the low-energy part of background photons, absorbers of 3 mm Pb plus 3 mm Cu were placed in front of the detectors at 127 degrees and 8 mm Pb plus 3 mm Cu were used for the detectors at 90 degrees. The target consisted of 2376.4 mg of natural indium, formed into a disk of 2 cm in diameter. The natural abundance of  $^{115}\text{In}$  is 95.7 %. The indium target was combined with a disk of 300.0 mg boron, enriched to 99.5 % in  $^{11}\text{B}$  which was used to determine the photon flux. Spectra of scattered photons were measured for 118 hours.

The photoabsorption cross section data of  $^{115}\text{In}$  obtained from the  $(\gamma, \gamma)$  experiment are shown in Figure 3, together with cross sections deduced from  $(\gamma, n)$  experiments [8] and with the TLO model in RIPL [21]. The  $^{115}\text{In}$   $(\gamma, \gamma)$  cross sections smoothly connect to the photoneutron data, and show extra enhanced resonances around 6 MeV and 9 MeV.

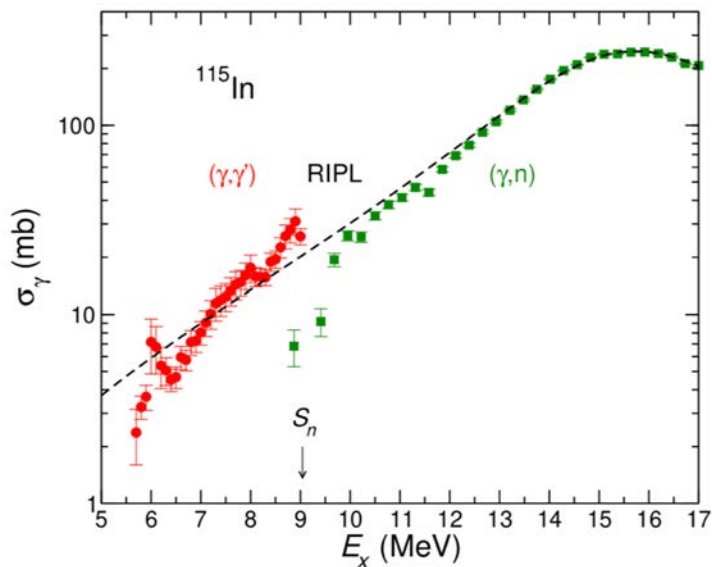


Figure 3. (Color online) Photoabsorption cross sections deduced from the present measurement (red circles) in comparison with  $(\gamma, n)$  data from Ref. [8] (green squares), and TLO [21] (black dashed curve).

### 3 Summary

The dipole-strength distribution in  $^{115}\text{In}$  up to the neutron-separation energy has been studied in an NRF experiment at the ELBE accelerator using a kinetic electron energy of 10.3 MeV. The  $^{115}\text{In}(\gamma, \gamma)$  cross section smoothly connects with the experimental photoneutron data. Extra enhancement of the PSF in  $^{115}\text{In}$  is also observed. A detailed analysis within nuclear models will be performed.

### Acknowledgments

We thank the crew of the ELBE accelerator for the cooperation during the experiment. This work was supported by Helmholtz-Zentrum Dresden-Rossendorf and Hokkaido University.

### References

- [1] M. Arnould, *Astron. Astrophys.* **46**, 117 (1976).
- [2] S. E. Woosley et al., *Astrophys. J., Suppl.* **36**, 285 (1978).
- [3] R. A. Ward et al., *Astron. Astrophys.* **103**, 189 (1981).
- [4] T. Hayakawa et al., *Phys. Rev. C* **94**, 055803 (2016).
- [5] K. Takahashi et al., *Atom. Data and Nucl. Data Tables* **36**, 3, 375 (1987).
- [6] A. J. Koning et al., *AIP Conf. Proc.* **769**, 1154 (2005).
- [7] S. C. Fultz et al., *Jour. Phys. Rev.* **186**, 1255, 6910 (1969).
- [8] A. Lepretre et al., *Jour. Nucl. Phys. A*, **219**, 39, 7401 (1974).
- [9] S. N. Belyaev et al., *Jour. IZV*, **62**, 2223 (1998).
- [10] O. V. Bogdankevich et al., *Jour. ZET*, **42**, 1502 (1962).
- [11] P. von Neumann-Cosel et al., *Z. Phys. A* **350**, 303 (1995).

- [12] M. Versteegen et al., Phys. Rev. C **94**, 044325 (2016).
- [13] R. Schwengner et al., Phys. Rev. C **76**, 034321(2007).
- [14] G. Rusev et al., Phys. Rev. C **77**, 064321(2008).
- [15] R. Schwengner et al., Phys. Rev. C **78**, 064314(2008).
- [16] N. Benouaret et al., Phys. Rev. C **79**, 014303(2009).
- [17] G. Rusev et al., Phys. Rev. C **79**, 061302(R)(2009).
- [18] R. Schwengner et al., Phys. Rev. C **81**, (2009).
- [19] A. Makinaga et al., Phys. Rev. C **82**, 024314(2010).
- [20] A. Makinaga et al., Phys. Rev. C **90**, 044301(2014).
- [21] R. Capote et al., Nucl. Data Sheets, **110**, 3107(2009).

This is a blank page.

## 21 Comparison between experimental and calculation neutron spectra of the $^{197}\text{Au}(\gamma, \text{sn})$ reaction for 17 MeV polarized photon

\*T. K. TUYET<sup>1</sup>, T. SANAMI<sup>1,2</sup>, H. YAMAZAKI<sup>1,2</sup>, T. ITOGA<sup>3</sup>, A. TAKEUCHI<sup>1</sup>,  
S. MIYAMOTO<sup>4</sup> and Y. ASANO<sup>4</sup>

<sup>1</sup>SOKENDAI, Shonan Village, Hayama, Kanagawa 240-0193 Japan

<sup>2</sup>KEK, 1-1 Oho, Tsukuba-shi, Ibaraki-ken 305-0801 Japan

<sup>3</sup>JASRI, 1-1-1, Kouto, Sayo-cho, Sayo-gun, Hyogo 679-5198, Japan

<sup>4</sup>University of Hyogo, 1-1-2, Kouto, Kamigori-cho, Ako-gun, Hyogo 678-1205, Japan

Email: tuyet@post.kek.jp

The double differential cross sections (DDX) were measured for the  $^{197}\text{Au}(\gamma, \text{sn})$  with 17 MeV polarized photons on a thin target. The DDX were compared with the result of PHITS calculation. To reproduce the energy spectra of neutrons, especially at the relatively high energy region, a physics model for the direct process should be implemented in addition to the evaporation model.

### 1. Introduction

In an electron accelerator, neutrons are produced by collision between a high energy photon and components of the accelerator through photonuclear reaction. The neutrons induce issues in radiation protection as well as dosimetry and accelerator designs. Additionally, the study of photo-neutrons from photonuclear reaction is useful tool for understanding the elementary processes of nuclear physics. Until now, there are researches about photo-neutrons production of photonuclear reaction [1,2,3]. In the previous study of our research group [1], the energy spectra of photo-neutrons, which were produced by the reaction of 17 MeV polarized photons on the thick Au target, were measured at various angles. The evaporation and direct components were identified in the energy spectra [1]. The angular distribution of evaporation component showed isotropic, while the direct component showed a dependence on the interaction angle between photon polarization and neutron emission [1].

These spectra are useful in the comparison the experimental and calculation spectra to evaluate parameters of theoretical calculation. However, there is no comparison between experimental and calculation spectra. For comparison, the double differential cross section (DDX) is preferable than the neutron spectra. It is because the self-attenuation effect in thick target can be avoided. Thus, in this study, we measured the DDX of the reaction of 17 MeV polarized photons on a thin Au target and compared the results with that of PHITS calculation.

### 2. Experiment

The experiment was performed at NewSUBARU-BL01, Hyogo, Japan [4][5]. Figure 1 indicates the schematic drawing of NewSUBARU-BL01. The 17 MeV linearly polarized photons were produced by the collision of the polarized laser and electron beam with the energy of 982.4 MeV. The beam current was 30 mA. A NdYVO4 laser system provided laser photons with a wavelength of 1.063  $\mu\text{m}$ .

The power was 20 W. The laser polarization direction was set to be parallel to the floor using a  $\lambda/4$  polarizer plate.

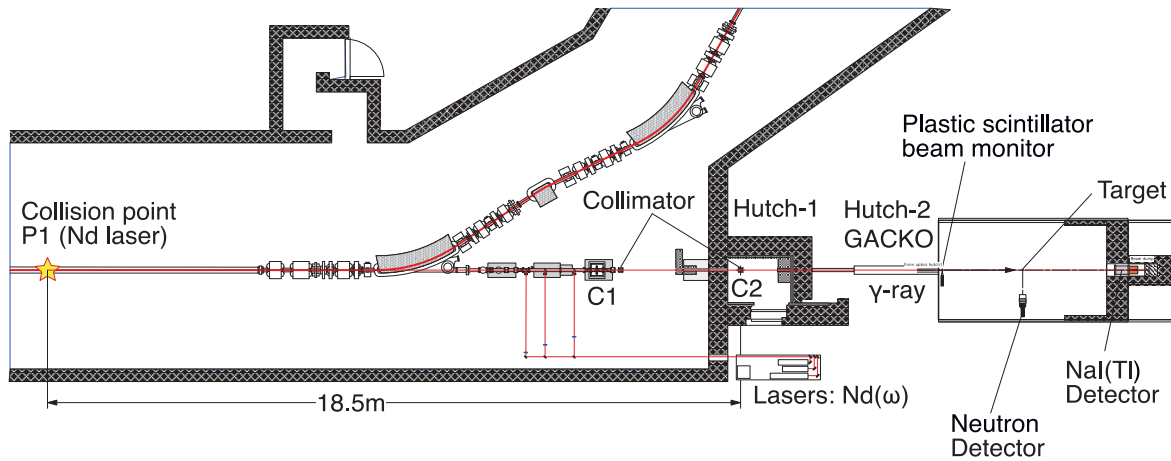


Figure 1. Schematic of NewSUBARU-BL01.

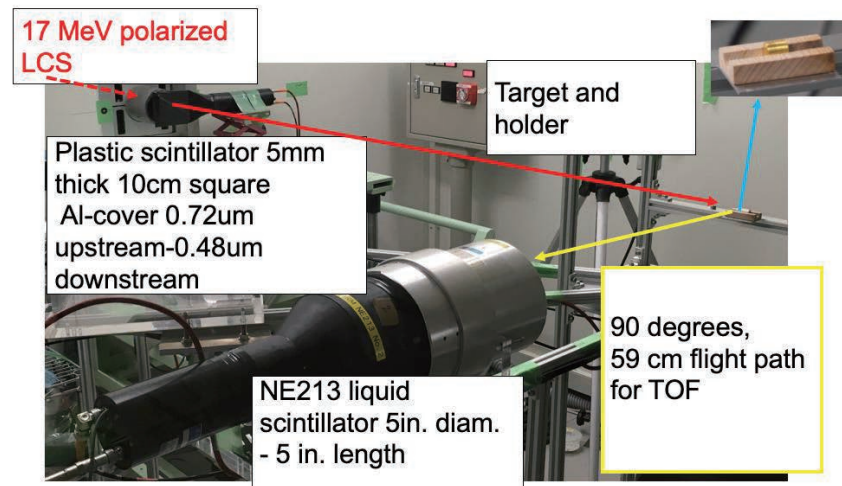


Figure 2. Picture of the experimental setup.

Figure 2 shows a picture of the experimental setup. Since the photo-neutron production per incident photon was considered, a plastic scintillator (thickness of 0.5 cm and surface area of 10 cm<sup>2</sup>) was placed at 179.7 cm upstream from the target. The incident photon beam was collimated into the center of the target by using two collimators, C1 and C2 as shown in figure 1. The Au target was prepared as a cylindrical pill whose diameter and thickness were 1 cm. In order to detect the neutron emitted from the target, a cylindrical NE213 organic liquid scintillator (12.7 cm<sup>φ</sup>×12.7 cm<sup>l</sup>) was set at 90 degrees (respected to the photon beam axis) and 59 cm distance from the target. The NE213 detector detected not only photo-neutrons from target but also gamma radiations. Thus, the pulse shape discrimination (PSD) method was applied to separate photo-neutron and gamma by obtaining the charge ratio of the whole and tail of the waveform. The energy of photo-neutron was measured by a time-of-flight (TOF)

spectroscopy to build up an energy histogram. For PSD and TOF analysis, a Data Acquisition (DAQ) system based on VME standard was set up with a QDC module to obtain the full charge and tail charge of signals from NE213, and a TDC to measure the time difference between the incident photon beam and NE213. The DAQ system also measured the charge of signals from the plastic scintillator.

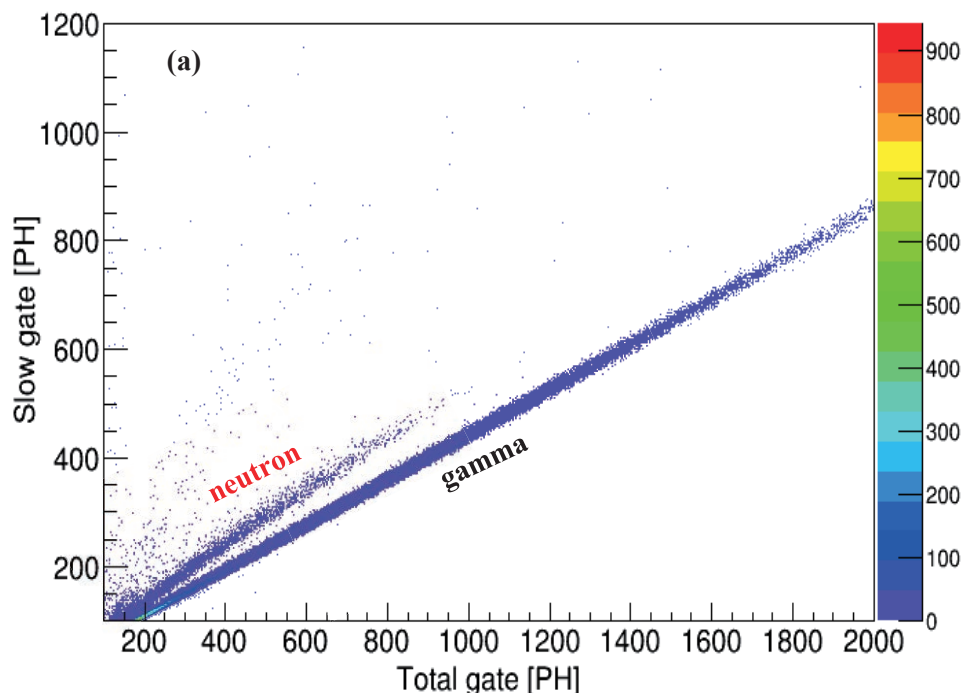
### 3. Data Analysis

We obtained the time of flight spectrum of neutron events by the PSD and TOF methods. The energy threshold employed for analysis was 0.25 MeVee. This threshold was determined by energy calibration using gamma radiations of  $^{137}\text{Cs}$ ,  $^{22}\text{Na}$ , and  $^{60}\text{Co}$ .

The time-walk effect can significantly affect the TOF measurement as well as neutron energy. For time measurement, we used the constant-fraction-discriminators (CFDs). Although the time-walk effect was small when using CFDs, this effect was still essential in the energy measurement of photo-neutron. To minimize the time-walk effect, the correction of TDC with the fitting function as the correlation of TDC and QDC was applied.

Figure 3 shows neutron gamma separation with total vs slow gates (a) and TOF vs the ratio of slow to total (b). We employ the latter correlation, for neutron and gamma separation.

The neutron energy was calculated by using TOF method. The efficiency of the neutron detector was estimated by  $^{252}\text{Cf}$  experiment and SCINFUL-QMD simulation [6] to evaluate the total number of neutrons emitted at 90 degrees from target. The energy spectrum was normalized by the solid angle, the number of incident photons and the number of target atom. Photon attenuation in the target was taken into account using PHITS calculation. The double-differential cross-section of the photo-neutron reaction was obtained by using the normalized data. In data analysis, the time resolution of gamma peak was 0.76 ns, and the energy resolution of neutron was less than 10%.



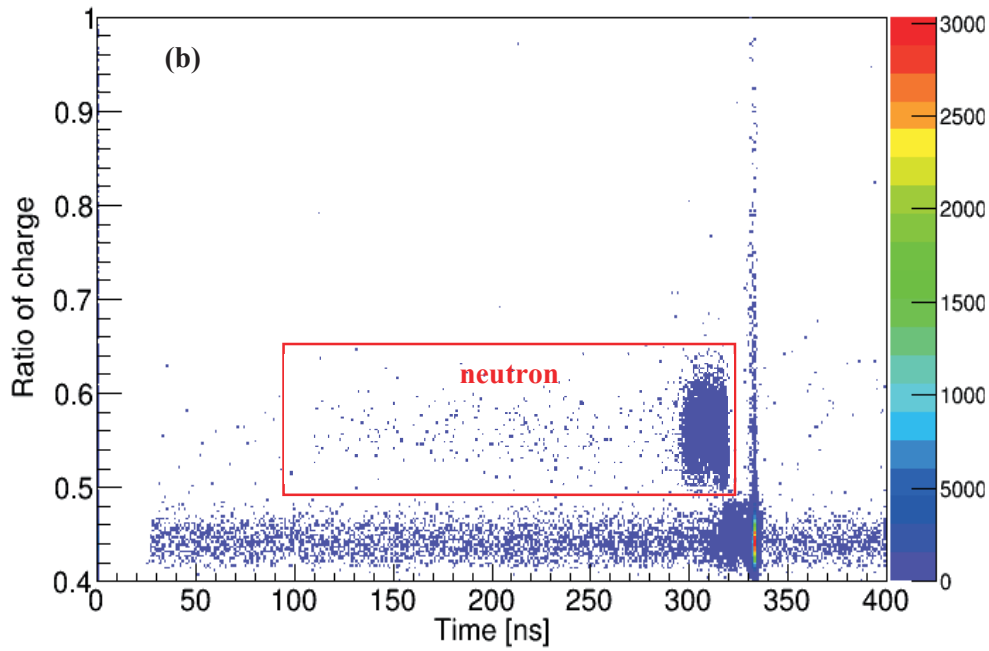


Figure 3. Neutron gamma separation with total vs slow gates (a) and TOF vs the ratio of slow to total (b).

#### 4. Calculation

PHITS (version 3.02) [7] was used to calculate the double-differential cross section (DDX) of photo-neutron produced by the  $^{197}\text{Au}(\gamma, \text{sn})$  reaction for 17 MeV polarized photon. A cylinder Au target whose diameter and thickness were 5  $\mu\text{m}$  was chosen to reduce the self-attenuation thickness effect of the target. The DDX was obtained on a detector ring, whose width is 5 cm, the ring placed at 90 degrees and 100 cm away from Au target.

Figure 4 shows the geometry of the DDX calculation in the PHITS code. Neutron production from the nuclear reaction was calculated by the Generalized Evaporation Model (GEM) model. Figure 5 indicates neutron flux distribution in the PHITS calculation.

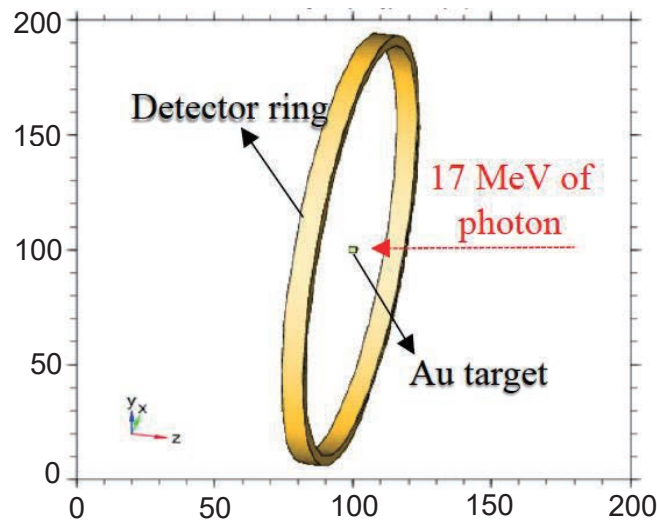


Figure 4. Geometry in PHITS.

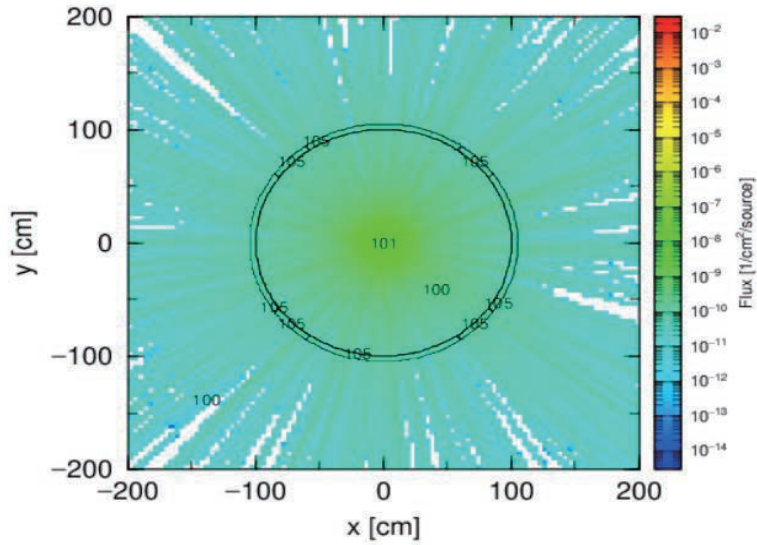


Figure 5. Neutron flux distribution.

### 5. Result

Figure 6 shows DDXs obtained from the experiment and the PHITS calculation. In this figure, closed circles indicate the experimental data and the solid line is the result of the calculation. The experimental spectrum shows two components; evaporation component and direct component. The energy region of the evaporation and direct component were less and more than 4 MeV, respectively. In contrast, the calculation result shows only the evaporation component, as expected. Thus, a model to reproduce the direct component should be included in the simulation for the photonuclear reaction. To develop the model, experimental data of DDX are strongly desired for various targets and energies.

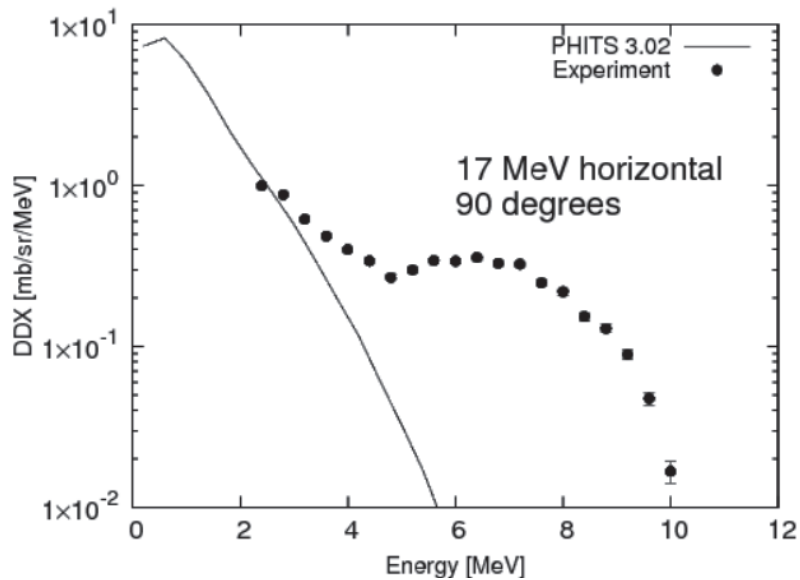


Figure 6. Experimental and calculation DDX.

## References

- [1] Y.Kirihara, H.Nakashima, T.Sanami, Y.Namito, T.Itoga, S.Miyamoto, A.Takemoto, M.Yamaguchi and Y.Asano, Neutron emission spectrum from gold excited with 16.6 MeV linearly polarized monoenergetic photons, *Journal of Nuclear Science and Technology* (2019), <https://doi.org/10.1080/00223131.2019.1691073>.
- [2] K.Horikawa, S.Miyamoto, T.Mochizuki, et al., Neutron angular distribution in ( $\gamma$ , n) reactions with linearly polarized  $\gamma$  -ray beam generated by laser Compton scattering, *Phys. Lett. B.*, (2014).
- [3] A.Agodi, *Nuovo Cimento*, 5, 21, (1) (1957).
- [4] Y.Asano, S.Miyamoto, Shielding design of laser electron photon beamlines at Sring-8, *Prog. Nucl. Sci. Tech.* (2014).
- [5] S.Miyamoto, Y.Asano, S.Amano, et al., Laser Compton back-scattering gamma-ray beamline on NewSUBARU, *Radiat. Meas.* (2007).
- [6] D.Satoh, S.Kunieda, Y.Iwamoto, et al., Development of SCINFUL-QMD code to calculate the neutron detection efficiencies for liquid organic scintillator up to 3 GeV, *Nucl. Sci. Tech.* (2002).
- [7] T.Sato, Y. Iwamoto, S. Hashimoto, T. Ogawa, T. Furuta, S. Abe, .T.Kai, P.Tsai, N. Matsuda, H. Iwase, N. Shigyo, L. Sihver and K. Niita, Features of Particle and Heavy Ion Transport code System (PHITS) version 3.02, *J. Nucl. Sci. Technol.* (2018), <https://doi.org/10.1080/00223131.2017.1419890>.

## 22 Measurement of neutron total cross-section of $^{93}\text{Nb}$ at J-PARC MLF ANNRI

Shunsuke Endo, Atsushi Kimura, Shoji Nakamura, Osamu Iwamoto, Nobuyuki Iwamoto, Yosuke Toh, Mariko Segawa, Makoto Maeda and Masayuki Tsuneyama  
*Japan Atomic Energy Agency, 2-4 Shirakata, Tokai-mura, Naka-gun, Ibaraki 319-1195*  
*endo.shunsuke@jaea.go.jp*

### Abstract

The neutron total cross-section of Nb was measured by a transmission method to examine the resonance data by J-PARC MLF ANNRI. During the measurements, a diffraction effect of the Nb sample was remarkably observed. The diffraction effect of Nb was also studied since its effect cannot be ignored in deriving the neutron total cross-sections in a low energy region. As a result of the discussion by assuming a simple model including structure, it is clear that the diffraction effect is not ignored below 0.2 eV. This article gives results of the neutron total cross-section measurement of Nb at J-PARC MLF ANNRI and discussions on the effect of diffraction.

### 1 Introduction

Niobium(Nb)-93, whose natural abundance is 100%, is one of material elements to strength-en stainless steel and is used in structural materials of nuclear reactors. Since Nb is also used as an element of superconductor alloys, it has been used in fusion reactors and accelerators. Niobium causes long-lived activities in stainless steel due to the long half-life of  $^{94}\text{Nb}$ , about 20 thousand years [1]. Determination of resonance parameters with high accuracy are therefore required to estimate the activation. The cross-sections of Nb were measured by Wang *et al.* [2], Meaze *et al.* [3], Drindak *et al.* [4] and so on. The resonance parameters determined by them have discrepancies as shown in Table 1. In particularly, there are discrepancies larger than uncertainties between the results of Wang *et al.* and those of Drindak *et al.*. In order to determine which resonance parameters are more likely, measurements of neutron total cross-sections were performed at Accurate Neutron-Nucleus Reaction measurement Instrument (ANNRI) of Material and Life Science Experimental Facility (MLF) in Japan Proton Accelerator Research Complex (J-PARC).

Table 1: Resonance parameters for the first resonance of  $^{93}\text{Nb}$  in past measurements.  $\Gamma_\gamma$ ,  $\Gamma_n$  and  $g$  are the gamma width, the neutron width and the statistical weight factor, respectively.

Reference	Resonance Energy [eV]	$\Gamma_\gamma$ [meV]	$2g\Gamma_n$ [meV]
Wang+(2011)[2]	$35.994 \pm 0.0026$	$224.61 \pm 20.82$	$0.0772 \pm 0.0037$
Meaze+(2011)[3]	$35.92 \pm 0.02$	$215.57 \pm 17.98$	$0.078 \pm 0.041$
Drindak+(2006) [4]	$35.922 \pm 0.004$	$191 \pm 8$	$0.125 \pm 0.001$
Sharapov+(1999) [5]	35.9	-	$0.11 \pm 0.01$
Saplagoglu+(1958)[6]	35.9	$205 \pm 51$	$0.15 \pm 0.01$
Mughabghah 6th(2018)[7]	$35.9 \pm 0.1$	$218 \pm 18$	$0.125 \pm 0.010$
JENDL-4.0(2010)[8] (=ENDF/B-VIII.0(2018)[9])	35.922	191	0.125

## 2 Experiment

Transmission measurements were performed at the ANNRI of MLF in J-PARC in June of 2019. In the MLF [10], neutrons were produced by spallation reactions of mercury targets. The 3-GeV rapid cycling synchrotron, producing pulsed proton beam, was operated in double-bunch mode and 500-kW beam power with a repetition rate of 25 Hz at that time. The ANNRI is one of beamlines in the MLF, where germanium gamma-ray detectors and Li-glass neutron detectors are installed to measure nuclear reactions. Cross-section measurements have been performed at the ANNRI [11].

Figure 1 shows the experimental scheme. Two types of Li-glass detectors were installed at ANNRI, one is  ${}^6\text{Li}$ -enriched (GS20) and the other one is  ${}^7\text{Li}$ -enriched (GS30). GS20 can detect  $\gamma$ -rays as well as neutrons in the reaction:  ${}^6\text{Li} + n \rightarrow {}^3\text{H} + \alpha$ . Time of flight (TOF) spectrum ascribed to only neutron can be obtained by subtracting the GS30 spectrum from the GS20 one. These Li-glass detectors were placed at 28.2-m flight length. Signals from detectors were processed by a V1720 module made in Costruzioni Apparecchiature Elettroniche Nucleari S.p.A. (CAEN) [12], and pulse height and TOF were recorded in each event. Neutron total cross-sections can be obtained by neutron transmission ratio. In order to determine the transmission ratio, measurements for beam open (blank) and Nb sample-in were performed for 10 hours and 12 hours, respectively.

The size of used Nb target is shown in Table 2. Table 3 shows the impurities contaminated in the Nb target. Since tantalum has similar chemical properties to Nb, it is included a little in Nb sample. In this article, when cross-section is derived, effects of Ta are not corrected because this effect is estimated to be the order of about  $10^{-3}$  b in a region lower than 1 eV.

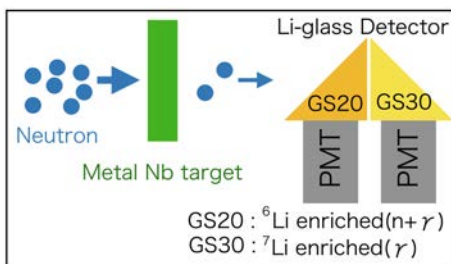


Figure 1: Experimental scheme

Table 2: The size of natural Nb target

Surface area	$653.3 \pm 5.7$ [ $\text{mm}^2$ ]
Thickness	$10.2834 \pm 0.0002$ [ $\text{mm}$ ]
Weight	$56.1112 \pm 0.0003$ [ $\text{g}$ ]
Surface density	$(5.567 \pm 0.049) \times 10^{-2}$ [ $\text{g}/\text{b}$ ]

Table 3: Impurities contaminated in the Nb target

Element	Ta	Fe	O	C	N	others
Content [ppm]	2000	200	100	50	50	35

## 3 Analysis

### 3.1 Corrections

Figure 2 shows pulse-height spectra by GS20 and GS30 in the measurement of the Nb sample. GS30 has a slight sensitivity to neutron since  ${}^6\text{Li}$  is contained by about 0.01%. In order to remove noises and low-energy  $\gamma$ -rays backgrounds, a threshold of pulse-height was set at 210 channel. Events were used when the pulse-height is higher than the threshold. Dead-time corrections were made using a dead-time of 625 ns determined by the setting of the V1720 module.

In the present measurements, there are two types of backgrounds due to neutrons of frame-overlap and to  $\gamma$ -rays. First, the frame-overlap neutrons were estimated by following function:

$$f(t) = a \exp\left(-\frac{t-37}{t_1}\right) + c, \quad (1)$$

where  $t$  represents TOF in ms and  $a$ ,  $t_1$  and  $c$  are fitting parameters. Frame-overlap effect was corrected by fitting this function to the TOF spectrum between 37 ms and 40 ms. Since the background events by this effect were much smaller than true events, this correction has little effect on the derivation of cross sections.

Second,  $\gamma$ -rays backgrounds were removed by subtracting TOF spectrum of GS30 from that of GS20 as mentioned in Section 2. Figure 3 shows the TOF spectra of GS20 and GS30 and estimated frame-overlap correction component.

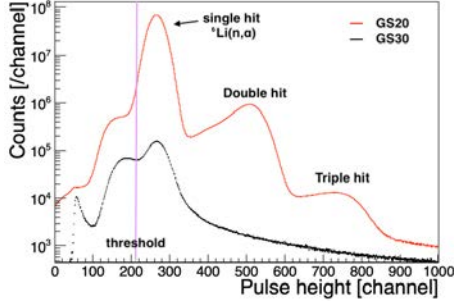


Figure 2: Pulse height spectra of GS20 (red line) and GS30 (black line) with threshold line (pink line)

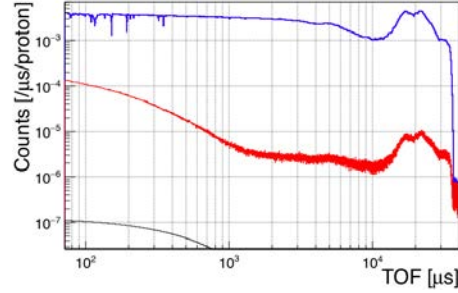


Figure 3: TOF spectra by Li-glass detectors A (blue line) and B (red line) and frame-overlap correction component (black line)

### 3.2 Derivation of total cross-sections

Transmission ratio ( $T$ ) was obtained by dividing the Nb sample-in spectrum ( $Y_{sample}$ ) by the blank spectrum ( $Y_{blank}$ ). The cross-section can be derived from

$$\sigma(E) = -\frac{1}{n} \ln \frac{Y_{sample}}{Y_{blank}} = -\frac{1}{n} \ln T(E), \quad (2)$$

where  $n$  is the surface density. The obtained cross-sections are plotted in Fig. 4 and Fig. 5 in comparison with other past measurements and JENDL-4.0. The effects of resolution function and doppler broadening were taken into account on JENDL-4.0 for comparison with experimental results. The resonances at 4.3 eV and 10.4 eV are ascribed to  $^{181}\text{Ta}$ . The cross-sections are fluctuated in a low energy region because of neutron diffraction. We thought this diffraction effects were observed clearly due to small capture cross-section of Nb (about 1.1 b at thermal energy). Wang *et al.* used spallation neutron sources as we did, while the other past group used nuclear reactor and fast chopper. Both of their results also are fluctuated in the same way as ours.

## 4 Estimation of neutron diffraction

### 4.1 The formalism of neutron diffraction

In the Nb measurements, neutron diffraction was clearly observed in a low energy region, and therefore we examined this neutron diffraction effect. Since the effect of neutron diffraction is due to crystal structure, it is not appropriate to discuss nuclear reactions in a single nucleus. For this reason, polycrystalline model (abbreviate this to PCM hereinafter) was used here for estimation of neutron diffraction.

In PCM, the total cross-section for scattering processes including neutron diffraction can be written [13] as:

$$\sigma_s(E) = \sigma_{\text{coh}}^b \left( S_{\text{coh}}^{\text{el}}(E) + S_{\text{coh}}^{\text{inel}}(E) \right) + \sigma_{\text{incoh}}^b \left( S_{\text{incoh}}^{\text{el}}(E) + S_{\text{incoh}}^{\text{inel}}(E) \right), \quad (3)$$

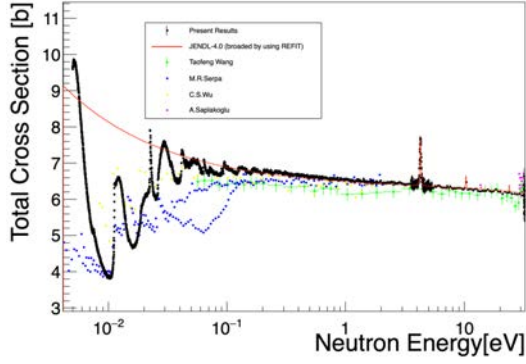


Figure 4: Neutron total cross-sections by the present and other past measurements at low energy

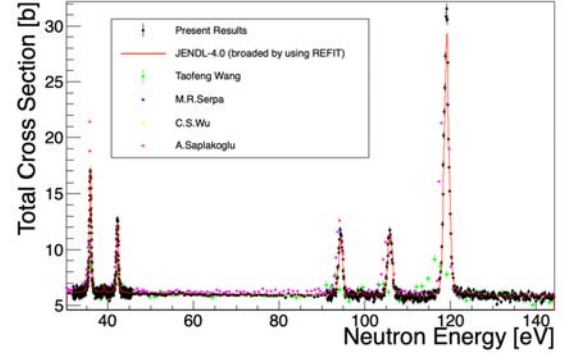


Figure 5: Neutron total cross-sections by the present and other past measurements at resonance region

where each function  $S(E)$  contains the information of sample system;  $\sigma_{\text{coh}}^{\text{b}}$  and  $\sigma_{\text{incoh}}^{\text{b}}$  are the bound coherent and incoherent cross-sections relating to cross-section  $\sigma$ :

$$\sigma^{\text{b}} = \left( \frac{A+1}{A} \right)^2 \sigma, \quad (4)$$

where  $A = M/m$ ;  $M$  and  $m$  are target mass and neutron mass, respectively. For Nb, incoherent effects can be ignored since  $\sigma_{\text{inc}}^{\text{b}}$  is negligibly small - about 0.038% against coherent effects. That is why the first term in Eq. (3) is only needed for estimation of neutron diffraction. The elastic coherent contribution of a polycrystalline solid can be given [13] by:

$$S_{\text{coh}}^{\text{el}}(E) = \frac{\pi^2 \hbar^2}{2mE v_0} \sum_{\tau_{hkl} < 2k_{\text{n}}} \frac{w(\tau_{hkl})}{\tau_{hkl}} \exp\left(-\frac{3\hbar^2 \phi_1(\Theta)}{2Mk_{\text{B}}\theta_{\text{D}}} \tau_{hkl}\right), \quad (5)$$

where  $k_{\text{n}}$ ,  $v_0$ ,  $\hbar$ ,  $k_{\text{B}}$  and  $\theta_{\text{D}}$  are neutron wave vector, the volume of the unit cell, the reduced Planck constant, Boltzmann constant and Debye temperature, respectively;  $w(\tau_{hkl})$  is the multiplicity of reciprocal lattice vectors  $\tau_{hkl}$ :

$$\tau_{hkl} = \frac{2\pi}{a} \sqrt{h^2 + k^2 + l^2}, \quad (6)$$

where  $a$  is lattice constant and  $h, k, l$  represent crystal planes. The  $\phi_m$  term is described as:

$$\phi_m(\Theta) = \int_{-1}^1 d\varepsilon \varepsilon^m (e^{\varepsilon/\Theta} - 1)^{-1}, \quad (7)$$

where  $\Theta = T/\theta_{\text{D}}$  and  $T$  is the absolute temperature. Here, inelastic coherent contribution involving phonons can be considered as the same as inelastic incoherent one [14]. The inelastic incoherent contribution [13-15] can be approximately expressed by the following equation:

$$S_{\text{inc}}^{\text{inel}}(E) = S_{\text{coh}}^{\text{inel}}(E) = \left( \frac{A}{A+1} \right)^2 \left\{ 1 + \frac{3}{4A} \phi_3(\Theta) \frac{k_{\text{B}}\theta_{\text{D}}}{E} \right\} - \frac{1}{12} \frac{Ak_{\text{B}}\theta_{\text{D}}}{E\phi_1(\Theta)} \left\{ 1 - \exp\left(-12 \frac{E}{Ak_{\text{B}}\theta_{\text{D}}} \phi_1(\Theta)\right) \right\}, \quad (8)$$

where the first term represents the total incoherent cross-section, consisted of elastic and inelastic incoherent processes, and the second term is the elastic incoherent one. Inelastic coherent cross-section can be obtained by Eq. (8) same as inelastic incoherent one.

Niobium crystal has a body-centered cubic lattice structure. In this case, summation in Eq. (5) is done when  $h+k+l$  is even. Figure 6 shows cross sections calculated with PCM by Nb parameters listed in Table 4, and experimental results and calculated ones with free gas model (FGM). Cross sections by FGM are normalized to that by PCM at 8 eV.

Table 4: Niobium parameters used for the PCM calculation

$\sigma_{\text{coh}}$	$\sigma_{\text{inc}}$	$\theta_{\text{D}}$	$a$
6.253 [b] [7]	0.0024 [b] [7]	265 [K] [16]	3.3004 [Å] [17]

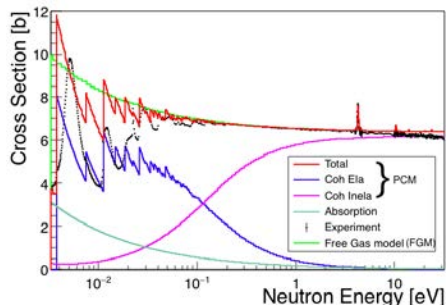


Figure 6: Cross-sections calculated with PCM and FGM and experimental results. Coh Ela and Coh Inela mean the coherent elastic and the coherent inelastic scattering cross-sections calculated by PCM. Total cross-sections of PCM are determined by adding Coh Ela, Coh Inela and absorption cross-sections.

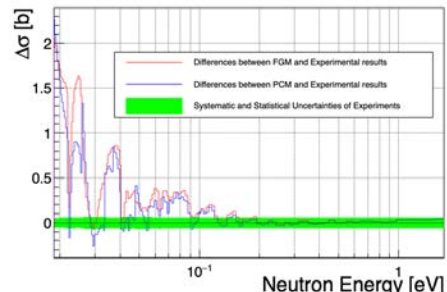


Figure 7: Differences between PCM, FGM and experimental results. Green band indicates the statistical and systematic uncertainties of experimental results.

## 4.2 Discussion of neutron diffraction and evaluation of nuclear data

Figure 7 shows differences in FGM and PCM from experimental results. Green band indicates the statistical and systematic uncertainties of experimental results. It is found that PCM has smaller discrepancy than FGM and that PCM can consider diffraction effects. Nevertheless, PCM is not enough to reproduce neutron diffraction effects. This might be due to the distortion of sample. From the region where the structure effect is not clear in PCM, it was decided not to use the present results below 0.2 eV where the difference between PCM and experimental results is larger than the experimental uncertainty. The uncertainty coming from the difference of the measured data might be also added to the systematic uncertainty.

## 5 Summary

The transmission measurements at J-PARC MLF ANNRI were performed in order to obtain neutron total cross-sections of  $^{93}\text{Nb}$ . In the Nb measurements, neutron diffraction was observed in the low energy region, and then this effect was examined with PCM. It became clear that PCM can consider diffraction effects, specially the energy occurring the fluctuation by diffraction. Since PCM is not enough to reproduce diffraction effects completely, it was decided not to use the present results below 0.2 eV. The total cross-sections obtained in this work will be analyzed with REFIT code to evaluate the resonance parameters.

## Acknowledgments

The authors would like to thank staffs for their efforts in operating the accelerators and the neutron production target of J-PARC MLF. This work was supported in part by Grants-in-Aid for Scientific Research (JP17H01076).

## References

- [1] M. Okoshi. Effects of Activation on the Dismantlement of Reactors - From the View Point of Radioactive Waste Management - RADIOISOTOPES. 1998;47:412-423.
- [2] T. Wang et al. Measurements of neutron total cross-sections and resonance parameters of niobium using pulsed neutrons generated by an electron linac. J Radioanal Nucl Chem 2011;289:945-952.
- [3] A. K. M. M. H. Meaze and G. N. Kim. Determinations of niobium and palladium resonance cross-sections by time-of-flight transmission experiment. Indian J. Phys. 2011;85(2):329-338.
- [4] N. J. Drindak et al. Neutron Capture and Transmission Measurements and Resonance Parameter Analysis of Niobium. Nuclear Science and Engineering. 2006;154:294-301.
- [5] E. I. Sharapov et al. Search for parity violation in  $^{93}\text{Nb}$  neutron resonances. Phys. Rev. C. 1999;59:1131-1135.
- [6] A. Saplakoglu et al. Properties of s-Wave and p-Wave Neutron Resonances in Niobium. Phys Rev 1958;109:1258-1262.
- [7] S. F. Mughabghab. Atlas of Neutron Resonances 6th ed, vol. 1. Amsterdam: Elsevier; 2018.
- [8] K. Shibata et al. JENDL-4.0: A New Library for Nuclear Science and Engineering. J. Nucl. Sci. Technol. 2011;48:1-30.
- [9] B. A. Brown et al. ENDF/B-VIII.0: The 8th Major Release of the Nuclear Reaction Data Library with CIELO-project Cross Sections, New Standards and Thermal Scattering Data. Nuclear data sheets 2018;148:1-142.
- [10] F. Maekawa et al. First neutron production utilizing J-PARC pulsed spallation neutron sources JSNS and neutronic performance demonstrated. Nucl Instruments Methods Phys Res Section. 2010;620:159-165.
- [11] K. Terada et al. Measurements of neutron total and capture cross sections of  $^{241}\text{Am}$  with ANNRI at J-PARC. J. Nucl. Sci. Technol. 2018;55:1198-1211.
- [12] CAEN web site, <https://www.caen.it>(Accessed: 2020-3-30).
- [13] J. R. Gradana. Total scattering cross section of solids for cold and epithermal neutrons. Z. Naturforsch. 1984;39a:1160-1167.
- [14] K. Binder. Total coherent cross section for the scattering of neutrons from crystals. Phys. Stat. sol. 1970;41:767-779.
- [15] G. Placze and L. V. Hove. Interference effects in the total neutron scattering cross-section of crystals. Il Nuovo Cimento. 1955;1:233-256.
- [16] C. Y. Ho et al. Thermal Conductivity of the Elements: A Comprehensive Review. Journal of Physical and Chemical Reference data. 1974;3:1-796.
- [17] M. E. Straumanis, and S. Zyszczyński. Lattice parameters, thermal expansion coefficients and densities of Nb, and of solid solutions Nb-O and Nb-N-O and their defect structure. J. Appl. Crystallogr. 1970;3:1-6.

# 23 High-Energy Measurement of the Neutron Capture Cross Section of $^{237}\text{Np}$

G. Rovira<sup>1\*</sup>, T. Katabuchi<sup>1</sup>, K. Tosaka<sup>1</sup>, S. Matsuura<sup>1</sup>, K. Terada<sup>1</sup>, Y. Kodama<sup>1</sup>  
H. Nakano<sup>1</sup>, O. Iwamoto<sup>2</sup>, A. Kimura<sup>2</sup>, S. Nakamura<sup>2</sup>, N. Iwamoto<sup>2</sup>

1) Laboratory for Advanced Nuclear Energy, Tokyo Institute of Technology

2) Japan Atomic Energy Agency

author: rovira.g.aa@m.titech.ac.jp

## Abstract

*The neutron capture cross-section of  $^{237}\text{Np}$  has been measured with the Accurate Neutron Nucleus Reaction Measurement Instrument (ANNRI) at the Materials and Life Science Facility (MLF) of the Japan Proton Accelerator Research Complex (J-PARC) using neutrons with energy ranging from thermal energy to 500 keV. The absolute cross-section was determined using the values for the whole shape of the first resonance from JENDL-4.0 and also with the total neutron flux derived from a  $^{197}\text{Au}$  sample measurement in which the first resonance was completely saturated. The results obtained from both techniques present agreement within 2%. In the high energy region, the cross-section was determined with uncertainty below 4% from 0.5 to 25 keV. Along with the cross section measurement, theoretical calculations were performed to reproduce the present results.*

## I. INTRODUCTION

Accurate nuclear data are of the essence for the nuclear transmutation of minor actinides (MAs) as the nuclear industry is set to tackle the issue of high-level waste (HLW) management. Nuclear transmutation facilities will take the task of converting HLW into short lived or even stable nuclei. Current evaluated nuclear data libraries are only suitable for the early stages of the design of nuclear transmutation systems. However, final designs and safety measures demand more precise nuclear data with a significant reduction in terms of their uncertainties [1, 2].

$^{237}\text{Np}$  has a long half-life of  $2.14 \times 10^6$  years and it is one of the most abundant MAs present in spent nuclear fuel.  $^{237}\text{Np}$  is also one of the main components of the Accelerator-Driven Systems (ADS) core, a subcritical reactor facility for nuclear transmutation. The region of interest for the core design is from 0.5 to 500 keV. Current uncertainties in JENDL-4.0 [3] from 0.5 to 500 keV for the neutron capture cross section of  $^{237}\text{Np}$  (6-10%) are much higher than the requirements of 3%. Hence, it is of utmost importance to accurately determine the neutron capture cross section at such energy range to reduce the uncertainties.

In the region from 0.5 to 500 keV, there are only two sets of data using time-of-flight (TOF) method that cover the whole energy range, those of Weston *et al* [4] and Esch *et al* [5]; and they present divergences from 15% to 35%. Experimental data by activation method exists in the 100-500 keV range but they differ from each other about 30-40% [6-8].

In this paper, results of the neutron capture cross section for  $^{237}\text{Np}$  are presented for incident neutron energy ranging from thermal energy to 500 keV with emphasis in the region of 0.5 keV to 500 keV. Moreover, in order to provide more accurate data, two normalization techniques were used to obtain an absolute value for the cross-section. The first technique was based on using the whole shape of the first resonance from JENDL-4.0 to determine a normalization factor. In the second technique, the energy-dependent cross-section was normalized using the total neutron flux obtained from a Au sample measurement in which the first resonance was completely saturated. In addition, the results of the experiments were complemented using the CCONE code [9] in order to assess the reliability of the results. Details of the experimental setup and the data analysis are also provided.

## II. EXPERIMENTAL PROCEDURE

### 1. Experimental Setup

The experiments were performed using the Accurate Neutron-Nucleus Reaction Measurement Instrument (ANNRI) at the Materials and Life Science Facility (MLF) of the Japan Proton Accelerator Research Complex (J-PARC). Intense pulsed neutrons were produced by the Japanese Spallation Neutron Source (JSNS) in the MLF using the 3 GeV proton beam of the J-PARC facility. The proton pulses were shot at the spallation target every 40 ms and with a beam power of 400 kW.

A TOF method was employed in the present experiment with a flight path of 27.9 m up to the sample position. Emitted  $\gamma$ -rays from the sample were detected by a NaI(Tl) detector. Detected capture events were stored sequentially with the corresponding TOF and energy value in a computer as a two-dimensional list format data.

A multi-event time digitizer FAST ComTec MPA4T [10] was employed for fast data acquisition purposes [10]. The time between the starting spallation trigger event and successive multiple stop from the detected  $\gamma$ -rays were digitized. The signal coming from the JSNS proton beam monitor was used as a trigger signal for the MPA4T module. The energy of the detected  $\gamma$ -rays was measured using traditional pulse-height method with the signal coming from the dynode of the photomultiplier tubes (PMT) from the NaI(Tl) detector. At the same time, in order to reduce the effect of the strong  $\gamma$ -rays emitted from the spallation reaction on the detected events in the keV region, the signal from the anode of the PMT was employed for pulse-width measurement to also determine the energy on the  $\gamma$ -rays. More information on the pulse width measuring technique employed at ANNRI can be found here [11].

### 2. Samples

A 200 mg (5 MBq)  $^{237}\text{Np}$  sample of 20 mm diameter and 1 mm thickness was utilized for the experiments. The  $^{237}\text{Np}$  sample consisted of 227 mg of neptunium dioxide ( $\text{NpO}_2$ ) powder binded with 624.5 mg of Al powder. The isotopic purity of  $^{237}\text{Np}$  for the sample was 99.99%. The powders were packed into a 30 mm diameter Al pellet with 0.4 mm thick walls. An exact replica of the Al dummy container was used to derive the background induced by the Al case. The incident neutron spectrum was reconstructed using  $\gamma$ -rays from the  $^{197}\text{Au}(n, \gamma)$  reaction with a 20 mm in diameter and 1 mm in thickness gold sample and, also, using the 478 keV  $\gamma$ -rays from the  $^{10}\text{B}(n, \alpha)^7\text{Li}$  reaction with a boron sample containing enriched  $^{10}\text{B}$  up to 90% and with a diameter of 10 mm and a thickness of 0.5 mm. Background events due to scattered neutrons were derived using a  $^{nat}\text{C}$  sample with a 10 mm diameter and 0.5 mm thickness.

## III. DATA ANALYSIS

### 1. Pulse Width to Pulse Height Conversion

Since pulse-width and pulse-height data were simultaneously recorded for all measured  $\gamma$ -ray, a conversion relation can be established by plotting both recorded data in a two-dimension histogram. More information about the pulse width analysis is described by Katabuchi *et al* [11].

### 2. Background Removal

In order to isolate the detected events coming from the  $^{237}\text{Np}(n, \gamma)^{238}\text{Np}$  reaction, different measurements and techniques were applied to the recorded data from the  $^{237}\text{Np}$  sample measurement run.

A dead time correction was applied offline to all measurements in order to estimate the count loss in the experiment [11]. The main cause for this count loss was the pile-up of two consecutive signals.

Capture events induced from slow neutrons coming from previous neutron bursts have to be subtracted. Every proton event induces neutron events with a frame length of 40 ms, as the proton beam repetition is 25 Hz. Overlapping background can be estimated using the operation pattern of J-PARC. A small part of the proton beam pulses from the 3-GeV synchrotron are injected into the 50-GeV synchrotron ring instead of JSNS. When no proton is shot into the JSNS, the measurable TOF is doubled since there is no trigger signal. Thus, the overlap background was estimated from the recorded events from 40 ms to 80 ms.

Blank background is subtracted using the data retrieved from a measurement with no sample. Likewise, the background events induced due to scattered neutrons at the sample and the events induced by the sample case are removed using the  $^{nat}\text{C}$  and the TOF spectra obtained from the aluminum case respectively.

### 3. Neutron Spectrum

The neutron spectrum was estimated using the gold and boron samples. The obtained TOF spectrum from both runs was divided by the reaction rate simulated using the PHITS program [12]. Figure 1 shows a good agreement of the incident neutron distribution between the two samples except for the resolved resonance region of gold. Hence, for better performance, only the neutron spectrum from the boron measurement was used in the analysis.

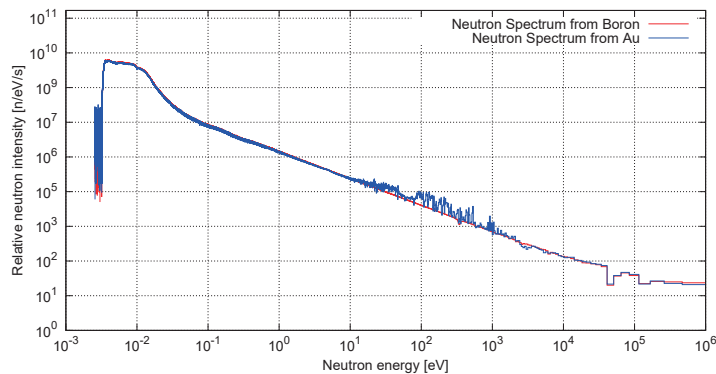


**Figure 1:** Incident neutron spectrum calculated from the gold and boron samples. Over 10 eV the neutron spectrum from the boron measurement offers better results.

### 4. Data Normalization

A relative capture cross-section can be obtained from the derived neutron capture yield and the incident neutron spectrum. However, since the measurement times and reaction rates are different for the Np and the boron samples, the obtained energy dependence of the cross-section has to be normalized.

The first normalization process consisted on using the evaluated data from JENDL-4.0 for the whole shape of the first resonance, from 0.25 eV to 0.7 eV, to normalize the cross-section results. The best fit for the normalization was obtained by minimizing the following residual:

$$\rho = \sum_{i=1}^n [y_i - N \cdot x_i]^2 \quad (1)$$

being  $n$  the number of energy points from 0.25 to 0.7 eV,  $y_i$  the evaluated cross-section values from JENDL-4.0,  $x_i$  the experimental results and  $N$  the normalization factor.

Alongside this method, the experimental data was also normalized using the saturated resonance technique to assess the reliability of the results. A gold sample used in the experiments was thick enough for the first resonance to be completely saturated. Since the resonance is saturated, all neutrons incoming with the energy of  $^{197}\text{Au}(n,\gamma)$  first resonance (4.9 eV) react with the sample. This assumption can be seen in figure 2. However, since the experimental setup has a detection threshold of 920 keV, a correction has to be made for the capture yield loss due to this threshold. The capture  $\gamma$ -ray spectrum for the  $^{197}\text{Au}(n,\gamma)^{198}\text{Au}$  and the  $^{237}\text{Np}(n,\gamma)^{238}\text{Np}$  reaction were calculated with CCONE at the energy of the  $^{197}\text{Au}(n,\gamma)^{198}\text{Au}$  first resonance. The capture yield loss for Au was estimated as the total energy loss, namely the total  $\gamma$ -ray emitted under the 920 keV threshold, divided by the total excitation energy.

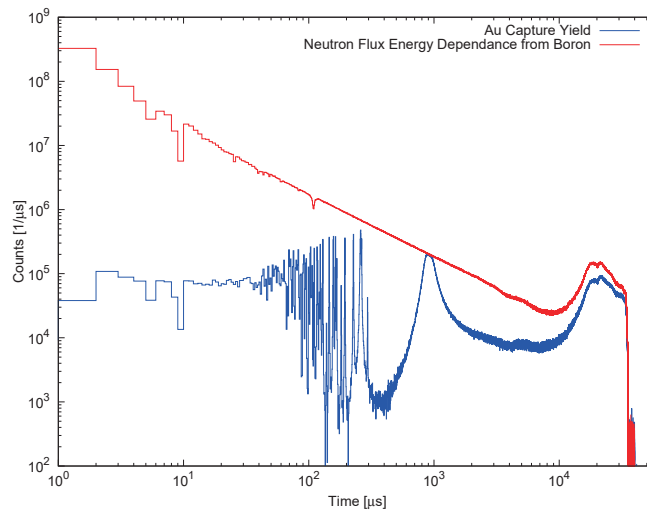


**Figure 2:** Energy dependence of the incident neutron flux (red) normalized to the  $^{197}\text{Au}$  neutron capture yield (blue) at the energy of the first resonance (4.9 eV).

This correction for the saturated resonance method,  $N_{sat}$  can be expressed as:

$$N_{sat} = \frac{1 - \frac{E_{Np(0-920)}}{B_n^{Np}} / \frac{E_{Np(tot)}}{B_n^{Np}}}{1 - \frac{E_{Au(0-920)}}{B_n^{Au}} / \frac{E_{Au(tot)}}{B_n^{Au}}} \cdot \frac{S_{Np}}{S_{Au}} \cdot \frac{1}{t_{Np}} \quad (2)$$

being  $E_{Np(0-920)}$  and  $E_{Np(tot)}$  the energy sum of the capture  $\gamma$ -rays from 0 to 920 keV and total emitted,  $B_n^{Au}$  and  $B_n^{Np}$  the binding energies for  $^{198}\text{Au}$  and  $^{238}\text{Np}$  respectively.  $S_{Np}$  and  $S_{Au}$  are the proton bursts shot during the Np and Au measurements and  $t_{Np}$  the Np sample thickness in at/b.

## 5. Uncertainty analysis

In this experiment, alongside the statistical uncertainties related to the counting rate, several systematic uncertainties have been considered. These systematic uncertainties relate to the normalization, dead-time correction, frame overlap subtraction, self-shielding and multiple scattering corrections and the neutron flux calculation.

The total error can be seen in figure 3 for both normalization techniques. The first resonance normalization offers better results as the normalization error is only of 0.5 %, whereas the error for the saturated resonance normalization is of 2.54%. The results with the first resonance normalization present uncertainties below 3% from 0.5 to about 2 keV and maintain a value of about 4% up to 25 keV. From this energy point, the effects of the neutron scattering induced by  $^{27}\text{Al}$  are visible as they reduce the incident neutron flux.

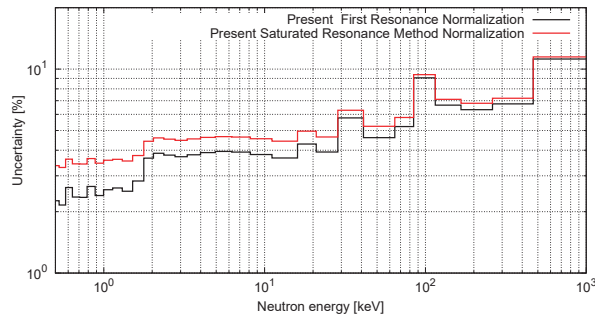


Figure 3: Total uncertainty.

#### IV. CROSS-SECTION RESULTS

The neutron capture cross section obtained from both normalization techniques can be seen in figure 4. The results from both normalization agree within uncertainties and offer good overall agreement with the evaluated data from JENDL-4.0.

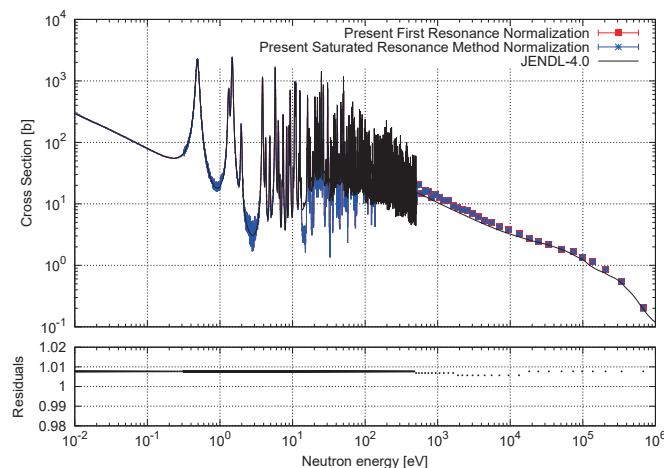


Figure 4:  $^{237}\text{Np}$  neutron capture cross-section from 10 meV to 1 MeV using the first resonance (red) and the saturated resonance method (blue) for normalization. The data residuals are plotted underneath.

In the region of interest, from 0.5 to 500 keV, only the results from the first resonance normalization have been considered as they provide less uncertainty.

Figure 5 shows a comparison with previously reported experimental data in the high energy region. As can be seen, the present data holds better agreement with the experimental data by Weston *et al* [4] than with the data from Esch *et al* [5]. In the energy range from 0.5 to 20 keV, where the discrepancies with JENDL-4.0 are over 15%, data from Esch *et al* [5] provides even lower values than those from JENDL-4.0, specially between energies of 1 to 10 keV where the differences with the data by Esch *et al* amount to 25%. Over 100 keV, only activation data by Lindner *et al* [7] is consistent with the present data as activation data from Trofimov *et al* [6] and Stupegia *et al* [8] overestimate both the present data and that of Lindner *et al* and also evaluated data from JENDL-4.0 and ENDF/B VIII.0 [13].

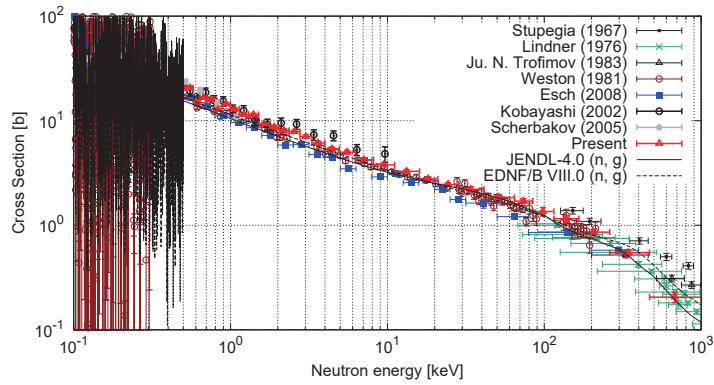


Figure 5: Neutron capture cross-section of  $^{237}\text{Np}$  from 0.5 keV to 1 MeV.

## V. THEORETICAL CALCULATIONS

The cross-section results of the  $^{237}\text{Np}$  neutron capture were evaluated by means of theoretical calculations using the CCONE code [9]. Since discrepancies exist with the current JENDL-4.0 data library, the aim of this analysis is not only to assess the reliability of the results but to provide a new tentative evaluation for the neutron capture cross-section of  $^{237}\text{Np}$ .

The  $^{237}\text{Np}$  neutron capture cross-section was derived by changing the E1 transition gamma strength function. For the rest of the calculations, the same parametrization as in the JENDL-4.0 were used from 0.5 keV to 1 MeV. The final results for all reaction channels are shown in figure 6 together with evaluated results from JENDL-4.0. The present evaluation shows good agreement for the fission and inelastic channels with JENDL-4.0. For the  $^{237}\text{Np}$  neutron capture cross-section, the results of the present evaluation provide better agreement with the experimental results in the whole energy range of the calculations.

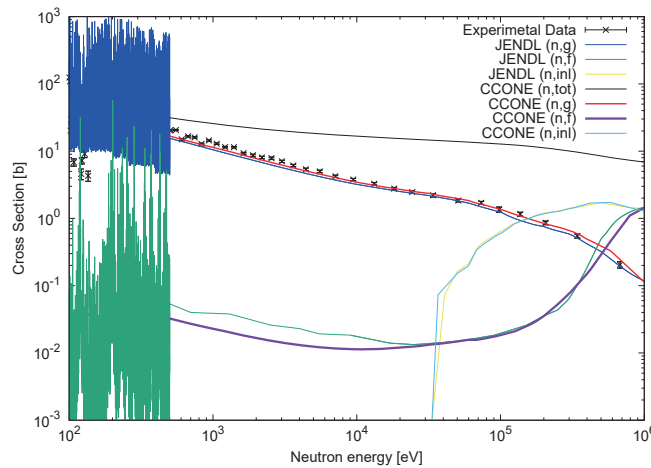


Figure 6: Evaluated  $^{237}\text{Np}$  neutron capture cross-section results from the CCONE calculation (red) in comparison with the results of JENDL-4.0 (blue)

## VI. CONCLUSIONS

The neutron capture cross-section of  $^{237}\text{Np}$  was measured with incident neutrons ranging from 10 meV to 500 keV. A time-of flight method was employed using the NaI(Tl) spectrometer of the ANNRI beamline at J-PARC. In the high energy region, the cross-section results were obtained with uncertainty below 4% from 0.5 to 25 keV. However, over that energy the uncertainty increases to over 8% due to an increase of the statistical uncertainty. Nonetheless, from 0.5 to 25 keV the results offer

a much lower total uncertainty than the uncertainty included in JENDL-4.0 of 6-10%. In comparison with experimental data, the present data holds better agreement with the experimental data by Weston *et al* [4] as the results from Esch *et al* [5] underestimate the present results. Theoretical calculations were performed with the CCONE code to reproduce the experimental results. The new calculations provided by the present analysis offer better agreement with the experimental data than JENDL-4.0, specially in the region from 0.5 to 20 keV where the differences between JENDL-4.0 and the present experimental amount to 10-25%.

## REFERENCES

- [1] H. Iwamoto et al., Nucl. Data Sheets 2014; 118:519-522.
- [2] Int. Eval. Co-op., Vol. 26, NEA/OECD, 2015.
- [3] K. Shibata et al., J. Nucl. Sci. Technol. 2011; 48:1-30.
- [4] L.W. Weston et al., Nucl. Sci. Eng. 1981; 79:184-196.
- [5] E-I. Esch et al., Phys. Rev. 2008; C77:034309.
- [6] Ju. N. Trofimov et al., Conf: 6. All-Union Conf. on Neut. Phys., Kiev, 2-6 Oct. 1983, 1983; 2:142.
- [7] M. Lindner et al., J. Nucl. Sci. Eng. 1976; 59:381.
- [8] D. C. Stupugia et al., J. Nucl. Sci. Eng. 1967; 29:218.
- [9] O. Iwamoto et al., Nucl. Data Sheets, 2016; 131:259-288.
- [10] FAST ComTec MPA4T, <https://www.fastcomtec.com/products/mpa/mpa4t0/>. [Accessed 2020-01-05.]
- [11] T. Katabuchi et al., Nucl. Ins. and Meth. in Phy. Res. A, 2014; 764:369-377.
- [12] T. Sato et al., J. Nucl. Sci. Technol. 2018; 55:684-690.
- [13] D.A.Brown et al., Nucl. Data Sheets. 2018; 149:1.

This is a blank page.

# 24 New Methods to Reduce Systematic Uncertainties of Capture Cross Section Measurement Using a Sample Rotation System

Y. KODAMA<sup>1\*</sup>, T. KATABUCHI<sup>1</sup>, G. ROVIRA<sup>1</sup>, H. NAKANO<sup>1</sup>, K. TERADA<sup>1</sup>,  
A. KIMURA<sup>2</sup>, S. NAKAMURA<sup>2</sup>, S. ENDO<sup>2</sup>

1) Tokyo Institute of Technology

2) Japan Atomic Energy Agency

author: kodama.y.ae@m.titech.ac.jp

## Abstract

*New methods to reduce systematic uncertainties of capture cross section measurement using a sample rotation system have been developed. Theoretical and experimental tests of these methods were conducted. Theoretical study using a Monte Carlo simulation code was performed. The calculated results were compared with test experimental results. The test experiment was carried out in Japan Proton Accelerator Research Complex.*

## I. INTRODUCTION

Accurate nuclear data for neutron-induced reactions are necessary for the design of nuclear transmutation system to reduce minor actinides (MA) and long lived fission products (LLFP) contained in nuclear waste. However current uncertainties of nuclear data such as MA and LLFP do not fulfill requirement for the design of transmutation facilities. Measurement of the neutron capture cross sections of MAs is ongoing at the Accurate Neutron Nucleus Reaction Measurement Instrument (ANNRI) in the Materials and Life Science Experimental Facility (MLF) of the Japan Proton Accelerator Research Complex (J-PARC).

Neutron capture cross section  $\sigma$  [ $cm^2$ ] is determined in experiments based on the following equation:

$$\sigma = \frac{1}{nt} \frac{\epsilon_\gamma N_\gamma}{\epsilon_n N_n}, \quad (1)$$

where  $n$  [atoms/ $cm^3$ ] is the atomic density of the sample,  $t$  [cm] is the sample thickness,  $\epsilon_\gamma$  and  $\epsilon_n$  are the efficiencies of  $\gamma$ -ray and neutron detectors, and  $N_\gamma$  ( $N_n$ ) is the number of detected  $\gamma$ -rays (neutrons) with the  $\gamma$ -ray detector (neutron detector). The capture cross section can be determined from remeasured  $N_\gamma$  and  $N_n$ . In the determination of capture cross section, the systematic uncertainty of final cross section is governed by two factors: the incident neutron energy spectrum and normalization to a standard value at a certain neutron energy.

In ANNRI experiments, the incident neutron energy spectrum is determined by measuring 478 keV  $\gamma$ -rays from the  $^{10}B(n,\alpha\gamma)^7Li$  reaction. Detected  $\gamma$ -ray counts are converted to the numbers of neutrons using the reaction rate of  $^{10}B(n,\alpha\gamma)^7Li$  reaction calculated from the cross section of the  $^{10}B(n,\alpha\gamma)^7Li$  reaction. The energy dependence of the reaction rate depends on the atomic area density of  $^{10}B$  in the boron sample because the neutron self-shielding factor increases with the  $^{10}B$  area density and also changes with the neutron energy. Thus, boron sample thickness ( $^{10}B$  atomic area density) is very important to determine the incident neutron energy spectrum.

The saturated resonance method is a commonly-used technique to obtain the absolute cross section [1]. This technique is based on the fact that neutron capture yield becomes equal to the number of the incident neutrons at a strong resonance when the sample is very thick and the resonance is fully

saturated. Although this technique allows for determining the absolute cross section value without any nuclear data as standard, it requires a thick sample that is sometimes not available.

In the present work, we suggest two new methods to reduce systematic uncertainties related to the two factors above using a sample rotation system.

## II. METHODOLOGY

### 1. Principle

Two methods employ change of the self-shielding effect with sample rotation angle. When a sample is tilted with respect to the beam axis, effective thickness of the sample becomes larger than the actual thickness. The reaction yield at the tilted angle  $\theta$  including the self-shielding effect is expressed as follows:

$$Y_\theta = c \frac{\sigma_{cap}}{\sigma_{tot}} \phi \left( 1 - e^{-Nt\sigma_{tot} \frac{1}{\cos\theta}} \right), \quad (2)$$

where  $c$  is correction factor of multiple-scattering effect and,  $\sigma_{cap}$  and  $\sigma_{tot}$  are the capture and total cross sections. The two new methods suggested below are based on the yield change with sample rotation.

### 2. Method 1: Boron sample thickness determination

The first method is for thickness determination of  $^{10}\text{B}$  sample which is used for measurement of the incident neutron spectrum in ANNRI experiments. The ratio of the reaction yield at a rotation angle of  $0^\circ$ ,  $Y_{0^\circ}$  to yield at  $\theta$ ,  $Y_{\theta^\circ}$  is written as:

$$R(T) = \frac{Y_{0^\circ}}{Y_{\theta^\circ}} = \frac{1 - e^{-Nt\sigma_{tot} \frac{1}{\cos\theta}}}{1 - e^{-Nt\sigma_{tot}}} \quad (3)$$

The energy dependence of the yield is measured by the neutron time-of-flight (TOF) method. Thus, the yield ratio  $R(T)$  is explicitly written as a function of TOF  $T$ .

The reaction yields of  $^{10}\text{B}(n,\alpha\gamma)^7\text{Li}$  for different boron thicknesses were calculated using a Monte Carlo simulation code. A typical calculated result of the yield ratio  $R(t)$  of  $0^\circ$  to  $45^\circ$  is shown in Fig. 1. The yield ratio  $R(t)$  is equal to 1 at low energies (slow TOF) and increases with neutron energy until  $1/\cos\theta$  that is 1.41 for  $45^\circ$ . The transient TOF region between the two constant values 1 and 1.41 changes with the sample thickness. We define  $T_{half}$  as the TOF value where  $R(t)$  becomes the half of the maximum.  $T_{half}$  changes with the sample thickness. In other words, the sample thickness can be determined from  $T_{half}$ . Figure 2 shows a plot of  $T_{half}$  vs sample thickness.

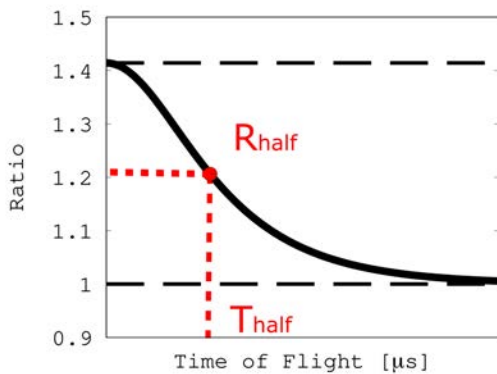


Figure 1: Reaction ratio TOF spectrum

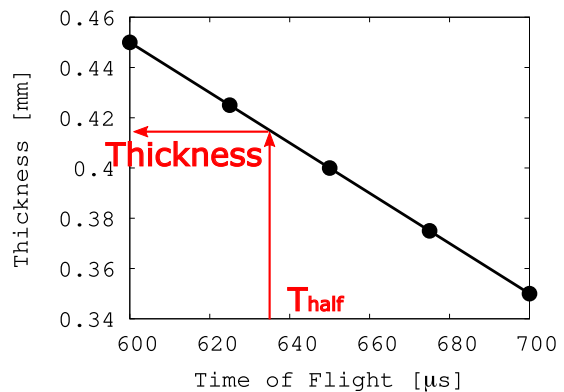


Figure 2: Plot of  $T_{half}$  vs TOF

### 3. Method 2: Capture reaction rate determination

The second method suggested in this work is to enable absolute normalization for capture cross section measurement even when a sample is not thick enough for the saturated resonance method. According to Eq. 3, the absolute reaction rate that is the ratio of capture yield to the number of the incident neutrons can be determined from a change of resonance peak height when the sample is tilted with respect to the neutron beam axis. Rotational change of the peak height of the first resonance of  $^{237}\text{Np}$  of the sample used in test experiments described in the next section was calculated. A plot of calculated resonance peak height vs  $1/\cos\theta$  is shown in Fig. 3. The resonance peak height is normalized to one at an angle of  $0^\circ$ . The self-shielding factor can be determined from this curve.

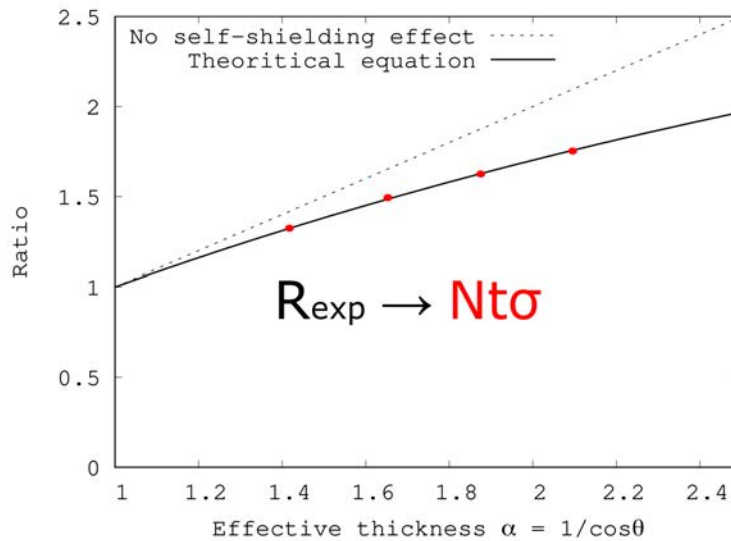


Figure 3: Ratio at the resonance peak

## III. SIMULATION AND EXPERIMENTS

We performed simulation studies using the Monte Carlo simulation code PHITS [2]. In simulation to test Method 1, the reaction rates of  $^{10}\text{B}(n,\alpha)^7\text{Li}$  in  $^{10}\text{B}$  90% enriched  $\text{B}_4\text{C}$  sample irradiated with neutron beam was calculated. Calculations were made for different sample thicknesses and  $T_{half}$  defined in the previous section were derived from the calculations. The obtained results are shown in Fig. 4. The simulation results are plotted as points. The curve is a fitting to the simulation results. This plot gives relation between  $T_{half}$  and the sample thickness that can be used to determine the sample thickness from  $T_{half}$  measured in experiments.

In simulation for Method 2, neutron capture reaction rates of  $^{237}\text{Np}$  were calculated. The total mass and dimensions of the  $^{237}\text{Np}$  sample was the same as the test experiments. Calculations were done for different tilted angles and the height of the first resonance peak was obtained. The peak height normalized to an angle of  $0^\circ$  is plotted as a function of  $1/\cos\theta$  shown as Fig. 5.

The sample rotation measurement was carried out at ANNRI in MLF of J-PARC. The  $^{237}\text{Np}$  sample was tilted with a sample rotation system. A  $^{237}\text{Np}$  sample (5.2 MBq) was irradiated with a neutron beam from a spallation neutron source of MLF. A TOF method was employed in this experiment with a neutron flight path of 27.9 m. Neutron capture  $\gamma$ -rays emitted from the sample were detected with a NaI(Tl) detector. After background subtraction, the peak heights of the first resonance of  $^{237}\text{Np}$  ( $E_n = 0.49$  eV) were derived for different tilted angles. The experimental results are plotted in Fig. 5. The simulation and experimental results do not agree well.

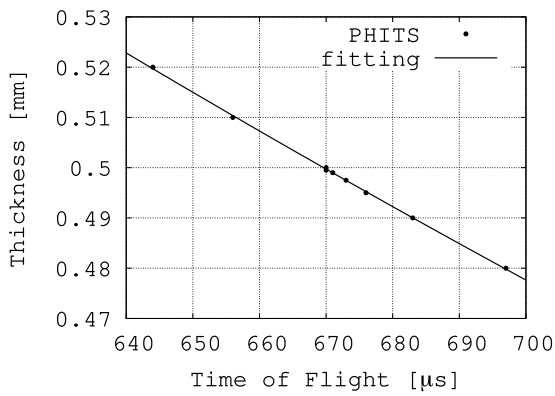


Figure 4: Calibration curve for the boron sample thickness

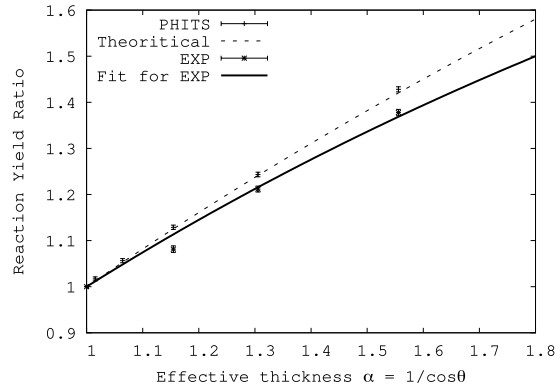


Figure 5: Reaction yield ratio at effective thickness of each tilted angle  $\theta$

#### IV. SUMMARY

In order to reduce systematic uncertainties of neutron capture cross section measurement, two new methods using a sample rotation system were proposed. In the first method, the thickness of a boron sample used to measure the incident neutron energy spectrum can be determined precisely. In the second method, the absolute capture reaction rate can be determined even when the sample is not thick enough for the saturated resonance method. Monte Carlo simulations were carried out and, for the second method, compared with results of a test experiment. Results showed that the calculation and the experimental results do not agree well. The cause of the disagreement is not yet clear. More investigation and study are necessary to improve agreement.

#### REFERENCES

- [1] Richard L. Macklin et al. ,Nuc. Ins. and Meth. 164, 1, 213-214(1979).
- [2] Tatsuhiro Sato et al. ,J. Nucl. Sci. Technol. 55, 684-690(2018).

## 25 Proton Spectra with Low-Energy-Threshold from 40- and 70-MeV Proton-Induced Reactions

Yuji YAMAGUCHI<sup>1</sup>, Toshiya SANAMI<sup>2</sup>, Yusuke KOBA<sup>3</sup> and Yusuke UOZUMI<sup>1</sup>

<sup>1</sup>Department of Applied Quantum Physics and Nuclear Engineering, Kyushu University  
744 Motooka, Nishi-ku, Fukuoka-shi, Fukuoka-ken 819-0395 Japan

<sup>2</sup>High Energy Accelerator Research Organization  
1-1 Oho, Tsukuba-shi, Ibaraki-ken 305-0801 Japan

<sup>3</sup>National Institute for Quantum and Radiological Science and Technology  
4-9-1 Anagawa, Inage-ku, Chiba-shi, Chiba-ken 263-8555 Japan  
e-mail: yyamaguchi@nucl.kyushu-u.ac.jp

We have developed a low-energy-threshold detector consisting of a Bragg curve counter (BCC), two silicon-surface barrier detectors and a bismuth germanate scintillator to obtain experimental double-differential cross section (DDX) data on (p, p'x) reactions for incident energies of several tens of MeV. The BCC can identify charged particles by itself and can do so for protons down to 1 MeV. The developed detector is used to measure proton spectra from <sup>nat</sup>C, <sup>27</sup>Al, <sup>nat</sup>Cu, <sup>nat</sup>Ag, <sup>nat</sup>Ta, and <sup>197</sup>Au targets at the detection angles in 60 – 150° with incident energies of 40 and 70 MeV. The minimum energy in the spectrum data is 1.3 MeV, which gives spectra in the whole energy range. Measured spectra are compared with the calculation of intranuclear cascade plus evaporation process.

### 1. Introduction

Energy and angular distributions of secondary particles from energetic proton-nucleus reactions are required to estimate the spatial distributions of energy deposition and radiation damage for the engineering design of an accelerator driven system and a particle radiation therapy facility. Because the estimation is performed using a Monte Carlo simulation code such as PHITS [1], the nuclear reaction models must have high predictive power in terms of energy and angular distributions. A two-stage model, which consists of an intranuclear cascade (INC) model [2, 3] and an evaporation model [4, 5], is generally used to describe the emission of secondary particles from proton-nucleus reactions up to several hundreds of MeV. In recent studies [6, 7], the INC model followed by the generalized evaporation model (GEM) has been improved for (p, p'x) reactions on light-to-heavy targets below 100 MeV. According to Ref. [7], the calculation results of the INC model covering high-energy range mainly above 10 MeV reproduce the energy and angular distributions of experimental data for targets from <sup>12</sup>C to <sup>209</sup>Bi at angles between 15° and 130°, but the GEM results covering low-energy range mainly below 10 MeV show discrepancies for heavy targets ( $A \geq 120$ ). To improve the GEM, systematic experimental data covering low-energy range for (p, p'x) reactions are required for not only heavy targets but also light and medium targets at various angles from forward to backward.

Bertrand et al. [8] and Harada et al. [9] have reported experimental data on light-to-heavy targets for incident proton energy  $E_p < 100$  MeV. Bertrand et al. obtained proton spectra for  $E_p = 29, 39,$  and  $62$  MeV, while Harada et al. obtained spectra for  $E_p = 42$  and  $68$  MeV. However, the spectra on a  $^{197}\text{Au}$  target exhibit different tendencies around  $55^\circ$  and  $120^\circ$  in the secondary energy range of  $2 - 6$  MeV between the data for  $E_p \sim 65$  MeV. In addition, both sets of data are insufficient below  $10$  MeV for  $E_p \sim 40$  MeV. The discrepancy at  $2 - 6$  MeV should be investigated and insufficient coverage of spectra for  $E_p \sim 40$  MeV should be updated for improvement of the GEM. Thus, new experimental data of  $(p, p'x)$  reactions are desired for secondary energies down to  $2$  MeV for  $E_p = 40$  and  $70$  MeV.

In this study, we take the data which satisfy the requirement above with various targets ( $^{nat}\text{C}$ ,  $^{27}\text{Al}$ ,  $^{nat}\text{Cu}$ ,  $^{nat}\text{Ag}$ ,  $^{nat}\text{Ta}$ , and  $^{197}\text{Au}$ ). For the measurement, we develop a low-energy-threshold detector consisting of a Bragg curve counter (BCC) [10], two silicon-surface barrier detectors (SSDs) and a bismuth germanate (BGO) scintillator.

## 2. Experiment

The experiment was performed at the cyclotron facility of National Institute of Radiological Sciences. The experimental setup and the low-energy-threshold detector are described in detail in Ref. [11]. Outlines of the setup and the detector are described herein. The plan view of the experimental setup is shown in Fig. 1. A scattering chamber was connected directly to the beam duct of the cyclotron and evacuated to less than  $10^{-3}$  Pa. Incident protons hit a thin-film target located inside the scattering chamber and entered a Faraday cup consisting of a stainless-steel pipe and a graphite beam dump. The targets for  $^{nat}\text{C}$ ,  $^{27}\text{Al}$ ,  $^{nat}\text{Cu}$ ,  $^{nat}\text{Ag}$ ,  $^{nat}\text{Ta}$ , and  $^{197}\text{Au}$  were mounted on a target changer. Thicknesses of  $11, 5, 3, 3, 3,$  and  $0.5 \mu\text{m}$  were chosen for polyethylene, aluminum, copper, silver, tantalum, and gold foils, respectively. For the  $^{nat}\text{C}$  target, a  $134\text{-}\mu\text{m}$ -thick graphite foil was also used to remove the proton component scattered by hydrogen in the polyethylene. Energy spectra of secondary particles emitted from the target were measured at  $60^\circ, 120^\circ,$  and  $150^\circ$  in the laboratory system using the low-energy-threshold detector.

The schematic drawing of the low-energy-threshold detector is shown in Fig. 2. This detector

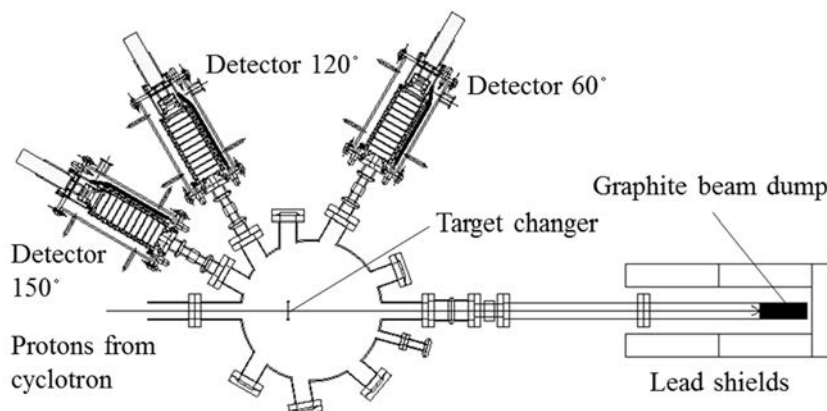


**Figure 1.** Plan view of experimental setup. Incident protons come from the left side of this view.

consists of a BCC, two SSDs, and a BGO scintillator. The BCC is a parallel-plate gas ionization chamber with a grid. The BCC can determine the energy  $E_{BCC}$  and the atomic number of a low-energy charged particle from the integral and peak height, respectively, of the anode signal, which reflects the charge distribution along the trajectory of the charged particle [10]. The Ar + 10 % CH<sub>4</sub> counting gas is kept inside the cylindrically shaped chamber using O-rings. The electrodes of the BCC consist of a cathode, nine field shaping rings, a grid, and an anode. The cathode-grid and grid-anode distances are 150 mm and 5 mm, respectively. The cathode is a stainless-steel disk with a central hole 10 mm in diameter covered with a 2.2- $\mu$ m-thick aluminized Mylar film. The Mylar film is electrically connected to the stainless-steel disk on the aluminized surface and is thin enough for low-energy charged particles to enter the BCC. The field shaping rings and the grid are arranged at equal intervals and connected with a chain of 1-M $\Omega$  resistors to maintain a uniform electric field. The anode plate is a stainless-steel disk with a central hole 32 mm in diameter and covered with a 5.7- $\mu$ m-thick aluminum foil. Thus, the anode enables energetic secondary particles to penetrate with small energy loss. The energetic particles are identified using  $\Delta E - E$  method with the BCC and rear detectors. In this case, the BCC works as a transmission detector.

The measured data were corrected to remove the effects of background component using data obtained without a target. The energy losses in the target, entrance window, and anode were compensated for by shifting the energy scale by calculation using the SRIM code [12]. Finally, DDXs were obtained by

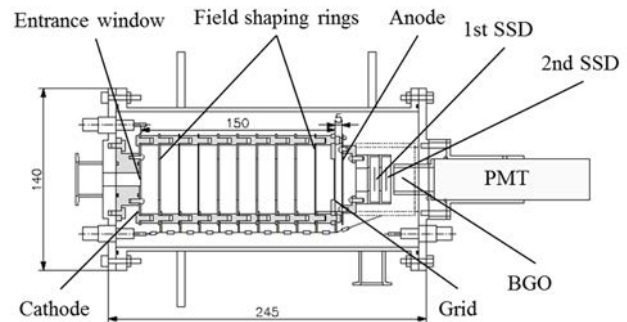


**Figure 2.** Schematic drawing of low-energy-threshold detector. Secondary particles come from the left side of this drawing and pass through the entrance window.

$$\frac{d^2\sigma}{d\Omega dE} = \frac{Y(E)}{s\phi\Delta\Omega\Delta E'} \quad (1)$$

where  $Y(E)$  is the number of charged particles,  $s$  is the number of target atoms per unit area,  $\phi$  is the number of incident protons,  $\Delta\Omega$  is the solid angle, and  $\Delta E'$  is the energy bin width. The solid angle  $\Delta\Omega$  was determined experimentally by  $\alpha$ -particle counting using an <sup>241</sup>Am check source placed instead of the target.

### 3. Results and discussion

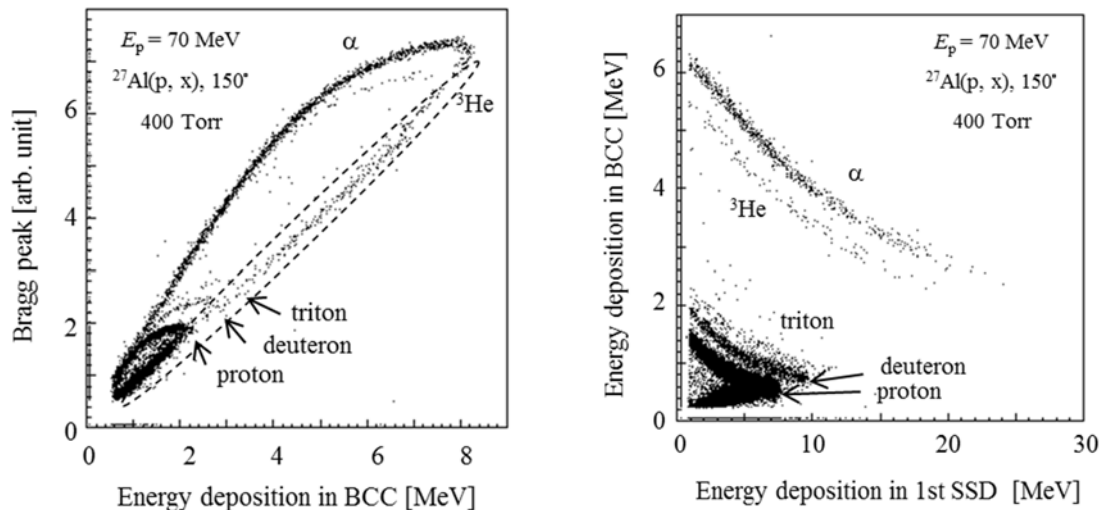
Figure 3 shows the plot of  $E_{BCC}$  versus Bragg peak height (atomic number) obtained using 53.3 kPa counting gas. In this figure, hydrogen and helium isotopes are identified. On the high-energy side, those particles that penetrated the anode are observed within dashed circles. In the energy range from 1 MeV to 3 MeV, the hydrogen isotopes of protons, deuterons and tritons are clearly identified because the

Bragg peak is characterized by the mass number of the charged particle besides the atomic number. Protons down to 1.1 MeV are separated from other particles in Fig. 3. Thus, the threshold energy of 1.1 MeV was achieved for proton identification.

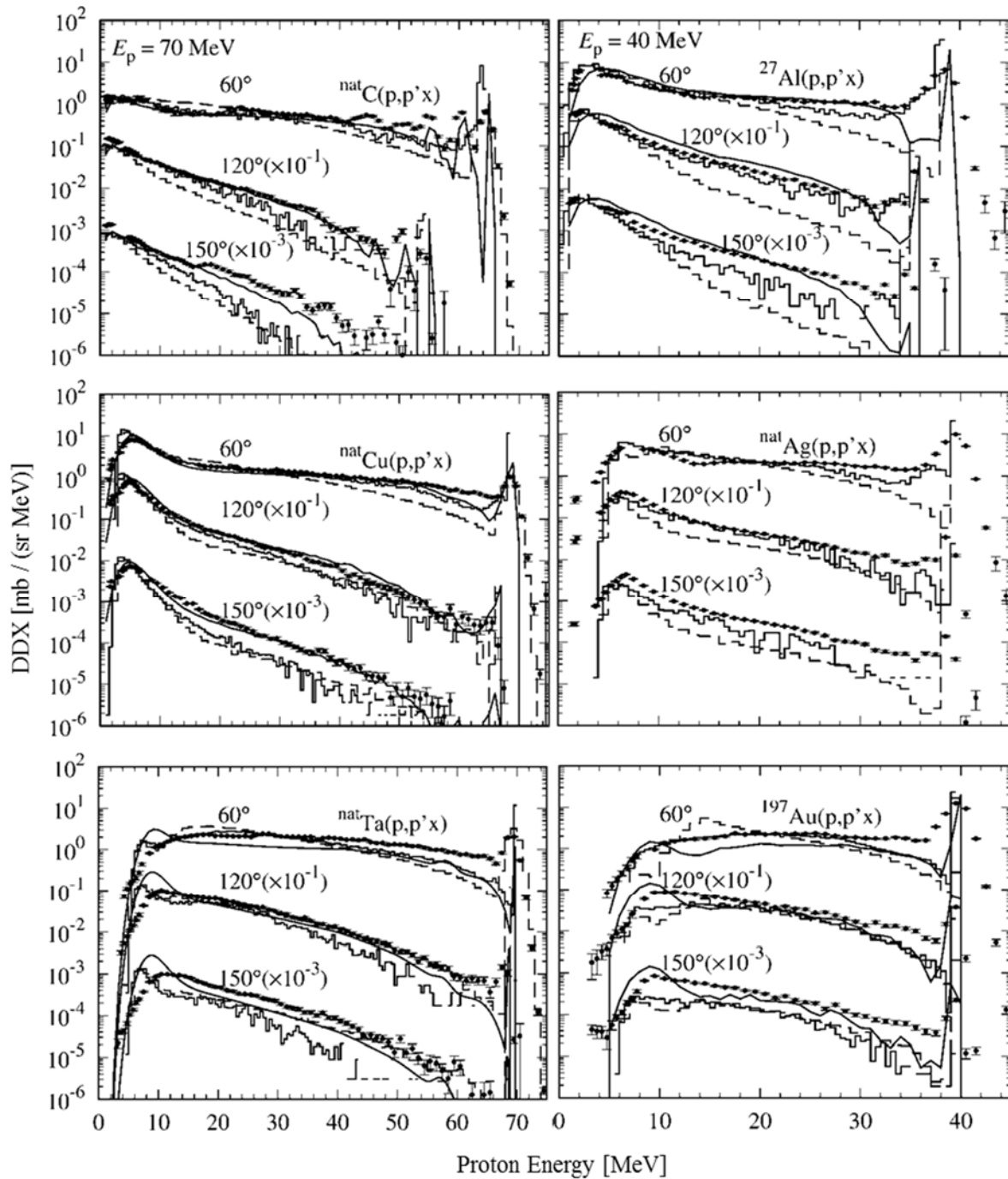
Figure 4 shows the plot of  $\Delta E$  (BCC) versus  $E$  (first SSD) obtained using 53.3 kPa counting gas. The hydrogen isotopes are also identified in this figure because of the satisfactory energy resolution of the BCC. Although the identified proton line overlaps partially with the folding-back lines of the hydrogen isotopes that penetrated the first SSD, the penetrating events can be removed using the signal of the second SSD in offline analysis.

Figure 5 shows proton spectra for 40- and 70-MeV incident protons on  $^{nat}C$ ,  $^{27}Al$ ,  $^{nat}Cu$ ,  $^{nat}Ag$ ,  $^{nat}Ta$ , and  $^{197}Au$  targets at  $60 - 150^\circ$ . The measured spectra were obtained in a wide energy range. The minimum energy of the measured data is 1.3 MeV, which is 0.2 MeV above the particle identification threshold because of compensating for the energy losses in the target foil and the entrance window. In comparison of the  $^{nat}Cu(p, p'x)$  spectra with the  $^{nat}Ta(p, p'x)$  spectra below 10 MeV for  $E_p = 70$  MeV, the  $^{nat}Cu(p, p'x)$  spectra show a broad peak whereas the  $^{nat}Ta(p, p'x)$  spectra show monotonic decrease as the proton energy decreases, which reflects the difference in the Coulomb barrier. This target dependence is also observed in comparison of  $^{nat}Ag(p, p'x)$  spectra with the  $^{197}Au(p, p'x)$  spectra for  $E_p = 40$  MeV.

Calculation results and spectra of JENDL-4.0/HE reproduce measured spectra for  $^{nat}C$ ,  $^{27}Al$  and  $^{nat}Cu$  targets below 10 MeV. However, calculations and JENDL spectra overestimate measured  $^{nat}Ta(p, p'x)$  spectra for  $E_p = 70$  MeV. The  $^{197}Au(p, p'x)$  spectra of the INC plus GEM have a threshold at 6 MeV for  $E_p = 40$  MeV whereas there are measured data below 6 MeV. This discrepancy is due to classical approximation in GEM calculation.



**Figure 3.** Plot of  $E_{BCC}$  versus Bragg peak height. **Figure 4.** Plot of  $\Delta E$  (BCC) versus  $E$  (first SSD). The particles identified as proton, deuteron, triton,  $^3He$  and  $\alpha$  are shown. The particles identified as proton, deuteron, triton,  $^3He$  and  $\alpha$  are shown.



**Figure 5.** Proton spectra for 40- and 70-MeV incident protons on  $^{nat}\text{C}$ ,  $^{27}\text{Al}$ ,  $^{nat}\text{Cu}$ ,  $^{nat}\text{Ag}$ ,  $^{nat}\text{Ta}$ , and  $^{197}\text{Au}$  targets at 60 – 150°. Measured spectra are shown using closed circles with bar indicating statistical uncertainties. Calculations of INC plus GEM in Ref. [7] and that in PHITS as the default model [2] are shown with solid and dashed histograms, respectively. Smooth curves show spectra of JENDL-4.0/HE.

#### 4. Conclusion

We developed a low-energy-threshold detector consisting of a BCC, two SSDs, and a BGO scintillator to obtain experimental data on (p, p'x) reactions  $E_p$  covering the low-energy range. We used the

detector and obtained proton spectra down to 1.3 MeV at 60 – 150° for targets of  $^{nat}\text{C}$ ,  $^{27}\text{Al}$ ,  $^{nat}\text{Cu}$ ,  $^{nat}\text{Ag}$ ,  $^{nat}\text{Ta}$ , and  $^{197}\text{Au}$  using 40- and 70-MeV protons. The resultant spectra were compared with results of the INC plus GEM and spectra of JENDL-4.0/HE. Below 10 MeV, calculation results and JENDL spectra reproduced measured spectra for  $^{nat}\text{C}$ ,  $^{27}\text{Al}$  and  $^{nat}\text{Cu}$  targets, but overestimated for the  $^{nat}\text{Ta}$  target.

### Acknowledgement

This work was conducted at Joint-use Research Facility for Collaborative Project with NIRS-Cyclotron.

### References

- [1] T. Sato, Y. Iwamoto, S. Hashimoto, et al. Features of particle and heavy ion transport code system (PHITS) version 3.02. *J. Nucl. Sci. Technol.* 2018;55(6):684-690.
- [2] A. Boudard, J. Cugnon, J. C. David, et al. New potentialities of the Liege intranuclear cascade model for reactions induced by nucleons and light charged particles. *Phys. Rev. C* 2013;87:014606.
- [3] Y. Sawada, Y. Uozumi, S. Nogamine, et al. Intranuclear cascade with emission of light fragment code implemented in the transport code system PHITS. *Nucl. Instrum. Methods Phys. Res. B* 2012;291:38-44.
- [4] S. Furihata, T. Nakamura. Calculation of nuclide productions from proton induced reactions on heavy targets with INC/GEM. *J. Nucl. Sci. Technol.* 2002;39(2):758-761.
- [5] J. Benlliure, A. Grewe, M. de Jong, et al. Calculated nuclide production yields in relativistic collisions of fissile nuclei. *Nucl. Phys. A* 1998;628:458-478.
- [6] Y. Uozumi, T. Yamada, S. Nogamine, et al. Intranuclear cascade model including collective excitations and trajectory deflections for (p, p'x) reactions around 50 MeV. *Phys. Rev. C* 2012;86:034610.
- [7] Y. Uozumi, T. Yamada, M. Nakano. Intranuclear cascade model for 50-MeV-region (p, p'x) reactions over a wide target mass range. *J. Nucl. Sci. Technol.* 2015;52(2):264-273.
- [8] F. E. Bertrand, R. W. Peelle. Complete hydrogen and helium particle spectra from 30- to 60-MeV proton bombardment of nuclei with  $A = 12$  to 209 and comparison with the intranuclear cascade model. *Phys. Rev. C* 1973;8:1045-1064.
- [9] M. Harada, Y. Watanabe, Y. Tanaka, et al. Light charged-particle production in proton-induced reactions on  $^{12}\text{C}$ ,  $^{27}\text{Al}$ ,  $^{58}\text{Ni}$ ,  $^{90}\text{Zr}$ ,  $^{197}\text{Au}$ , and  $^{209}\text{Bi}$  at 42 and 68 MeV. *J. Nucl. Sci. Technol.* 2002;39(2):393-396.
- [10] T. Sanami, M. Hagiwara, T. Oishi, et al. A Bragg curve counter with an active cathode to improve the energy threshold in fragment measurements. *Nucl. Instrum. Methods Phys. Res. A* 2008;589:193-201.
- [11] Y. Yamaguchi, T. Sanami, Y. Koba, et al. Low-energy-threshold detector for measuring proton spectra at several tens of MeV using Bragg curve spectroscopy. *Nucl. Instrum. Methods Phys. Res. A* 2020;953:163158.
- [12] J. F. Ziegler, M. D. Ziegler, J. P. Biersack. SRIM – The stopping and range of ions in matter (2010). *Nucl. Instrum. Methods Phys. Res. B* 2010;268:1818-1823.

## 26 Charged particle emission reactions induced by 100-MeV/u $^{12}\text{C}$ ions

Kazuhito YOSHIDA<sup>1\*</sup>, Yuji YAMAGUCHI<sup>1</sup>, Ryota IMAMURA<sup>1</sup>, Tatsuki KAKEBAYASHI<sup>1</sup>,  
Mizuki YAMADA<sup>1</sup>, Yuki FUKUDA<sup>1</sup>, Tomoe KATAYAMA<sup>1</sup>, Toshiya SANAMI<sup>2</sup>,  
Yosuke IWAMOTO<sup>3</sup>, Naruhiro MATSUFUJI<sup>4</sup>, Yusuke KOBAYASHI<sup>4</sup>, Zviadi TSAMALAIIDZE<sup>5</sup>,  
Petr EVTOUKHOVITCH<sup>5</sup>, and Yusuke UOZUMI<sup>1</sup>

<sup>1</sup>Department of Applied Quantum Physics and Nuclear Engineering, Kyushu University

<sup>2</sup>High Energy Accelerator Research Organization

<sup>3</sup>Japan Atomic Energy Agency

<sup>4</sup>National Institute for Quantum and Radiological Science and Technology

<sup>5</sup> Joint Institute for Nuclear Research, Dubna, Russia

e-mail: yoshida@nucl.kyushu-u.ac.jp

The measurement was performed at the Heavy Ion Medical Accelerator in Chiba (HIMAC), National Institute for Radiological Sciences, Japan. The carbon-ions were accelerated to 100 MeV/u and bombarded the target (C, Al, and Co). Emitted charged particles were detected by counter-telescopes installed at the PH2. Light particles (p, d, t,  $^3\text{He}$  and  $\alpha$ ) were detected with two  $\Delta E$ -E telescopes comprising two silicon-surface-barrier detectors (SSDs), a GSO(Ce) crystal and four PWO crystals. Particles heavier than  $\alpha$  were detected with two  $\Delta E$ -E telescopes consisting of two SSDs and a CsI(Tl) crystal. Thanks to their high energy resolutions, isotope separation was achieved for many of detected particles. This report describes experimental results obtained during 2018-2019 at HIMAC.

### I. INTRODUCTION

With respect to a role in radiotherapy, carbon-ions offer excellent advantages [1]. One is the high relative biological effectiveness (RBE) thanks to its high linear energy transfer (LET). Another advantage of carbon-ion therapy is that it provides highly conformal dose distributions due to the Bragg peak, and therefore it is possible to deliver a large and uniform dose to the target while sparing normal tissues. However, there is a certain potential that they induce undesired dose outside the primary beam field. The undesired dose arises from secondary particles produced through beam interactions with the patient's body. These dose distributions provide a low integral dose to surrounding healthy tissues. The low dose exposure of the normal tissue raised concerns about the occurrence of secondary malignancies as the long-term effects.

When a primary carbon ion traverses the patient body, it can undergo nuclear fragmentation. According to the breakup model [2] and the abrasion-ablation model [3,4], highly energetic particles including clusters, which have approximately the same velocities as that of the projectile, are observed in an extreme forward cone in the laboratory angles. Therefore, they are responsible for the dose tail observed after

the distal edge of the Bragg Peak [5,6]. In order to understand the dose tail, many experiments were carried out. The energy-angle double differential cross sections (DDXs) of charged particle productions were also measured [7,8] at angles smaller than 20 degrees including zero degrees. In contrast, little attention has been paid to DDXs of the lateral angles. The charged composite particles, which have high LET and large RBE, emitted laterally have been supposed to have low energies [3,4], and to be stopped within the primary beam diameter. Then, the importance of lateral doses was expected to be negligible. In recent years the increasing concern about low dose exposure requires accurate estimation of lateral doses. However, DDXs of lateral emission of charged composite particles were not reported at larger angles than 20 degrees.

The purpose of this work was to measure DDXs of charged particle emissions to lateral directions from interaction between clinical carbon-ion beam and elements constituting the human body. The measurement covered charged particles from protons to  $^{12}\text{C}$ , and DDXs were determined for most of the isotopes. In this report, we describe the experimental equipment and method, and present some preliminary DDX data measured at the beam energy of 100 MeV/u.

## II. EXPERIMENTS

**Table 1 Targets used in this work.**

	$^{27}\text{Al}$	$^{\text{nat}}\text{C}$	$^{59}\text{Co}$
Thickness [mm]	0.1 and 2.0(for calibration)	0.1	0.05

Experiments were carried out at the Heavy Ion Medical Accelerator In Chiba (HIMAC), National Institute for Radiological Sciences, Japan.  $^{12}\text{C}$  beam was focused on a target in a spot of about 5-mm diameter. The target was set at the center of a vacuum chamber of 50-cm diameter. The targets used were  $^{12}\text{C}$ ,  $^{27}\text{Al}$ , and  $^{59}\text{Co}$ , which are all natural metals. Their thicknesses are listed in Table 1.

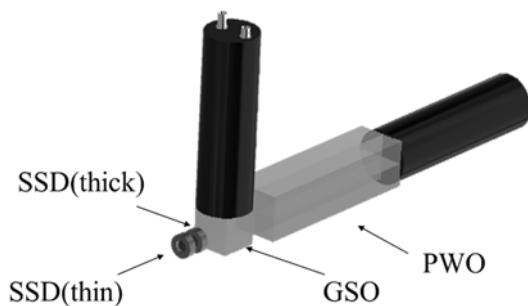


**Fig. 1 Telescope for p, d, t,  $^3\text{He}$ , and  $\alpha$**

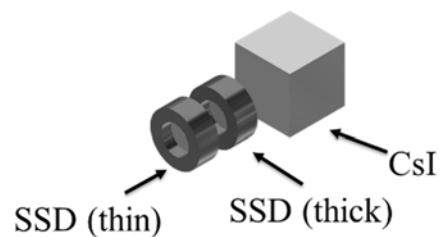


**Fig. 2 Telescope for particles heavier than  $\alpha$**

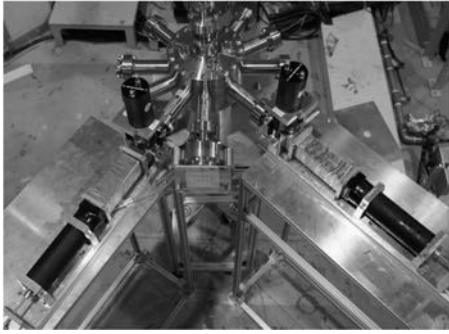


**Fig3. A system for measurement the light particles**

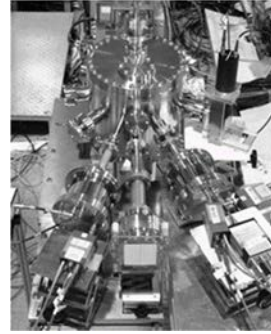


**Fig4. A system for measurement the heavy particles**

The energy of emitted particles was measured with two stacked scintillator spectrometer which are shown schematically in Fig. 1. Light particles (p, d, t,  $^3\text{He}$  and  $\alpha$ ) were detected with two  $\Delta E$ -E telescopes comprising two silicon-surface-barrier detectors (SSDs), a GSO(Ce) crystal and four PWO crystals. Particles heavier than  $\alpha$  were detected with two  $\Delta E$ -E telescopes consisting of two SSDs and a CsI(Tl) crystal. The first and second SSD were  $\Delta E$  detectors of 100  $\mu\text{m}$  and 2 mm in thickness, respectively. The GSO(Ce) crystal was cubic with an edge length of 43mm. The PWO crystal was cuboidal with  $50 \times 50 \times 199\text{mm}$ . The CsI(Tl) scintillator was cubic with an edge length of 28mm.

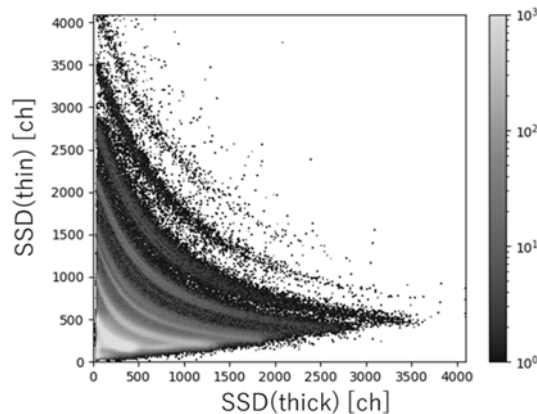


**Fig. 5 Two dimensional scatter plot of first and second SSD**

At first, DDX of the  $\text{Al}(\text{C},\text{px})$  reaction was determined in a proton energy range of 70-120 MeV at 30 and 45 degrees. The thick target (2-mm-thick  $^{27}\text{Al}$  plate) and the low intensity beam were used in these measurements, where the number of incident  $^{12}\text{C}$  ions was counted directly by a plastic scintillator detector. Second, experiments with a thin target (0.5-mm-thick  $^{27}\text{Al}$  plate) and the high-intensity beam were performed for the  $\text{Al}(\text{C},\text{px})$  reaction to measure proton spectra over a range of 10-500 MeV. The spectra were converted to DDXs by normalizing to the thick target data. During these measurements, a beam monitor consisting of a plastic scintillator detector was used to count the secondary particles scattered from a thin metal foil. The readout of the beam monitor was also normalized to that of the counter used for thick-target experiments. Lastly, the DDX values for other reactions were measured with a thin target, a high intensity beam, and the beam The telescope which used for measuring light particles (p, d, t,  $^3\text{He}$  and  $\alpha$ ) had sufficient

depth to stop 480-MeV protons and 1200-MeV  $\alpha$ -particles. Figure 5 shows example data measured by the telescope for the heavy particles. The telescope which was used for measuring particles heavier than  $\alpha$  had sufficient depth to stop 730-MeV  ${}^6\text{Li}$  ions and 1200-MeV  ${}^{12}\text{C}$  ions. One of the faces of the GSO(Ce) scintillator and the PWO scintillator were each connected to a photomultiplier tube (PMT) and that of the CsI(Tl) scintillator was connected to a photo diode to convert scintillation light into electric signals and amplify the signal. Electric signals from detectors were fed into a spectroscopic amplifier via a preamplifier. Their pulse heights were analyzed by an amplitude-to-digital converter. The digitized data were transferred to a PC through the CAMAC system and recorded on hard-drive. Energy calibration was performed by referring to proton energy which was calculated by the Bethe formula. The spectrometers which were used for measuring light particles was installed outside the chamber. The telescopes which were used for measuring the heavy particles were installed into the vacuum chamber. Energy spectra of light particles were measured at laboratory angles from  $30^\circ$  to  $120^\circ$ . Energy spectra of the heavy particles were measured at laboratory angles from  $15^\circ$  to  $20^\circ$ .

High-energy particles may undergo nuclear reactions before being stopped or may scatter out of the crystal. The ratio between the number of stopped particles and the total number of particles is referred to as the peak efficiency of the spectrometer and is necessary to determine absolute cross sections. Thus far, the peak efficiency has been determined as a function simulated by PHITS calculation. The DDXs are determined by

$$\frac{d^2\sigma}{d\Omega d\varepsilon} = \frac{Y}{PS_t\phi\Delta\Omega\Delta\varepsilon},$$

where  $\Delta\varepsilon$  is the energy bin width required for data reduction,  $\Delta\Omega$  is the solid angle of the detector,  $P$  is the peak efficiency,  $S_t$  is the surface density of the target, and  $\phi$  is the total charge of the incident  ${}^{12}\text{C}$  beam.

The number of emitted particles in  $\Delta\varepsilon$ , which is represented by  $Y$ , is obtained by the particle identification (PI) technique. The quantity PI is given by

$$\text{PI} = E_{\text{tot}}^b - (E_{\text{tot}} - \Delta E)^b,$$

where  $E_{\text{tot}}$  is the total energy deposited in the detector and  $\Delta E$  is the energy measured in the  $\Delta E$  detectors. The parameter  $b$  is set 1.73, which is the optimum value to separate the isotopes. A two dimensional plot of PI versus emission energy of Be and B was shown in Fig.6.

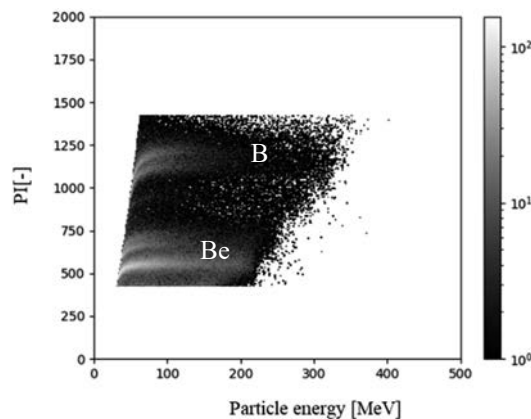


**Fig. 6 Two-dimensional plot of PI versus particle energy (Be and B).**

### III. RESULT AND DISCUSSION

Preliminary data have been obtained for the reaction of 100-MeV/u  $^{12}\text{C}$  ion on the  $^{27}\text{Al}$  target. The spectra of DDXs for 100-MeV/u  $^{27}\text{Al}(^{12}\text{C}, \text{px})$  and  $^{27}\text{Al}(^{12}\text{C}, \alpha\text{x})$  reactions at 30, 45, 60, 120 degrees are shown in Fig.7 and Fig.8, respectively. The spectra of DDXs for 100MeV/u  $^{27}\text{Al}(^{12}\text{C}, ^7\text{Bex})$  reactions at 15 and 20 degrees are shown in Fig.9. The maximum energy of proton was 210 MeV at 60degrees. The highest observed energy of  $\alpha$ -particle was 230 MeV at 60 degrees. The highest observed energy of  $^7\text{Be}$  was 490 MeV at 20 degrees.  $\alpha$ -particle of 230 MeV has the range of 28.5 mm in water. Therefore, healthy tissues around the beam axis to cancerous tissues can be affected by such high-energy particles. As shown in Fig.6, 470 MeV  $\alpha$ -particles were measured at 30degrees. In previous study, 285 MeV proton was observed for 400 MeV  $^{nat}\text{C}(\alpha, \text{px})$  reactions at 30 degrees. Considering secondary nuclear reactions, the influence of charged particle emission over 30 degrees for a human cannot be ignored.

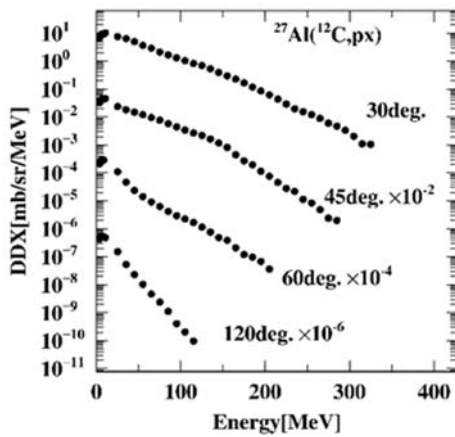


Fig. 7 DDXs of  $^{27}\text{Al}(^{12}\text{C}, \text{px})$  reaction

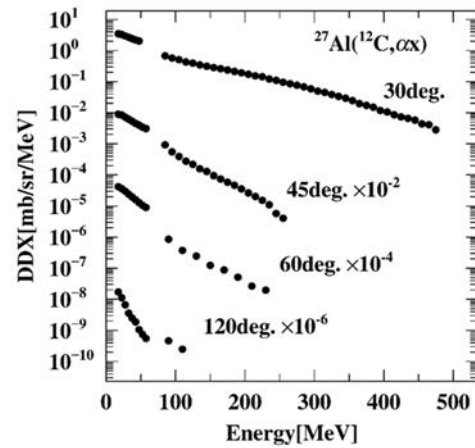


Fig. 8 DDXs of  $^{27}\text{Al}(^{12}\text{C}, \alpha\text{x})$  reaction

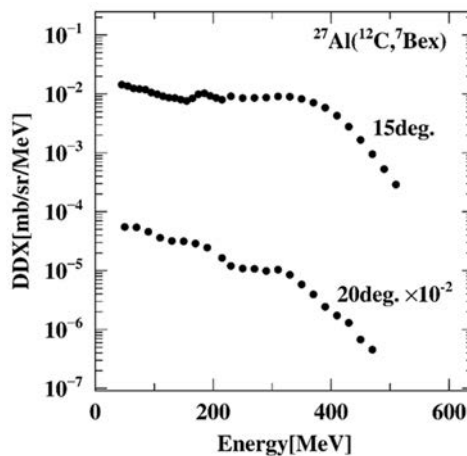


Fig. 9 DDXs of  $^{27}\text{Al}(^{12}\text{C}, ^7\text{Bex})$  reaction

#### IV. CONCLUSION

We measured DDXs of charged particle emission reactions induced by 100MeV/u  $^{12}\text{C}$  ions on three targets (C, Al, Co) at 15, 20, 30, 45, 60, and 120 degrees at HIMAC, NIRS. DDXs of emitted particles (p, d, t,  $^3\text{He}$ ,  $\alpha$ ,  $^6\text{Li}$ ,  $^7\text{Li}$ ,  $^7\text{Be}$ ,  $^9\text{Be}$ ,  $^{10}\text{Be}$ ,  $^{10}\text{B}$ ,  $^{11}\text{B}$ ,  $^{10}\text{C}$ ,  $^{11}\text{C}$ ,  $^{12}\text{C}$ ) were determined in wide ranges of emission energies. The notable point is that high-energy particles are observed at large angles. Particularly,  $\alpha$  particles above 100 MeV show certain values of DDXs. This fact suggests that the high-energy heavy-ions can have a long range over the beam diameter, and the healthy tissues around the initial beam axis may have late effects low-dose exposure of heavy ions.

#### ACKNOWLEDGMENTS

This work was conducted under the research project with heavy ions at NIRS-HIMAC, program number H350. This work was supported by JSPS KAKENHI Grant Number JP17H03522.

#### REFERENCES

- [1] D. Schardt, T. Elsässer, and D. Schulz-Ertner, “Heavy-ion tumor therapy: Physical and radiobiological benefits,” *Rev. Mod. Phys.* 82, 383 (2010).
- [2] J. R. Wu, C. C. Chang, and H. D. Holmgren, “Breakup of  $\alpha$  Particles in the Fields of Nuclei,” *Phys. Rev. Lett.* 40, 1013 (1978).
- [3] R. Serber, “Nuclear reactions at high energies,” *Phys. Rev.* 72; 1114–1115, (1947).
- [4] J. Hüfner, K. Schäfer, B. Schürmann, “Abrasion-ablation in reactions between relativistic heavy ions,” *Phys. Rev. C* 12, 1888 (1975).
- [5] N. Matsufuji, A. Fukumura, M. Komori et al. “Influence of fragment reaction of relativistic heavy charged particles on heavy-ion radiotherapy,” *Phys. Med. Biol.*, 48. 1605-1623, (2003).
- [6] N. Matsufuji, T. Kanai, N. Kanematsu, T. Miyamoto, M. Baba, T. Kamada, H. Kato, S. Yamada, J. Mizoe and H. Tsujii, “Specification of Carbon Ion Dose at the National Institute of Radiological Sciences (NIRS),” *J. Radiat. Res.* 48; Suppl. A:A81-6 (2007).
- [7] M. De Napoli et al., “Carbon fragmentation measurements and validation of the Geant4 nuclear reaction models for hadrontherapy,” *Phys. Med. Biol.* 57, 7651-7671 (2012).
- [8] M. Toppi et al., “Measurements of  $^{12}\text{C}$  ion fragmentation on thin carbon target from the FIRST collaboration at GSI,” *Jour. Phys. Conference Series* 590, 012035 (2015).

## 27 Measurement of Neutron Energy Spectra of 345 MeV/u $^{238}\text{U}$ Incidence on a Copper Target

Kenta SUGIHARA<sup>1,2</sup>, Nobuhiro SHIGYO<sup>1</sup>, Atsuko AKASHIO<sup>2</sup> and Kanenobu TANAKA<sup>2</sup>

1. *Department Applied Quantum Physics and Nuclear Engineering, Kyushu University  
Motooka, Nishi-ku, Fukuoka, 819-0395, Japan*

2. *RIKEN Nishina Center, RIKEN, 2-1 Hirosawa, Wako, Saitama 351-0198, Japan*  
e-mail: k.sugihara@kune2a.nucl.kyushu-u.ac.jp

Thick target neutron yields produced by 345 MeV/u  $^{238}\text{U}$  incidence on a copper target were measured at 45° and 90° with the time-of-flight method. The experimental results were compared with those calculated using the JAERI Quantum Molecular Dynamics (JQMD) model ver.1.0 followed by Generalized Evaporation Model implemented in PHITS ver.3.10. It was demonstrated that the JQMD model underestimates measured data.

### 1 Introduction

Radioactive Isotope Beam Factory (RIBF) at RIKEN is an accelerator facility[1]. RIBF has an ability to accelerate heavy ions (e.g. Ca, Kr, Xe, U) up to 345 MeV/u through superconducting ring cyclotron (SRC). It is in progress to conduct a lot of researches with the utilization of Radioactive Isotope (RI) beams which are generated by reactions between primary beams and RI generating targets. A number of neutrons are produced at the target and a beam dump. Therefore, areas around the target and the beam dump is a high dose rate region.

Radiation shielding around the high dose rate area was basically designed by the Moyer model[2]. As a source term of the model, neutron thick target yield (TTY) by 345 MeV/u  $^{238}\text{U}$  beam is essential. There is an available data of TTY for 1 GeV/u  $^{238}\text{U}$  incidence on iron measured at Gesellschaft für Schwerionenforschung (GSI)[3]. Neutron energy spectra for forward directions were measured in the study. As RIBF is located in the underground, measured data for side directions are of great importance. There is no measured data of TTY from 345 MeV/u  $^{238}\text{U}$  incidence on copper, which is beam dump material at RIBF.

Particle transport code PHITS[4] has been recently applied for radiation shielding design. Measured data for examining the accuracy of physics models in the code is not sufficient. Experimental data of neutron TTY is highly desired for verifying neutron emissions to optimize radiation shielding design.

In this study, neutron TTYs at 45° and 90° were measured from 345 MeV/u  $^{238}\text{U}$  incidence on copper. Simulation TTYs are calculated by JAERI Quantum Molecular Dynamics (JQMD)[5] model ver.1.0 followed by Generalized Evaporation Model[6] implemented in PHITS ver.3.10. These TTYs are compared to validate how accurate the physics model is.

### 2 Experiment

The experiment was carried out at Zero Degree Spectrometer of RIBF. The experimental arrangement is illustrated in Figure 1.

The incident energy of  $^{238}\text{U}$  beam was 345 MeV/u. The beam intensity was about  $10^6$  pps. As radio frequency (RF) of SRC was 18.5 MHz, the beam pulse came every 54 ns. A copper target with a thickness of 10 mm was positioned at the F10 chamber. The target was three times as thick as the range of the  $^{238}\text{U}$  beam.

Neutrons produced in the target were measured with NE213 liquid organic scintillators. The light output of the scintillators was recorded by charge sensitive analog-to-digital converters (ADCs). The timing of incident particles on the detectors was registered in a time-to-digital converter (TDC). The

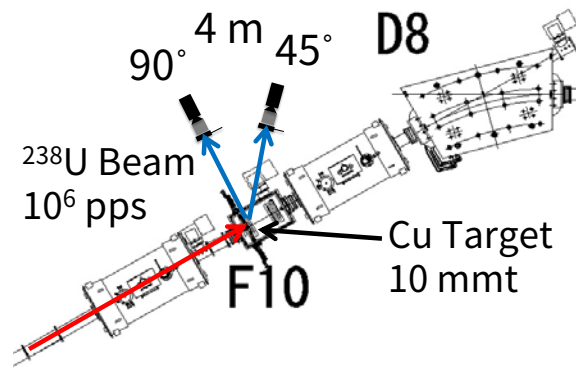


Figure 1 Illustration of the experimental setup for the TOF measurement.  $345 \text{ MeV/u } ^{238}\text{U}$  beam irradiated a copper target. Neutron and veto detectors were located at  $45^\circ$  and  $90^\circ$  from the beam axis. Both flight path lengths were 4.0 m.

neutron detectors were located at  $45^\circ$  and  $90^\circ$  with respect to the beam axis. Both the diameter and length of the detectors are 12.7 cm. The flight path lengths from the target to each neutron detector were 4.0 m as shown in Figure 1. Kinetic energies of detected neutrons were determined by the inverse time-of-flight (TOF) method[7]. Start and stop signals came from neutron detectors and RF signals of SRC, respectively. Energies of neutrons overlapped with preceding beam pulse were less than 17.6 MeV. The threshold level in the analysis was set to 12.3 MeVee which was two times higher than the Compton edge of 6.13 MeV  $\gamma$ -ray from a  $^{244}\text{Cm}$ - $^{13}\text{C}$  neutron source. This corresponds to the maximum light output of 18.4 MeV neutron. These low energy neutrons were automatically removed in data analysis because their pulse heights were smaller than the bias level. To eliminate charged particle events from total events, an NE102A plastic scintillator of 2 mm in thickness (veto detector) was used in front of each neutron detector.

The background neutrons scattered from the floor were measured by an iron shadow bar of 1 m long, which was installed between the F10 chamber and each neutron detector.

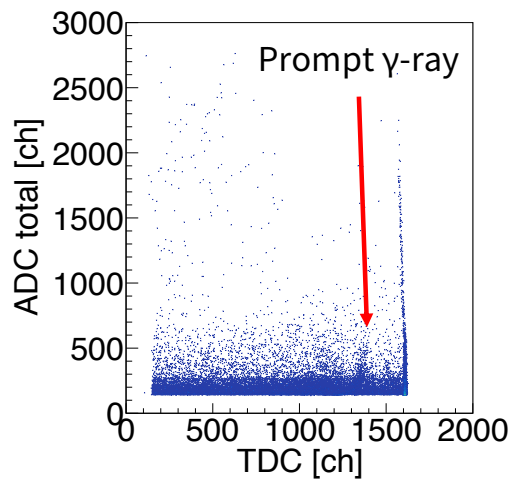


Figure 2 TDC-ADC two-dimensional plot for the NE213 scintillator at  $90^\circ$ . Prompt  $\gamma$ -rays appear about 1400 ch. Slow neutrons, the channel of which was less than about 160 ch, were not measured due to the RF frequency. Therefore, the maximum time difference between neutrons and prompt  $\gamma$ -rays was 34 ns because the time resolution of TDC was 0.0274 [ns/ch].

### 3 Analysis

Neutron energy spectra were derived from the flight time and data of pulse height distribution of the neutron detectors[7]. Neutron events were identified with the two gate integration method[8]. After neutron events were extracted, kinetic energies of the neutrons were obtained from the time difference between the neutrons and prompt  $\gamma$ -rays in Figure 2. Neutron detection efficiency was calculated by the SCINFUL-QMD code[9][10]. Finally, measured data were converted into neutron production TTYs.

### 4 Results and Discussion

The measured data of neutron TTYs were compared with the JQMD model ver.1.0 implemented in PHITS ver.3.10. The measured and calculated neutron TTYs for 345 MeV/u  $^{238}\text{U}$  bombardment on copper are shown in Figure 3. Only statistical error in the measured data was included in Figure 3.

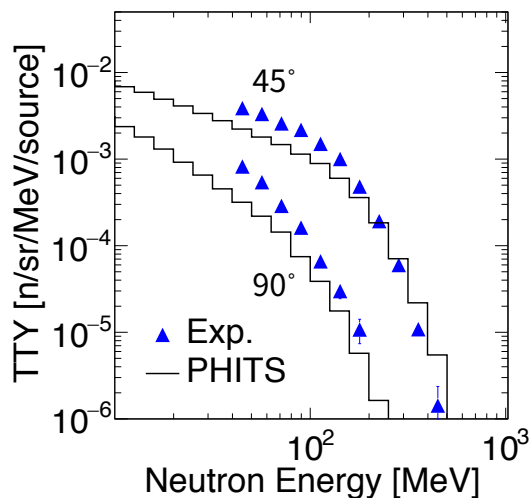


Figure 3 Neutron TTYs from 345 MeV/u  $^{238}\text{U}$  incidence on copper. Blue triangles and black solid lines represent the experimental data and the results of PHITS calculation using JQMD ver.1.0 model, respectively.

Integral of the experimental and calculated energy spectra above 40 MeV is shown in Table 1. Statistical errors are less than 1 % for both the experiment and PHITS calculation. According to Table 1, the number of produced neutrons for PHITS was 0.61 time as large as that of our experimental data at 45°. The ratio for 90° was 0.44.

Table 1 Angular distribution of neutron production integrating neutron energy spectrum above 40 MeV.

	45° [n/sr/source]	90° [n/sr/source]
Exp.	$2.8 \times 10^{-1}$	$2.7 \times 10^{-2}$
PHITS	$1.7 \times 10^{-1}$	$1.2 \times 10^{-2}$

### 5 Conclusion

Neutron TTYs at 45° and 90° were measured from 345 MeV/u  $^{238}\text{U}$  incidence on a copper target with the TOF method. The PHITS calculations underestimate the measured data. The experimental data will be useful for the estimation of the source term in the Moyer model.

## 6 Acknowledgement

This experiment was performed at RI Beam Factory operated by RIKEN Nishina Center and CNS, the University of Tokyo. The PHITS calculation was performed using the supercomputer system of RIKEN.

## References

- [1] K. Tanaka, N. Inabe, K. Yoshida *et al.* Evaluation of radiation levels and comparison with PHITS calculations for the BigRIPS separator in Radioactive Isotope Beam Factory. *Prog. in Nucl. Sci. Technol.* 2014;4:201-204.
- [2] B. J. Moyer. Method of Calculation of the Shielding Enclosure for the Berkeley Bevatron. in *Proc. 1st Int. Conf. Shielding around High Energy Accelerators*, Presses Universitaires de France, Paris 1962;65.
- [3] O. Yordanov, K. Gunzert-Marx, P. Adrich *et al.* Neutron yields from 1 GeV/nucleon  $^{238}\text{U}$  ion beams on Fe target. *Nucl. Instr. Methods B.* 2005;240:863-870.
- [4] T. Sato, Y. Iwamoto, S. Hashimoto *et al.* Features of Particle and Heavy Ion Transport code System (PHITS) version 3.02. *J. Nucl. Sci. Technol.* 2018;55:684-690.
- [5] K. Niita, S. Chiba, T. Maruyama *et al.* Analysis of the (N, xN') reactions by quantum molecular dynamics plus statistical decay model. *Phys. Rev. C.* 1995;52(2620):2620-2635.
- [6] S. Furihata. Statistical analysis of light fragment production from medium energy proton-induced reactions. *Nucl. Instr. Methods, B.* 2000;171:251-258.
- [7] D. Satoh, D. Moriguchi, T. Kajimoto *et al.* Measurement of neutron-production double-differential cross-sections on carbon bombarded with 290-MeV/nucleon carbon and oxygen ions. *Nucl. Instr. Methods A.* 2011;644:59-67.
- [8] M. Moszynski, G.J. Costa, G. Guillaume *et al.* Identification of different reaction channels of high energy neutrons in liquid scintillators by the pulse shape discrimination method. *Nucl. Instr. Methods, A.* 1994;343:563.
- [9] D. Satoh, S. Kunieda, Y. Iwamoto *et al.* Development of SCINFUL-QMD code to calculate the neutron detection efficiencies for liquid organic scintillator up to 3 GeV. *J. Nucl. Sci. Technol.* 2002;39(sup2):657-660.
- [10] T. Kajimoto, N. Shigyo, T. Sanami *et al.* Measurement of absolute response functions and detection efficiencies of an NE213 scintillator up to 600 MeV. *Nucl. Instr. Methods A.* 2011;665:80-89.

## 28 Measurement of the energy spectra of hydrogen isotopes from nuclear muon capture in $^{nat}\text{Si}$

Seiya MANABE<sup>1</sup>, Yukinobu WATANABE<sup>1</sup>, Takumi MAHARA<sup>1</sup>, Keita NAKANO<sup>1</sup>, Takeshi Y. SAITO<sup>2</sup>, Megumi NIIKURA<sup>2</sup>, Daisuke SUZUKI<sup>3</sup>, Yoshitaka KAWASHIMA<sup>4</sup>, Dai TOMONO<sup>4</sup>, Akira SATO<sup>4,5</sup>

<sup>1</sup>*Department of Advanced Energy Engineering Science, Kyushu University, Kasuga 816-0811, Japan*

<sup>2</sup>*Department of Physics, the University of Tokyo, Hongo 113-0033, Japan*

<sup>3</sup>*Nishina Center for Accelerator-Based Science, RIKEN, Wako 351-0198, Japan*

<sup>4</sup>*Research Center for Nuclear Physics (RCNP), Osaka University, Suita 567-0047, Japan*

<sup>5</sup>*Department of Physics, Osaka University, Toyonaka 560-0043, Japan*

e-mail: manabe@aees.kyushu-u.ac.jp

We have measured the energy spectra of protons and deuterons generated via the nuclear muon capture reaction on Si. The experiment was performed using the M1 beam line of Muon Science Innovative muon beam Channel (MuSIC) at Research Center for Nuclear Physics (RCNP), Osaka University. A 100- $\mu\text{m}$  thick silicon target was irradiated by the negative muon beam and the emitted protons and deuterons from the Si target were successfully measured by using a  $\Delta\text{E}$ -E telescope that consists of a 325- $\mu\text{m}$  thick silicon detector ( $\Delta\text{E}$ ) and a 25-mm thick CsI(Tl) detector (E). The measured spectra are preliminarily compared with those calculated by the particle and heavy ion transport code system (PHITS).

### 1. Introduction

Soft errors induced by cosmic ray have been recognized as a major threat for the electronics used at the ground level. The soft error is caused by an upset of the memory information induced by the energy deposition in devices by energetic ionizing radiation. Recently, cosmic-ray muon-induced soft errors have attracted much attention due to the reduction of soft error immunity on static random access memories. Our previous work [1],[2] reported that the negative muon has much more serious effect on the occurrence of SEUs compared to the positive one because of the emission of ions from nuclear muon capture in Si. Moreover, it was pointed out that helium ions, namely alpha particles have a predominant contribution to SEUs among all particle and ion species.

Figure 1 shows a schematic illustration of the physical process of the nuclear muon capture in  $^{28}\text{Si}$ . After losing incident kinetic energy and stopping in  $^{28}\text{Si}$ , the negative muon is captured by the atom into high orbital momentum states, forming a muonic atom. The captured muon cascades down to the 1-s orbit while emitting characteristic X-rays. Approximately 35% of the captured negative muons decay into an electron and two neutrinos in the 1-s orbital. The remaining negative muons are finally absorbed by the nucleus, and highly excited nuclei are formed. Then, the nucleus is deexcited by emission of neutrinos, photons, neutrons, and other light ions [3]. Thus, the capture reaction generates a heavy recoiling nucleus with simultaneous emission of secondary light ions (protons, deuterons,  $\alpha$ -particles, etc.).

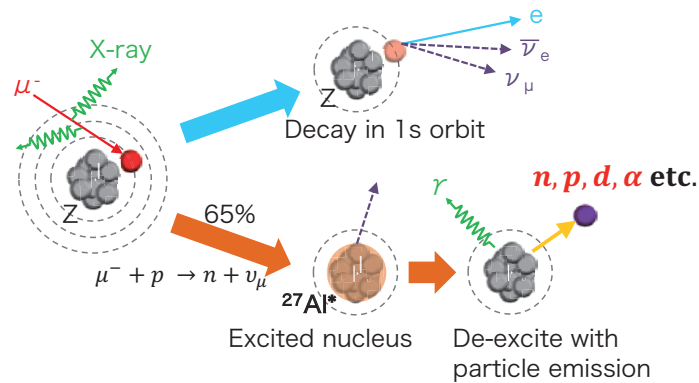


Figure 1: Physical process of the nuclear muon capture reaction on  $^{28}\text{Si}$ .

S. Sobottka and E. Wills have conducted the experiment to investigate the energy spectra of these ions [4]. A Si(Li) detector was irradiated by a muon beam and a spectrum of the energy deposition by the light ions and recoiling nucleus in the detector was measured. As a result, they suggested that the charged-particle emission probability per muon capture is  $0.15 \pm 0.02$ . The particle identification (PID) of the emitted ion was not performed in the experiment. Hence, the energy spectra of the individual light ions species have not been measured so far. Therefore, there is an uncertainty in the estimation of the muon-induced soft error rate. Under these circumstances, we have performed a new measurement of the energy spectra of light ions emitted from the nuclear muon capture in Si.

## 2. Experimental method

The experiment was conducted in the M1 muon beam line of RCNP-MuSIC. The facility produced pions through nuclear reaction between a 392-MeV proton beam and a graphite target. The produced pions almost decay into muons in a superconducting solenoid magnet and the decayed muons are transported downstream to the beam exit. During the experiment, the K400 ring cyclotron was operated with the average current of  $1.1 \mu\text{A}$ .

Figure 2 shows the experimental setup placed in the M1 beam line. A vacuum chamber was connected to the beam exit. Two 100- $\mu\text{m}$  thick Si targets were mounted at the center of the chamber at an angle of  $45^\circ$  to the beam direction. The size of the target is  $5 \text{ cm} \times 5 \text{ cm}$ . The targets were irradiated by the muon beam with the average momentum of  $36 \text{ MeV}/c$ . Two forward plastic scintillators (PSs) with the size of  $5 \text{ cm} \times 7 \text{ cm} \times 0.5 \text{ cm}^t$  were set to count the number of incident muons. Another PS for veto counting was placed to detect muons passing through the targets. Two telescopes were mounted parallelly to the targets at both the upstream and downstream of the targets to detect the secondary ions and measure their kinetic energy. The distance between the targets and telescopes was 15 cm. The telescope consists of a 325- $\mu\text{m}$  thick silicon detector ( $\Delta E$ ) and a 25-mm thick CsI(Tl) detector (E).

During the experiment, the coincidence event of the upstream PSs was set to be the trigger of the data acquisition (DAQ) system. The signals from individual detectors were amplified and shaped by shaping amplifiers for the pulse height measurement. The outputs from the amplifiers were fed into an analog-to digital converter (ADC). Thus, the energy deposition in each detector was measured during the experiment.

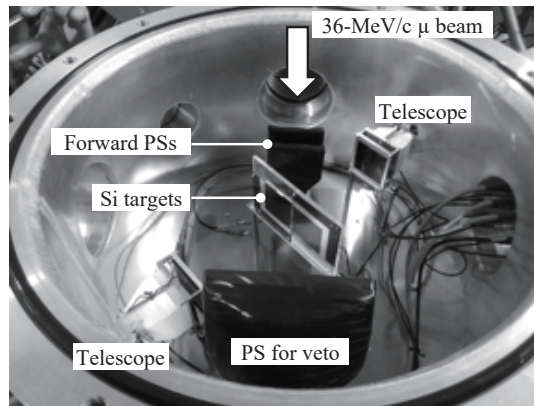


Figure 2: A picture of the experimental setup.

### 3. Experimental result

The PID was performed event by event by a conventional  $\Delta E$ -E method using the energy loss ( $\Delta E$ ) in the 325- $\mu\text{m}$  thick Si detector ( $\Delta E$ ) and the total energy (E) that is obtained by the sum of  $\Delta E$  and the deposition energy in the 25-mm CsI detector. Figure 3 shows a two-dimensional event plot of  $\Delta E$  versus total energy E. The PID was successfully achieved and each hydrogen isotope is clearly separated. The total event numbers of protons and deuterons were approximately 2400 and 800 during the 26-hour irradiation time, respectively. Figure 4 shows the measured energy spectra of proton and deuteron. The vertical axis in Fig. 4 represents the number of events observed during the experiment. The absolute values of the emission probabilities are now under analysis.

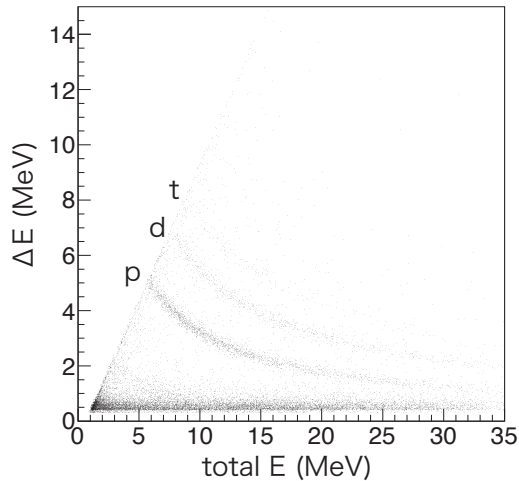


Figure 3: Energy loss in the silicon detector versus total energy obtained from silicon and CsI detectors.

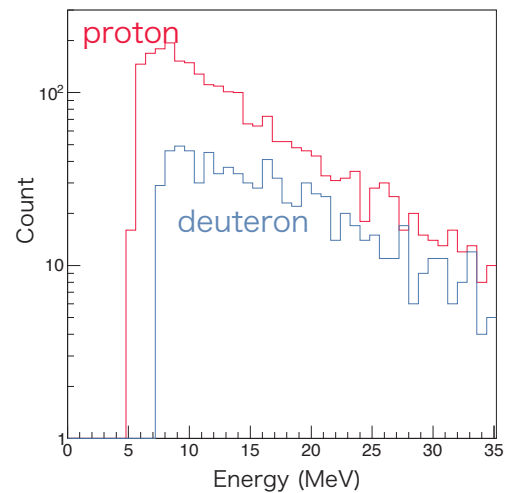
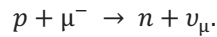


Figure 4: The energy spectra of proton and deuteron emitted from nuclear muon capture in  $^{nat}\text{Si}$ .

### 4. Comparison with the PHITS calculation

The PHITS code can calculate the energy spectra of particles emitted from the nuclear muon capture reaction. In the PHITS calculation [5], a proton in the nucleus is randomly selected and converted to a neutron to simulate the elementary process:



The energy that corresponds to the mass of muon is distributed to the neutron and the muon neutrino. Then, the time evolution of all nucleons inside the nucleus is simulated by JQMD (JAERI quantum molecular dynamics) [6] and a few fast nucleons and/ or light cluster ions (d, t, alpha, etc.) are emitted via this dynamical process. The subsequent evaporation process is calculated by GEM (generalized evaporation model) [7]. The details of the calculation are described in [5].

Figure 5 shows the calculated energy spectra of protons and deuterons from the nuclear capture reaction on  $^{nat}\text{Si}$ . Currently, we cannot make a direct comparison of the yields of the proton and deuteron between the calculated spectra and the experimental ones shown in Fig. 4, because the absolute value of the emission probability has not yet been determined for the experimental data. Hence, the yield ratios of proton to deuteron in the energy range from 7 to 35 MeV are compared between both the calculation and measurement. The calculated ratio is 29:1, while the experimental one is 3:1. Thus, we found a large inconsistency between the simulation and experiment with respect to the yield ratios of proton to deuteron.

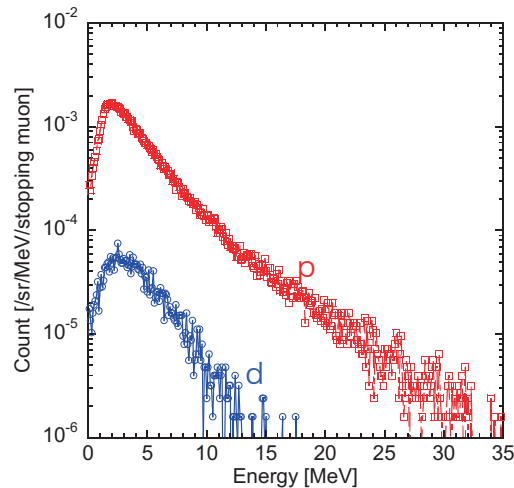


Figure 5: The calculated energy spectra of proton and deuteron by PHITS.

## 5. Summary and future plan

The energy spectra of protons and deuterons emitted from the nuclear muon capture reaction were successfully measured by using the  $\Delta E$  (325- $\mu\text{m}$  thick silicon)- $E$  (25-mm thick CsI) telescope. In addition to the measurement, we performed the preliminary comparison of the yield ratios of proton to deuteron in the energy range from 7 to 35 MeV with the result calculated by PHITS, and found that there is a large discrepancy between the simulation and experiment. For more quantitative comparison with the simulation and the estimation of muon-induced soft error rates based on this measurement, it will be necessary to determine the absolute value of the measured energy spectra. Moreover, we plan to measure the energy spectrum of alpha-particle that is expected to have the most crucial effect on negative muon induced single-event upsets as suggested in [1].

### **Acknowledgement**

This work was supported by JST-OPERA Program Grant Number JPMJOP172, JAPAN, Grant-in-Aid for Scientific Research (B) (No.16H03906) and JSPS Fellows (No.19J12649) from the Japan Society for the Promotion of Science (JSPS) and Kyushu University Platform of Inter/Transdisciplinary Energy Research (Q-PIT).

### **References**

- [1] S. Manabe et al., IEEE Trans. Nucl. Sci., 65:8, 1742-1749 (2018).
- [2] W. Liao et al., IEEE Trans. Nucl. Sci., 65:8, 1734-1741 (2018).
- [3] D. F. Measday, Phys. Rep., 354, 243-409 (2001).
- [4] S. E. Sobottka et al., Phys. Rev. Lett., 20:12, 596-598 (1968).
- [5] S. Abe et al., J. Nucl. Sci. Technol., 54:1, 101-110 (2016).
- [6] K. Niita et al., Phys. Rev. C, 52:26, 2620-2635 (1995).
- [7] S. Furihata et al., Japan Atomic Energy Research Institute; 2001. (JAERI-Data/Code 2001-015).

This is a blank page.

## 29 Detailed examination of benchmark method for large angle scattering reaction cross section at 14MeV for a flake target

Kazuki FUKUI, Atsuki YAMAGUCHI, Yuki FUJIWARA, Shingo TAMAKI,

Sachie KUSAKA, Fuminobu SATO, Isao MURATA

*Graduate School of Engineering, Osaka University,  
Yamada-oka 2-1, Suita, Osaka 565-0871, Japan  
e-mail: fukui@qr.see.eng.osaka-u.ac.jp*

Large angle scattering reaction cross sections are crucial in neutronics design of a fusion reactor. However, there are differences observed in the large angle elastic scattering reaction cross section among different nuclear data libraries. In order to confirm the cross section accuracy, the authors' research group developed a benchmark method focusing on the large angle scattering reaction cross section. And the first benchmark experiment was conducted on iron, the most important fusion material, at a DT neutron source facility, OKTAVIAN, of Osaka University, Japan. In this benchmark experiment, the target was a lump of iron. However, it is expected that in future flake targets should be used especially, for example, light materials. In the present study, we examine the benchmark method to be able rigorously to treat a flake target. In the case of a flake target, we need to additionally consider a container and lid for flakes. We finally found that the same process of the massive sample case could be used, that is, conducting four experiments to extract only the contribution of neutrons scattered at large angles by the target correctly. In the next step, we will carry out a benchmark experiment for silicon with the present benchmark method.

### 1. Introduction

Reaction cross section data of back scattering are normally not focused on in fusion reactor design, because the reaction cross section of large angle elastic scattering is much smaller than that of forward scattering especially when the energy of incident neutrons is as high as fusion neutron. However, in the case of the gap streaming phenomenon around the blanket of ITER, the reaction cross section value of large angle scattering may have a large effect on the design calculation results.

For instance, the elastic scattering reaction cross sections of  $^{56}\text{Fe}$  at 14 MeV, which is the

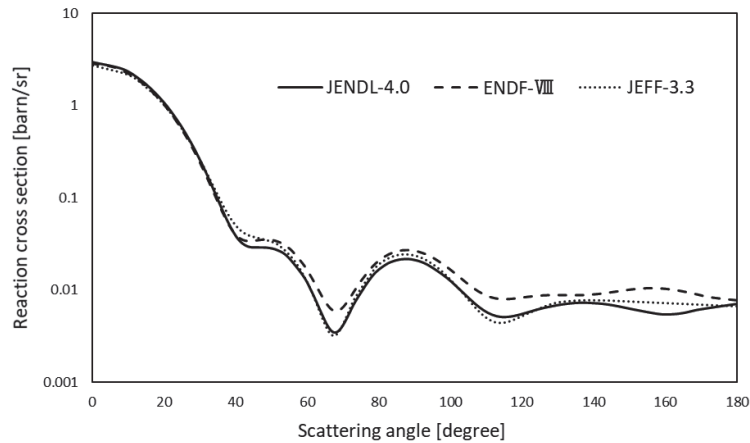


**Fig. 1. 14 MeV neutron elastic scattering angular distribution of iron.**

most important fusion material, vary for large angle elastic scattering among nuclear data libraries as shown in Fig. 1. For improvement of the cross section, previously, there were measurements of double differential cross sections of secondary neutrons at 14 MeV [1]. It also contained the angular differential cross section. However, such measurements are technically difficult, because the large angle elastic scattering reaction cross section is very small as shown in Fig. 1, so that there were very few experimental approaches reported so far to directly measure or benchmark large angle scattered neutrons.

For the last few years, the benchmark method was proposed by the group of authors to test large angle scattering reaction cross sections, which was an integral experiment with an activation foil of niobium to cover wide scattering angles. Using the experimental method, a benchmark experiment of iron was performed in a previous study [2]. In the present study, we try to benchmark silicon in SiC that would be a candidate material for the first wall. However, it is difficult to prepare a large massive sample of silicon. We thus need to cope with flake silicon sample. In future, for benchmarking of other materials like light elements, we expect that benchmarks should be performed using flaky targets. In the present study we hence investigate in the exact benchmark method for flaky targets by the numerical analysis.

## 2. Previous Study

Figure 2 shows the experimental system of the benchmark method for iron, which was proposed in the previous study [2]. This experimental system consists of a DT neutron source, an iron shadow bar, a cylindrical iron target plate and Nb foil as a neutron detector. The shadow bar plays a role in blocking neutrons from directly entering the detection foil. The shadow bar is made of iron and has a truncated cone shape. The distance between the shadow bar and target plate is 1 cm. If the target plate thickness is appropriate, the neutrons incident on the target plate will have at

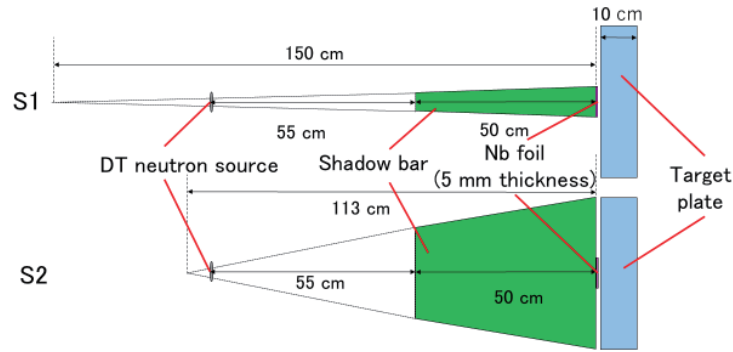


Fig. 2. Iron benchmark experiment system.

most one scattering. If the scattering is forward, neutrons can pass through the target plate after the scattering. And if it is a back scattering, neutrons can enter the detection foil directly without another scattering. Therefore, the Nb foil can detect only large angle elastic scattering neutrons from the target plate. However, the irradiation room used for this experiment is not so large and surrounded by a 1 m thick shielding wall. So it is necessary to consider the contribution of neutrons scattered in the wall, so-called room return neutrons. Therefore, we use two types of shadow bars having different shapes represented by S1 and S2 as in Fig. 2.

The narrow shadow bar of S1 is 50cm, 2cm in diameter at the top, 3cm in diameter at the bottom and measures all neutron contributions except direct incidence on the target plate through the shadow bar. On the other hand, the thick shadow bar of S2 has a length of 50cm, a top diameter of 8.3cm, and a bottom diameter of 15cm. The diameter of the target plate is set so as to be equal to the bottom diameter of the shadow bar. Therefore, the contribution of neutrons that are directly incident on the target and back-scattered in the target plate is removed, and only the contribution of neutrons from the surrounding wall is measured. The dimensions in Fig. 2 were optimized by parameter survey calculations using MCNP-5 [3]. Then, four types of experiments, TC with the target and C without the target, using these two types of shadow bars are performed as shown in Fig. 3.

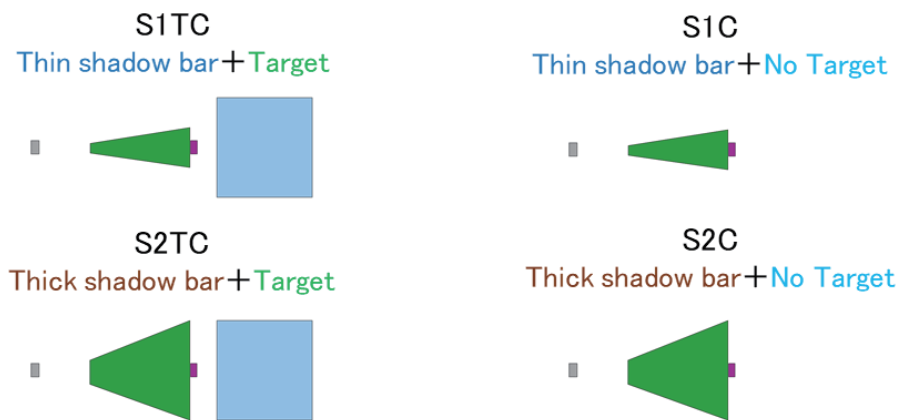


Fig. 3. Four types of iron benchmark experiments.

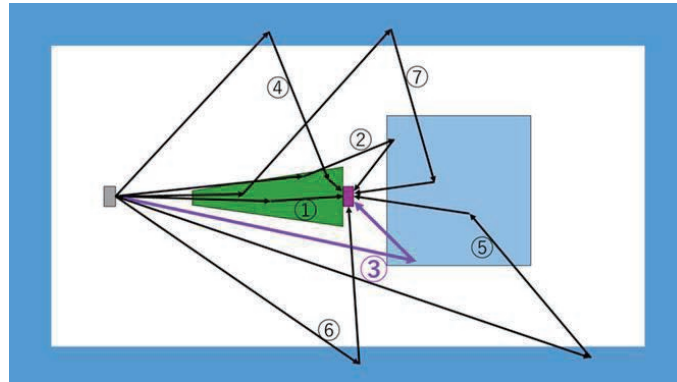


Fig. 4. Neutron path at iron target.

In the iron benchmark experiment, we carried out neutron transport path analysis with MCNP-5 in advance. In the analysis, three cells should be considered, that can be passed by neutrons, i.e., shadow bars, walls, and targets. As paths through which neutrons pass, seven paths ( $=_3C_1+_3C_2+_3C_3$ ) in total should be taken into account as shown in Fig. 4. Out of these seven paths, path ③ is the path of large angle scattering neutrons that we want to measure. Clearly the contribution of path ③ appears only in the S1TC experimental system. By performing the four experiments shown in Fig. 3, the contribution of neutron paths other than path ③ can be estimated and removed. Practically, by substituting the total reaction rate of niobium for each experiment into the following equation (1), the contribution of neutrons other than path ③ is canceled out, and only the contribution of path ③ can be extracted.

$$\text{Path } \textcircled{3} = (\text{S1TC}) - (\text{S1C}) - ((\text{S2TC}) - (\text{S2C})) \cdot \cdot \cdot (1)$$

### 3. Experimental System for Flake Target

In the case of a flake-form silicon target, a container for containing the flakes and its lid are required. The container is made of iron and the lid is made of aluminum, and both are 1 mm thick. The target thickness is 28 cm including the container and lid. Fig. 5 shows the experimental system when a container and a lid are added. The red part facing the Nb foil is the lid. Experimental conditions other than the container and lid, such as the neutron source and shadow bar, are the

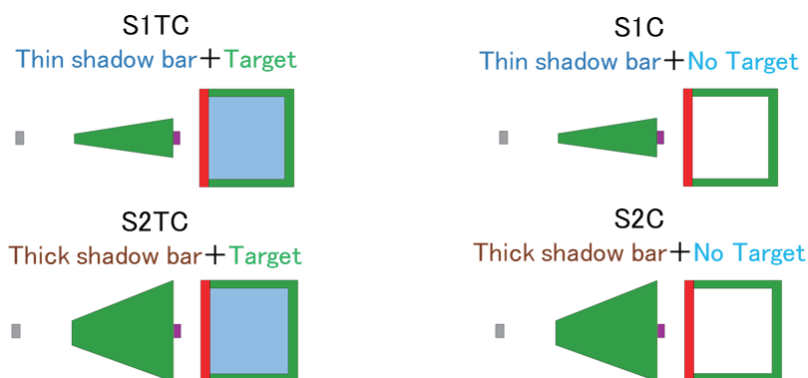


Fig. 5. Four types of benchmark experiments for flake silicon targets

same as those for the iron system. In the calculation, it was assumed that silicon was uniformly packed with the density, which was estimated as a bulk density measured after packing silicon flakes into the container.

In this experimental system, cells that can be passed through by neutrons are the shadow bar, the wall, the target, and in addition, the container and its lid. Initially, we considered that there were 31 paths mathematically calculated by  ${}_5C_1+{}_5C_2+{}_5C_3+{}_5C_4+{}_5C_5$  as transporting paths through which neutrons passed. However, it was found that there were 12 paths where neutrons could not physically pass. For example, a path does not exist, in which a neutron enters the detection foil via the target plate without passing through the lid. Therefore, we removed such paths and finally considered 19 paths (31-12) through which neutrons can pass. Figure 6 shows all the 19 paths. Among the 19 paths, path ⑥ is the path of large angle scattering neutrons that we want to measure.

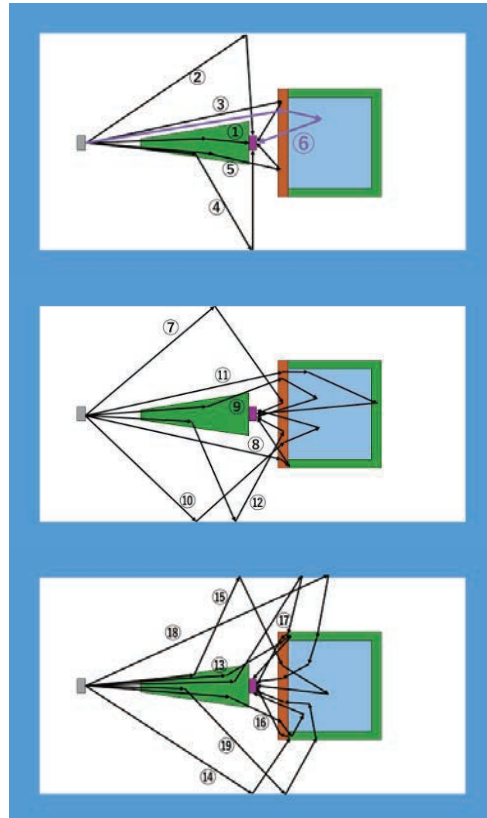


Fig. 6. Neutron pathways for flaky silicon targets.

#### 4. Numerical Simulation Result

Table 1 shows the results of MCNP-5 simulation of the four experimental systems shown in Fig. 5 using the nuclear data library of JENDL-4.0 [4]. In most routes, there are two pairs

Table 1. Reaction rate of 19 paths in simulation of each experimental system  
[unit:  $10^{-9}$  reaction/source neutron].

	S1TC	S1C	S2TC	S2C	S1TC-S1C-(S2TC-S2C)
①	0.02	0.02	0.13	0.13	0.00
②	0.79	0.79	0.25	0.25	0.00
③	0.24	0.24	0	0	0.00
④	1.09	1.09	0.67	0.67	0.00
⑤	0.01	0.01	0.00	0.00	0.00
⑥	3.82	0	0	0	3.82
⑦	0.04	0.04	0.04	0.04	0.00
⑧	0.00	0.00	0	0	0.00
⑨	0.07	0	0.00	0	0.07
⑩	0.01	0.00	0.00	0.00	0.01
⑪	0.10	0.16	0	0	-0.06
⑫	0.00	0.00	0.00	0.00	0.00
⑬	0.00	0.00	0	0	0.00
⑭	0.00	0.00	0.00	0.00	0.00
⑮	0.00	0	0.00	0	0.00
⑯	0.00	0.00	0.00	0	0.00
⑰	0.00	0.00	0.00	0.00	0.00
⑱	2.05	3.08	2.03	3.02	-0.04
⑲	0.02	0.01	0.04	0.05	0.02
Total number of reaction	$8.26 \pm 0.06$	$5.44 \pm 0.06$	$3.16 \pm 0.05$	$4.16 \pm 0.05$	$3.82 \pm 0.12$

observed. For example, in path ①, reaction rates of S1TC and S1C are the same to become a pair, and S2TC and S2C are also in pair. In addition, it can be seen that the neutron contribution of path ⑥ only appears in the experimental system of S1TC.

The bottom values for columns S1TC, S1C, S2TC and S2C are the sum of reaction rates in 19 paths and correspond to obtained reaction rates in the four experiments. By substituting these four reaction rates into equation (1), the value of "3.82" is deduced, which is exactly the same as the reaction rate of the route ⑥. Consequently, this result proves that the present benchmark method of the large angle scattering cross section could be utilized even in the case of a flake target.

## 5. Conclusion

In this study, the benchmark experiment method for large angle elastic scattering reaction cross section using flake target was numerically investigated. MCNP-5 simulations by setting flags to five cells including shadow bar, wall, target plate, and in addition, container and lid, we successfully extract the contribution of large angle scattering neutrons with a simple equation in Eq. (1) with four experimental reaction rates. It can thus be concluded that the present benchmark technique could be used even with a flake silicon target. In the future, we will conduct experiments various samples including silicon and discuss the practical feedback method from the experimental results to the nuclear data library.

## Acknowledgment

The authors would like to express their sincere gratitude to Dr. Seiki Ohnishi for his warm support on numerical analysis with ptrac option in MCNP.

## References

- [1] A. Takahashi, E. Ichimura, Y. Sasaki, H. Sugimoto, "Double and Single Differential Neutron Emission Cross Sections at 14.1 MeV: Vol. 1", OKTAVIAN Report A-87-03, 385p (1987), A. Takahashi, M. Gotoh, Y. Sasaki, H. Sugimoto, "Double and Single Differential Neutron Emission Cross Sections at 14.1 MeV: Vol. 2", OKTAVIAN Report A-92-01, 577p (1992).
- [2] N. Hayashi et al. , "Optimization of Experimental System Design for Benchmarking of Large Angle Scattering Reaction Cross Section at 14 MeV Using Two Shadow Bars", Plasma and Fusion Research, 13,2405002, 4p (2018).
- [3] MCNP Team, "MCNP5-1.40 RSICC Release Notes", LA-UR-05-8617 (2005).
- [4] K. Shibata, O. Iwamoto, T. Nakagawa, N. Iwamoto, A. Ichihara, S. Kunieda, S. Chiba, K. Furutaka, N. Otuka, T. Ohsawa, T. Murata, H. Matsunobu, A. Zukeran, S. Kamada, and J. Katakura, "JENDL-4.0: A New Library for Nuclear Science and Engineering", J. Nucl. Sci. Technol. 48(1), 1-30 (2011).

# 30 Integration test with a Gaseous Detector and a Solenoidal Magnet for the Precise Neutron Lifetime Measurement

Kodai YANO<sup>1\*</sup>, Yasuhiro MAKIDA<sup>2</sup>, So MAKISE<sup>1</sup>, Kenji MISHIMA<sup>2</sup>, Hidetoshi OTONO<sup>3</sup>,  
Naoyuki SUMI<sup>1</sup> and Tamaki YOSHIOKA<sup>3</sup>

<sup>1</sup>*Department of Physics, Kyushu University, Fukuoka 819-0395, Japan*

<sup>2</sup>*KEK, High Energy Accelerator Research Organization, Tsukuba 305-0801, Japan*

<sup>3</sup>*Research Center for Advanced Particle Physics (RCAPP), Kyushu University, Fukuoka 819-0395, Japan*

*E-mail: yano@epp.phys.kyushu-u.ac.jp*

The neutron lifetime ( $\tau_n$ ) is an important parameter for particle physics and cosmology. The neutron lifetime was measured by two major methods. One of them is called the bottle method, and the other one is called beam method. Though, there is an 8.6 sec ( $4.0\sigma$ ) deviation between these two measured results. To solve this problem, a new type of method, the electron counting method, is implemented at BL05 MLF J-PARC using a pulsed cold neutron beam to measure the true neutron lifetime with the same or better accuracy than the previous measurement. A Time Projection Chamber (TPC) records both the electrons from neutron  $\beta$  decay and protons from the  $^3\text{He}$  neutron capture reactions to estimate the neutron flux that enters the TPC. However, electron background signals require the largest correction and they are the source of uncertainty for this experiment. It is confirmed by Monte Carlo simulation that a uniform magnetic field generated by a solenoidal magnet along the neutron beam can greatly reduce this background. Hence, we proposed another experiment (LiNA experiment) using a solenoidal magnet to validate this simulation result. The detector has been produced and the integration test with a magnet has been finished. The status of progress is reported in this paper.

**KEYWORDS:** neutron lifetime, time projection chamber, solenoidal coil

## 1. Introduction

### 1.1 Motivation

The neutron lifetime is one of the most important parameters for Big Band Nucleosynthesis (BBN). The light elements, such as helium and lithium, were produced by a combination of neutrons and protons. Therefore, the number of light elements produced in the early universe depends on the number of neutrons that are left. Moreover, since neutron decays have the advantage of no nuclear physics uncertainties, neutron lifetime is also an important parameter for the Cabibbo-Kobayashi-Maskawa (CKM) matrix element  $V_{ud}$ .

The averaged neutron lifetimes are  $879.4 \pm 1.0$  sec [1]. The recent neutron lifetime measurements have been performed by two different experimental methods. One of them is called the bottle method [2], in which neutrons are stored in a special material or magnetic bottle, and neutrons that survive after a certain time are measured. Another method is the beam method [3], where neutrons are measured with a flux monitor while protons from neutron  $\beta$  decay are measured using another detector. Though, there is an 8.6 sec ( $4.0\sigma$ ) deviation between the results from these two methods. A new type of measurement with the same accuracy is therefore required to resolve the difference.

### 1.2 A new type of beam method

We have discussed a new type of beam method, the electron counting beam method, which gives different systematic errors from previous experiments. In this new method, neutron lifetimes are derived

by simultaneous measurement of electrons from  $\beta$  decay and from  ${}^3\text{He}$  neutron capture reactions recorded by a Time Projection Chamber (TPC). As a neutron source, we use a high-intensity pulsed neutron beam provided at the Japan Proton Accelerator Research Complex (J-PARC). This method was originally developed by Kossakowski et al. [4]. The neutron lifetime  $\tau$  is calculated by the following equation,

$$\tau = \frac{1}{\rho\sigma v} \left( \frac{S_{{}^3\text{He}}/\epsilon_{{}^3\text{He}}}{S_{\beta}/\epsilon_{\beta}} \right) \quad (1)$$

where  $\rho$  is the  ${}^3\text{He}$  density,  $\sigma$  is the cross section of neutron capture by  ${}^3\text{He}$  and  $v$  is the neutron velocity. Since the cross section is inversely proportional to neutron velocity,  $\sigma v$  could be treated as constant ( $\sigma v = \sigma_0 v_0$ ), so we can use the thermal velocity  $v_0 = 2200$  m/s and cross section  $\sigma_0 = 5333 \pm 7$  barn for all neutron velocities.  $S$  and  $\epsilon$  are the number of signals and the selection efficiency for each reaction, respectively. We aim to measure the neutron lifetime with  $O(0.1\%)$  ( $\sim 1$  sec) accuracy using this method.

### 1.3 Largest correction

The largest two corrections for this experiment are the estimation of scattered background neutrons in the beam by the TPC operation gas and selection efficiency for  $\beta$  decay electrons. The scattered neutrons will be captured by the detector material and emit the  $\gamma$  ray, in then produce the electron via Compton scattering. Because this electron has similar space, energy and time distributions to  $\beta$  decay electrons, we cannot reject them by signal selection nor discriminate using the method of time of flight. Lithium fluoride ( ${}^6\text{LiF}$ ) can suppress the number of emitted prompt  $\gamma$  rays down to 0.01%. However, it is estimated by Monte Carlo simulation that these backgrounds remain 4% of the  $\beta$  events, which causes a large systematic uncertainty. We can improve the purity of the  $\beta$  decay signal with a tighter selection process, but larger efficiency corrections are required. In any case, minimizing corrections is essential for precise measurement.

## 2. Methodology

Figure 1 shows a schematic view of the experimental apparatus. The uniform magnetic field is applied along the neutron beam axis to separate  $\beta$  decay electrons from a background [5]. Moreover,  $\beta$  decay electrons remain in the signal region. Better signal efficiency and a lower level correction requirement can be achieved by decreasing these backgrounds. The magnet we use for this experiment is a superconducting solenoidal coil that was originally prepared for the BESS experiment [6]. The drift direction of the TPC is vertically upward.

## 3. Performance

We have evaluated the performance of background reduction with a Monte Carlo simulation based on Geant4 [7]. Figure 2 shows particle tracks in the vacuum chamber as a projection to the orthogonal plane to the beam axis. Each figure in Fig. 2(a) corresponds to  $\beta$  decay and background with and without a magnetic field. The central boxes indicate the signal region. One can see that while only a few background tracks remain (right bottom plot) under the non-magnetic field, all  $\beta$  decay tracks remain in the signal region (left bottom plot) under the magnetic field. Figure 2(b) shows that the background is suppressed to a few % compared to the case without the field. Moreover, the magnetic field recovers the  $\beta$  decay signal efficiency, because  $\beta$  decay electrons do not reach the inner wall and kept in the signal region. A magnetic field to 400 mT is enough to decrease the correction size to  $O(0.1\%)$  for the neutron lifetime measurement.

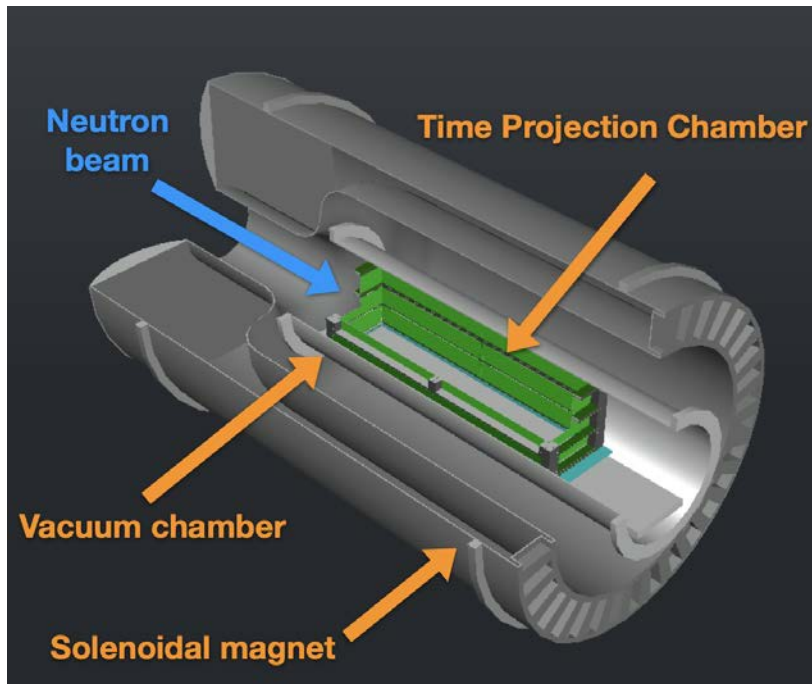


**Fig. 1.** A schematic view of the experimental apparatus. In this setup, TPC, vacuum chamber and solenoidal magnet are installed in order from the center. The bunched neutron beam shorter than TPC length passes through the center of TPC.

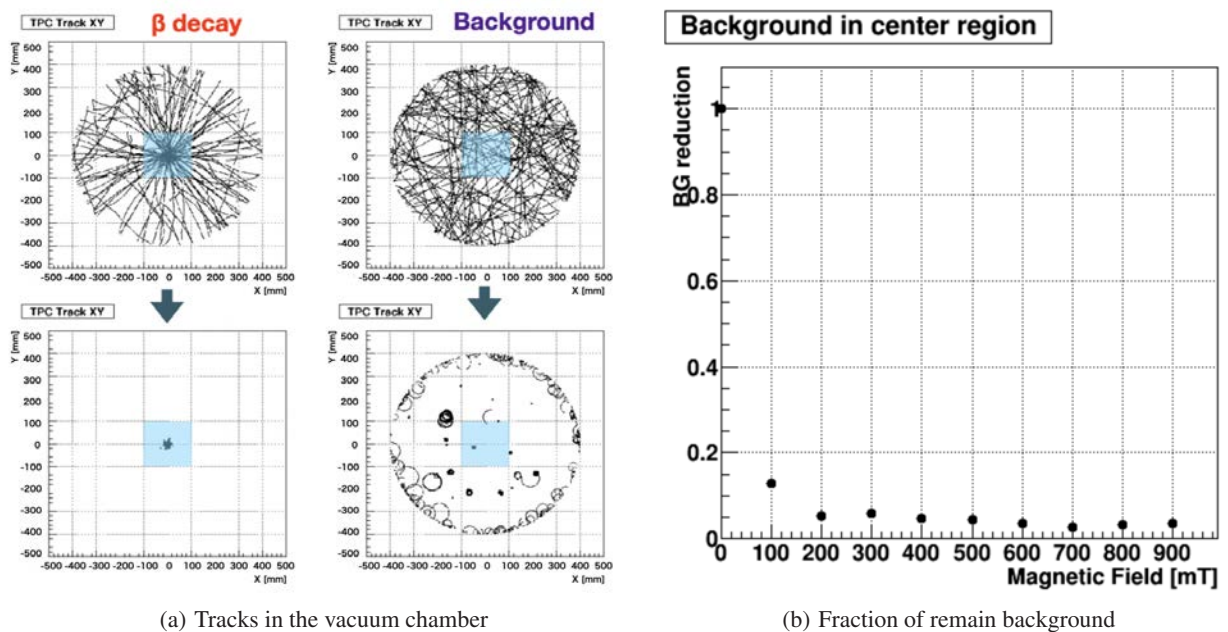


**Fig. 2.** Background reduction performance with the solenoidal magnet was evaluated by Monte Carlo simulation. (a) Tracks in the vacuum chamber with and without magnetic field (600 mT). Central box indicate signal region for neutron  $\beta$  decay signals. (b) Background reduction performance in the central signal region.

## 4. New TPC and integration test

### 4.1 Production

To distinguish the central signal and other background signals, we produced a different type of TPC, the TPC that has multiple layers. Chip condensers and resistances were soldered on the circuits. Drift and anode wires (Be-Cu  $\phi 100 \mu\text{m}$  and Au-W  $\phi 30 \mu\text{m}$ ) are mounted to the circuits. Figure 3 shows the final form of new TPC. The new TPC consists of three layers and non-magnetic material, such as Aluminum, stainless and polycarbonate resin. Most of the components such as the Aluminum frame and circuits were designed and produced at Kyushu University.



**Fig. 3.** A picture of TPC we have constructed. The TPC consists of 3 drift layers, and the signal region is in the middle layer.

### 4.2 Integration test with a solenoidal magnet

Figure 4 shows the overall view of the setup. We have carried out an integration test with this setup at KEK to evaluate several detector capabilities, for instance, background reduction capabilities and energy resolution. Let us show the result of the background exclusion test. Figure 5 shows the reduction of background by applying a magnetic field. We incident a  $\gamma$  ray irradiated from a radiation source ( $^{60}\text{Co}$ ,  $^{137}\text{Cs}$ ,  $^{152}\text{Eu}$ ) from outside the vacuum chamber to produce an electron assumed as background events. With a magnetic field, most of the background events cannot invade the signal region, compared to the one without the magnetic field. The background events excluded down to only a few %, which is consistent with simulation results.



**Fig. 4.** A picture of TPC installed inside the vacuum chamber and solenoidal magnet. The integration test with this setup has carried out at KEK.

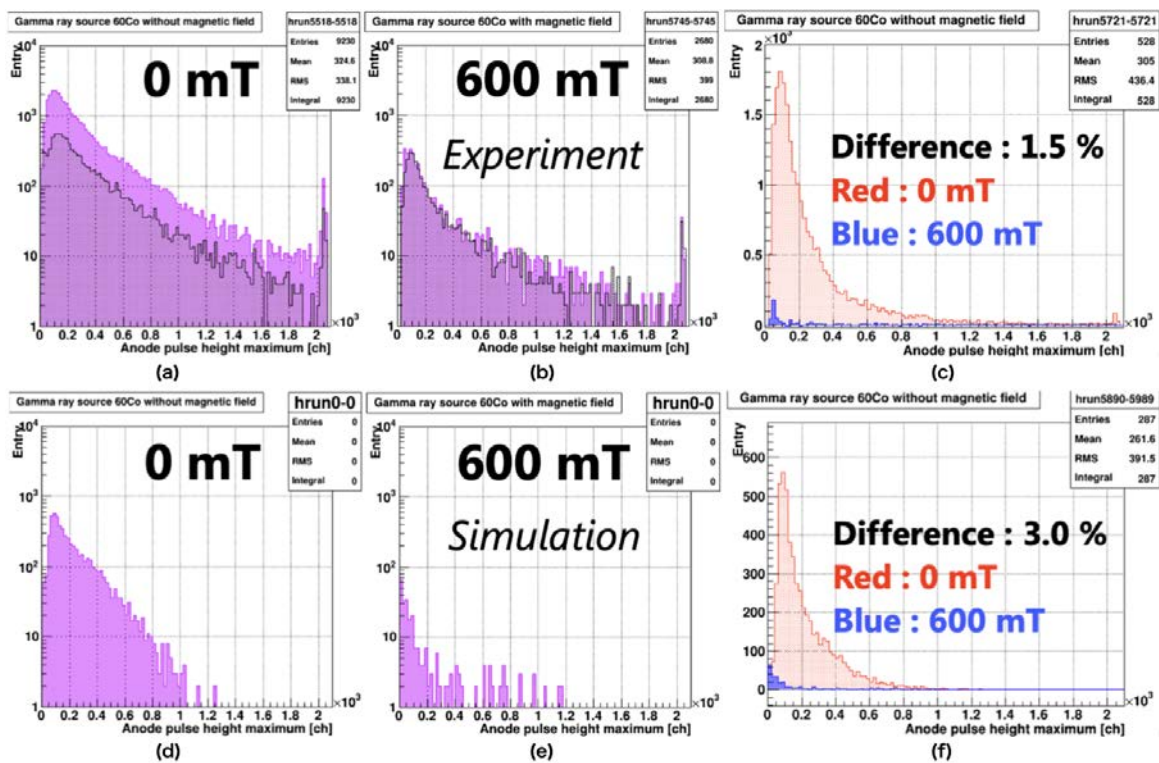


**Fig. 5.** A plot of the event entering the signal region. We used a radiation source(<sup>60</sup>Co) for emitting an electron assumed as a background. Left ((a) and (d)) and middle plots ((b) and (e)) show the entry events with only an environment (purple plot with black lines) and the environment with background events (pink plot without black lines), with and without a magnetic field, respectively. The right plot ((c) and (f)) shows the entries of background events. The background events are dramatically reduced in the presence of a magnetic field. The plot above ((a), (b) and (c)) and below ((d), (e) and (f)) show the experimental and simulation results, respectively.

## 5. Summary and prospect

We aim to measure the neutron lifetime with  $O(0.1\%)$ ( $\sim 1$  sec) accuracy by using the electron beam method. The background in the central region can be suppressed by using a multi-layered TPC and solenoidal magnetic field. The two largest corrections can be decreased to  $O(0.1\%)$  of the neutron lifetime according to the Monte Carlo simulation. A new multi-layered TPC was produced, and an integration test with a solenoidal magnet at KEK has been finished. The current setup at J-PARC MLF BL05 will be replaced by this magnet setup, and we will prepare for neutron beam operation.

## Acknowledgement

This work was supported by JSPS KAKENHI Grant Number 18H01231 and 18J10106.

## References

- [1] M. Tanabashi et al., (Particle Data Group), Phys. Rev. D 98, 030001 (2018) and 2019 update.
- [2] A. P. Serebrov et al., "Neutron lifetime measurements using gravitationally trapped ultracold neutrons", Phys. Rev. C **78**, 035505 (2008).
- [3] J. S. Nico et al., "Measurement of the neutron lifetime by counting trapped protons in a cold neutron beam", Phys. Rev. C **71**, 055502 (2005).
- [4] K. Schreckenbach, G. Azuelos, P. Grivot, R. Kossakowski, and P. Liaud, "Neutron decay measurements with a helium-filled time projection chamber", Nuclear Instruments and Methods in Physics Research A **284**, 120 (1989).
- [5] H. Otono, "LiNA-Lifetime of neutron apparatus with time projection chamber and solenoid coil", Nuclear Instruments and Methods in Physics Research Section A (Volume **845**, 2017, Pages 278-280).
- [6] Y. Makida et al., "Ballooning of a thin superconducting solenoid for particle astrophysics", IEEE Transactions on Applied Superconductivity (Volume: 5, Issue: 2, June 1995).
- [7] S. Agostinelli et al., "Geant4 - A Simulation Toolkit", Nuclear Instruments and Methods A **506** (2003) 250-303.

## 31 HUNS Upgrade; Simulation of the Beam Profile for a Thermal Neutron Source in HUNS-2

Kaoru Y. HARA<sup>1)\*</sup>, Fumiaki SATO<sup>2)</sup>, and Takashi KAMIYAMA<sup>1)</sup>

1) Faculty of Engineering, Hokkaido University, Sapporo 060-8628, Japan

2) School of Engineering, Hokkaido University, Sapporo 060-8628, Japan

\*e-mail: hara.kaoru@eng.hokudai.ac.jp

The upgrade of HUNS-2 is ongoing to increase the intensities of the electron and neutron beams. The profiles of neutron beam have been calculated using the PHITS code to design a TMRA of thermal neutron source in HUNS-2. In the calculation, a trial TMRA enhanced the intensity of thermal neutron beam as compared with the original one.

### 1. Introduction

The electron linear accelerator in the Hokkaido University Neutron Source (HUNS [1]) facility was recently upgraded toward HUNS-2 to increase the electron beam current. The HUNS-2 is an accelerator-driven neutron source that is equipped with a cold-, thermal- and fast-neutron type of sources. Experiments such as small angle neutron scattering [2], neutron transmission imaging [3] and neutron irradiation test have been currently conducted using the HUNS-2 for studies of material science and developments of measurement method.

In this work, the neutron beam profile for the HUNS-2 thermal neutron source was calculated with the Monte Carlo simulation code PHITS [4] (version 2.80/ 3.02) to improve a target-moderator-reflector-assembly (TMRA) of the original thermal neutron source system. The TMRA consists mainly of a neutron production target with a tungsten disc, lead blocks and water channels, a polyethylene moderator, graphite reflectors [5]. Through the simulations, a position and size of TMRA have been designed for increasing the intensity of thermal neutron beam.

## 2. Original HUNS thermal neutron source

In the HUNS facility, the thermal neutron source is located on the “CENTER” beam course. The horizontal cross-section view of the TMRA of the original HUNS thermal neutron source is illustrated in Fig. 1. Neutrons are produced by irradiation of the neutron production target with the electron beam, where the neutron production target is composed of a tungsten plate, lead blocks, and stainless water channels as shown in the inset of Fig. 1. First, in the neutron production target, the bremsstrahlung photons are generated and the photonuclear reactions are induced when the electron beam is stopped. Second, the neutrons, which are emitted from the photonuclear reaction, are thermalized through the polyethylene moderator and graphite reflectors. Finally, the thermalized neutron beam is collimated into the perpendicular direction with respect to the electron beam axis. To reduce the contamination of “gamma flash” on the neutron beam course, in addition, three lead blocks are placed near the neutron production target.

For a typical transmission experiment with the thermal neutron source, a distance between a neutron detector and the polyethylene moderator ( $L$ ) is approximately 7 m. The integrated intensity of neutron beam that was measured at  $L = 7$  m was  $10^3$  n/cm<sup>2</sup>/pulse in the neutron energy range of 0.01–0.1 eV [6]. The energy, current, and repetition rate of the electron beam were 34 MeV, 35  $\mu$ A, and 50 Hz, respectively, at the measurement for the neutron intensity. The schematic view of experimental setup is shown in Fig. 2, where a <sup>6</sup>Li glass detector [7] (or <sup>3</sup>He gas counter) was used. An aperture size of B<sub>4</sub>C collimator near the detector was 1 cm  $\times$  1 cm.

The original HUNS thermal neutron source is involved in a composite source system which can alternatively produce the neutron or X-ray beam. The composite source system has been used for developing a complementary imaging technique [3]. In the simulation for the thermal neutron beam, therefore, the geometry of composite source system is defined in the PHITS input file as shown in Fig 3. The neutron and X-ray sources are located respectively at the upside and downside of the composite source system. A more information about the configuration and usage of the composite source system is provided in the references [3, 5]. Additional walls for radiation shields and an up-and-down stage are ignored in the simulation while these are at outside of the composite source system in the actual situation. The calculated energy distribution of the thermal neutron beam is shown in Fig. 4 by the red line. In our previous work [5], a

neutron point source with the Maxwell-Boltzmann distribution of  $kT = 1.3$  MeV was defined at the neutron production target as an initial source. In this work, an electron beam was defined as a more realistic initial source to produce photoneutrons. The initial source is described in the next section.

In the simulation, the geometry of the X-ray source was remained the same because the focus of this work was the neutron source. For the X-ray beam production, as usual, the 9-MeV electron beam will irradiate a copper plate to generate bremsstrahlung photons. The threshold energies in the  $^{63,65}\text{Cu}(\gamma, n)$  reactions are above 9 MeV. The peak energy of the calculated energy distribution of X-ray beam is 100–200 keV.

### 3. Simulation to design the HUNS-2 thermal neutron source

The beam profile of thermal neutron source for a trial TMRA was simulated using the PHITS code, where the geometry was based on the original TMRA but somewhat different configuration. The particle transport calculation was divided into two steps by using a “DUMP option” in order to reduce the computation time. At the first step, kinematical information of neutron particles was output to a dump file after a pencil-like electron beam of 1 cm in diameter irradiated the neutron production target at 34 MeV. The neutron production target was only defined in an air space instead of TMRA. A rectangular tally for the dump covered the neutron production target and had almost same size as the target. At the second step, the dumped neutron data was used for each trial TMRA as the initial source because the first step needed a long computation time. The evaluated nuclear data of JENDL-4.0 [8] was utilized for the simulation with respect to the neutron-induced nuclear reactions. The neutrons were counted by a tally at the distance of  $L = 1$  m from the moderator.

An improved TMRA which enhances the intensity of thermal neutron beam is shown in Fig. 5. The points are (1) positions of neutron production target and polyethylene moderator, (2) a size of polyethylene moderator, and (3) an additional graphite reflector with an entrance. For the improved and original TMRA, the calculated energy distributions of neutron beam are shown in Fig. 4 by the blue and red lines, respectively. The energy distribution for the improved TMRA is similar to the one for the original TMRA while the integrated intensity of neutron beam in the energy range of 0.01–0.1 eV is increased up to 1.6 times. In the both calculations, here, the density of graphite reflectors ( $= \rho_c$ ) was  $2.3 \text{ g/cm}^3$  (theoretical density) although the graphite reflectors with

$\rho_c = 1.6 \text{ g/cm}^3$  was used for the actual original TMRA.

#### 4. Conclusion

In order to increase the intensity of thermal neutron beam in HUNS-2, the configuration of TMRA for the thermal neutron source was investigated using the PHITS code. The improved TMRA was obtained through the simulation of the energy distribution of thermal neutron beam. The TMRA of thermal neutron source will be upgraded based on the results of this work.

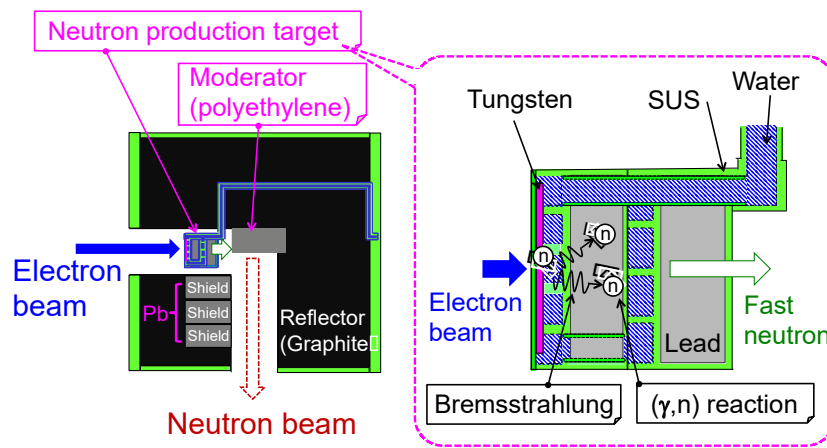


Figure 1: Original TMRA of the thermal neutron source in the HUNS facility.

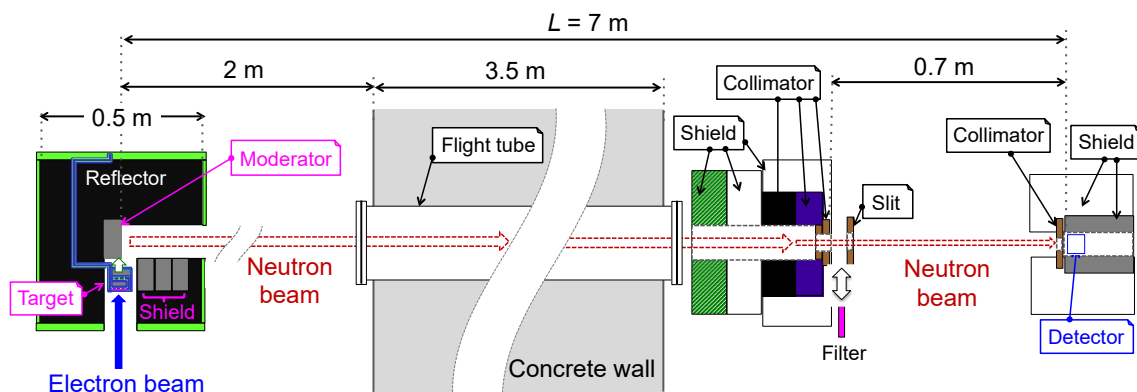


Figure 2: Experimental setup in the measurement of the neutron beam intensity.

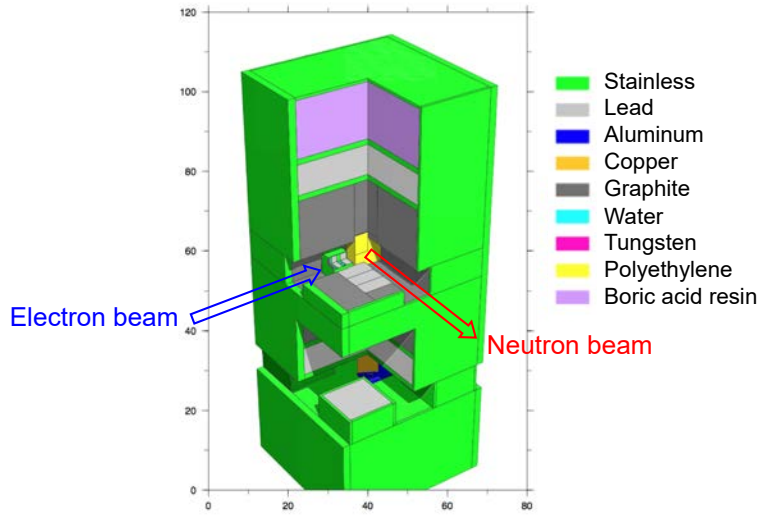


Figure 3: Geometry of the composite source system of neutron and X-ray sources.

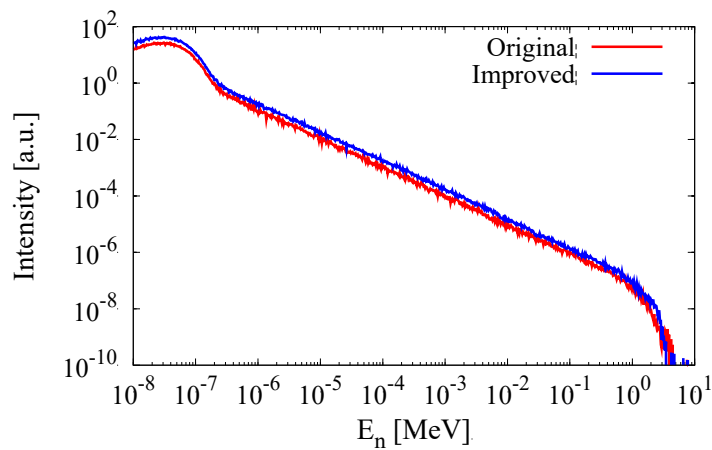


Figure 4: Energy distribution of thermal neutron beam.

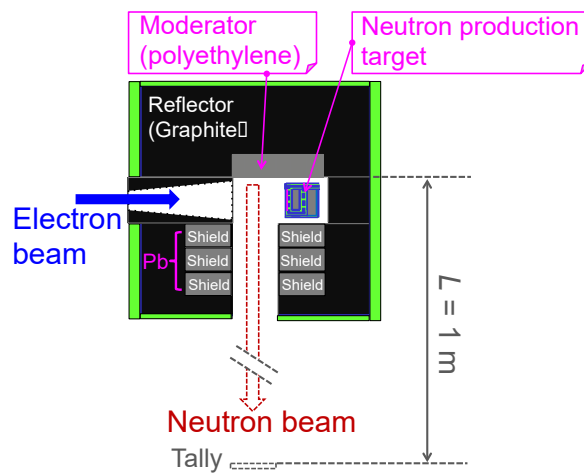


Figure 5: Improved TMRA of the thermal neutron source.

## References

- [1] Furusaka M, Sato H, Kamiyama T, Ohnuma M, Kiyanagi Y, Activity of Hokkaido University Neutron Source, HUNS. Phys. Proc. 2014;60:167–174.
- [2] Ishida T, Ohnuma M, Seong BS, Furusaka M, Intermediate-angle Neutron Scattering Instruction for Quantitative and Non-destructive Characterization of Nanostructure in Steel and Other Alloy, ISIJ Int. 2017;57:1831–1837.
- [3] Hara KY, Sato H, Kamiyama T, Shinohara T, Measurement and simulation for a complementary imaging with the neutron and X-ray beams, EPJ Web Conf. 2017;146: 03032-1–4.
- [4] Sato T, Iwamoto Y, Hashimoto S, Ogawa T, Furuta T, Abe S, Kai T, Tsai P, Matsuda N, Iwase H, Shigyo N, Sihver L, Niita K, Features of Particle and Heavy Ion Transport code System (PHITS) version 3.02, J. Nucl. Sci. Technol. 2018;55:684–690.
- [5] Kamiyama T, Hara KY, Sato H, Taira H, Convertible Source System of Thermal Neutron and X-ray at Hokkaido University Electron Linac Facility, Nuovo Cimento 2015;38C:187–192.
- [6] Uehara Y, Hara KY, Asako M, Sato H, Kamiyama T, Shinohara T, AESJ 2017 Fall Meeting Poster, Hokkaido University, Sapporo;2017 Sep11–13.
- [7] Kino K, Furusaka M, Hiraga F, Kamiyama T, Kiyanagi Y, Furutaka K, Goko S, Harada H, Harada M, Kai T, Kimura A, Kin T, Kitatani F, Koizumi M, Maekawa F, Meigo S, Nakamura S, Ooi M, Ohta M, Oshima M, Toh Y, Igashira M, Katabuchi T, Mizumoto M, Measurement of energy spectra and spatial distributions of neutron beams provided by the ANNRI beamline for capture cross-section measurements at the J-PARC/MLF, Nucl. Instrum. Methods. 2011;A626–627:58–66.
- [8] Shibata K, Iwamoto O, Nakagawa T, Iwamoto N, Ichihara A, Kunieda S, Chiba S, Furutaka K, Otuka N, Ohsawa T, Murata T, Matsunobu H, Zukeran A, Kamada S, Katakura J, JENDL-4.0: a new library for nuclear science and engineering, J. Nucl. Sci. Technol., 2011;48:1–30.

## 32 Preliminary experiment on characterization of RANS-II neutron production via the ${}^7\text{Li}(p, n){}^7\text{Be}$ reaction with 2.49 MeV proton injection

S. IZUMITANI<sup>1</sup>, Y. IKEDA<sup>2</sup>, T. KOBAYASHI<sup>2</sup>, S. IKEDA<sup>2</sup>, Y. WAKABAYASHI<sup>2</sup>,  
K. FUJITA<sup>2</sup>, K. SUGIHARA<sup>1,2</sup>, N. SHIGYO<sup>1</sup>, K. TANAKA<sup>2</sup>, Y. OTAKE<sup>2</sup>

*1 Kyushu University, Fukuoka, 819-0395, Japan*

*2 RIKEN, Wako, 351-0198, Japan*

e-mail: shog0311@kune2a.nucl.kyushu-u.ac.jp

Experiments associated with the first measurement for neutron production characteristics via the  ${}^7\text{Li}(p, n){}^7\text{Be}$  reaction at RANS-II were performed by applying two methods of the long counter with a  ${}^3\text{He}$  gas counter and the foil activation technique using an indium foil. The experimental data in a form of reaction rate were compared with calculations by using the PHITS code simulating the experimental condition. As the results, it was found that the calculations of reaction rates overestimated the experiments in both methods. We have investigated possible causes for the discrepancies between experiments and calculations. Although the data of the experiments and calculations are very preliminary, we report tentative analyses concerning the p-Li neutron production cross section, the proton beam energy and proton beam position and profile on the Li target. We listed major sources related uncertainties and errors to be clarified.

### 1 Introduction

To meet increasing demands for neutrons, RIKEN has developed the proton accelerator based compact neutron source, called RANS (RIKEN Accelerator-driven compact Neutron Source) by using the  ${}^9\text{Be}(p, n){}^9\text{B}$  reaction with 7 MeV proton injection for the neutron production [1, 2]. RANS comes up with achievements in several application fields demonstrating a promising potential capability of CANS (a Compact Accelerator-driven Neutron Source) such as a non-destructive diagnostic tool for infrastructure concrete media [1]. From the compactness point of view, accelerator and neutron production target are recognized as key technological elements to be R&D items. RANS-II has been developed as a prototype of a more realistic compact source by using the  ${}^7\text{Li}(p, n){}^7\text{Be}$  reaction, which produces neutrons by rather low energy proton incidence. RANS-II adopted this reaction with the 2.49-MeV proton accelerator mainly because of the compactness requirement. Although the cross section of this reaction has been studied for many years [3–9], there is still an issue to confirm as the compact neutron source performance using a thick Li target configuration with intense proton beam injection. Thus, we started an experimental program to evaluate neutron characteristics in terms of neutron yield and angular distribution of RANS-II using the  ${}^7\text{Li}(p, n){}^7\text{Be}$  reaction as its accomplishment test of the system accepting the proton beam on the Li target.

The experimental data in a form of reaction rate were obtained using a  ${}^3\text{He}$  long counter and indium activation foils for the  ${}^{115}\text{In}(n, n'){}^{115m}\text{In}$  and  ${}^{115}\text{In}(n, \gamma){}^{116m}\text{In}$  reactions. In this paper, we report the validity of calculations and the current status of evaluation through comparison with calculations by using PHITS-2.88 [10] simulating the experimental condition. Although the data of experiments and calculations were very preliminary, sources concerning uncertainties and errors were analyzed as much as possible.

## 2 Experiment

Two experiments were conducted to obtain reaction rates by the methods with the  $^3\text{He}$  long counter (i) and indium foil activation (ii) as the first experiment on neutron flux of RANS-II. Reasons for applying the two methods were as follows; the TOF method, which is assumed to be the most efficient for the neutron spectrum measurement, is not effective at the RANS-II as shown in **Figure 1**, because an available neutron flight path length is short and a proton pulse width is long. Alternatively, a proton recoil spectrometer is used for a measurement of an energetic neutron spectrum. However, it is difficult to determine a neutron energy below 1 MeV using the spectrometer. The representative energy range of RANS-II is 0.4–0.8 MeV in this neutron production by the  $^7\text{Li}(p, n)$  reaction at 2.49 MeV. Therefore, the  $^3\text{He}$  long counter was applied to survey the neutron intensity around the target station. The indium foils were preliminary used to measure neutron distribution around the target using the  $^{115}\text{In}(n, n')^{115m}\text{In}$  and  $^{115}\text{In}(n, \gamma)^{116m}\text{In}$  reactions.

### (i) $^3\text{He}$ long counter

The configuration of  $^3\text{He}$  long counter is shown in **Figure 2**. An LND 252295  $^3\text{He}$  counter was used. The applied voltage was 1600 V. The counter was put in a moderator composed of polyethylene cylinder and a 0.3 cm thick 50 wt%  $\text{B}_4\text{C}$  rubber thermal neutron shield. First, neutron reaction rates were measured using a 3.6 MBq  $^{252}\text{Cf}$  source. The distances between the source and the detector were 100, 50, and 15 cm. Next, neutron reaction rates were measured with proton beams. The distance from a Li target to the  $^3\text{He}$  long counter was 288.7 cm. The proton beam currents were between 0.066 and 0.10  $\mu\text{A}$ .

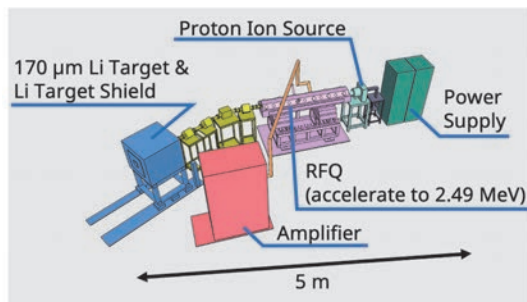


Figure 1 Configuration of RANS-II

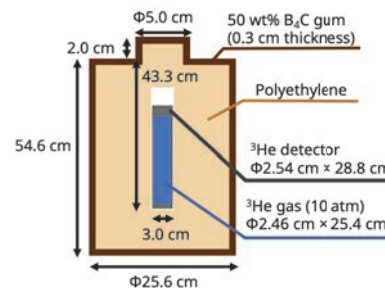


Figure 2 Configuration of  $^3\text{He}$  long counter

### (ii) Indium foil activation

Four indium foils (In#1–In#4) were placed on a cardborad sheet at a position of 1.6 cm from the target. **Figure 3** shows the arrangement of the foils. The size and weight of indium foils and the distances from In#1 are shown in **Table 1**. The proton beam with an average current of 3.9  $\mu\text{A}$  irradiated for 15 minutes. After the irradiation, the foils were cooled and the 336-keV decay  $\gamma$ -rays of the  $^{115}\text{In}(n, n')^{115m}\text{In}$  reaction and the 1293-keV decay  $\gamma$ -rays of the  $^{115}\text{In}(n, \gamma)^{116m}\text{In}$  reaction were measured by an HPGe detector. In#1–In#3 were placed at 2.7 cm from the surface of the HPGe detector while In#4 was placed at 0.20 cm from the surface. The relative efficiency of the HPGe detector was 10 %.

## 3 Simulation

Reaction rates were calculated using PHITS-2.88. ENDF-B/VII.0 [11] was used for the  $^7\text{Li}(p, n)$  reaction cross section. JENDL-4.0 [12] was used for cross sections of neutron induced reaction. A proton beams with a diameter of 1.0 cm and with an uniform distribution was incident on the center of a Li target (diameter 5 cm, thickness 170  $\mu\text{m}$ ) to generate neutrons. The number of neutrons generated from the Li target was  $1.21 \times 10^{-4}$  per proton.

### (i) $^3\text{He}$ long counter

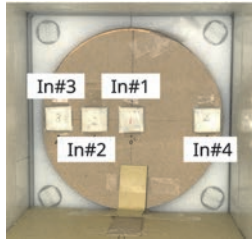


Figure 3 Experimental setup of four indium foils

Table 1 Specifications of indium foils

	Size [cm×cm×cm]	Weight [g]	Distance from In#1 [cm]
In#1	1.8 × 1.7 × 0.20	4.66	0
In#2	1.7 × 1.8 × 0.20	4.99	2.8
In#3	1.8 × 1.9 × 0.20	4.98	5.5
In#4	1.7 × 1.9 × 0.20	4.90	5.4

Figure 4 illustrates the computational geometry using PHITS. Only the RANS-II target shield and the <sup>3</sup>He long counter were assumed because scattered neutrons from the floor, the walls, and the roof were considered to be negligible. Neutron track lengths in the <sup>3</sup>He effective area were calculated by a T-track tally. Additionally, the calculations of neutrons emitted from a <sup>252</sup>Cf source were performed. The energy distribution defined by JIS Z 4521 [13] was applied as an initial source in the simulation.

(ii) Indium foil activation

Figure 5 depicts the geometry of the simulation. Indium foils were placed on the same positions as the experiment. Only the RANS-II target shield and the indium foils were assumed. Neutron track lengths in the foils were obtained by T-track tallies.

Reaction rates were calculated using the T-track results. In the calculations, JENDL-4.0 was used for <sup>3</sup>He(n, p) cross section of the <sup>3</sup>He detector, and JENDL dosimetry file 99 [14] was used for <sup>115</sup>In(n, n') and <sup>115</sup>In(n, γ) reaction cross sections of the indium foil activation.

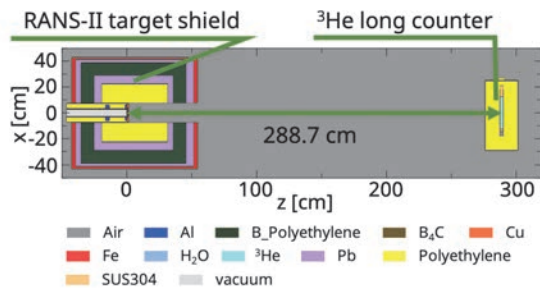


Figure 4 Geometry of calculation for the <sup>3</sup>He long counter

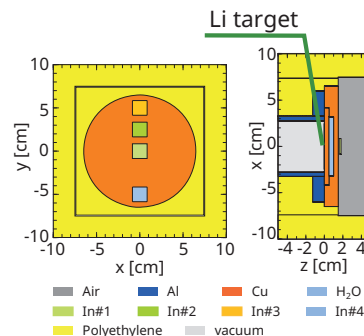


Figure 5 Geometry of calculation for the indium foil activation

## 4 Results

(i) <sup>3</sup>He long counter

Table 2 shows the measured and calculated reaction rates with the <sup>252</sup>Cf source. Errors in the tables correspond to statistical errors. The calculation to experiment ratio (C/E) using the <sup>252</sup>Cf source was within the range of 1.76 to 1.90. The origin of the discrepancies is under investigation. Possible reasons for the discrepancies are uncertainties in the gas pressure and sensitive area of the <sup>3</sup>He long counter. For example, when the pressure is 1 atm, the reaction rate at 100 cm is 51.3 s<sup>-1</sup>, which is 41 % smaller than that for 10 atm. Table 3 shows the measured and calculated reaction rates with the proton beam. For the measurements at the proton beam current of 0.066–0.10 μA, The C/E was 8.48–8.77. Therefore, the PHITS calculation in Tables 2 and 3 overestimated the experimental values.

(ii) Indium foil activation

Table 2 Comparison between the measured and calculated reaction rates with  $^{252}\text{Cf}$  source

Distance [cm]	Exp. [/s]	PHITS [/s]	C/E
100	$71.0 \pm 0.7$	125	1.76
50	$260 \pm 1$	495	1.90
15	$2317 \pm 5$	4264	1.84

Table 3 Comparison between the measured and calculated reaction rates with the proton beams

Current [ $\mu\text{A}$ ]	Exp. [/s]	PHITS [/s]	C/E
0.066	$217 \pm 1$	1842	8.48
0.085	$278 \pm 2$	2379	8.56
0.10	$329 \pm 3$	2884	8.77

Table 4 Comparison between the measured and calculated reaction rates for the  $^{115}\text{In}(n, \gamma)^{116m}\text{In}$  reaction at 3.9  $\mu\text{A}$

	Exp. [/s]	PHITS [/s]	C/E
In#1	$5.5 \times 10^{-17}$	$2.3 \times 10^{-16}$	4.2
In#2	$5.3 \times 10^{-17}$	$1.8 \times 10^{-16}$	3.4
In#3	$4.9 \times 10^{-17}$	$1.8 \times 10^{-16}$	3.7
In#4	$4.1 \times 10^{-17}$	$1.8 \times 10^{-16}$	4.4

Table 5 Comparison between the measured and calculated reaction rates for the  $^{115}\text{In}(n, n')^{115m}\text{In}$  reaction at 3.9  $\mu\text{A}$

	Exp. [/s]	PHITS [/s]	C/E
In#1	$(5.5 \pm 0.1) \times 10^{-20}$	$4.4 \times 10^{-19}$	8.0
In#2	$(3.4 \pm 0.1) \times 10^{-20}$	$1.9 \times 10^{-20}$	0.56
In#3	$(1.6 \pm 0.2) \times 10^{-21}$	$1.8 \times 10^{-21}$	1.1

**Tables 4** and **5** show the reaction rates of the  $^{115}\text{In}(n, \gamma)^{116m}\text{In}$  and  $^{115}\text{In}(n, n')^{115m}\text{In}$  reactions, respectively. Errors in the table correspond to statistical errors. The C/E for the  $^{115}\text{In}(n, \gamma)^{116m}\text{In}$  reaction was 3.4–4.4 while that for the  $^{115}\text{In}(n, n')^{115m}\text{In}$  reaction was 0.56–8.0. One of the possible causes for the differences of C/E between the two reactions is that the proton beam position between the experiment and the simulation is different. Neutrons from the  $^7\text{Li}(p, n)$  reaction with at most 800 keV are easily slowed below 336 keV of the  $^{115}\text{In}(n, n')^{115m}\text{In}$  reaction threshold. In addition, these neutrons tend to be emitted in the forward direction. Therefore, reaction rates for different beam positions were calculated by PHITS.

**Tables 6** and **7** show the reaction rates of the  $^{115}\text{In}(n, \gamma)^{116m}\text{In}$  and  $^{115}\text{In}(n, n')^{115m}\text{In}$  reactions, respectively, when position of proton beam is moved 1.2 cm toward In#2. These results show that the reaction rates for the  $^{115}\text{In}(n, n')^{115m}\text{In}$  reaction largely depends on the proton beam position.

Table 6 Reaction rates for the  $^{115}\text{In}(n, \gamma)^{116m}\text{In}$  reaction at 3.9  $\mu\text{A}$  when the position of the proton beam is moved 1.2 cm toward In#2

	Exp. [/s]	PHITS [/s]	C/E
In#1	$5.5 \times 10^{-17}$	$2.2 \times 10^{-16}$	4.0
In#2	$5.3 \times 10^{-17}$	$2.0 \times 10^{-16}$	3.8
In#3	$4.9 \times 10^{-17}$	$1.8 \times 10^{-16}$	3.7
In#4	$4.1 \times 10^{-17}$	$1.6 \times 10^{-16}$	3.9

Table 7 Reaction rates for the  $^{115}\text{In}(n, n')^{115m}\text{In}$  reaction at 3.9  $\mu\text{A}$  when the position of the proton beam is moved 1.2 cm toward In#2

	Exp. [/s]	PHITS [/s]	C/E
In#1	$(5.5 \pm 0.1) \times 10^{-20}$	$2.3 \times 10^{-19}$	4.2
In#2	$(3.4 \pm 0.1) \times 10^{-20}$	$1.2 \times 10^{-19}$	3.5
In#3	$(1.6 \pm 0.2) \times 10^{-21}$	$4.2 \times 10^{-21}$	2.6

## 5 Discussion

The PHITS calculation overestimated the reaction rates for both experiments. Based on the results, we considered three possible causes of the difference; proton beam energy (I), proton beam profile (II), and the  $^7\text{Li}(p, n)$  cross section (III).

### (I) Proton beam energy

**Figure 6** shows the number of neutrons generated by the  ${}^7\text{Li}(p, n)$  reaction for several proton energies. When the proton energy is changed from 2.49 to 2.1 MeV, neutron yields decrease to about 1/4. One of the possible causes of low neutron yield in the experiment is that incident proton energy is lower than expected. It is required to measure the proton beam energy directly.

**(II) Proton beam profile**

Since there was a possibility that the beam was shifted from the center of the Li target in the activation experiments, it is presumed that all incident protons did not hit the Li target. In order to measure proton beam profile, an additional experiment is planned.

**(III)  ${}^7\text{Li}(p, n)$  cross section**

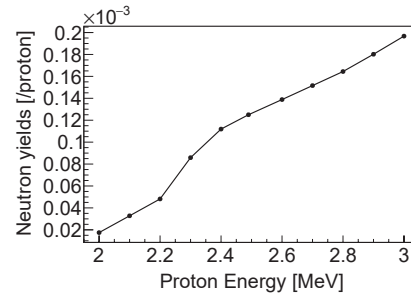


Figure 6 Neutron yields from Li target for incident proton energy

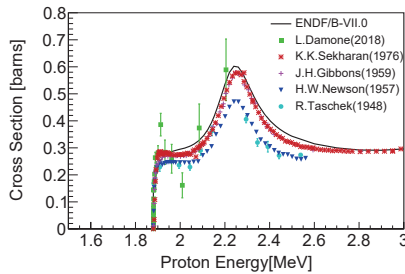


Figure 7 Cross section of the  ${}^7\text{Li}(p, n){}^7\text{Be}$  reaction as a function of the proton energy

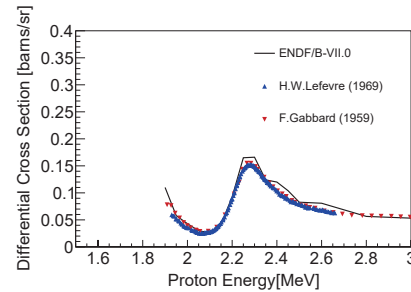


Figure 8 Differential cross section of the  ${}^7\text{Li}(p, n){}^7\text{Be}$  reaction at  $0^\circ$  as a function of the proton energy

Comparisons between ENDF/B-VII.0 and existing data were performed in terms of validation of ENDF/B-VII.0. **Figures 7** and **8** show the  ${}^7\text{Li}(p, n)$  cross sections and the angular differential cross sections at  $0^\circ$ , respectively [3–9]. In **Fig. 8**, the angular differential cross section which is calculated by PHITS with ENDF/B-VII.0 is shown by the solid line. Both the cross sections and differential cross sections of ENDF/B-VII.0 agree with the experimental data within 10 % below 2.49 MeV.

One of major sources of uncertainties is the incident proton energy because the neutron yield is closely related to the total cross section of p-Li reaction having the proton energy dependence. The differential cross section of p-Li reaction depends on the proton energy also.

Another major source is the proton beam profile (such as the number of protons and the proton beam position) on the Li target during the measurement. As it is still underway to establish a reliable diagnostics monitor system, we tentatively applied data for the number of protons based on the present system at RANS, which is obtained from electric charge data of the whole beam pipe including the Li target.

In addition, the proton beam position on the target is a key to analyze the data. The data analysis for the activation technique in particular could be affected by the beam position because the indium foil was placed at a very near position and a considerable large solid angle with respect to the target center. However, the present measurement system has a limit to identify the correct position of the proton beam. Thus we investigated its effect very tentatively as described in Section 4 (ii).

## 6 Summary

To validate the RANS-II neutron production via the  ${}^7\text{Li}(p, n){}^7\text{Be}$  reaction with 2.49 MeV proton injection, experiments were performed by using the long-counter using the  ${}^3\text{He}$  counter with the polyethylene moderator and the foil activation technique for the  ${}^{115}\text{In}(n, n'){}^{115m}\text{In}$  and  ${}^{115}\text{In}(n, \gamma){}^{116m}\text{In}$  reactions with the 336 keV threshold energy. The reaction rates for both reactions of interest were compared with the simulation calculations by PHITS. We found that there was rather a large overestimation in the calculations systematically. As the discrepancies were not able to be negligibly small, we have tried to investigate to understand possible sources of the overestimation. As noted in the uncertainty section, due to many elements to obtain the reaction rate, their contributions should be confirmed one by one. Although the process is still underway to finalize data of both experiments and calculations, in conclusion at present, the effect of proton beam shift in the Li target on the neutron flux, and the uncertainty of nuclear data for p-Li neutron production are not a major source for the overestimation.

## Acknowledgement

The authors would like to acknowledge the support from Neutron Beam Technology Team, RIKEN.

## References

- [1] Otake Y. RIKEN Compact Neutron Systems with Fast and Slow Neutrons. *Plasma Fusion Res.* 2018;13:2401017.
- [2] Kobayashi T, Otake Y, Kushima Y, et al. Development of Accelerator-driven Transportable Neutron source for Non-destructive Inspection of Concrete Construct. *Proc 2017 IEEE NSS/MIC 2017*:8532890.
- [3] Damone L, Barbagallo M, Mastromarco M, et al.  ${}^7\text{Be}(n, p){}^7\text{Li}$  Reaction and the Cosmological Lithium Problem: Measurement of the Cross Section in a Wide Energy Range at n\_TOF at CERN. *Phys Rev Lett.* 2018;121(4):042701.
- [4] Sekharan KK, Laumer H, Kern BD, et al. A Neutron Detector For Measurement of Total Neutron Production Cross Sections. *Nucl Instrum Meth.* 1976;133(2):253–257.
- [5] Gibbons JH, Macklin RL. Total Neutron Yields from Light Elements under Proton and Alpha Bombardment. *Phys Rev.* 1959;114(2):571–580.
- [6] Newson HW, Williamson RM, Jones KW, et al.  $\text{Li}^7(p, n)$ ,  $(p, p'\gamma)$ , and  $(p, \gamma)$  Reactions near Neutron Threshold. *Phys Rev.* 1957;108(5):1294–1300.
- [7] Taschek R, Hemmendinger A. Reaction Constants for  $\text{Li}^7(p, n)\text{Be}^7$ . *Phys Rev.* 1948;74(4):373–385.
- [8] Lefevre HW, Din GU. Zero Degree Neutron Yield from the  ${}^7\text{Li}(p, n){}^7\text{Be}$  Reaction Near  $2 \cdot 2$  MeV. *Aust J Phys.* 1969;22(6):669–678.
- [9] Gabbard F, Davis RH, Bonner TW. Study of the Neutron Reactions  $\text{Li}^6(n, \alpha)\text{H}^3$ ,  $\text{F}^{19}(n, \gamma)\text{F}^{20}$ , and  $\text{I}^{127}(n, \gamma)\text{I}^{128}$ . *Phys Rev.* 1959;114(1):201–208.
- [10] Sato T, Iwamoto Y, Hashimoto S, et al. Features of Particle and Heavy Ion Transport code System (PHITS) version 3.02. *J Nucl Sci Technol.* 2018;55(6):684–690.
- [11] Chadwick MB, Oblozinsky P, Herman M, et al. ENDF/B-VII.0: Next Generation Evaluated Nuclear Data Library for Nuclear Science and Technology. *Nucl Data Sheets.* 2006;107(12):2931 – 3060.
- [12] Shibata K, Iwamoto O, Nakagawa T, et al. JENDL-4.0: A New Library for Nuclear Science and Engineering. *J Nucl Sci Technol.* 2011;48(1):1–30.
- [13] Japanese Industrial Standards Committee (JISC). Method of calibration for neutron dose equivalent (rate) meters. Japan: JISC; 2006. JIS Z 4521.
- [14] Kobayashi K, Iguchi T, Iwasaki S, et al. JENDL Dosimetry File 99 (JENDL/D-99). JAERI. 2002;1344:1–133.

## 33 Development of a neutron beam monitor for nuclear data measurement using spallation neutron source

Hideto NAKANO<sup>1\*</sup>, T. KATABUCHI<sup>1</sup>, G. ROVIRA<sup>1</sup>, Y. KODAMA<sup>1</sup>, K. TERADA<sup>1</sup>  
A. KIMURA<sup>2</sup>, S. NAKAMURA<sup>2</sup>, S. ENDO<sup>2</sup>

1) Laboratory for Advanced Nuclear Energy, Tokyo Institute of Technology

2) Japan Atomic Energy Agency

e-mail: nakano.h.ag@m.titech.ac.jp

In neutron capture cross section measurement, the number of the incident neutrons is necessary to derive the neutron capture cross section. However, in measurement with ANNRI, neutron monitoring detection has not been employed. To avoid possible failure of the proton pulse counting method and make measurement with ANNRI more robust, an additional neutron beam monitor is under development. A plastic scintillator and <sup>6</sup>Li are adopted for a detector. A test detector system was built to study the feasibility of the method. Neutron detection is confirmed in experiment results.

### I. INTRODUCTION

Highly precise neutron nuclear data are required in nuclear transmutation research of long-lived minor actinides (MA) in nuclear waste. It has been difficult to measure neutron-induced reaction cross sections of MAs due to large background of the decay gamma-rays from radioactive samples. In recent years, with the advent of spallation neutron sources, the qualities of cross section measurements of MAs were significantly improved. The Japanese Spallation Neutron Source (JSNS) in the Japan Proton Accelerator Research Complex (J-PARC) was started in operation in 2008. In order to utilize a high-intensity pulsed neutron beam from JSNS for nuclear data measurement, the Accurate Neutron Nucleus Reaction Measurement Instrument (ANNRI) was built and has been used for the past ten years [1].

In neutron capture cross section measurement, the number of the incident neutrons is necessary to derive the neutron capture cross section. To normalize the detected gamma-ray yield to the number of the incident neutrons, the neutron count is usually monitored by detecting the incident neutrons with a neutron detector. However, in measurement with ANNRI, neutron monitoring detection has not been employed and, instead, the number of proton beam pulses injected into the spallation target has been used based on the assumption that the number of proton beam pulses is proportional to the number of incident neutrons. This assumption is mostly plausible but could fail when the conditions of the proton accelerator or the neutron source change. To avoid possible failure of the proton pulse counting method and make measurement with ANNRI more robust, an additional neutron beam monitor is under development.

### II. DETECTOR DESIGN

To develop a neutron beam monitor for ANNRI, there are two issues to overcome. First, very high intensity neutron beam from JSNS requires a fast detector system that can process signals at a high counting rate. Second, gamma-flash, an intense gamma-ray burst produced when the proton beam pulse bombards the spallation target, can paralyze a detector. Thus, gamma-ray sensitivity of the neutron monitor should be low. In order to fulfill the requirements, a thin sheet-type plastic scintillator

combined with a thin  ${}^6\text{Li}$  layer on a Mylar film is adopted for the present neutron monitor. The incident neutrons react with  ${}^6\text{Li}$  and the  ${}^6\text{Li}(n,t){}^4\text{He}$  reaction occurs. The emitted particles, tritons and alphas, are detected with the plastic scintillator. The short ranges of tritons and alphas allow for using a thin plastic scintillator film, and the thin detector leads to low gamma-ray sensibility. Another requirement for fast detection is achieved by the fast response property of plastic scintillator. Simulation studies using Monte Carlo simulation code PHITS [2] was performed to optimize the detector design, especially thickness of the  ${}^6\text{LiF}$  layer. In Fig. 1, the overall geometric design is shown.

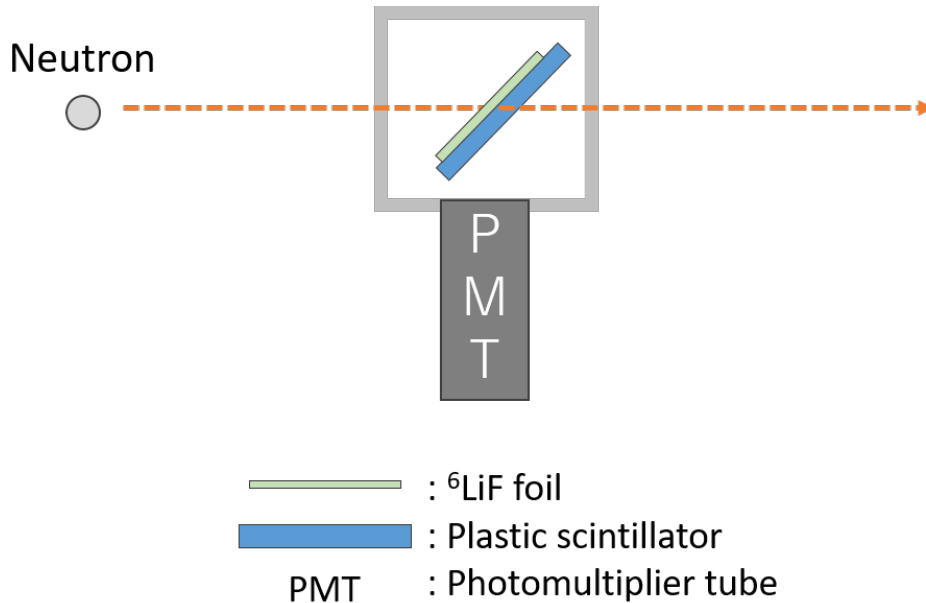


Figure 1: Detector geometric design.

### III. EXPERIMENTS

A test detector system was built to study the feasibility. LiF was deposited on a Kapton film by a vacuum deposition method. The LiF layer was thin enough for tritons and alpha particles to penetrate and reach the plastic scintillator. Li was not isotopically enriched. The isotopic ratio of  ${}^6\text{Li}$  was the natural abundance of 7.6%. The photomultiplier tube is HAMAMATSU R1306-22ASSY. Test experiments were carried out at ANNRI. The detector was placed at a flight length of 29 m. Two measurements with and without LiF foil were conducted. In Fig. 2, time-of-flight (TOF) spectra are shown. TOF measurement was started by a signal from the J-PARC accelerator and stopped by PMT signal. In Fig. 2, a strong peak is observed in the TOF region from 1 to 2.5  $\mu\text{s}$ . This peak is created by gamma-flash from the spallation target. No events are observed in the TOF region from 3 to 7  $\mu\text{s}$ . This was caused by dead time of the system. The intense gamma-ray burst was detected in each TOF cycle and paralyzed the system for the system dead time. In Figs. 3 and 4, pulse-height (PH) spectra are shown. One is for full TOF range and the other is for TOF larger than 3  $\mu\text{s}$ . A peak between 300 and 1200 ch is observed only in full TOF range and disappears in larger than 3  $\mu\text{s}$ . The peak is observed in both with and without LiF. This suggests that the peak is created by the gamma-flash events. The  ${}^6\text{Li}(n,t){}^4\text{He}$  events are a broad continuum component observed only in Fig. 3.

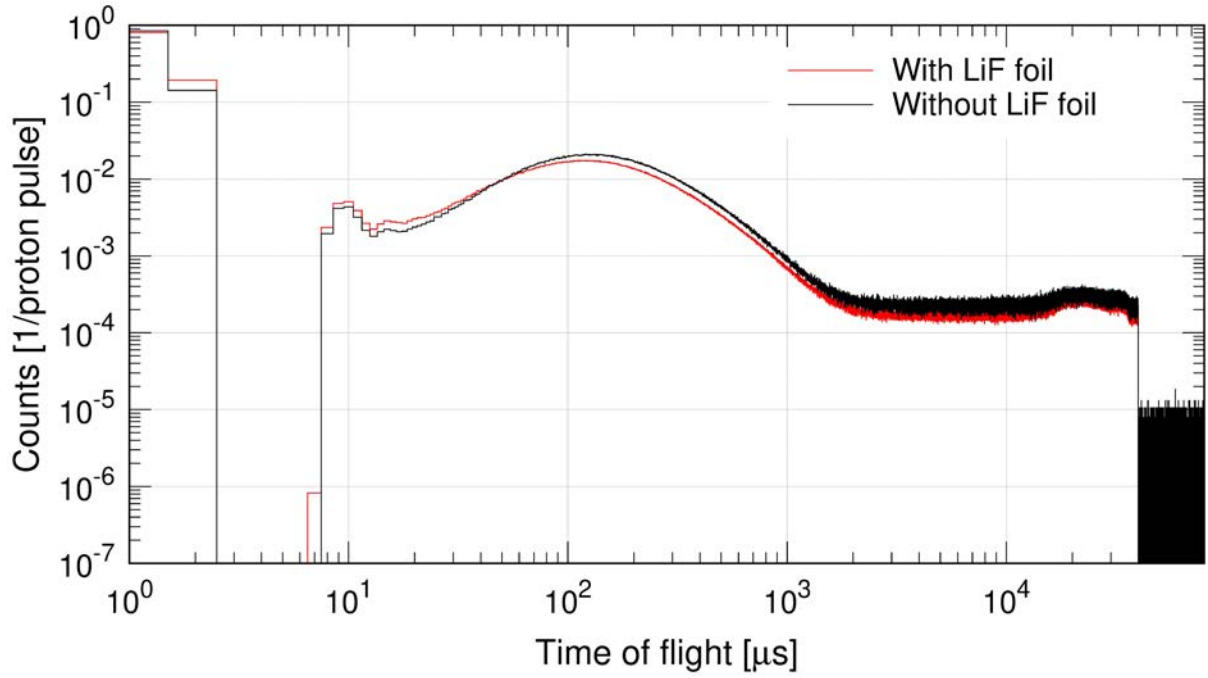


Figure 2: TOF spectra with and without LiF.

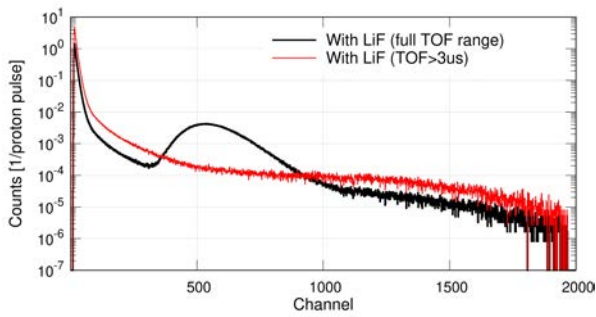


Figure 3: PH spectra with LiF of full TOF range and larger than 3  $\mu$ s.

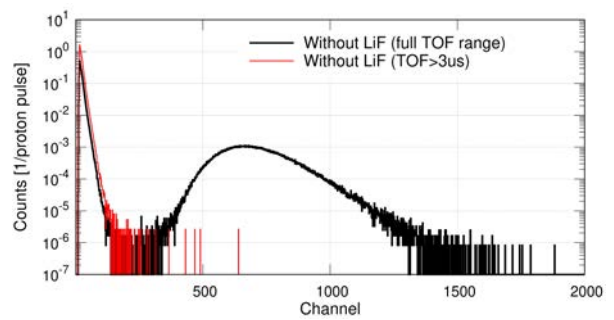


Figure 4: PH spectra without LiF of full TOF range and larger than 3  $\mu$ s.

## IV. SUMMARY

A new neutron detector system was designed and built. Signal from the  ${}^6\text{Li}(n, t){}^4\text{He}$  reaction was clearly observed. In the future plan, an enriched  ${}^6\text{Li}$  will be used and the system will be optimized. A waveform acquisition system is also planned to use to reduce the dead time. The new system will be tested at J-PARC and its performance will be evaluated.

## REFERENCES

- [1] Kino, K., et al. Nucl. Instrum. Methods Phys. Res. A 626, pp. 58-66, 2011.
- [2] Tatsuhiko S, et al. Journal of Nuclear Science and Technology, Vol. 55, No. 6, pp. 684-690, 2018.

## 34 Model Analysis of Isotope-Production Cross Sections for Proton- and Deuteron-Induced Reactions on $^{93}\text{Zr}$

Keita NAKANO\*, Yukinobu WATANABE, and Shoichiro KAWASE  
Department of Advanced Energy Engineering Science, Kyushu University,  
6-1 Kasuga-koen, Kasuga, Fukuoka 816-8580, Japan  
\*E-mail: knakano@aees.kyushu-u.ac.jp

Measurements of isotope-production cross sections in proton- and deuteron-induced reactions on  $^{93}\text{Zr}$  at 50, 105, and 209 MeV/nucleon have been performed so far. The calculation by a combination of INCL4.6 and GEM (INCL4.6/GEM) implemented in Particle and Heavy Ion Transport code System (PHITS) shows remarkable underestimation in the neutron-deficient region of odd-atomic number isotopes, where isotopes are produced predominantly via the evaporation process described by GEM. In contrast, the calculation by INCL++/ABLA07 reproduces their production cross sections successfully. The model analysis by using INCL++/ABLA07 and INCL++/GEM reveals that the reexamination of level density used in GEM is required to improve underestimation seen in the production cross sections calculated by PHITS.

### 1. Introduction

Treatment of High-Level radioactive Waste (HLW) is one of the crucial issues for nuclear energy developments because of the long-term radiotoxicity of long-lived fission products (LLFPs) included in HLW. Nuclear transmutation technology has received much attention as a possible method of the burden reduction of disposal of HLW by converting LLFPs into stable and/or short-lived nuclei. So far, measurements of isotope-production cross sections in proton- and deuteron-induced reactions on  $^{93}\text{Zr}$  at 50 [1], 105 [2], and 209 [3] MeV/nucleon have been performed in order to provide the fundamental data necessary for the design of nuclear transmutation system with spallation reaction. The measured data were compared with the theoretical model calculation by Particle and Heavy Ion Transport code System (PHITS) [4] to validate the reliability of PHITS calculation for use in the design of the optimized transmutation system. From the comparison, remarkable underestimation by PHITS calculation in the neutron-deficient region of odd-atomic number isotopes such as Nb and Y isotopes were seen regardless of incident particle and energy as shown in Fig. 1.

In PHITS calculation, the spallation reaction is described by a two-step process: an excited pre-fragment is formed by hard nucleon-nucleon binary collisions in an Intranuclear Cascade process (INC process), and subsequent de-excitation by emissions of light particles is simulated in an evaporation process. The Liège Intranuclear Cascade model (INCL4.6) [5] and the Generalized Evaporation Model (GEM) [6] are used for the INC process and the evaporation process in PHITS calculations, respectively. The magnitude of the production cross section in the neutron-deficient region is mainly determined in the evaporation process. Therefore, the underestimation is inferred

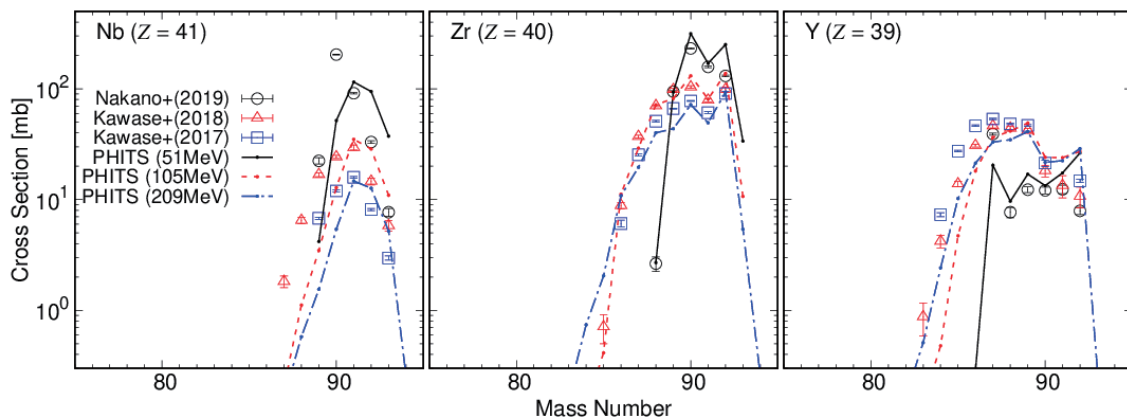


Fig. 1, Isotope-production cross section in proton-induced reaction on  $^{93}\text{Zr}$  for Nb (Left), Zr (Center), and Y (Right) isotopes. The circles, triangles, and squares represent the measured data at 51 MeV [1], 105 MeV [2], and 209 MeV [3], respectively. The solid, dashed, and dot-dashed lines indicate the calculated data by PHITS at 51, 105, and 209 MeV, respectively.

to be originated from GEM calculation. In this work, the cause of the underestimation seen in the isotope-production cross sections calculated by PHITS was investigated to achieve a better description of the isotope-production cross sections in the spallation reaction with PHITS.

## 2. Method

INCL++/ABLA07, which is a combination of C++ version of the Liège Intranuclear Cascade model [7] as the INC process and ABLA07 [8] as the evaporation process, successfully reproduces the isotope-production cross section, especially in the neutron-deficient region of odd-atomic-number isotopes. Therefore, the comparison between ABLA07 and GEM may provide information on the cause of the underestimation in the PHITS calculation. Figure 2 shows the measured isotope-production cross sections in the proton-induced reaction on  $^{93}\text{Zr}$  at 105 MeV [2] together with the calculations by INCL4.6/GEM implemented in PHITS and INCL++/ABLA07. The circles, the solid lines, and the dashed lines correspond to the measured data, the PHITS calculation, and the INCL++/ABLA07 calculation, respectively. As mentioned above, INCL++/ABLA07 reproduces the production cross sections in the neutron-deficient region of odd-atomic number isotopes well. While, PHITS fails to predict them. In GEM implemented in PHITS, charged particle emissions are enhanced from the original GEM. To remove the effect of this enhancement, the calculation by using INCL4.6 and original GEM was performed, and the result is shown by the dot-dashed lines in Fig. 2. The underestimation was improved by using the original GEM, but still two times underestimated. Prior to detailed comparisons between ABLA07 and original GEM, we examined the difference in isotope production caused by INC calculations with different codes. The calculation by using INCL++ and original GEM was performed as shown by the dotted lines in Fig. 2. In the regions of interest, the effect by the INC process is negligible. Therefore, we have performed the comparison between ABLA07 and GEM by INCL++/ABLA07 calculation and that by INCL++ and original GEM (INCL++/GEM).

For the comparison, the  $^{93}\text{Zr} + p$  reaction at 105 MeV was chosen. Since the two-step process

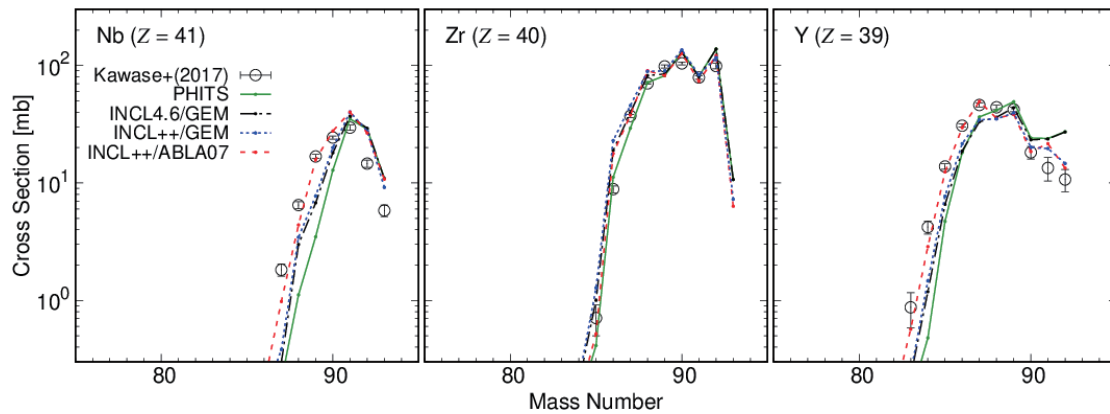


Fig. 2, Isotope-production cross section in proton-induced reaction on  $^{93}\text{Zr}$  at 105 MeV for Nb (Left), Zr (Center), and Y (Right) isotopes. The circles represent the measured data [2], and the lines indicate the calculated data by PHITS (solid), INCL4.6/GEM (dot-dashed), INCL++/GEM (dotted), and INCL++/ABLA07 (dashed).

is employed, the de-excitation process depends on the mass and atomic number of pre-fragment and its excitation energy. Monte Carlo calculations of the  $^{93}\text{Zr} + p$  reaction at 105 MeV were performed  $10^7$  times by using INCL++/ABLA07 and INCL++/GEM. For each calculation, the atomic number, the mass number, and the excitation energy of the pre-fragment formed in the INC process described by INCL++ were recorded. Then the evaporation processes were simulated by using the two evaporation codes, ABLA07 and GEM, and the atomic number, the mass number, and the kinetic energy of both the residual nuclei and emitted particles were recorded. The recorded data were analyzed event-by-event to clarify the difference in particle emissions between ABLA07 and GEM.

### 3. Results and Discussion

Figure 3 shows the branching ratios of proton and neutron emissions from  $^{93}\text{Nb}^*$  (Left),  $^{92}\text{Zr}^*$  (Center), and  $^{92}\text{Y}^*$  (Right) pre-fragments as a function of excitation energy. The dashed and the solid lines represent GEM calculation and ABLA07 calculation, respectively. The error bars show the statistical error. Large fluctuations in branching ratio at high excitation energy are not significant because of low statistics. In the GEM calculation, proton emission branching ratios in  $^{93}\text{Nb}^*$  and  $^{92}\text{Y}^*$  are twice as large as those in the ABLA07 calculation over the whole excitation energy. Conversely, the ABLA07 calculation shows a larger proton emission branching ratio in  $^{92}\text{Zr}^*$  than that in the GEM calculation. The branching ratios of other charged particle emission from  $^{93}\text{Nb}^*$  and  $^{92}\text{Y}^*$  are almost the same as those of proton emission. This tendency leads to the underestimation seen in the isotope-production cross sections of odd-atomic number isotopes. In the GEM calculation, the large proton emission branching ratio in Nb pre-fragment enhances the decays from Nb isotopes to Zr isotopes, but the decays from Zr isotopes to Y isotopes are suppressed due to the small proton emission branching ratio in Zr pre-fragments. As a result, the odd-atomic number isotopes have smaller yields in the evaporation stage in the GEM calculation, resulting in the underestimation in the neutron-deficient region of odd-atomic number isotopes.

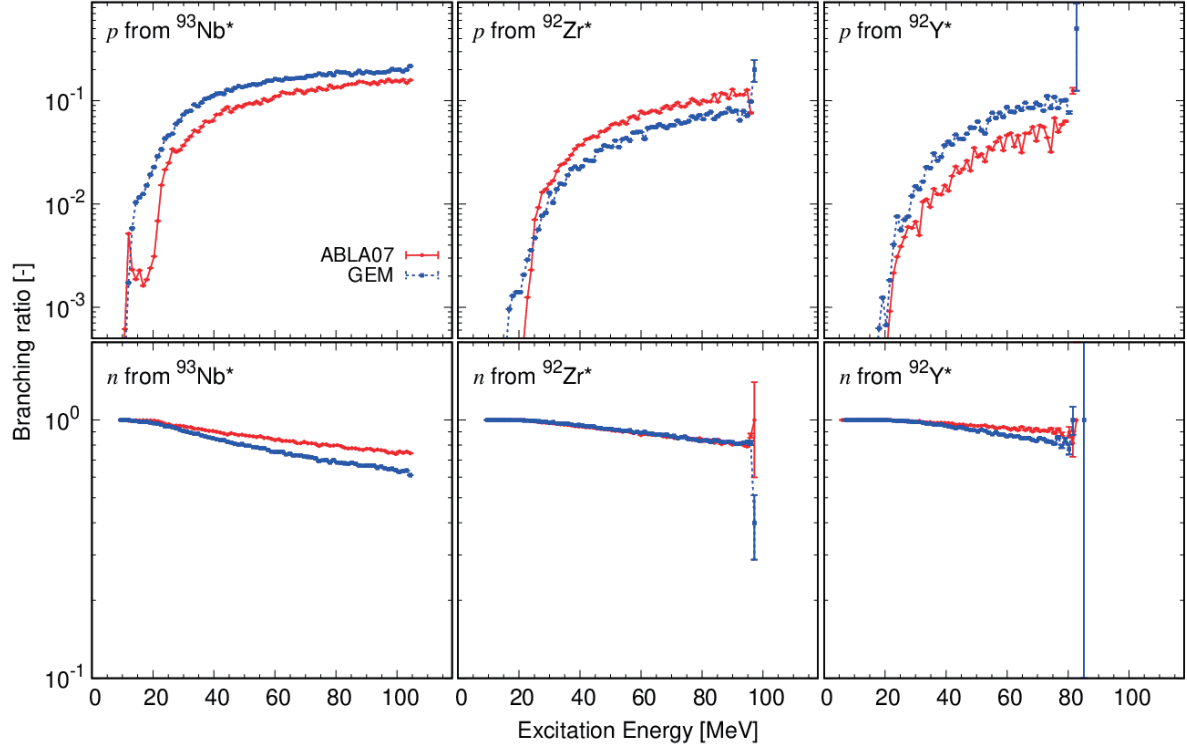


Fig. 3, Branching ratios for proton (Upper) and neutron (Lower) emissions from  $^{93}\text{Nb}^*$  (Left),  $^{92}\text{Zr}^*$  (Center), and  $^{92}\text{Y}^*$  (Right) pre-fragments calculated by GEM and ABLA07 codes as a function of the excitation energy of pre-fragment. The dashed and solid lines correspond to the GEM and ABLA07 calculations, respectively.

Next, we investigate the reason why the differences are seen in the branching ratios calculated in GEM and ABLA07. In GEM and ABLA07, the decay width of emitted particle  $j$  is calculated from the inverse cross section and the level density based on the Weisskopf-Ewing formalism [9]:

$$\Gamma_j \propto \int_V^{E_x-Q} \sigma_{\text{inv}}(\varepsilon) \frac{\rho_{\text{fin}}(E_x - Q - \varepsilon)}{\rho_{\text{init}}(E_x)} \varepsilon d\varepsilon, \quad (1)$$

where  $E_x$ ,  $Q$ ,  $V$ , and  $\varepsilon$  represent the excitation energy of the parent nucleus, the  $Q$ -value of the reaction, the Coulomb barrier between the daughter nucleus and the emitted particle, and the kinetic energy of the emitted particle. Also,  $\sigma_{\text{inv}}$  denotes the inverse cross section corresponding to the cross section of the inverse process, that is, the incident of the emitted particle into the daughter nucleus. The variables  $\rho_{\text{init}}$  and  $\rho_{\text{fin}}$  correspond to the level densities of the parent and the daughter nucleus, respectively. Here, both or either  $\sigma_{\text{inv}}$  or  $\rho$  can be the cause of the underestimation. As the first step, we checked the behavior of  $\sigma_{\text{inv}}$  with attention to the difference between the odd- and even-atomic number isotopes. Figure 4 shows the  $\sigma_{\text{inv}}(\varepsilon)$  implemented in GEM and ABLA07. The inverse cross section of the proton emission from  $^{93}\text{Nb}^*$ , which corresponds to the proton-induced reaction on  $^{92}\text{Zr}$ , is drawn by the dashed lines. That of proton emission from  $^{92}\text{Zr}^*$ , which corresponds to the proton-induced reaction on  $^{91}\text{Y}$ , is displayed by the dotted lines. We found that there is no appreciable odd-even effect on the inverse cross section used in both the calculations. Therefore, it is confirmed that the inverse cross section has no dependence on the

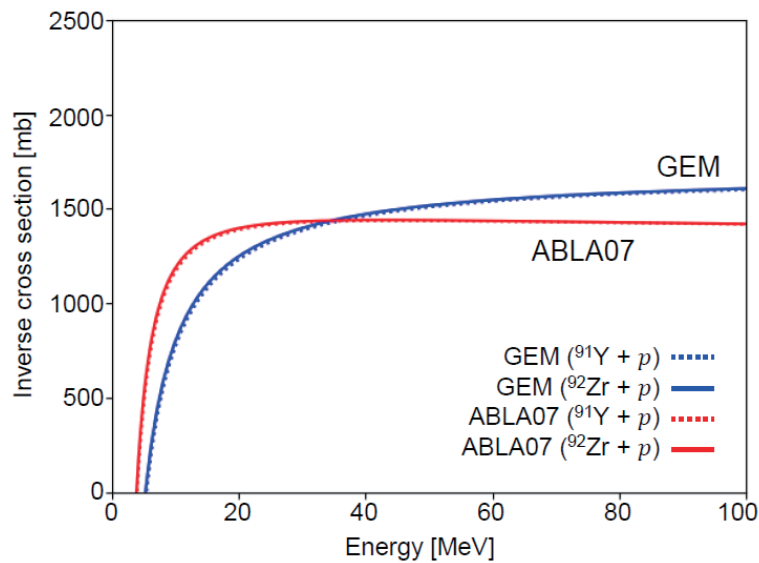


Fig. 4, Inverse cross sections calculated by GEM and ABLA07 as a function of the kinetic energy of the emitted particle. The dotted and solid lines show the inverse reactions of proton emission from pre-fragments of  $^{92}\text{Zr}^*$  ( $^{91}\text{Y} + p$ ) and  $^{93}\text{Nb}^*$  ( $^{92}\text{Zr} + p$ ), respectively.

even-odd of pre-fragment although the difference of the isotopic production between GEM and ABLA07 calculations originated from the inverse cross section is seen. This strongly implies that the level densities implemented in GEM is the cause of the remarkable underestimation in the Nb and Y isotopes, and should be reconsidered to resolve the underestimation as discussed in Ref. [10].

#### 4. Conclusion

The isotope-production cross section calculated by INCL4.6/GEM implemented in PHITS shows remarkable underestimation in the neutron-deficient region of odd-atomic number isotopes such as Nb and Y isotopes. The cause of the underestimation was investigated by comparing the calculations by INCL++/GEM and INCL++/ABLA07. From the calculated branching ratios, the proton emissions from the isotopes with the odd-atomic number are greatly enhanced in GEM calculation compared to ABLA07 calculation, resulting in the underestimation of isotope-production cross sections in the neutron-deficient region of odd-atomic number isotopes. Since the inverse cross sections in GEM and ABLA07 show no difference between neighboring nuclei with odd and even atomic numbers, the enhanced proton emission can be originated from the level density in GEM and the modification of the level density may improve the underestimation. In the future, the improvement of the level density in GEM, *e.g.* modification of the pairing correction, is expected.

#### References

- [1] K. Nakano, S. Kawase, Y. Watanabe, et al., Isotope-production cross sections of residual nuclei in proton- and deuteron-induced reactions on  $^{93}\text{Zr}$  at 50 MeV/u, presented at ND2019 International Conference on nuclear data for science and technology, 2019 May 19-24, Beijing,

China.

- [2] S. Kawase, K. Nakano, Y. Watanabe, et al., Study of proton- and deuteron-induced spallation reactions on the long-lived fission product  $^{93}\text{Zr}$  at 105 MeV/nucleon in inverse kinematics, Prog. Theor. Exp. Phys. 2017;2017:093D03.
- [3] S. Kawase, Y. Watanabe, K. Nakano, et al., Measurement of isotopic production cross sections of proton- and deuteron-induced reactions on  $^{93}\text{Zr}$  at 200 MeV/nucleon, JAEA-Conf 2018-001, 2018:111-114.
- [4] T. Sato, Y. Iwamoto, S. Hashimoto, et al., Features of Particle and Heavy Ion Transport code System (PHITS) version 3.02, J. Nucl. Sci. Technol. 2018;55(6);684-690.
- [5] A. Boudard, J. Cugnon, J.-C. David, et al., New potentialities of the Liège intranuclear cascade model for reactions induced by nucleons and light charged particles, Phys. Rev. C 2013;87:014606.
- [6] S. Furihata, Statistical analysis of light fragment production from medium energy proton-induced reactions, Nucl. Instrum. Meth. B 2000;171:251-258.
- [7] D. Mancusi, A. Boudard, J. Cugnon, et al., Extension of the Liège intranuclear-cascade model to reactions induced by light nuclei, Phys. Rev. C 2014;90:054602.
- [8] A. Kelic, M.V. Ricciardi, K.-H. Schmidt, ABLA07 – towards a complete description of the decay channels of a nuclear system from spontaneous fission to multifragmentation, arXiv:0906.4193, 2009.
- [9] V.F. Weisskopf, D.H. Ewing, On the Yield of Nuclear Reactions with Heavy Elements, Phys. Rev. 1940;57:472-485.
- [10] S. Sato, Y. Watanabe, Effect of the level density on odd-even staggering in proton- and deuteron-induced spallation reactions on  $^{93}\text{Zr}$  and  $^{107}\text{Pd}$ , JAEA-Conf 2019-001 2019:103-108.

## 35 Systematical calculation of probabilities of beta-delayed neutron emission and fission in the entire region of nuclear chart

Hiroyuki KOURA

Advanced Science Research Center, Japan Atomic Energy Agency

Shirakata 2-4, Tokai-mura, Ibaraki 319-1195, Japan

Fumitaka Endo

Department of Physics, Tohoku University, Aoba, Sendai, Miyagi 980-8578, Japan

e-mail: koura.hiroyuki@jaea.go.jp

In the very neutron-rich nuclei, the beta-decay occurs with some accompanying processes as neutron emissions. The beta-delayed fission also takes place in the superheavy nuclear mass region. The beta-delayed neutron process is an important phenomenon for manipulating nuclear reactor, and the beta-delayed fission critically affects the termination of the r-process nucleosynthesis in stars. We performed a systematical calculation of probabilities of beta-delayed neutron and beta-delayed fission in the entire region of nuclear chart with the improved gross theory of beta-decay and the KTUY mass model.

### 1. Introduction

The  $\beta^-$  decay occurs with a weak interaction in the neutron-rich nuclear mass region and nucleus releases electron, gamma-ray and anti-neutrino. Many neutron-rich nuclei can emit neutrons through  $\beta$  decay, called delayed neutrons. Delayed neutrons play an important role in allowing nuclear reactors to be safely controlled, due to the delay that causes between neutron-induced fission events and their eventual emission. Moreover, in the superheavy nuclear mass region, some of nuclei occur fission process due to the repulsive Coulomb force between protons. Regarding the beta decay, beta-delayed fission can occur if the fission barrier of daughter nucleus is lower than the beta-decay Q-value of parent nucleus. These nuclei are expected to be very neutron-rich and superheavy nuclear mass region.

In order to estimate  $\beta$ -decay rate, delayed neutron probability, and delayed fission probability theoretically, calculation of the nuclear matrix elements of the  $\beta$  decay is required. The gross theory is a type of macroscopic model to describe various  $\beta$ -decay properties. It is based on sum rules of the  $\beta$ -decay strength function, and treats the transitions to all the final nuclear levels in a

statistical manner. The gross theory has been successful in describing  $\beta$  decay for the entire nuclear mass range [1–6]. The results of the gross theory provide a guide to experiments on  $\beta$  decay, especially, for newly measured nuclear data of very neutron-rich nuclei, and for purely theoretical nuclear data extremely far from known nuclei. Due to its statistical treatment, the gross theory only describes macroscopic features. Recently, we have introduced a treatment of spin and parity to the gross theory, and have improved decay rate in especially the forbidden transition [7-9].

In this report, we perform a systematical calculation of probabilities of beta-delayed neutron and beta-delayed fission in the entire region of nuclear chart with the improved gross theory of beta-decay and the KTUY nuclear mass model [10] and fission barrier calculation [11].

## 2. Beta decay

The decay constant of the  $\beta$ -decay can be divided by the types of  $\beta$ -decay operators,  $\Omega$ , and the decay constant is obtained as the sum of partial decay constants,  $\lambda_\Omega$ . If we take into account the allowed and first forbidden transitions, the total  $\beta$ -decay rate is expressed as

$$\lambda_\beta = \lambda_F + \lambda_{GT} + \lambda_{1st} + \dots,$$

where the right-hand represents the decay rates of the Fermi transition, Gamow-Teller transition, and the first-forbidden transition. The first two terms are the allowed transitions.

Under the usual approximation, each decay rate can be written with the nuclear matrix elements,  $|M_\Omega(E)|$ , which can be calculated in the framework of the nuclear physics, and the integrated Fermi function,  $f$ , which represents a distortion of wave functions due to the Coulomb force. The actual expressions for the allowed transitions are

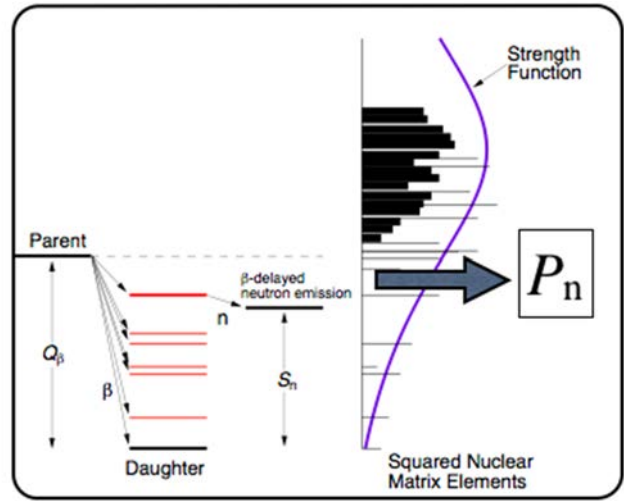


Figure 1: Illustration of beta decay and beta-delayed neutron emission. (Left): Level scheme of beta decay. (Right): Strength function of beta decay. The (black) histograms indicate the intensity of beta decay, which is equal to squared nuclear matrix element,  $|M_\Omega(E)|^2$ . The purple line is the strength function averaged with each intensity.  $P_n$ : Beta-delayed neutron emission probability. This decay is available with  $Q_\beta - S_n > 0$ .

$$\lambda_F = \frac{m_e^5 c^4}{2\pi^3 \hbar^7} |g_V|^2 \int_{-Q_\beta}^0 |M_F(E)|^2 f(-E) dE,$$

$$\lambda_{GT} = \frac{m_e^5 c^4}{2\pi^3 \hbar^7} |g_A|^2 \cdot 3 \times \int_{-Q_\beta}^0 |M_{GT}(E)|^2 f(-E) dE,$$

Here, the coefficients are composed of the coupling constant of the weak interaction and the physical constants as the mass of electron,  $m_e$ , the light velocity,  $c$ , the Planck constant per  $2\pi$ ,  $\hbar$ . The coupling constant of the weak interaction has two types: the vector type as  $g_V$  and the axial vector type as  $g_A$ , respectively. The integral is performed from  $-Q_\beta$  to 0 and  $Q_\beta$  is the total (maximum) decay energy from the ground-state of parent to daughter nuclei, or  $\beta$ -decay  $Q$ -value.

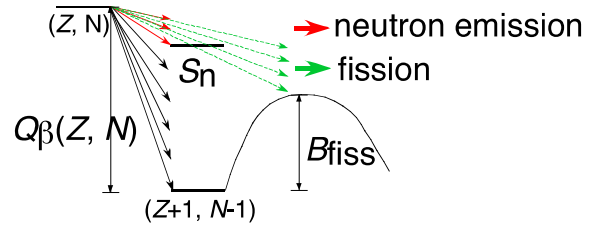
The emission of delayed neutrons is a phenomenon that accompanies  $\beta$  decay. Figure 1 shows a schematic illustration of the  $\beta$  decay and delayed neutron emission processes. In  $\beta$  decay, a nucleus decays from the parent ground state to a particular daughter state. If the neutron separation energy for the daughter nucleus,  $S_n$ , is smaller than  $Q_\beta$ , the nucleus can emit a neutron with an energy from 0 to  $Q_\beta - S_n$ , measured from the ground state of the parent nucleus. This process occurs in the transmission process of the quantum mechanics. The situation of beta-delayed fission is the same as the delayed neutron (Fig. 2).

However, the fission process occurs in the tunneling penetration, which is rather different from the neutron emission. The decay widths of delayed neutron emission and delayed fission probabilities are calculated by the following expressions:

$$\Gamma_n(E) = \frac{1}{2\pi} \frac{1}{\rho(E)} \frac{2MR^2}{\hbar^2} g \int_0^{E-S_n} \rho^*(E - S_n - \varepsilon) \varepsilon d\varepsilon,$$

$$\Gamma_f(E) = \frac{1}{2\pi} \frac{1}{\rho(E)} \int_{-\infty}^{E-B_{\text{fiss}}} \frac{\rho^*(E - B_{\text{fiss}} - \varepsilon)}{1 + \exp\left[-\frac{2\pi E}{\hbar\omega}\right]} d\varepsilon,$$

where,  $M$  is the mass of the nucleus,  $R$  is the radius,  $g$  is the weight,  $\rho^*(E)$  is the level density of the daughter nucleus,  $\omega$  is the width of the fission barrier, and  $B_{\text{fiss}}$  is the fission barrier height of



$\beta$ -delayed neutron emission and  $\beta$ -delayed fission  
Figure 2: Illustration of beta-delayed neutron emission and beta-delayed fission.

the daughter nucleus.

With the use of these decay widths and that of gamma transition,  $\Gamma_\gamma$ , the probabilities of beta-delayed neutron and beta-delayed fission are calculated as

$$P_k = \frac{C}{\lambda} \int_{-Q_\beta}^0 S_\beta(E) f(-E) \frac{\Gamma_k}{\Gamma_\gamma + \Gamma_n + \Gamma_f} dE,$$

where,  $k$  is indication of the decay process ('n' for delayed neutron, and 'f' for delayed fission). The coefficient  $C$  is a constant related to the coefficients outside the integrals. The decay constant of the beta decay,  $\lambda$ , and the beta-decay strength function,  $S_\beta(E)$ , are calculated from the improved gross theory [7-9].

### 3. Results

Figure 3 shows examples of calculated beta-delayed neutron emission probabilities. Due to the shell closures from the KTUY nuclear mass model, discontinuity of the probabilities along  $N=82$ ,  $126$ ,  $184$ , and  $228$  appears. Generally, the probabilities increase with increasing of neutron-rich can be seen. This trend continues even in the superheavy nuclear mass region.

The beta-delayed fission probabilities are also shown in Fig. 4. In the landscape of fission-barrier height with the

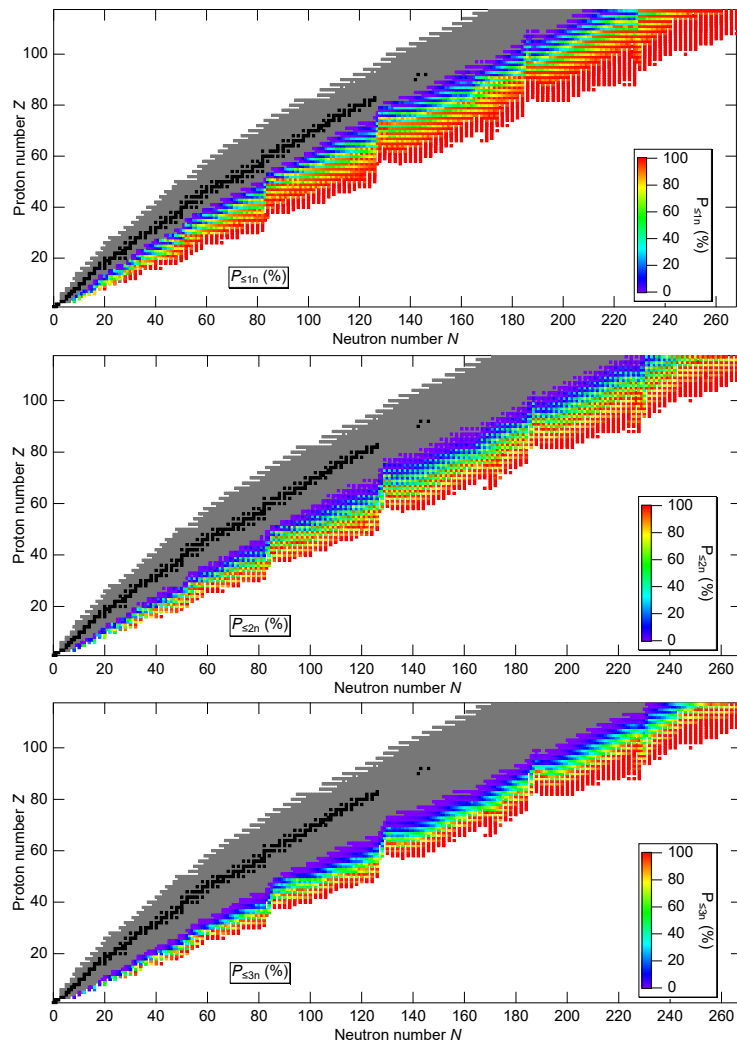


Figure 3: Examples of beta-delayed neutron emission probabilities for one-, two- and three- neutron emissions.  $P_{\leq 1n}$ : Probability of one-neutron emission excluding two or more neutrons.  $P_{\leq 2n}$ : Probability of two-neutron emission excluding three or more neutrons.  $P_{\leq 3n}$ : three-neutron emission excluding four or more neutrons. Black square indicates the long-lived nuclei and gray one shows estimated proton and neutron-drip lines.

KTUY mass model in super- and extremely super-heavy mass region, the “conventional” island of stability is found near nuclei with  $Z=114$  and  $N=184$ , while there is “peninsula” along  $N=228$ , which appeared in Ref. [11]. The  $N=228$  peninsula is caused by single-particle shell gap of  $N=228$  as described in Ref. [12]. These properties affect the beta-delayed fission probabilities. In Figure 4, there are lower probabilities

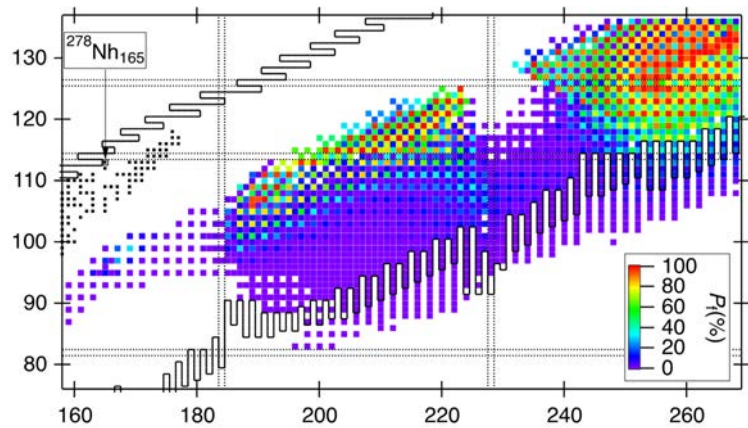


Figure 4: Beta-delayed fission probabilities. The black points indicate experimentally-identified nuclides until 2018, from the chart of the JAEA nuclides 2018 [13].

around  $Z=126$  and  $N=228$ . This trend comes from higher fission barrier of the KTUY model around the same region. Below the region of  $N=228$ , beta-delayed fission process is limited only along beta-stable mass region, which locates nearly  $Z=114$  and  $N=184$ , and  $Z=126$  and  $N=228$ . Above the region of  $N=228$ , beta-delayed fissioning region dominates. The beta-delayed fission affects the abundance of the rapid neutron capture process (r-process) in stars. The fission acts as termination and probably recycling of synthesis of nuclides.

#### Acknowledgment

This work was financially supported by the Japan Society for the Promotion of Science KAKENHI (Grants No. 18K03631 and No. 17H06090) as a program ‘Effects of fission to isotopic abundances on the r-process synthesis in star’ and ‘Study of the origin of heavy elements using an innovative mass spectrograph’.

#### References

- [1] K. Takahashi, M. Yamada, Prog. Theor. Phys. 41, 1470 (1969)
- [2] S. Koyama, K. Takahashi, M. Yamada, Prog. Theor. Phys. 44, 663 (1970)
- [3] K. Takahashi, M. Yamada, T. Kondoh, Atom. Dat. Nucl. Dat. Tab. 12, 101 (1973)
- [4] T. Kondoh, T. Tachibana, M. Yamada, Prog. Theor. Phys. 74, 708 (1985)
- [5] T. Tachibana, M. Yamada, Y. Yoshida, Prog. Theor. Phys. 84, 641 (1990)
- [6] T. Tachibana, M. Yamada, Proc. Int. Conf. on Exotic Nuclei and Atomic Masses, ENAM95,

(Editions Frontueres, Gif-sur-Yvette, 2015), p. 763, and references therein.

<https://wwwndc.jaea.go.jp/nuclldata/beta-decay-properties.pdf> (accessed 2020/03/24).

[7] H. Koura, T. Yoshida, T. Tachibana, S. Chiba, EPJ Web of Conferences 146, 12003 (2017)

[8] H. Koura, S. Chiba, Phys. Rev. C 97, 06430 (2017)

[9] F. Endo, H. Koura, Phys. Rev. C 99, 034303 (2019)

[10] H. Koura, T. Tachibana, M. Uno, M. Yamada, Prog. Theor. Phys. 113, 305 (2005)

[http://wwwndc.jaea.go.jp/nuclldata/mass/KTUY04\\_E.html](http://wwwndc.jaea.go.jp/nuclldata/mass/KTUY04_E.html) (accessed 2020/03/24).

[11] H. Koura, Prog. Theor. Exp. Phys. 2014, 113D02 (2014)

[12] H. Koura, S. Chiba, J. Phys. Soc. Jpn. 82, 014201 (2013)

[13] H. Koura, J. Katakura, T. Tachibana and F. Minato, JAEA-Conf 2019-001, 151-156 (2019)

## **36 Development of multi-group neutron activation cross-section library from JENDL/AD-2017**

Chikara KONNO

Japan Atomic Energy Agency

Email: konno.chikara@jaea.go.jp

JENDL Activation Cross Section File for Nuclear Decommissioning 2017 (JENDL/AD-2017) was released in 2018. Then a multi-group neutron activation cross-section library (MAXS/AD-2017) with the same format as MAXS-2015 by Dr. Okumura has been developed from JENDL/AD-2017 by using PREPRO 2018 for activation calculations in nuclear facility decommissioning. MAXS/AD-2017 will be converted to ORIGEN libraries and be tested with the JPDR decommissioning data. In future MAXS/AD-2017 will be released.

### **1. Introduction**

JENDL Activation Cross Section File for Nuclear Decommissioning 2017 (JENDL/AD-2017) [1] was released in 2018. This file includes the data of neutron-induced nuclear reactions for 311 nuclides from  $10^{-5}$  eV to 20 MeV. Dr. Okumura et al. developed a multi-group neutron activation cross-section library (MAXS2015) based on the nuclear data libraries JENDL-4.0 [2] and JEFF-3.0/A [3] for activation calculations in nuclear facility decommissioning [4]. A multi-group neutron activation cross-section library (MAXS/AD-2017) with the same format as MAXS-2015 has been developed from JENDL/AD-2017 in order to make it possible to use the new JENDL file for activation calculations in nuclear facility decommissioning.

### **2. How to make MAXS/AD-2017**

JENDL/AD-2017 includes total production cross sections (MF3) of radioactive and stable nuclides, branching ratios (MF9) and partial production cross sections (MF10) for the ground and isomer states of nuclides. JENDL/AD-2017 has the following four versions;

- MF3, MF9 and MF10 at 0 K,
- MF3, MF9 and MF10 at 293.6 K,
- MF3 and MF10 at 0 K (for NJOY [5] processing),
- MF3 and MF10 at 293.6 K (for NJOY processing).

MAXS-2015 was produced with the NJOY2012 [5] code. However it was found that GENDF files produced with the group module in NJOY2012 did not include production cross sections to isomer states. Then the PREPRO 2018 [6] code was adopted for producing a group-wise file of JENDL/AD-2017 (MF3, MF9 and MF10 at 0 K). The following modules in PREPRO 2018 were used; ENDF2C, LINEAR, RECENT, SIGMA1, ACTIVATE, FIXUP, DICTIN, GROUPIE. The calculation conditions are as follows;

- Temperature : 300 K,

- Group structure : 199 groups (VITAMIN-B6 [7]),
- Weighting spectrum : Maxwell + 1/E + Fission,
- Infinite dilution cross section.

The produced group-wise file of JENDL/AD-2017 was converted to MAXS/AD-2017 of the MAXS format [4] with a small program. Figure 1 shows the data of  $^{59}\text{Co}$  in MAXS/AD-2017 as an example. Figure 2 plots the capture cross section (red line) of  $^{59}\text{Co}$  in MAXS/AD-2017 with the continuous energy one (blue line), where the red line represents the blue line well.

The following issues were pointed out in this processing.

- No information of decay data (MF8) in the capture reaction of  $^{187}\text{W}$  and  $^{193}\text{Os} \rightarrow \text{Add}$
- The MT number of the (n,t) reaction of  $^6\text{Li}$  is changed from 105 to 107 for ORIGEN-S [8] because ORIGEN-S cannot treat the (n,t) reaction.
- The MAXS format includes no data for the (n,n') reaction  $\rightarrow$  MAXS/AD-2017 includes the data for the (n,n') reaction, though ORIGEN-S cannot treat the (n,n') reaction.

A similar procedure for a DCHAIN-SP [9] library was also established, and was provided to the PHITS group. Users can use the DCHAIN-SP library of JENDL/AD-2017 in the latest PHITS (PHITS3.16) [9].

### 3. Summary

A multi-group neutron activation cross-section library (MAXS/AD-2017) with the MAXS format was developed from JENDL/AD-2017 for activation calculations in nuclear facility decommissioning. Next MAXS/AD-2017 will be converted to ORIGEN-S libraries and be tested with the JPDR decommissioning data [10]. Then MAXS/AD-2017 will be released.

### 4. References

- [1] <https://www.ndc.jaea.go.jp/ftpnd/jendl/jendl-ad-2017.html> (current as of Jan. 2020).
- [2] K. Shibata, O. Iwamoto, T. Nakagawa et al., JENDL-4.0: “a new library for nuclear science and engineering”, J. Nucl. Sci. Technol. 48, 1 (2011).
- [3] J-Ch. Sublet, A.J. Koning, R.A. Forrest, and J. Kopecky, “The JEFF-3.0/A Neutron Activation File—New Features, Validation, and Usage”, AIP Conference Proceedings 769, 203 (2005).
- [4] K. Okumura, K. Kojima, K. Tanaka, “Development of multi-group neutron activation cross-section library for decommissioning of nuclear facilities”, Proc. of 2014 Symposium on Nuclear Data, p. 43, JAEA-Conf 2015-003(2016).
- [5] R.E. MacFarlane, D. W. Muir, R. M. Boicourt, A. C. Kahler, “The NJOY Nuclear Data Processing System, Version 2012”, LA-UR-12-27079, Los Alamos National Laboratory (2012).
- [6] <https://www.nds.iaea.org/public/endl/prepro2018/> (current as of Jan. 2020).
- [7] J.E. White, et al., “Production and Testing of the Revised VITAMIN-B6 Fine-Group and the BUGLE-93 Broad-Group Neutron/Photon Cross-Section Libraries Derived From ENDF/B-VI.3 Nuclear Data”, ORNL/TM-6795/R1 (2000).

- [8] I.C. Gauld, O.W. Hermann, R.M. Westfall, “ORIGEN-S: SCALE SYSTEM MODULE TO CALCULATE FUEL DEPLETION, ACTINIDE TRANSMUTATION, FISSION PRODUCT BUILDUP AND DECAY, AND ASSOCIATED RADIATION SOURCE TERMS”, ORNL/TM-2005/39 Version 6 Vol. II, Sect. F7 (2009).
- [9] <https://phits.jaea.go.jp/News.html#news0030> (current as of Jan. 2020).
- [10] N. P. Kocherov (Ed.), “International benchmark calculations of radioactive inventory for fission reactor decommissioning”, INDC(NDS)-355 (1996).



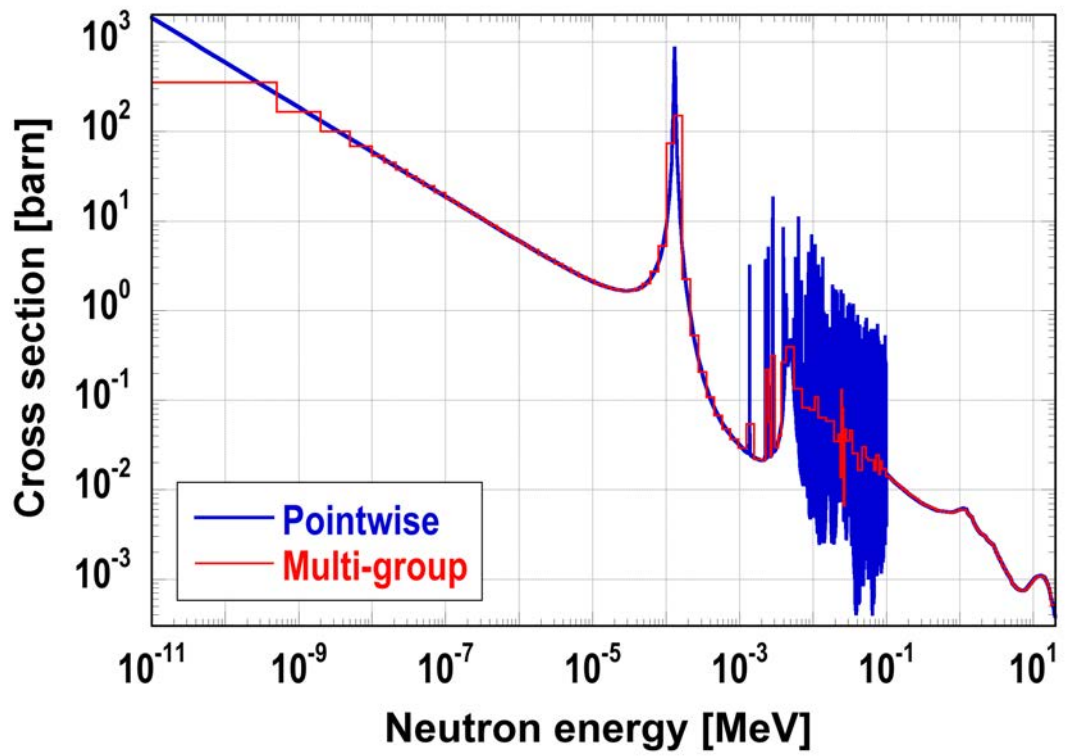


Fig. 2 Capture cross section of  $^{59}\text{Co}$  in JENDL/AD-2017 (Red line : MAXS/AD-2017).

This is a blank page.

## 37 Quantification of Integral Data Effectiveness Using the Concept of Active Sub-Space in Nuclear Data Testing

Go CHIBA, Daichi IMAZATO

*Faculty of Engineering, Hokkaido University*

*Kita-13 Nishi-8, Kita-ku, Sapporo, Hokkaido, 060-8628 Japan*

e-mail: go\_chiba@eng.hokudai.ac.jp

Several methods based on the concept of the active sub-space are proposed to quantify integral data effectiveness, and they are adopted to existing 32 integral data with multi-group cross section representation. Dimensions of sub-spaces spanned by integral data in a nuclear data space can be quantified with the proposed method using orthogonal projections of each integral data vector to the sub-space. In addition, a method to choose a minimum independent integral data set is proposed, and it is demonstrated that this method can properly choose a wide variety of integral data among a set of dependent integral data.

### 1 Introduction

In the field of nuclear and radiation engineering, a huge amount of experimental data related to the reactor physics and the radiation shielding have been obtained at various facilities in the world, and some of them have been released to the public as open data to validate numerical tools solving reactor physics and radiation shielding problems. Experimental data which can be utilized to validate nuclear data are referred to as *integral data* in the field of nuclear data engineering, and so many integral data have been accumulated through international projects such as ICSBEP and IRPhEP. Those integral data have been efficiently utilized to test evaluated nuclear data files.

As described above, the number of available integral data has become enormous now, so it is important to choose a proper set of integral data when testing evaluated nuclear data files with them. To do so, dependency among integral data should be carefully examined, so a procedure how to choose proper integral data is desired. We have proposed to adopt the concept of the active sub-space to this problem in our previous study and have tested our method with a set of existing integral data with one-energy group approximation[1] and a set of fictitious integral data with multi-group treatment[2] in the past.

In the present work, we propose a new procedure to quantify independency of a set of integral data and a new method to choose a minimum set of independent integral data among a huge amount of integral data. These methods are adopted to actual integral data with multi-group representation.

### 2 Theory

#### 2.1 Basic concept of the proposed method

We regard each of nuclear data (ND) is a vector which is orthogonal to other ND vectors, and a *nuclear data space* can be defined from a set of these ND vectors. A sensitivity of integral data with respect to ND is regarded as a vector in the nuclear data space, and a set of sensitivity vectors can span a sub-space, which we call an *integral data space*. Dimension of the integral data space can be defined, and is equal to or smaller than the number of sensitivity vectors. An orthonormal set of basis vectors of the integral data space can be also derived.

If a ND vector exists on the integral data space, this means that this ND can be independently validated with this set of the integral data. On the other hand, if a ND vector does not exist on the integral data space, it is impossible to independently validate this ND with this set of the integral data. In our method, possibility of the independent validation of each ND is quantified by a norm of an orthogonally-projected vector of this ND vector to the integral data space. This is illustrated in **Fig. 1** where a two-dimensional integral data space and a ND vector are presented.

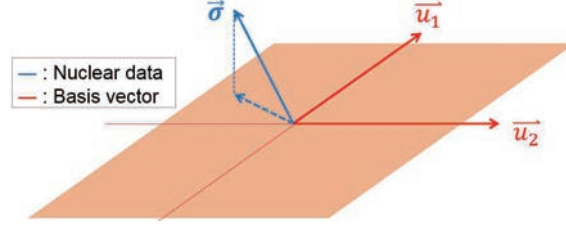


Fig. 1: Relation of an integral data space and a nuclear data vector

## 2.2 On quantification of integral data space dimension

An orthonormal basis set of an integral data space can be obtained by the singular value decomposition of a sensitivity matrix  $\mathbf{S}_{I \times J} = (\mathbf{s}_1 \ \mathbf{s}_2 \ \cdots \ \mathbf{s}_J)$  where  $\mathbf{s}_j$  is a sensitivity vector of the  $j$ th integral data and is defined as  $\mathbf{s}_j = \left( \frac{dp_j}{d\sigma_1} \ \frac{dp_j}{d\sigma_2} \ \cdots \ \frac{dp_j}{d\sigma_I} \right)^T$ , where  $p_j$  is a parameter of the  $j$ th integral data and  $\sigma_i$  is the  $i$ th nuclear data. The superscript  $T$  is for vector transposition. The numbers of nuclear data and integral data are denoted to as  $I$  and  $J$  here. To obtain dimension and an orthonormal basis of the integral data space, the singular value decomposition of  $\mathbf{S}$  is carried out as  $\mathbf{S} = \mathbf{U}\mathbf{D}\mathbf{V}^T$  where  $\mathbf{U}_{I \times I} = (\mathbf{u}_1 \ \mathbf{u}_2 \ \cdots \ \mathbf{u}_l \ \cdots \ \mathbf{u}_I)$  and

$$\mathbf{D}_{I \times J} = \begin{pmatrix} \sigma_1^2 & 0 & \cdots & 0 & 0 & \cdots & 0 \\ 0 & \sigma_2^2 & \cdots & 0 & 0 & \cdots & 0 \\ \vdots & \vdots & \ddots & 0 & 0 & \cdots & 0 \\ 0 & 0 & 0 & \sigma_l^2 & 0 & \cdots & 0 \\ 0 & 0 & 0 & 0 & 0 & \cdots & 0 \\ \vdots & \vdots & \vdots & \vdots & \vdots & \ddots & 0 \\ 0 & 0 & 0 & 0 & 0 & \cdots & 0 \end{pmatrix}, \quad (1)$$

where  $l$  is the dimension and  $\mathbf{u}_i$  ( $1 \leq i \leq l$ ) are orthonormal basis of the integral data space considered here.

**Figure 2** shows singular values distributions of several sensitivity matrices obtained in the previous study[1]. Generally, the same number of singular values as the number of integral data is numerically calculated, so we need to determine a threshold value for singular values to separate meaningful components from noise (meaningless) components. As this figure suggests, however, it is very difficult to do this since there is no clear boundary showing drastic change in the behavior.

In the present work, we propose the following procedure to determine the dimension of the integral data space:

1. A set of orthonormal basis vectors is obtained by the singular value decomposition of a sensitivity matrix. Set  $n=1$ .
2. Choose  $n$  principal basis vectors corresponding to the largest singular values, and construct a  $n$ -dimensional sub-space spanned by these  $n$  basis vectors.

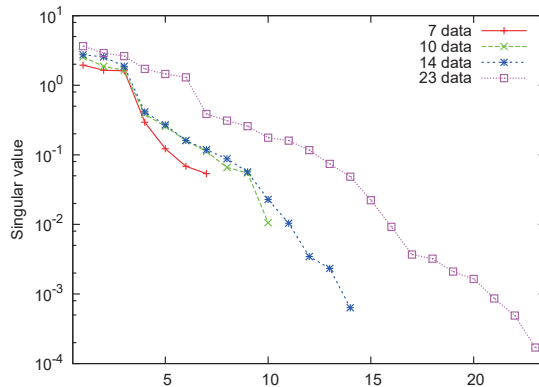


Fig. 2: Example of singular values distributions of sensitivity matrices.[1] The X-axis corresponds to the singular value index.

3. Each of sensitivity vectors is orthogonally projected to this sub-space, and norms of the projected vectors are calculated. Note that sensitivity vectors are normalized so as to make their norms unity in this step.
4. If the minimum value of the norms obtained at the step 3 is smaller than a criteria,  $n$  is increased by one, and a procedure from the step 2 is carried out again. If the minimum norm is larger than this criteria, this procedure is terminated and the dimension of the integral data space is determined as  $n$ .

This procedure is based on rather a physical aspect than a mathematical aspect simply setting a criteria on singular values. In the present work, this criteria is set 0.99. Note that obtained results with the proposed method should depend on this parameter setting.

### 2.3 A method choosing minimum independent data set

There are a huge amount of available integral data, but it is unrealistic to use all of them when testing evaluated nuclear data files. Here we propose a method to choose a minimum independent data set from integral data. The procedure is as follows:

1. The first principal basis vector of the integral data space having the largest singular value is taken, and inner products of this vector and each of sensitivity vectors are calculated. After doing this, a sensitivity vector which gives the largest inner product is chosen as the first integral data.
2. Construct a sub-space spanned by sensitivity vectors of the chosen integral data.
3. Each of non-chosen normalized sensitivity vectors is orthogonally projected to the sub-space constructed at the step 2. If norms of all these projected vectors are larger than a criteria, this procedure is terminated. If not, a sensitivity vector which gives the minimum norm is chosen, and go back to the step 2.

The criteria at the step 3 is arbitrary, and 0.99 is chosen in the present work.

## 3 Numerical result

The proposed method is adopted to a set of existing integral data shown in **Table 1**. All of these integral data are reactor physics parameters obtained at fast neutron systems, and intetgral

data with indices 1 to 14 are for criticality (neutron multiplication factor  $k$ ), and the others are for fission reaction rate ratio at a core center position. F25, F28, F37 and F23 stand for fission reaction rates of uranium-235, -238, neptunium-237 and uranium-233, respectively. Sensitivities are calculated with 70-group cross section data based on JENDL-4.0. Energy mesh structure of this 70-group cross section data is the same as the JAERI fast set-3, and a whole energy range is divided to 70 with constant lethargy width except the final group. Forward and (generalized) adjoint angular neutron fluxes are calculated by a discrete-ordinate neutron transport solver SNR of the CBZ code system, and sensitivities are calculated with them based on the first-order (generalized) perturbation theory. Sensitivity vectors are normalized so as to make norms of them unity since sensitivities about different reactor physics parameters,  $k$  and reaction rate ratio, are considered here.

Table 1: Integral data with their indices

Index	Name	Index	Name
1	Jezebel	17	F23/F25 in Godiva
2	Jezebel-Pu	18	F49/F25 in Godiva
3	Jezebel-233	19	F28/F25 in Jezebel
4	Godiva	20	F37/F25 in Jezebel
5	Flattop-Pu	21	F23/F25 in Jezebel
6	Flattop-U	22	F49/F25 in Jezebel
7	Flattop-233	23	F28/F25 in Jezebel-233
8	Big-ten	24	F37/F25 in Jezebel-233
9	Thor (Pu w Th Ref.)	25	F28/F25 in Flattop-U
10	PMF010 (Pu w NU Ref.)	26	F37/F25 in Flattop-U
11	U3MF002-1 (U-233 w HEU Ref.)	27	F23/F25 in Flattop-U
12	U3MF002-2 (U-233 w HEU Ref.)	28	F49/F25 in Flattop-U
13	U3MF003-1 (U-233 w NU Ref.)	29	F28/F25 in Flattop-Pu
14	U3MF003-2 (U-233 w NU Ref.)	30	F37/F25 in Flattop-Pu
15	F28/F25 in Godiva	31	F28/F25 in Flattop-233
16	F37/F25 in Godiva	32	F37/F25 in Flattop-233

As nuclear data, we consider 8 reactions of  $(n,f)$ ,  $(n,\gamma)$ ,  $(n,n)$ ,  $(n,n')$ ,  $(n,2n)$ ,  $\bar{\mu}$ ,  $\bar{\nu}$  and  $\chi$  for the following 10 nuclides: uranium-233, -234, -235, -238, plutonium-239, -240, -241, -242, thorium-232 and neptunium-237. Corresponding indices of these nuclear data are listed in **Table 2**. Since the number of energy groups is 70, the dimension of the nuclear data space considered here is  $8 \times 10 \times 70 = 5,600$ .

A normalized-singular values distribution of the sensitivity matrix is shown in **Fig. 3**. Two results with and without sensitivity vectors normalization are shown here. The effect of the sensitivity vectors normalization on the singular values distribution is small in the present case.

The principal basis vectors having the largest singular values are shown in **Fig. 4**. On the first basis vector, the first and second highest peaks are observed in  $(n,f)$  cross sections of uranium-235 and neptunium-237, respectively, and signs of these components are opposite to each other. This can be considered due to strong contribution of fission reaction rate ratio data of F37/F25. On the second basis vector, the first and second highest peaks are observed in  $\bar{\nu}$  and  $(n,f)$  cross sections of uranium-233. This can be also considered due to contribution of criticality data of uranium-233-loaded cores. On the third basis vector, the first and second highest peaks are observed in  $\bar{\nu}$  and  $(n,f)$  cross sections of plutonium-239, and this would be due to contribution of criticality data of plutonium-239-loaded cores.

A dimension of a sub-space spanned by these sensitivities is calculated as 13 with the procedure mentioned above. Since the total number of integral data is 32, it can be concluded that the present data set includes highly-dependent integral data. The result obtained by the proposed method is

Table 2: Nuclear data with their index.

Index	Nuclide	ND	Index	Nuclide	ND	Index	Nuclide	ND
1-	U-233	(n,f)	2241-	Pu-239	(n,f)	4481-	Th-232	(n,f)
71-	U-233	(n,g)	2311-	Pu-239	(n,g)	4551-	Th-232	(n,g)
141-	U-233	(n,n)	2381-	Pu-239	(n,n)	4621-	Th-232	(n,n)
211-	U-233	(n,n')	2451-	Pu-239	(n,n')	4691-	Th-232	(n,n')
281-	U-233	(n,2n)	2521-	Pu-239	(n,2n)	4761-	Th-232	(n,2n)
351-	U-233	$\bar{\mu}$	2591-	Pu-239	$\bar{\mu}$	4831-	Th-232	$\bar{\mu}$
421-	U-233	$\bar{\nu}$	2661-	Pu-239	$\bar{\nu}$	4901-	Th-232	$\bar{\nu}$
491-	U-233	$\chi$	2731-	Pu-239	$\chi$	4971-	Th-232	$\chi$
561-	U-234	(n,f)	2801-	Pu-240	(n,f)	5041-	Np-237	(n,f)
631-	U-234	(n,g)	2871-	Pu-240	(n,g)	5111-	Np-237	(n,g)
701-	U-234	(n,n)	2941-	Pu-240	(n,n)	5181-	Np-237	(n,n)
771-	U-234	(n,n')	3011-	Pu-240	(n,n')	5251-	Np-237	(n,n')
841-	U-234	(n,2n)	3081-	Pu-240	(n,2n)	5321-	Np-237	(n,2n)
911-	U-234	$\bar{\mu}$	3151-	Pu-240	$\bar{\mu}$	5391-	Np-237	$\bar{\mu}$
981-	U-234	$\bar{\nu}$	3221-	Pu-240	$\bar{\nu}$	5461-	Np-237	$\bar{\nu}$
1051-	U-234	$\chi$	3291-	Pu-240	$\chi$	5531-	Np-237	$\chi$
1121-	U-235	(n,f)	3361-	Pu-241	(n,f)			
1191-	U-235	(n,g)	3431-	Pu-241	(n,g)			
1261-	U-235	(n,n)	3501-	Pu-241	(n,n)			
1331-	U-235	(n,n')	3571-	Pu-241	(n,n')			
1401-	U-235	(n,2n)	3641-	Pu-241	(n,2n)			
1471-	U-235	$\bar{\mu}$	3711-	Pu-241	$\bar{\mu}$			
1541-	U-235	$\bar{\nu}$	3781-	Pu-241	$\bar{\nu}$			
1611-	U-235	$\chi$	3851-	Pu-241	$\chi$			
1681-	U-238	(n,f)	3921-	Pu-242	(n,f)			
1751-	U-238	(n,g)	3991-	Pu-242	(n,g)			
1821-	U-238	(n,n)	4061-	Pu-242	(n,n)			
1891-	U-238	(n,n')	4131-	Pu-242	(n,n')			
1961-	U-238	(n,2n)	4201-	Pu-242	(n,2n)			
2031-	U-238	$\bar{\mu}$	4271-	Pu-242	$\bar{\mu}$			
2101-	U-238	$\bar{\nu}$	4231-	Pu-242	$\bar{\nu}$			
2171-	U-238	$\chi$	4411-	Pu-242	$\chi$			

equivalent with ignoring components whose normalized singular values are less than around 0.075.

Finally, a minimum set of the independent integral data is also chosen by the proposed method. As a result, the following 18 integral data are chosen. These are presented in the descending order based on their priority: 32, 1, 11, 8, 25, 21, 4, 28, 19, 23, 5, 26, 27, 30, 7, 22, 9 and 2. Detailed information on the first five chosen integral data are provided in **Table 3**. A wide variety of integral data is properly chosen by the proposed algorithm.

## 4 Conclusion

Several methods based on the concept of the active sub-space have been proposed to quantify integral data effectiveness, and they have been adopted to existing 32 integral data with multi-group cross section representation. Dimensions of sub-spaces spanned by integral data in the nuclear data space can be quantified with the proposed method using orthogonal projections of each integral data vector to the sub-space. In addition, a method to choose a minimum independent integral

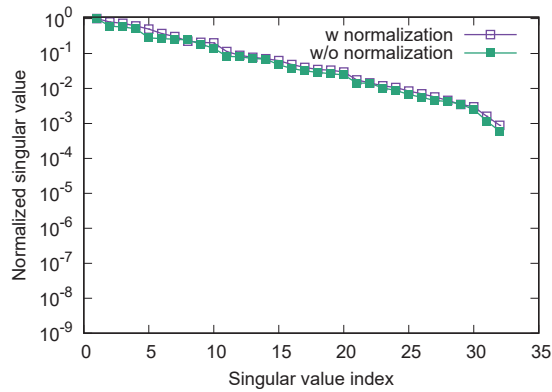


Fig. 3: Singular values distribution of a sensitivity matrix consisting of 32 actual integral data

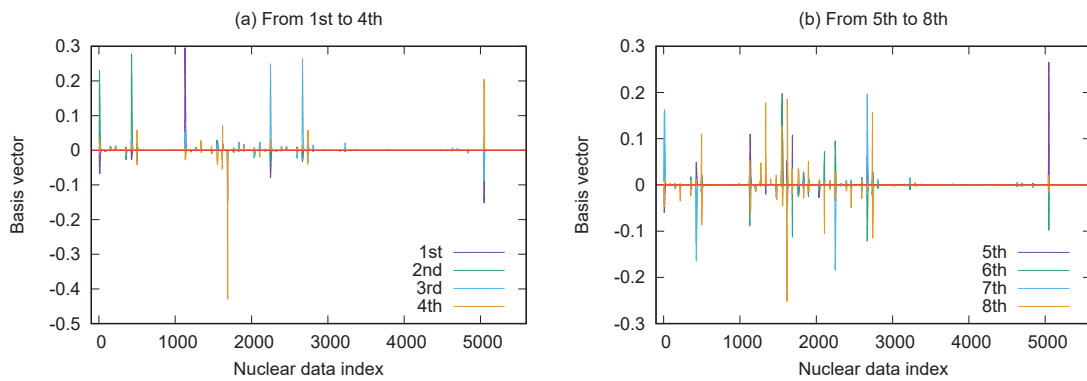


Fig. 4: Principal basis vectors spanning the integral data space of 32 actual integral data

Table 3: Detailed information on the chosen integral data

Priority	Index	Parameter	Fuel material	Reflector material
1	32	F37/F25	U-233	U-238
2	1	$k$	Pu-239	-
3	11	$k$	U-233	U-235
4	8	$k$	U-235, -238	U-238
5	25	F28/F25	U-235	U-238

data set has been proposed, and it has been demonstrated that this method can properly choose a wide variety of integral data among a set of dependent integral data.

## References

- [1] G. Chiba: “Application of active sub-space method to nuclear data integral testing,” *the AESJ spring meeting 2016*, (2016).
- [2] D. Imazato, G. Chiba: “Quantification of integral data effectiveness by active sub-space,” *Proc. of Reactor Physics Asia 2019, RPHA19, Osaka, Japan, Dec. 1-3, 2019*, (2019).

## 38 Uncertainty estimation of conventional neutron-spectrum unfolding codes with Monte-Carlo based method

Katsumi AOKI<sup>1</sup>, Tadahiro KIN<sup>1</sup>, Md Kawchar Ahmed PATWARY<sup>1</sup>, Kosuke YOSHINAMI<sup>1</sup>,  
Masaya YAMAGUCHI<sup>1</sup>, Masatoshi ITOH<sup>2</sup>, Yukinobu WATANABE<sup>1</sup>

<sup>1</sup>*Department of Advanced Energy Engineering Science, Kyushu University, 6-1 Kasuga-koen, Kasuga, Fukuoka, 816-8580 Japan*

<sup>2</sup>*Cyclotron and Radioisotope Center, Tohoku University, 6-3 Aoba, Aramaki, Aoba-ku, Sendai, Miyagi, 980-8578 Japan*

e-mail: aoki.katsumi.473@s.kyushu-u.ac.jp

Unfolding process has been applied to neutron spectra derivation of many measurement methods. Previously, many types of unfolding techniques have been developed. Many codes of them, however, cannot calculate uncertainty propagation, and thus uncertainty characteristics comparison of some codes has not been investigated. To solve this problem, we have developed an uncertainty estimation method based on Monte-Carlo technique. Moreover, we have investigated characteristics of uncertainty propagation of two unfolding codes, GRAVEL and MAXED. For demonstration, we measured a double-differential thick-target neutron yield (DDTTNY) of the  $C(d,n)$  reaction induced by 20-MeV deuterons with the multiple-foil activation method at Cyclotron and Radioisotope Center, Tohoku University. The measured data were analyzed by GRAVEL and MAXED, and their uncertainty propagation was estimated by using the present method. As a result, we found that the uncertainty of DDTTNY has neutron energy dependence, and the dependency trend is different between GRAVEL and MAXED codes.

### 1. Introduction

Accelerator-based neutron source has recently been applied to various fields such as boron neutron capture therapy (BNCT) [1], radioisotopes (RIs) production [2, 3], nuclear transmutation [4], and nuclear fusion engineering [5]. Among them, we have been focusing on medical RIs production using neutrons generated by the  $(d,n)$  reaction with a neutron convertor made of thick carbon or beryllium. The generated neutrons irradiate a raw material, and RI is produced. In the RI production system, <sup>64</sup>Cu [6], <sup>92</sup>Y [7], and <sup>99m</sup>Tc [8] productions were proposed previously.

In research and development of the RI production method, numerical simulation plays an important role for estimation of production amount and its purity, the design of irradiation system, and shielding calculation. For accurate simulation, double-differential thick-target neutron yields (DDTTNYs) should be preknowledge. In practical RI production applications, the DDTTNYs of the  $(d,n)$  reactions with the energy range from 10- to 50-MeV deuterons are necessary. However, systematically sufficient experimental data are not available.

Therefore, we have measured the DDTTNYs by the multiple-foil activation method. In this method,

DDTTNY  $\phi_{E_j}$  is derived by unfolding process that is to solve an inverse problem expressed by the following equation:

$$\begin{pmatrix} N_x \\ N_y \\ \vdots \\ N_i \\ \vdots \\ N_n \end{pmatrix} = \begin{pmatrix} R_{x,E_1} & R_{x,E_2} & \cdots & R_{x,E_j} & \cdots & R_{x,E_m} \\ R_{y,E_1} & R_{y,E_2} & \cdots & R_{y,E_j} & \cdots & R_{y,E_m} \\ \vdots & \vdots & \ddots & \vdots & & \vdots \\ R_{i,E_1} & R_{i,E_2} & \cdots & R_{i,E_j} & \cdots & R_{i,E_m} \\ \vdots & \vdots & & \vdots & \ddots & \vdots \\ R_{n,E_1} & R_{n,E_2} & \cdots & R_{n,E_j} & \cdots & R_{n,E_m} \end{pmatrix} \begin{pmatrix} \phi_{E_1} \\ \phi_{E_2} \\ \vdots \\ \phi_{E_j} \\ \vdots \\ \phi_{E_m} \end{pmatrix}, \quad (1)$$

where  $N_i$  and  $R_{i,E_j}$  represent the number of produced atoms via the reaction  $i$  and the response function of reaction  $i$  with a neutron energy group  $j$ , respectively. In general, the number of activation reactions of interest ( $n$ ) is less than the number of neutron energy groups ( $m$ ). In the past, many unfolding algorithms have been developed, for example, an iterative approximation method [9], a maximum entropy method [10], an iterative Bayesian method [11], and an artificial neural network (ANN) method [12]. However, characteristics of the propagated uncertainty of unfolding codes are not known.

To overcome the situation, we have developed a random sampling algorithm of estimating the uncertainty propagation in DDTTNYs derived by the unfolding process. In our study, we pay attention to GRAVEL [9] and MAXED [10] codes which are conventionally used for neutron spectrum unfolding. These codes are based on the iterative approximation method and the maximum entropy method, respectively. The GRAVEL code cannot analytically calculate the propagation of experimental uncertainties. Using the random sampling algorithm, we have compared the uncertainty propagation in the unfolding process with GRAVEL and MAXED.

## 2. Monte-Carlo based uncertainty estimation method

We proposed an algorithm for estimating uncertainty based on Monte-Carlo technique for unfolding process. The flow chart of the algorithm is shown in Fig. 1.

Firstly, measured number of produced atoms  $N_i$  of interested reaction is randomly changed by Gaussian distribution having statistical uncertainty. The changed number of atoms  $N'_i$  is calculated by following equation:

$$N'_i = N_i + \varepsilon_i N_i d, \quad (2)$$

where  $d$  and  $\varepsilon_i$  represent a random number generated by standard normal distribution and experimental relative uncertainty of  $i$ -th reaction. Secondly, we derived a neutron spectrum by an unfolding code with  $N'_i$ . The process, which  $N'_i$  is generated and neutron spectrum is derived, is conducted iteratively. Then, neutron spectra give two-dimensional distribution like Fig. 2. In each neutron energy group, we calculate standard deviation of DDTTNYs. The standard deviations mean propagated uncertainty of DDTTNY. The algorithm is considered only statistical uncertainty of the measured number of atoms  $N_i$ .

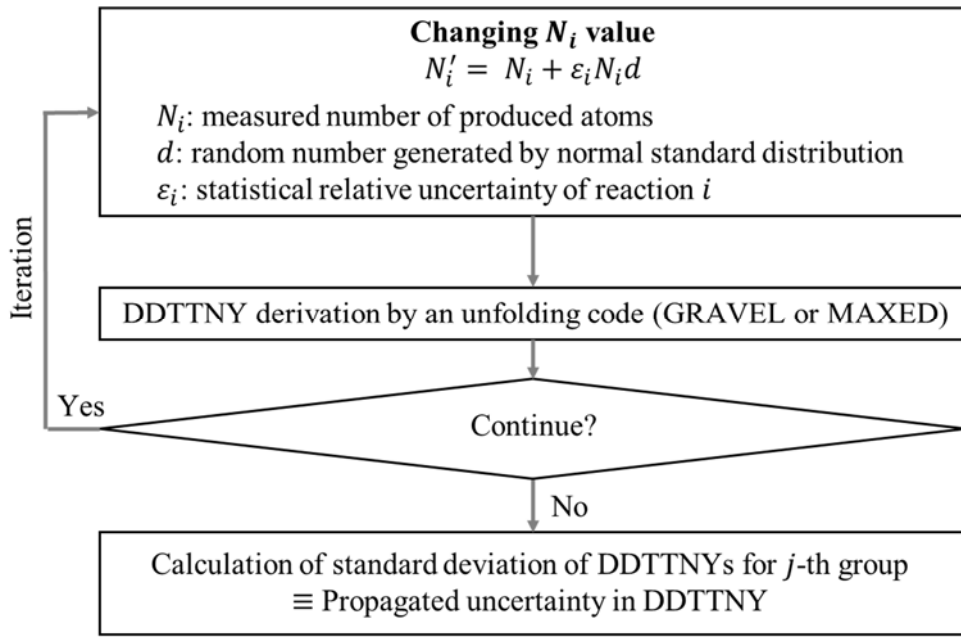


**Fig. 1** Flow chart of a random sampling algorithm for estimating propagated uncertainty in unfolding process of deriving DDTTNYs.

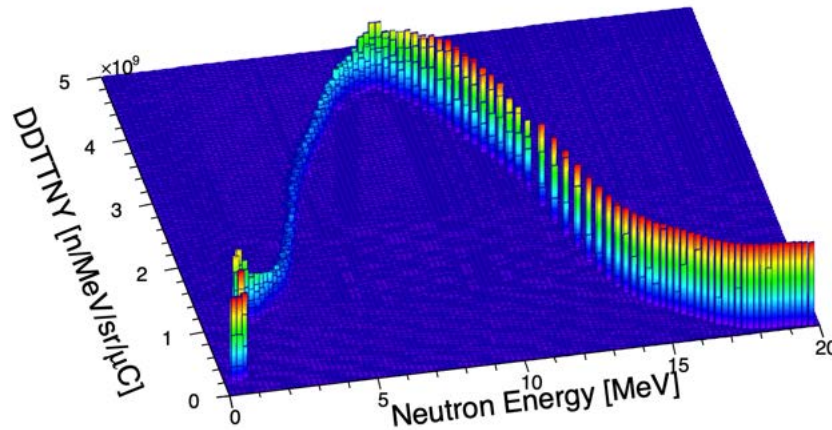


**Fig. 2** Example of two-dimension distribution of distorted DDTTNYs for bins of neutron energy and DDTTNY.

### 3. Experiment

We performed DDTTNY measurement by multiple-foil activation method at Cyclotron and Radioisotope Center (CYRIC), Tohoku University. Deuterons were accelerated to 20 MeV by an AVF930 cyclotron and bombarded on a thick carbon target (23 mm × 23 mm × 2 mm<sup>l</sup>). The accelerator-based neutrons were generated via the <sup>nat</sup>C( $d,n$ ) reaction. The generated neutrons irradiated multiple foils (50 mm × 50 mm). The foils were made of <sup>27</sup>Al (0.025 mm<sup>l</sup>), <sup>nat</sup>Fe (0.02 mm<sup>l</sup>), <sup>59</sup>Co (0.1 mm<sup>l</sup>), <sup>nat</sup>Ni (0.1 mm<sup>l</sup>), <sup>nat</sup>Zn (0.2 mm<sup>l</sup>), <sup>nat</sup>Zr (0.1 mm<sup>l</sup>), and <sup>nat</sup>Mo (0.05 mm<sup>l</sup>). The foils placed at 1,215 mm downstream to the carbon target at 0 degree

to direction of deuteron beam. Average deuteron beam current was about 2.0  $\mu\text{A}$  during 19-hours irradiation. Fig. 3 shows the schematic view of irradiation setup. After the irradiation, we measured gamma-ray emitted from activated multiple foils with HPGe detector.

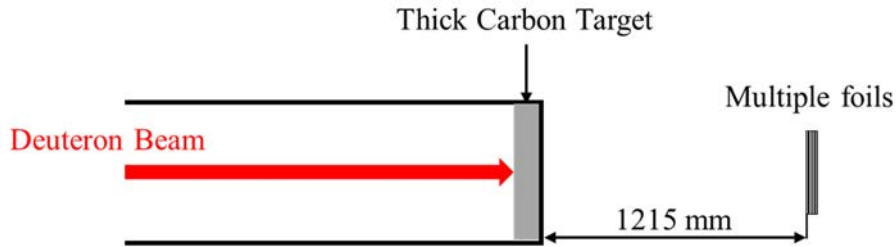


**Fig. 3** Schematic view of the irradiation setup. The accelerator-based neutrons generated via the  $^{12}\text{C}(d,n)$  reaction irradiated multiple foils ( $^{27}\text{Al}$ ,  $^{56}\text{Fe}$ ,  $^{59}\text{Co}$ ,  $^{58}\text{Ni}$ ,  $^{64}\text{Zn}$ ,  $^{96}\text{Zr}$  and  $^{96}\text{Mo}$ ).

#### 4. Results and Discussion

Firstly, the number of produced atoms by activation reactions of interest was derived from counting rate of photo peaks in measured gamma-ray spectra. The derived number of atoms and their statistical uncertainties are shown in Table 1.

**Table 1** Interested activation reaction, the number of produced atoms, and statistical uncertainty measured in the gamma-ray experiment.

Reaction	Half life	gamma-ray energy	Number of produced atoms
$^{27}\text{Al}(n,a)^{24}\text{Na}$	15.0 h	1369 keV	$5.30 \times 10^7 \pm 2.30 \times 10^5$
$^{56}\text{Fe}(n,p)^{56}\text{Mn}$	2.58 h	1811 keV	$1.28 \times 10^7 \pm 1.37 \times 10^5$
$^{59}\text{Co}(n,a)^{56}\text{Mn}$	2.58 h	846.8 keV	$1.90 \times 10^7 \pm 1.12 \times 10^5$
$^{59}\text{Co}(n,p)^{59}\text{Fe}$	44.5 d	1099 keV	$2.68 \times 10^8 \pm 1.38 \times 10^6$
$^{58}\text{Ni}(n,2n)^{57}\text{Ni}$	35.6 h	1378 keV	$1.24 \times 10^7 \pm 1.03 \times 10^5$
$^{64}\text{Zn}(n,p)^{64}\text{Cu}$	12.7 h	1346 keV	$6.91 \times 10^8 \pm 9.56 \times 10^6$
$^{67}\text{Zn}(n,p)^{67}\text{Cu}$	61.8 h	184.6 keV	$7.59 \times 10^6 \pm 7.76 \times 10^4$
$^{96}\text{Zr}(n,2n)^{95}\text{Zr}$	64.0 d	756.7 keV	$7.00 \times 10^7 \pm 7.49 \times 10^5$
$^{96}\text{Mo}(n,p)^{96}\text{Nb}$	23.4 h	568.8 keV	$1.63 \times 10^6 \pm 2.47 \times 10^4$

Secondly, we calculated response functions ( $R_{i,E_j}$ ) of unfolding process by following equation:

$$R_{i,E_j} = \sigma_{i,E_j} \times \Omega \times \rho_N \times C \times C_d, \quad (3)$$

where  $\sigma_{i,E_j}$  is the cross section [ $\text{cm}^2$ ] stored in JENDL-4.0 [13],  $\Omega$  is solid angle of each foil [sr],  $\rho_N$  is surface density of atoms [ $\text{cm}^{-2}$ ],  $C$  is total charge of deuteron beam [ $\mu\text{C}$ ], and  $C_d$  is decay correction. Only cross section is a function of neutron energy, other parameters are constant values. The cross sections are shown in Fig. 4 (a).

Both GRAVEL and MAXED require initial guess spectrum in unfolding process to derive resultant spectrum. The initial guess spectrum was calculated by deuteron-induced reaction analysis code system

(DEURACS) [14] which is a theoretical calculation code for deuteron induced reactions. The calculated spectrum is shown in Fig. 4 (b).

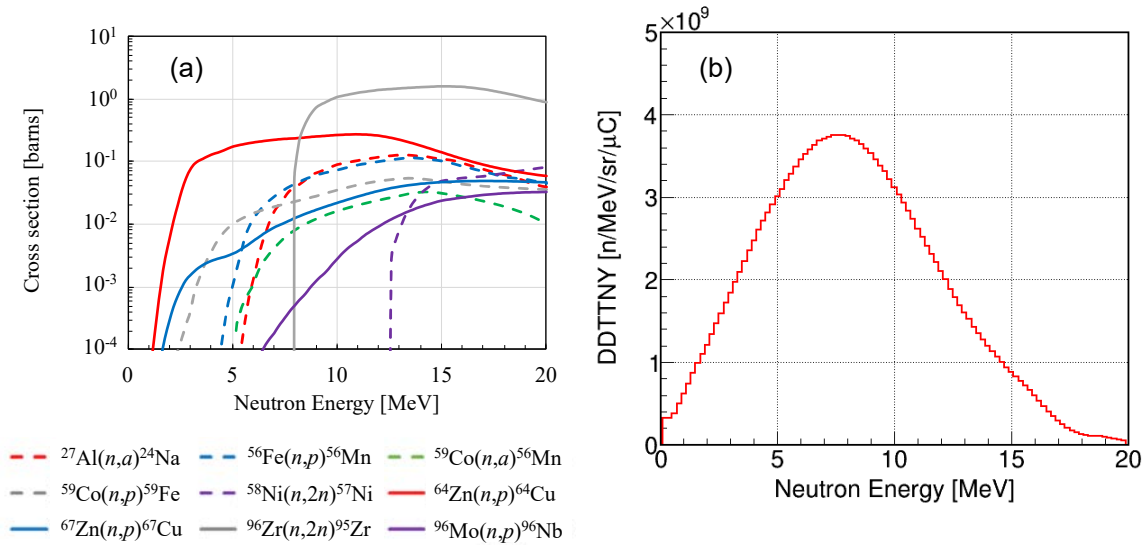


**Fig. 4** For unfolding process, (a) cross sections plotted as a function of neutron energy for each activation reaction and extracted from JENDL-4.0. (b) Initial guess spectrum is calculated by DEURACS which is theoretical calculation model.

The propagated uncertainties of each code were calculated by the developed algorithm. The standard deviation  $\varepsilon_i$  of eq. (2) was set to the original experimental statistical relative uncertainty. Then, 1,000 spectra were calculated by random sampling as shown in Fig.1. Fig. 5 shows two-dimensional histograms of the 1,000 DDTNYs for case of DDTNY derivation in (a) GRAVEL and (b) MAXED codes. For each code, we found that uncertainties have neutron energy dependence and the trend is completely different even they used same original uncertainties. In resultant DDTNY of GRAVEL has large propagated uncertainty around 1-7 MeV of neutron energy range. In contrast to that, resultant DDTNY of MAXED has large propagated uncertainty around higher energy range around 7-16 MeV. Moreover, the resultant spectrum is almost same as the initial guess spectrum in lower energy range (1-5 MeV). That is because our interested reactions were not occurred in this energy range, and unfolded DDTNYs never adjusted in the range in the unfolding process by MAXED which is well-known to have strong initial guess spectrum dependency.

## 5. Conclusion

We have developed an algorithm for estimating propagated uncertainty in unfolding process of deriving DDTNY. The algorithm is based on Monte-Carlo method and can apply to many unfolding codes. In this work, we applied it to GRAVEL and MAXED used in unfolding process and investigated difference of neutron energy dependence of propagated uncertainty between two unfolding codes. For demonstration, we conducted accelerator-based neutron spectrum measurement by multiple-foil activation method. We derived the DDTNY and its uncertainty by using our developing algorithm. From the results, we found neutron

energy dependency and trend of the dependencies are completely different.

In the future, we will apply the algorithm to other unfolding codes based on the iterative Bayesian and artificial neural network methods.

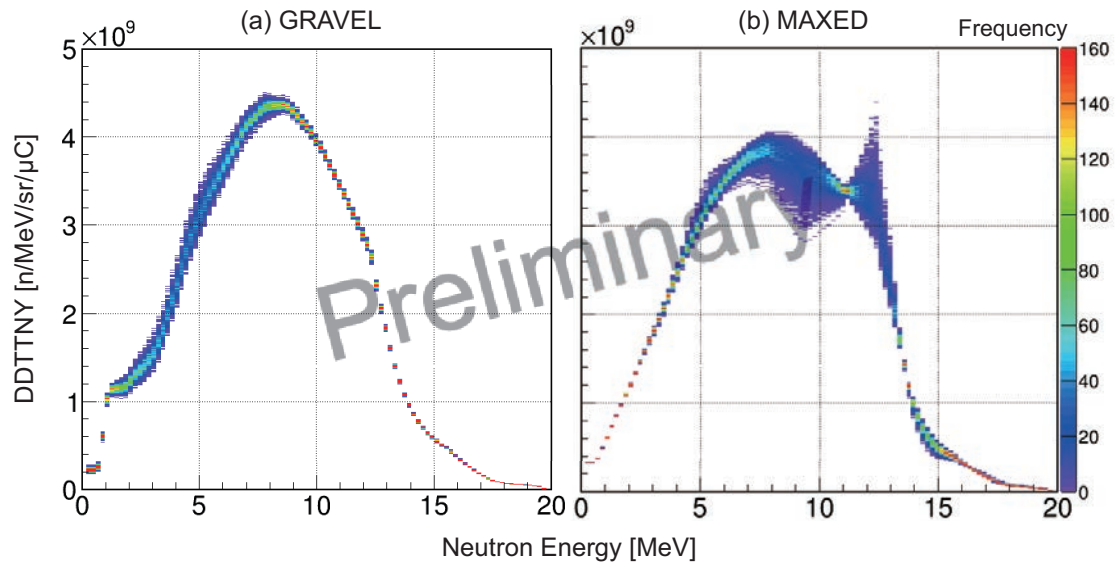


**Fig. 5** Preliminary results about two-dimensional histogram of 1000 DDTNYs derived in (a) GRAVEL and (b) MAXED.

## References

- [1] M. Yoshioka, Review of Accelerator-based Boron Neutron Capture Therapy Machines, in Proceedings of IPAC 2016, 3171, 2016 (2016).
- [2] Y. Nagai, et al., J. Phys. Soc. Jpn. 82, 064201 (2013).
- [3] T. Kin, et al., J. Phys. Soc. Jpn. 24, 011031 (2019).
- [4] Implications of Partitioning and Transmutation in Radioactive Waste Management, Number 435 in Technical Reports Series, IAEA, Vienna (2004).
- [5] A. Moeslang, et al., Fusion Engineering and Design 81, 863 (2006).
- [6] T. Kin, et al., J. Nucl. Sci. Technol. 54, 1123 (2017).
- [7] T. Kin, et al., M. Itoh, EPJ Web Conf. 146, 08009 (2017).
- [8] Y. Nagai, et al., J. Phys. Soc. Jpn. 78, 033201 (2009).
- [9] M. Matzke, Report PTB-N-19 (1994).
- [10] M. Reginatto, et al., Nucl. Instrum. Methods, A476, 242 -246 (2002).
- [11] T. Adye, Proc. of the PHYSTAT 2011 Workshop, 313 (2011).
- [12] Y. Sanzen, et al., Proc. 2016 Symp. Nucl. Data, JAEA-Conf 2017-001, 157 (2017).
- [13] K. Shibata, et al., J. Nucl. Sci. and Technol. 48, 1 (2011).
- [14] S. Nakayama, et al., Phys. Rev. C 94, 014618 (2016).

## 39 The Influence of B and Li Burnable Poison on Effective Multiplication Factor in the HTGR

Yuki KOGA<sup>1</sup>, Hideaki MATSUURA<sup>1</sup>

<sup>1</sup>Department of Applied Quantum Physics and Nuclear Engineering, Kyushu University,  
744 Motooka Nishi-ku, Fukuoka, 319-0395 Japan  
e-mail: koga\_yuki@nucl.kyushu-u.ac.jp

Tritium is required for the engineering tests and the initial DEMO fusion reactor. In order to establish a tritium supply method, tritium production using the high temperature gas-cooled reactor (HTGR) was proposed. The B burnable poison (BP) is replaced with Li for tritium production. Li is loaded as a solid unit called Li rod. There is a possibility that difference in an effective multiplication factor ( $k_{\text{eff}}$ ) arises by using Li instead of B. The  $k_{\text{eff}}$  difference in the HTTR is evaluated and discussed. The same evaluation is also conducted for the GTHTR300. It is revealed how the difference appears and how the HTGR types influence on the results.

### 1. Introduction

A fusion reactor using T(d,n) $\alpha$  reaction requires tritium for its R&D. Tritium is produced artificially because it hardly exists in nature, while deuterium is obtained from water. Approximately 400 g of tritium is burned per day in a 3 GW thermal output power. A sufficient amount of initial tritium is required to start up a fusion reactor. It was reported that this amount of tritium for the Demo reactor was several 100 g -approximately 27 kg [1,2]. In addition, 100 g or more of tritium is required for an engineering test using tritium before construction of DEMO reactors. The tritium consumed on a fusion reactor for the ITER project has been produced by using the Canadian Deuterium Uranium reactors, although it has not been clarified that the way to supply tritium for the initial DEMO reactors, in particular Japan. Therefore, we proposed a tritium production method using the high temperature gas-cooled reactor (HTGR) [3] by loading a Li compound as a burnable poison (BP). The HTGR is composed by mainly graphite (moderator) and He (coolant). They are chemically stable and do not react with the Li compound. An enough amount of Li can be loaded into the HTGR without <sup>6</sup>Li concentration. It is because the HTGR core size is larger than other types of fission reactor. Normal BP (B rod) is a cylindrical B<sub>4</sub>C and solid states so that Li compound is loaded as same shape without significantly changing the original core design. We consider Li compound is loaded as Li rod. The Li rod includes LiAlO<sub>2</sub> in a cylindrical alumina case with Ni coated Zr pebbles (tritium absorber) [4]. It can produce and contain tritium during the operation time. We are planning an irradiation test on the High Temperature engineering Test Reactor (HTTR) [5] in order to confirm the Li rod performance and to demonstrate the tritium production on the HTGR [6].

The absorption cross-sections and loaded amounts are different in Li and B. Accordingly Li rod reactivity may be different from B rod and the HTGR characteristic may be changed by loading Li rods. In order to operate the HTGR loaded Li rods, it needs to clarify the characteristic change. The purpose of this paper is the evaluation and discussion of the HTGR reactor characteristic difference in the B rod and the Li rod. The effective multiplication factors ( $k_{\text{eff}}$ ) during operation are evaluated as the reactor characteristics. We selected the HTTR with 30 MW thermal output [5] and the Gas Turbine High Temperature Reactor 300 (GTHTR300) with 600 MW thermal output

[7] for the evaluation. The HTGR characteristic difference by the BP change is also discussed for the two reactors.

## 2. Analysis model

We assumed the original designs of the B rod for the evaluation. Fig.1 shows the designs of the B rod for the HTTR [8] and GTHTR300 [7]. We designed the Li rod to fit each BP hole sizes. Fig.2 shows the Li rod design for the HTTR. Its diameter is 14 mm, height is 450 mm,  $\text{Al}_2\text{O}_3$  layer thickness is 1.9 mm, Zr layer thickness is 0.1 mm,  $\text{LiAlO}_2$  thickness is 2.7 mm and hollow radius is 2.3 mm respectively. The hollow inside the Li rod is full of Zr pebbles coated Ni which diameter is 1 mm. Fig.3 shows the Li rod design for the GTHTR300. Its diameter is 44 mm, height is 950 mm,  $\text{Al}_2\text{O}_3$  layer thickness is 6.3 mm, Zr layer thickness is 1 mm,  $\text{LiAlO}_2$  thickness is 2.5 mm and hollow radius is 12.2 mm respectively. The hollow is full of the same Zr pebbles coated Ni.

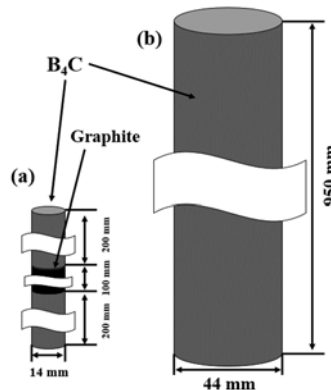


Fig.1. A schematic view of the normal B rods for the HTTR (a) and the GTHTR300 (b).

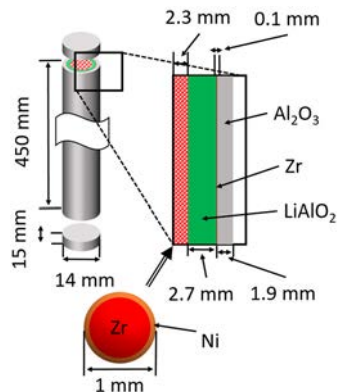


Fig.2. A schematic view of the Li rod for the HTTR.

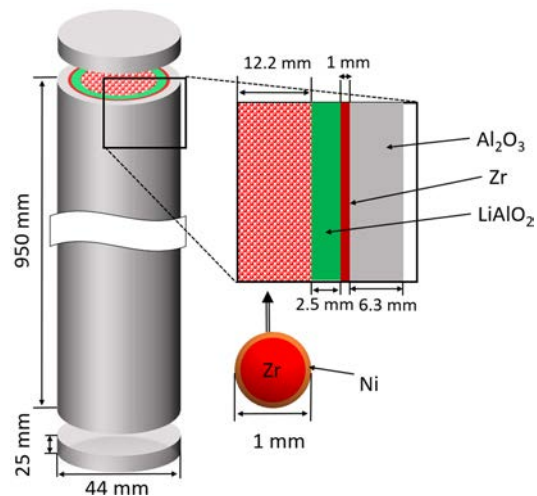


Fig.3. A schematic view of the Li rod for the GTHTR300

In order to evaluate  $k_{\text{eff}}$  and the cumulative weight of produced tritium, we conducted nuclear burning calculations using the continuous-energy Monte Carlo transport code MVP-BURN [9,10] with a nuclear data JENDL-4.0 [11]. We assumed a HTTR core system with 300 B rods or 450 Li rods and a GTHTR300 core system with 2160 B rods or 2160 Li rods. Therefore, the amounts of loaded  $^6\text{Li}$  for the HTTR and the GTHTR300 are 193 g and 6674 g respectively. The operation period in these calculations is 360 days and all control rods were assumed to be pulled out. We set the time steps in the calculations were 0, 1, 5, 30, 60, 120, 180 and 360 days. 600,000 neutrons were generated for each the time steps. The statistical error of  $k_{\text{eff}}$  were less than 0.1 % in the all

calculation, which is sufficient accuracy. Zr was not included in those calculations because Zr does not influence on  $k_{\text{eff}}$  and tritium production by its cross-section.

### 3. Results and discussion

Fig.4 shows the accumulative produced tritium and  $k_{\text{eff}}$  (B and Li rod) by the operation time for the HTTR. The  $k_{\text{eff}}$  maintained nearly 1.05 during the operation when the B rods were loaded, which corresponded with the  $k_{\text{eff}}$  in the reference [5]. This is because the B rods suppress excessive reactivity by burning of  $^{10}\text{B}$  atoms inside them in the early period of operation, and the B rods decrease their negative reactivity in the latter period of operation. The  $k_{\text{eff}}$  decreased straightly during the operation when Li rods were loaded and produced 30.3 g of tritium in 360 days.  $^6\text{Li}$  atoms in the Li rods are not burned quicker than  $^{10}\text{B}$  atoms and remain more in the late time of operation, because the cross-section of  $^6\text{Li}$  is 940 b for thermal neutron whereas that of  $^{10}\text{B}$  is 3837 b for it. The  $k_{\text{eff}}$  decreased immediately after the operation starts in the both of those calculations, by Xe generates.

The accumulative produced tritium and  $k_{\text{eff}}$  (B and Li rod) by the operation time for the GTHTR300 is shown in Fig.5. When the B rods were loaded, the  $k_{\text{eff}}$  increased until 360 days because the design of the GTHTR300 is assumed 2 years continuous operation. It was same tendency to the reference [7]. When the Li rods were loaded, the  $k_{\text{eff}}$  decreased straightly as well as in the case for the HTTR and they produced 818 g of tritium. However, the difference of  $k_{\text{eff}}$  by the BP change during the operation for GTHTR300 was more than that for HTTR. It means there is more neutron to suppress by control rod in the GTHTR300 operation.

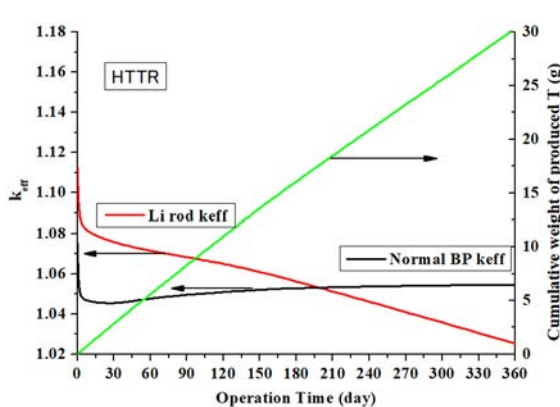


Fig.4. The accumulative produced T and  $k_{\text{eff}}$  by the operation time for the HTTR.

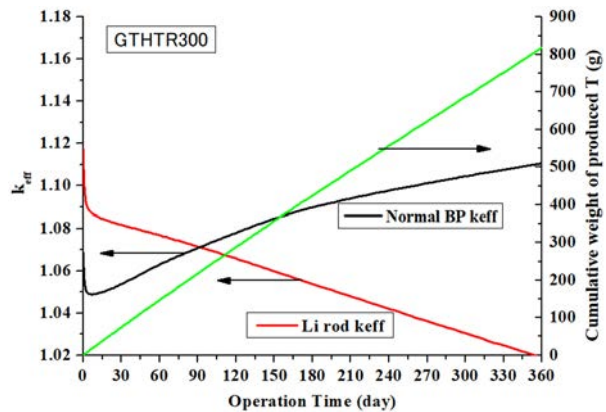


Fig.5. The accumulative produced T and  $k_{\text{eff}}$  by the operation time for the GTHTR300.

At first we confirmed the amount of loaded  $\text{LiAlO}_2$  and the volume of a fuel block in Table 1 to investigate this reason. The amount of loaded  $\text{LiAlO}_2$  into the GTHTR300 is about 7 times of that into the HTTR in order to produce 800 g of tritium, while the difference of fuel block volume is smaller. Therefore, the Li/Block volume ratio for the GTHTR300 is about 9 times of that for the HTTR. The increase of the ratio decreases  $^6\text{Li}$  burnability by self-shielding effect when the  $\text{LiAlO}_2$  shapes are same.

Table 1. The amount of loaded  $\text{LiAlO}_2$  into The HTGRs.

	Loaded $\text{LiAlO}_2$ ( $\text{cm}^3$ )	Fuel block volume ( $\text{cm}^3$ )	Ratio of Li/Block volume	T production (g)
GTHTR	201	$3.86 \times 10^4$	$5.20 \times 10^{-3}$	818
HTTR	28	$4.75 \times 10^4$	$5.87 \times 10^{-4}$	30.3

Next, we analyzed the outputs of the nuclear burning calculations. Fig.6 shows the amount of burned BP atoms by the operation time.  $^{10}\text{B}$  atoms were burned quicker than  $^6\text{Li}$  for both of the HTGRs in those calculations, which fits to the above theory. The amount of burned  $^6\text{Li}$  atoms for the HTTR was about 10 mol and almost same to that of  $^{10}\text{B}$  atoms (the difference is about 3 %). On the other hand, the amount of burned  $^6\text{Li}$  atoms for the GTHTR300 was about 270 mol and more than that of  $^{10}\text{B}$  atoms, which difference is about 21 %. It was caused by loading large amount of  $\text{LiAlO}_2$  to produce maximum tritium in the GTHTR300. Fig.7 shows the ratio of remained BP by the operation time. When the B rods are loaded, the remain ratio of the HTTR was 28 %. It was more than that of the GTHTR300 slightly. The reason is two B rods are loaded into each HTTR fuel blocks while three B rods are loaded into those of the GTHTR300.  $^{10}\text{B}$  atoms in the HTTR is less burn than that in the GTHTR300 by the increase of Li heterogeneous. when the Li rods were loaded, the remain ratio of the GTHTR300 was 75 %, whereas the ratio of the HTTR was 69 %. It follows the relation of the Li/Block volume ratio between  $^6\text{Li}$  burnability by self-shielding effect. Therefore, excessive load and low burnability of  $^6\text{Li}$  on the GTHTR300 makes the  $k_{\text{eff}}$  during the operation bad by neutron efficiency reduction.

It was reported that the GTHTR300 has potential to produce additional 40 % amount of tritium which the Li rods can produce [12]. However, it does not show the way to improve the  $k_{\text{eff}}$  but one to increase the amount of produced tritium. The decrease of Li heterogeneous can improve the  $k_{\text{eff}}$  and the remain ratio because self-shielding effect is weakened and  $^6\text{Li}$  becomes more burnable. Loading many smaller Li rods is one of the solutions to reduce Li heterogeneous. We conducted a model calculation under the assumption that  $^6\text{Li}$  was mixed into the GTHTR300 fuel blocks so as to show the improvement example. Fig.8 is the accumulative produced tritium and  $k_{\text{eff}}$  by the operation time for the GTHTR300 under this assumption. 4718 g of  $^6\text{Li}$  was mixed into the fuel blocks in this calculation to keep  $k_{\text{eff}}$  more than 1.03 after 360 days operation. All the Li rods for the GTHTR300 included 6674 g of  $^6\text{Li}$ . The  $k_{\text{eff}}$  during the operation maintained nearly 1.05 until 180 days, which was similar to the case that B rods were loaded. The ratio of remained  $^6\text{Li}$  was 63 % consequently the amount of produced tritium achieved 873 g.

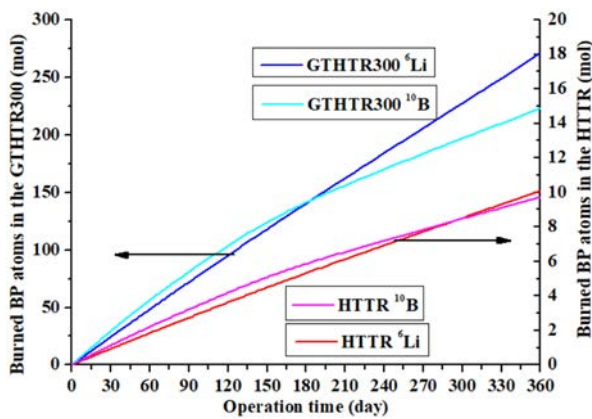


Fig.6. The amount of burned BP atoms by the operation time.

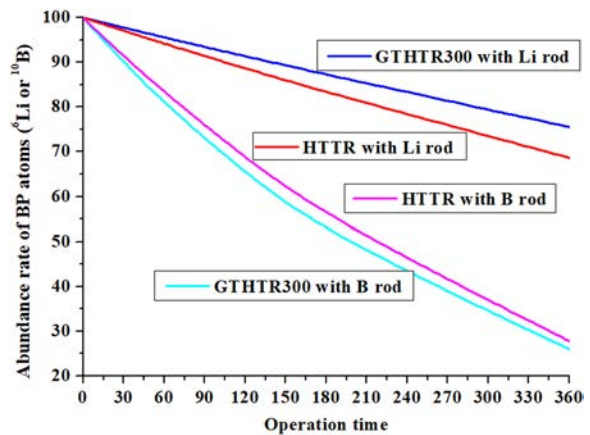


Fig.7. The ratio of remained BP by the operation time.

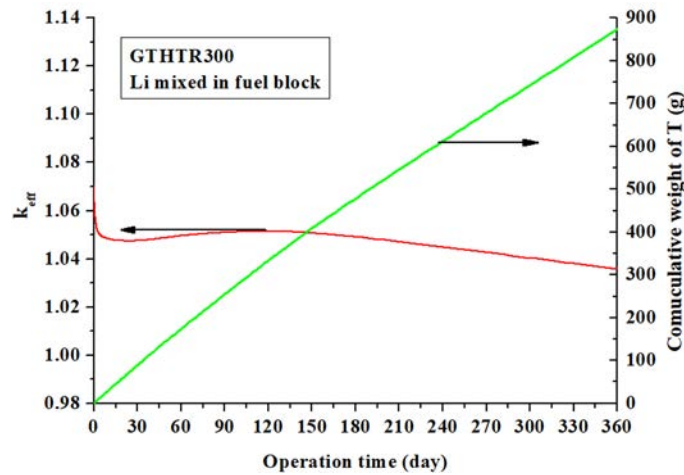


Fig.8. The accumulative produced T and  $k_{eff}$  by the operation time for the GTHTR300 under the assumption Li are mixed in the fuel blocks.

#### 4. Conclusion remarks

We evaluated effective multiplication factors ( $k_{eff}$ ) during operation of the HTTR and the GTHTR300 for the evaluation and discussion of the HTGR reactor characteristic difference in the B rod and the Li rod. The  $k_{eff}$  kept up to a value or increased during the operation when the B rods were loaded into the HTGRs. The  $k_{eff}$  decreased straightly during the operation when Li rods were loaded for tritium production because  ${}^6\text{Li}$  atoms are not burned quicker than  ${}^{10}\text{B}$  atoms and more remain in the late time of operation.

The excessive load of  $\text{LiAlO}_2$  to produce 800 g of tritium using the GTHTR300 increases more the difference of  $k_{eff}$  by the BP change than that using the HTTR to produce 30 g of tritium. The GTHTR can improve its  $k_{eff}$  characteristic by decrease Li heterogeneous, which reduces the amount of loaded  $\text{LiAlO}_2$  and increases  ${}^6\text{Li}$  burnability.

## References

- [1] R. Hiwatari, J Atomic Energy Society Japan [in Japanese] 60 (8) (2018) 52-56.
- [2] Y. Asaoka., et al., Fusion Tech. 30 (1996) 853-863.
- [3] H. Matsuura, et al., Nucl. Eng. Des.243(2012) 95-101.
- [4] H. Matsuura, et al., Fusion Eng. Des. 146 (2019) 1077-1081.
- [5] S. Saito, et al., JAERI 1332 (1994).
- [6] Y. Koga, et al., Fusion Eng. Des. 136 (2018) 587-591.
- [7] T. Nakata, et al., JAERI-Tech 2002-066, (2002) [in Japanese].
- [8] N. Fujimoto and N. Nojiri, JAEA-Technology 2005-008, (2006) [in Japanese].
- [9] Y. Nagaya, et al., JAEA-Data/Code 2016-019, (2017) [in Japanese].
- [10] K. Okumura, et al., J. Nucl. Sci. Tech., 37 (2000), 128-138.
- [11] K. Shibata, et al., J. Nucl. Sci. Technol. 48(1) (2011) 1-30.
- [12] S. Nagasumi et al., Spring Meeting of AESJ (2016) 2L06.

## 40 Evaluation of radioactive concentration produced in electric equipments and materials on the decommissioning of nuclear power plants

Hirokuni YAMANISHI<sup>1\*</sup>, Genichiro WAKABAYASHI<sup>1</sup>, Takahiro YAMADA<sup>1</sup>,  
Masateru HAYASHI<sup>2</sup>, Tetsushi AZUMA<sup>2</sup>, Takayuki IKEDA<sup>3</sup>

<sup>1</sup>Atomic Energy Research Institute, Kindai University,  
Higashi-Osaka, Osaka, 577-8502, Japan

<sup>2</sup>Advanced Technology R&D Center, Mitsubishi Electric Corporation,  
Amagasaki, Hyogo, 661-8661, Japan.

<sup>3</sup>Power Plant Engineering & Construction Center, Mitsubishi Electric Corporation,  
Osaka, Osaka, 661-8661, Japan.

\*E-mail: yamanisi@kindai.ac.jp

A various cables used in nuclear power plants are treated as wastes in decommissioning. If part of them is treated as non-radioactive wastes, the amount of radioactive waste can be reduced. Furthermore, valuable resources such as copper can be recycled, and that contributes to the efficient use of resources. In this study, we have evaluated the produced nuclides in representative PWR cables by neutron irradiation calculated with the activation cross section data. As the results of evaluation, we have confirmed the possibility of the Ni-63 concentration exceeding the criterion for clearance near reactor vessel. To improve the accuracy of inventory evaluation, the uncertainty evaluation of activation cross section will be important.

### 1. Introduction

Aging nuclear power plants will increase in the coming decades, and most of them are expected to be shut down. Therefore decommissioning of nuclear power plant is one of the most important issue. Decommissioning of 1 GW class PWR (Pressurized Water Reactor) is estimated to generate hundreds kilotons of waste. If the part of them could be treated as non-radioactive wastes, the amount of radioactive waste could be reduced. Furthermore, valuable resources such as copper which used in electric equipments can be recycled, and that contributes to the efficient use of resources.

Radioactivity concentration of core component and main structure such as concrete or steel has been evaluated in several leading plant[1, 2], but sufficient investigation has not been conducted on electric components. Most of the cables laid outside the reactor pressure vessel are considered as non-radioactive waste due to relatively low neutron flux and small neutron cross section of copper.

In this study, we have evaluated the radioactivity inventory of copper material used in electric equipments.

### 2. Method

The evaluation method consists of the following three steps: (1) Chemical composition analysis of target material, (2) Neutron flux and spectrum evaluation at target position, (3) Activity inventory calculation.

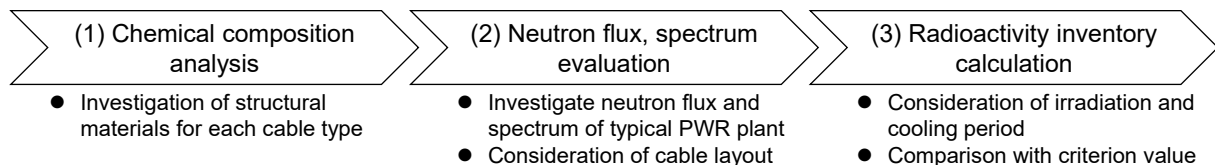


Fig. 1 Steps of evaluation.

#### (1) Chemical composition analysis of target material

Cables used in PWR plants are roughly classified into five types: (A) High voltage cable, (B) Low voltage cable, (C) Control cable, (D) Instrumentation cable, and (E) Special instrumentation cable. Figure 2 shows the cross sectional view of typical cable and table 1 shows the structural material of each layer. Then we have performed the chemical composition analysis using SEM/EDX (Scanning Electron Microscope /

Energy Dispersive X-ray Spectroscopy) and ICP–OES (Inductivity coupled plasma optical emission spectrometer) for principal component. In addition, we have performed activation analysis using UTR-KINKI to investigate trace components below the detection limit of ICP–OES analysis.

Table 1 Structural material of each layer.

Layer	Cable type					
	A: High voltage	B: Low voltage	C: Control	D: Instrument	E: Special	
1 Conductor	Copper	TPCS	TPCS	TPCS	TPCS	
2 Insulator	CLPE	FREP / FRV	FREP / FRV	FREP / FRV	FRV / CLPE	
3 Strand	Jute	Jute	Jute	Jute	Jute	
4 Shield	Copper tape	TPCT	TPCT	TPCT	TPCT	
5 Tape	Fabric	Fabric	Fabric	Fabric	Fabric / PS	
6 Sheath	FRV / FRPE	FRV / FRPE	FRV / FRPE	FRV / FRPE	FRV / FRPE	

TPCS: Tin plated copper strand  
 CLPE: Cross-linked polyethylene  
 FRV: Flame retardance vinyl  
 TPCT: Tin plated copper tape  
 FREP: Flame retardance EP rubber  
 FRPE: Flame retardance polyethylene  
 PS: Polystyrene

(2) Neutron flux and spectrum evaluation at target position

Since most of cables are located outside the reactor pressure vessel in PWR plant, it is considered that thermal neutrons are dominant at the target position. Therefore, in this study we have focused on thermal neutrons. However, the thermal neutron flux at target position depends on the reactor type, then we used  $10^{11}$  n/cm<sup>2</sup>/s at the surface of reactor pressure vessel as the typical value of PWR plant[2, 3].

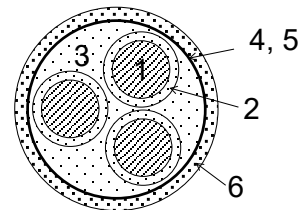


Fig. 2 Cross sectional view of typical cable.

(3) Radioactivity inventory calculation

In this study, radioactivity inventory calculation was performed using PHITS 3.17 and DCHAIN-SP[4]. Considering that most of the reactors in Japan will be shutting down in 40 years and start the decommissioning process, we have set the irradiation period to 40 years. The neutron flux was constant during irradiation period without any suspension period due to the maintenance or accident. After irradiation period, the radioactivity concentration of each nuclide was compared with clearance level[5] as criterion.

3. Results

3.1 Chemical composition analysis of target material

(1) SEM/EDX measurement

We have performed SEM/EDX measurement to investigate the main component of each layer of cable. Each measurement samples that selected to cover the structural materials polished the cut surface after fill the resin. SEM/EDX measurement was performed using Hitachi High Technologies Inc. SU-8000 with the acceleration voltage was 15 kV. As a results of measurement, metal elements except copper were not detected from the conductor layer. On the other hand, Na, Mg, Al, Si, Cl, Ca, Zn, Sb and Pb were detected from the other layers.

(2) ICP–OES measurement

We have performed ICP–OES measurement to investigate the trace component. Considering the SEM/EDX results, we have selected element to be measured for the following reasons:

- Sc, Ti, V, Cr, Mn, Fe, Co, Ni, Cu, Zn: Elements have the potential to produce <sup>63</sup>Ni, <sup>60</sup>Co and <sup>54</sup>Mn by neutron reaction
- Mg, Al, Si, Ca, Sn, As, Bi, Pb: Elements have the potential to be contained as a trace element in conductor

For ICP–OES, each measurement sample was dissolved by adding acid and heating after disassemble and separated into conductors and layers. ICP–OES measurement was performed using SII Nano Technology Inc. SPS-3100. Table 2 shows the result of measurement. Ca and Sn were detected as trace element. The detection limit was approximately several tens of ppm.

Table 2 Detected elements in conductor.

Element	Composition (wt%)	Detection limit
Cu	99.95	2.1 ppm
Ca	$1.192 \times 10^{-3}$	8.3 ppm
Sn	0.051	21 ppm

(3) Activation analysis

To investigate trace elements less than the detection limit of ICP–OES measurement, we have performed activation analysis using UTR–KINKI. Each measurement sample that was disassemble and separated into each layer filled in U–8 vessel has irradiated in the central stringer of the reactor. After the irradiation, we have performed the radionuclide analysis produced from trace element by the gamma spectroscopy using a HPGe detector. As a result of analysis, any significant trace elements were not detected. Therefore, we have decided the standard chemical composition of cable conductor as shown in table 2

3.2 Radioactivity inventory calculation

At the beginning, we have calculated average neutron flux inside the conductor region using PHITS 3.17 with parallel neutron beam to cable side. Figure 3 shows the two dimensional neutron flux.

Then we have calculated the radioactivity concentration in the conductor using DCHAIN-SP with JENDL/AD-2017[6] activation cross section. The irradiation period was 40 years, and the concentration was calculated from 20 years after the irradiation stopped. Figure 4 shows the calculation results. As a result of calculation,  $^{41}\text{Ca}$ ,  $^{63}\text{Ni}$ ,  $^{65}\text{Zn}$ ,  $^{119, 121, 121\text{m}}\text{Sn}$ ,  $^{125}\text{Sb}$  and  $^{125\text{m}}\text{Te}$  was confirmed as a long half-life nuclide. Compared to the clearance level, radioactive concentration of  $^{63}\text{Ni}$  and  $^{65}\text{Zn}$  are greater than the clearance criterion at 40 years. Note that  $^{119, 121, 121\text{m}}\text{Sn}$ ,  $^{125}\text{Sb}$ ,  $^{125\text{m}}\text{Te}$  are excluded in this study due to the domestic regulation. Table 3 shows the calculated radioactivity concentration of  $^{41}\text{Ca}$ ,  $^{63}\text{Ni}$  and  $^{65}\text{Zn}$  at 40, 50 and 60 years.

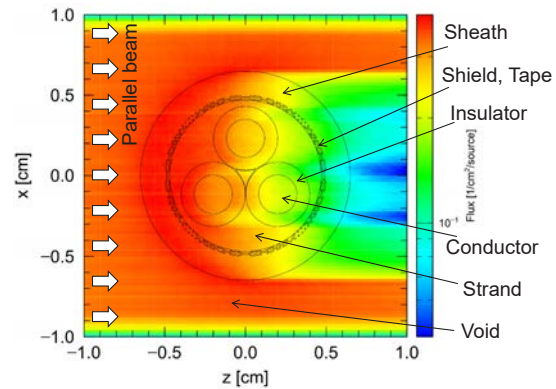


Fig. 3 Example of PHITS calculation (Two dimensional neutron flux).

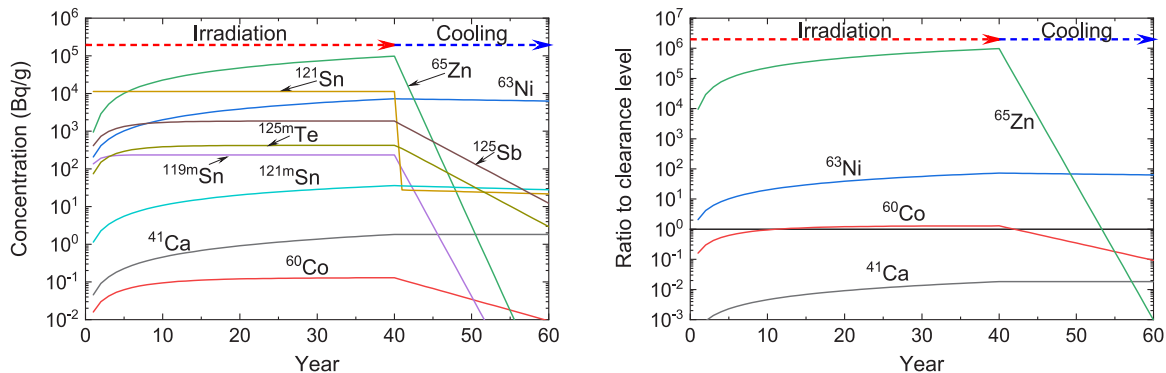


Fig. 4 Calculated radioactivity concentration (left) and ratio to clearance level (right).

Table 3 Calculated radioactivity concentration.

Nuclide	$T_{1/2}$	Clearance level (Bq/g)	Radioactivity concentration (Bq/g)		
			40 y	50 y	60 y
$^{41}\text{Ca}$	$1.03 \times 10^5$ y	100	1.85	1.85	1.85
$^{63}\text{Ni}$	101.2 y	100	$2.71 \times 10^3$	$2.53 \times 10^3$	$2.36 \times 10^3$
$^{65}\text{Zn}$	244.06 d	0.1	$1.02 \times 10^5$	3.16	$9.81 \times 10^{-5}$

#### 4. Discussion

As a result of calculation,  $^{65}\text{Zn}$  is a dominant nuclide present in a cable as the irradiation is stopped, however  $^{63}\text{Ni}$  becomes dominant in a few years due to the short half-life of  $^{65}\text{Zn}$ . Moreover, 10 years after irradiation stops, the radioactivity concentration of  $^{63}\text{Ni}$  becomes more than 90% of total amount.

In this case, evaluation of  $^{63}\text{Ni}$  radioactivity concentration must be required for clearance. However, direct measurement of  $^{63}\text{Ni}$  is difficult due to its low energy  $\beta$  ray emission (maximum 0.0659 MeV, average 0.0174 MeV[7]) and no  $\gamma$  ray emission.

Therefore, it is necessary to consider evaluation using calculations including uncertainty evaluation. For this purpose, uncertainty evaluation of activation cross section is important. Figure 5 shows the comparison of cross section data between nuclear data libraries. The cross section of  $^{40}\text{Ca}(n, \gamma)^{41}\text{Ca}$  reaction in each library is almost same. On the other hand, the cross section of  $^{63}\text{Cu}(n, p)^{63}\text{Ni}$  reaction has a large difference of about 10 times between libraries, especially in the thermal neutron region where no experimental data has been obtained. For this reason, it is considered that the uncertainty of the nuclear data contributes significantly to the uncertainty of the  $^{63}\text{Ni}$  radioactivity inventory evaluation.

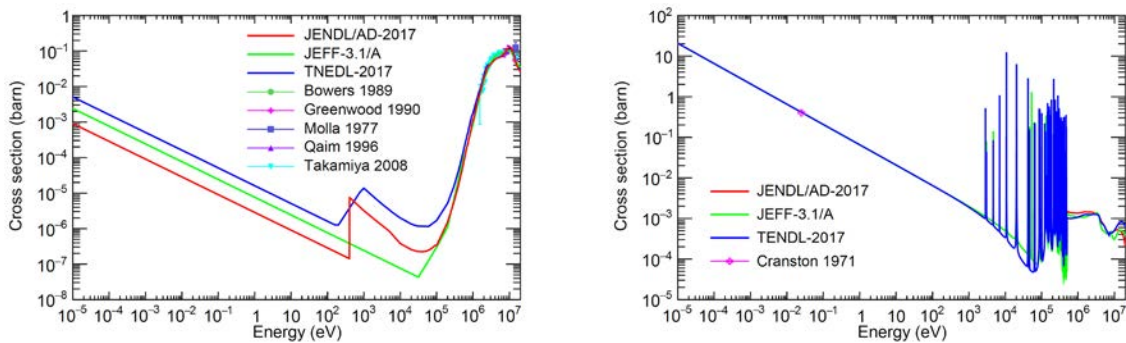


Fig. 5 Comparison between activation nuclear data libraries and experimental data of  $^{63}\text{Cu}(n, p)^{63}\text{Ni}$  reaction (left) and  $^{40}\text{Ca}(n, \gamma)^{41}\text{Ca}$  reaction (right).

#### 5. Conclusion

In this study, we have evaluated the radioactivity inventory of copper material used in electric equipments by the basis of (1) Chemical composition analysis of target material, (2) Neutron flux and spectrum evaluation at target position and (3) Activity inventory calculation. As a result of evaluation, we have confirmed the radioactive concentration of  $^{63}\text{Ni}$  and  $^{65}\text{Zn}$  in the cable near the reactor vessel may exceed the clearance criterion and the radioactivity concentration of  $^{63}\text{Ni}$  becomes more than 90% of total amount. after 10 years from irradiation stops. Since the direct measurement of  $^{63}\text{Ni}$  is difficult, it is necessary to improve uncertainty evaluation of inventory calculation. For that purpose, the uncertainty evaluation of activation cross section is important.

#### References

- [1] T. Sukegawa, M. Hatakeyama, S. Yanagihara, "Evaluation of Methodology on Radioactive Inventory Estimation in the Japan Power Demonstration Reactor Decommissioning Program", J. Nucl. Sci. Technol. 37, p.367 (2000).
- [2] Electric Power Research Institute Inc., "Radiological Characterizations for Reactor Pressure Vessel and Internals Enhanced SAFSTOR", EPRI Technical report 1008018, (2003).
- [3] C. Le Loirec, M. Soulard, G. Ritter, Y. Pénéliou, "Benchmark of DEMAIN, a new calculation package for decommissioning purposes", Prog. Nucl. Energy, p.118 (2020).
- [4] T. Sato, Y. Iwamoto, S. Hashimoto, et. al., "Features of Particle and Heavy Ion Transport code System (PHITS) version 3.02", J. Nucl. Sci. Technol. 55, p.684 (2018).
- [5] IAEA, "Application of the Concepts of Exclusion, Exemption and Clearance, Safety Standard Series No. RS-G-1.7", (2004).
- [6] K. Shibata, N. Iwamoto, S. Kunieda, et. al., "Activation Cross-section File for Decommissioning of LWRs" JAEA-Conf 2016-004, p.47, (2016).
- [7] M.G. Stabin and L. Luz, "Decay data for internal and external dose assessment", Health Physics Vol. 83, p.471-475, (2002).

## 41 Evaluation of scattered radiation on the contralateral breast in breast-conserving therapy

Rikuto HARA<sup>1</sup>, Ayano MAKINAGA<sup>1</sup>

<sup>1</sup>*Department of Radiological Technology, Teikyo University, 6-22, Misaki-machi, Omuta, Fukuoka 836-8505, Japan*  
e-mail: 16RT044e5@stu.teikyo-u.ac.jp

Breast-conserving therapy is a standard local treatment for breast cancer up to stage II after breast-conserving surgery. In this study, we evaluated the effect of scattered radiation on the contralateral breast by the difference in irradiation conditions on the affected breast using Monte Carlo simulation code PHITS. The contralateral dose was less than the target dose farther away from the inner edge of the affected breast. In addition, the larger the breast size, the more the effect of scattered radiation increased.

### 1. Introduction

Breast-conserving therapy is a standard modality for breast cancer up to stage II after breast conserving surgery. An irradiation method called “tangential irradiation” that applies irradiation from two directions is usually used as a standard irradiation technique for breast irradiation. A field-in-field method or intensity modulated radiation therapy (IMRT) is also used to make a uniform dose distribution. In addition, respiratory gated irradiation may be used to reduce exposure for an organ at risk such as the lung or heart. The standard treatment requires a treatment period of 4.5~5.5 weeks with 45~50.4Gy/25~28 fractions [1]. In breast-conserving therapy, radiation therapy has been reported to significantly reduce local recurrence rates and contribute to the survival rate. However, radiation therapy has advantages and disadvantages. For example, one of the early effects is dermatitis. When choosing the dose rate, radiation induced pneumonia and mammary gland hardening should be also considered carefully. Case-control studies and large cohort studies show that postoperative irradiation of breast cancer increases the incidence of contralateral breast cancer. In a report by Taylor et al., an irradiation risk ratio of 1.20 was showed for contralateral breast cancer [2]. One of the causes has been suggested to be the effect of low-dose exposure to the contralateral breast due to scattered radiation.

In this study, we evaluate the effect of scattered radiation on the contralateral chest using the Monte Carlo simulation code PHITS [3].

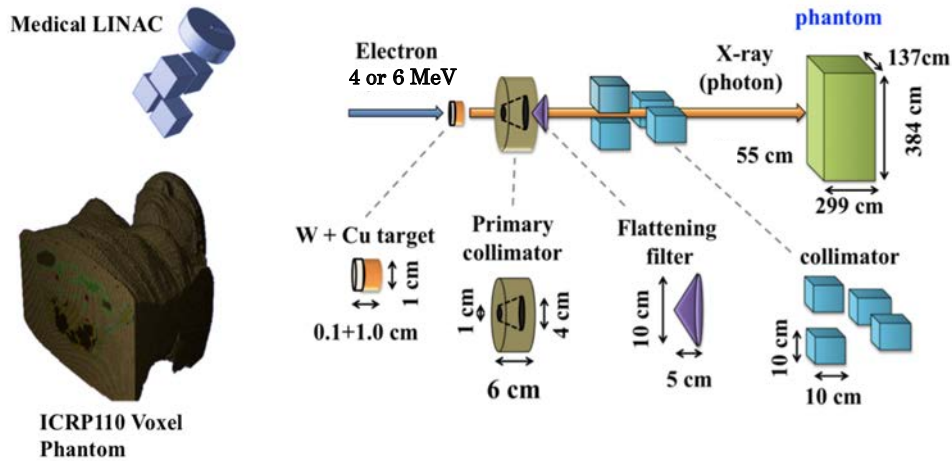


Figure 1 Geometry definition in the PHITS code. A voxel space with a height of 384 cm, a width of 137 cm, and a depth of 299 cm was used. The human voxel phantom, which is 163 cm tall, was placed in the voxel space.

## 2. Simulation study of radiation therapy using PHITS

To evaluate the effect of scattered radiation dose on the contralateral chest, we used Monte Carlo simulation code PHITS. Medical Linac and the human voxel phantom (ICPR 110: female phantom) were defined in the calculation. As seen in Figure 1, an X-ray radiator was constructed with W and Cu material. The collimator material was defined with  $^{184}\text{W}$ -90.5 %,  $^{58}\text{Ni}$ -6.5 %,  $^{56}\text{Fe}$ -3.0 %, and the flattening filter is made from  $^{63}\text{Cu}$ -69.0 %,  $^{65}\text{Cu}$ -31.0 %. In the calculation, we used typical X-ray energy of 4 MV and 6 MV. The field size of the irradiation was 10 cm x 10 cm. To determine the irradiation angle and isocenter for the chest phantom, we used the calculation algorithm reported in [4]. The isocenter is the area where radiation is most concentrated in radiation therapy. The calculated isocenter coordinate was  $(x, y, z) = (-21 \text{ cm}, 19 \text{ cm}, 5 \text{ cm})$ .

Irradiation angles of tangential irradiation from two directions were 60 degrees and 231 degrees (see Figure 2). We calculated the following dose distributions using PHITS.

- (1) Absorbed dose of the affected chest region including the breast area.
- (2) Absorbed dose in the contralateral chest region including the breast area by the scattered radiation.

As described above, in breast-conserving therapy, the entire conserved breast is irradiated approximately 50 Gy in divided dose as prescribed dose. We note the present dose calculation results in Figure 3 show the values before the normalization to therapeutic prescription doses.

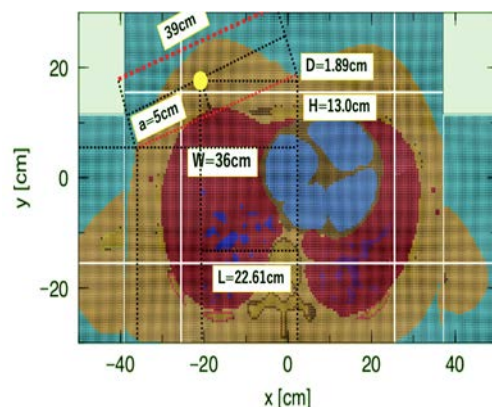


Figure 2 Simulation condition of the irradiation to the breast phantom.

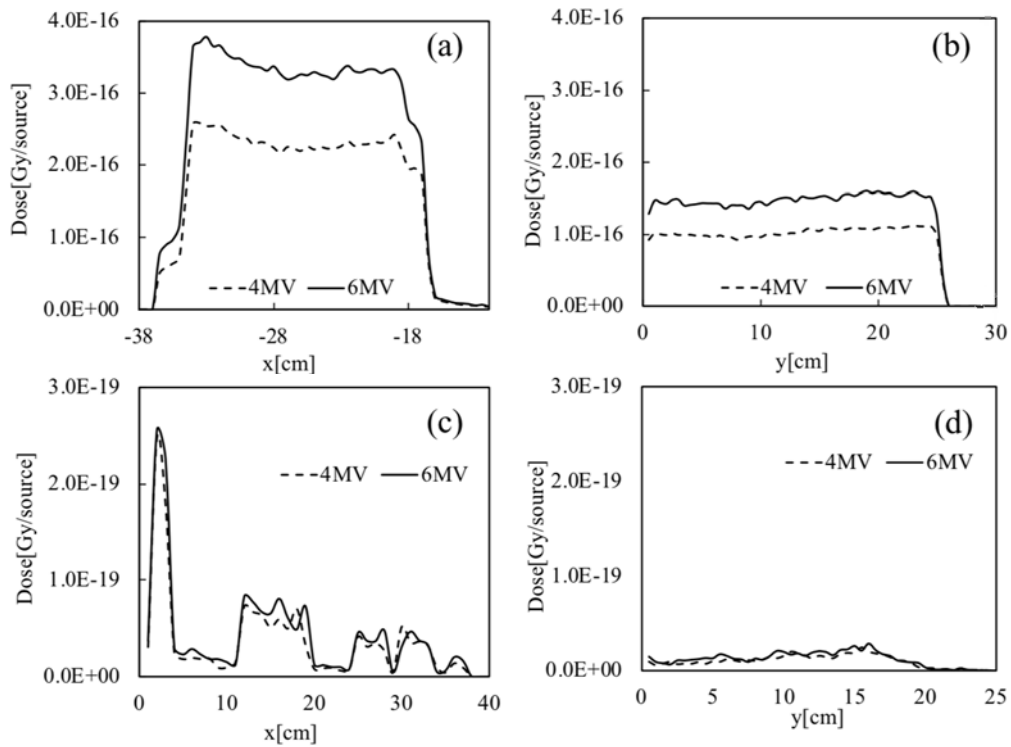


Figure 3 Absorbed dose distributions. (a) The affected chest area including breast area. The horizontal axis is displayed as x coordinate. In this case, the range of y-axis is from 0cm to 25cm. (b) the affected chest area including breast area. The horizontal axis is displayed as y coordinate. The range of the x-axis is from -40cm to 0cm. (c) the scattered radiation on the contralateral chest area including breast area. The horizontal axis is displayed as x coordinate. The range of y-axis is from 0cm to 25cm, and (d) the scattered radiation on the contralateral chest area including breast area. The horizontal axis is displayed as y coordinate. The range of the x-axis is from 0cm to 40cm.

### 3. Results

As seen in figure 3 (a) and (b), the absorbed dose distribution on the x-direction is larger than that for y-direction. Prescription dose shows an almost overall uniform dose distribution in the chest area. Figure 3 (c) and (d) show the absorbed dose for scattered radiation on the contralateral chest area. Figure 3 (c) shows that the effect of scattered radiation was large inside of the contralateral chest area. Numerical results are also shown in Table 1 and 2.

In this evaluation, we just evaluated the dose distribution of the chest area, not breast itself. So, some low absorption dose areas in the figure are considered as an absorption in the heart or/and lung region and so on. Precise analysis of the dose distribution for breast region will be performed in the near future.

**Table 1 the absorbed dose of the affected breast**

Direction	Dose (Gy/source) 4MV	Dose (Gy/source) 6MV
R-L (x-direction)	8.6E-15	1.2E-14
P-A (y-direction)	5.1E-15	7.4E-15

**Table 2 the absorbed dose of the contralateral breast**

Direction	Dose (Gy/source) 4MV	Dose (Gy/source) 6MV
R-L (x-direction)	4.9E-19	1.2E-18
P-A (y-direction)	5.1E-19	6.1E-19

#### 4. Summary

Absorbed dose for the scattered radiation on the contralateral evaluated chest region is about 4 orders of magnitude smaller than the absorbed dose in the affected chest region. During breast-conservation therapy, the contralateral breast may be irradiated about 5 mGy. This is equivalent to 2 times of the mammography dose, suggesting that treatment planning should be done carefully considering low-dose exposure to the contralateral chest region.

#### Acknowledgement

We thank Dr. S. Hashimoto (JAEA) for his support of PHITS and Dr. K. Sutherland (Hokkaido Univ. and Stanford Univ.) for checking the manuscript.

#### References

- [1] Japanese Society for Radiation Oncology, Radiation treatment planning guidelines 2016:170-176.
- [2] C. Taylor, C. Correa, et al., Early Breast Cancer Trialists' Collaborative Group. Estimating the risks of breast cancer radiotherapy: evidence from modern radiation doses to the lungs and heart and from previous randomized trials, *J. Clin. Oncol.* 2017;35(15):1641-9.
- [3] T. Sato, Y. Iwamoto et al., Features of Particle and Heavy Ion Transport code System (PHITS) version 3.02, *J. Nucl. Sci. Technol.* 55, 684-690, 2018.
- [4] General Incorporated Association Japan Breast Cancer Society, Guidelines for the Practice of Breast Cancer Treatment 2018 Edition, 4th Edition: 308-315.

## 42 Burnup Calculation with Different Fission Yield Data

Atsuya ISO, Yuya YAMASAKI, Taichi TAKEISHI, Satoshi TAKEDA, Takanori KITADA

*Osaka University, 2-1 Yamada-oka, Suita, Osaka 565-0871, Japan*

*e-mail : a-iso@ne.see.eng.osaka-u.ac.jp*

The fission yield has recently been evaluated in Japan based on the various theories. In order to evaluate the effect of different fission yield data on burnup calculation, burnup chain and/or fission yield data used in a burnup calculation is to be modified so as to obtain reasonable results because different/additional isotopes are stored among the data, especially for isomers.

The comparison between JENDL/FPY-2011 and new fission yield evaluated by Tokyo Tech was performed with SWAT4.0 for the PIE data: BM5 sample of Swiss Beznau-1 PWR, and the results shows that there is relatively a large impact on the results. This shows the importance of how to handle the burnup chain and/or fission yield data on the comparison among different fission yield data.

### 1. Introduction

Fission yield is an important physical quantity to evaluate the amount of fission products after irradiation. The fission yield used in Japanese Evaluated Nuclear Data Library (JENDL) employs ENDF/B [1] data, but recently the new fission yield was evaluated by Tokyo Tech [2] and the fission yield is planned to be adopted in the next version of JENDL. The validation of the data is inevitable before the adoption of new fission yield, and the validation is to be performed with different fission yield data through the comparison of the burnup calculation results to the PIE data. However, there are some concerning points in the comparison of the burnup calculation results with different fission yield, where the nuclides stored in the data are different among different fission yield.

Different/additional isotopes are stored among the data, especially for isomers. Therefore, it is necessary to properly modify burnup chain and/or fission yield data used in a burnup calculation in order to obtain valid results.

This paper shows the effect of modification of the burnup chain and/or fission yield on burnup calculation for the comparison between fission yields.

### 2. Modification of Burnup Chain and Fission Yield

The latest version of JENDL/FPY-2011 [3] (FPY-2011) and fission yields newly evaluated by Tokyo Tech are discussed in this study. These fission yields were replaced on the cross-sectional library set of

ORLIBJ40 [4]. Since ORLIBJ40, FPY-2011, and the data of Tokyo Tech are different in nuclides which are given the fission yield as shown in Table 1, the burnup chain and/or fission yield in ORLIBJ40 need to be modified.

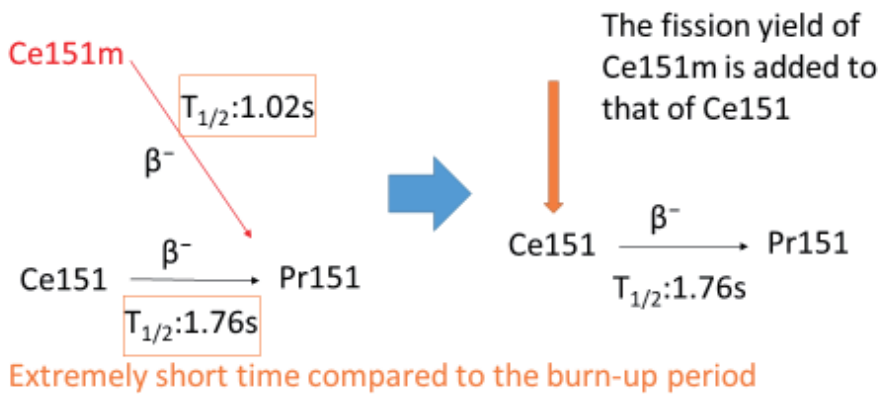
**Table 1 Difference in number of stored nuclides between FPY-2011 and fission yield evaluated by Tokyo Tech**

	ORLIBJ40	FPY-2011	Tokyo Tech yield
Number of stored nuclides	1200	1260	1250

Table 1 shows that there are many differences in stored nuclides, and this fact requires the modification in burnup chain and/or fission yield data. There are two cases to be considered in the modification.

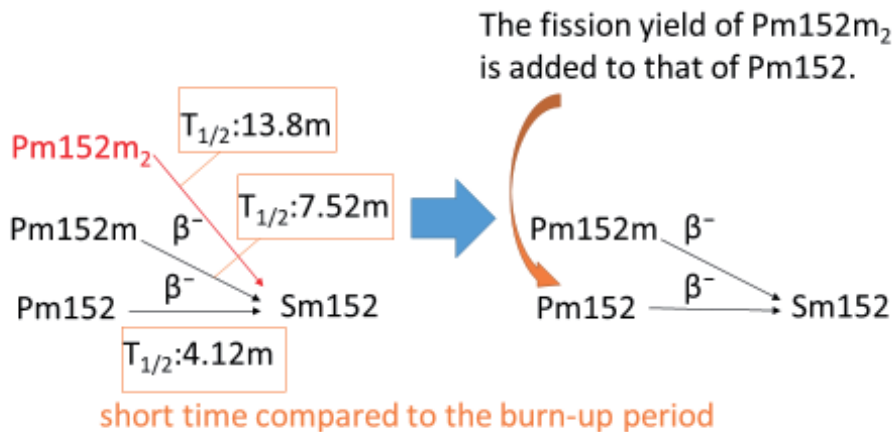
- Case-1 : the nuclide which is not used in burnup chain, but of which fission yield is given only for one or two fission yield data,
- Case-2 : the nuclide which is used in burnup chain, but of which fission yield is not given for one or two fission yield data,

As for Case-1, there are several examples as shown in Figures 1 and 2.  $^{151m}\text{Ce}$  is not used in burnup chain of SWAT4.0 [5], but the fission yield is given in FPY-2011, and not given in both ORLIBJ40 and the fission yield evaluated by Tokyo Tech. Here the fission yield of  $^{151m}\text{Ce}$  was added to that of  $^{151}\text{Ce}$  which is used in the burnup chain, with the consideration that the half-life of  $^{151m}\text{Ce}$  (1.02[s]) is similar to that of  $^{151}\text{Ce}$  (1.76[s]), and the daughter nuclide ( $^{151}\text{Pr}$ ) is the same to  $^{151}\text{Ce}$ . Another example is for  $^{152m2}\text{Pr}$ . The fission yield of  $^{152m2}\text{Pr}$  is not used in burnup chain of SWAT4.0, but the fission yield is given only in FPY-2011.  $^{152}\text{Pr}$  and  $^{152m1}\text{Pr}$  are given in the burnup chain, so the fission yield is added to that of  $^{152}\text{Pr}$  in this study.



Pu241	ORLIBJ40	FPY-2011	Fission yield evaluated by Tokyo Tech		Pu241	ORLIBJ40	FPY-2011	Fission yield evaluated by Tokyo Tech
Ce151	3.02E-01	3.63E-02	3.04E-01	→	Ce151	3.02E-01	2.51E-01	3.04E-01
(Ce151m)		2.15E-01			Ce151			

**Fig. 1 Case1-1: In burnup chain, ground state is given, but meta-stable state is not given**  
 Figures show the decay chain around <sup>151</sup>Ce before and after the modification of fission yield. Tables show fission yields of <sup>151</sup>Ce and <sup>151m</sup>Ce before and after modification. The fission yield of the meta-stable nuclides not used in burnup chain of SWAT4.0 is added to ground nuclide.



Pu241	ORLIBJ40	FPY-2011	Fission yield evaluated by Tokyo Tech		Pu241	ORLIBJ40	FPY-2011	Fission yield evaluated by Tokyo Tech
Pm152	1.55E-03	6.42E-04	1.74E-03	→	Pm152	1.55E-03	1.55E-03	1.74E-03
Pm152m	2.70E-03	2.70E-03	2.40E-03		Pm152m	2.70E-03	2.70E-03	2.40E-03
(Pm152m <sub>2</sub> )		9.10E-04						

**Fig. 2 Case1-2: In burnup chain, ground state and meta-stable state are given, but meta-stable2 state is not given**

Figures show the decay chain around <sup>152</sup>Pm before and after the modification of fission yield. Tables show fission yields of <sup>152</sup>Pm, <sup>152m</sup>Pm and <sup>152m2</sup>Pm before and after modification.

As for Case-2, there are also several examples as shown in Figures 3. <sup>84m</sup>As is used in the burnup chain, but the fission yield is not given in FPY-2011 and new fission yield. In this case, we don't have any fission yield data for the nuclide, therefore the fission yield for the nuclide is set to be zero, although

<sup>84</sup>As is used in the burnup chain and the fission yield data is given for all fission yield data.

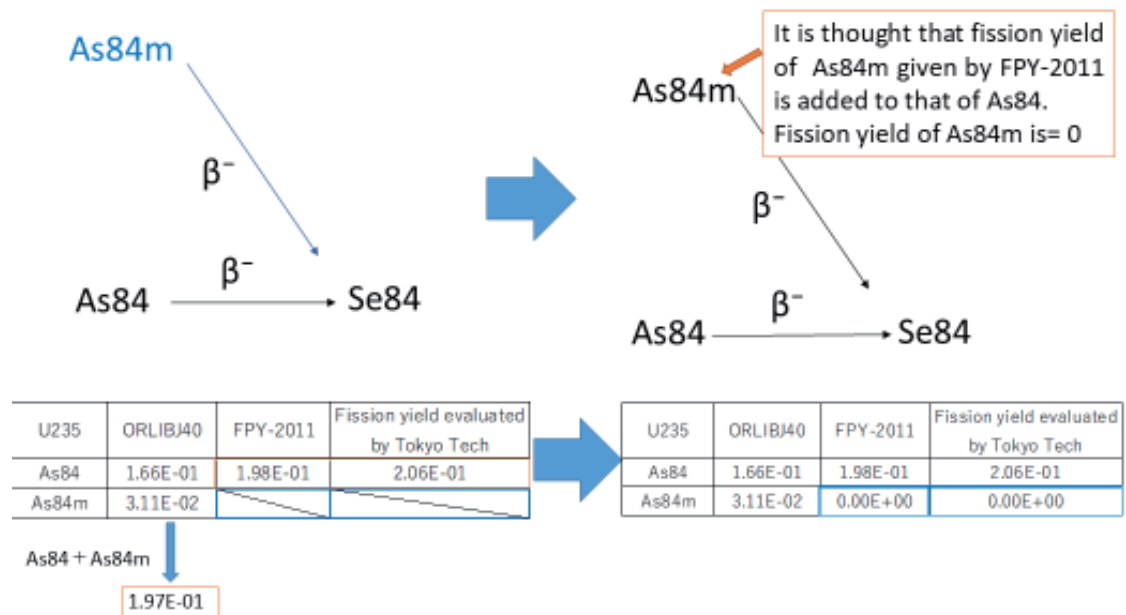


Fig. 3 Case2-1: In burnup chain, ground state is given, but meta-stable state is not given

Figures show the decay chain around <sup>84</sup>As before and after the modification of fission yield. Tables show fission yields of <sup>84</sup>As and <sup>84m</sup>As before and after modification. Fission yields of <sup>84m</sup>As not given by FPY-2011 and fission yield evaluated by Tokyo Tech are 0.

### 3. PIE analysis with different modification in burnup chain and fission yield

PIE analysis is usually performed to check the validity of the data used in the calculation such as fission yield data, and the modification described in the previous chapter brings the difference in the results as easily expected. Thus the impact of the different modifications on the PIE analysis results is evaluated in this study.

PIE used in the calculation is performed in ARIANE program and the sample of BM5 [6] is the target fuel to evaluate the nuclide composition after irradiation, as shown in Figure 4. The PIE data is selected as the experimental results because of small uncertainty among the reported results.

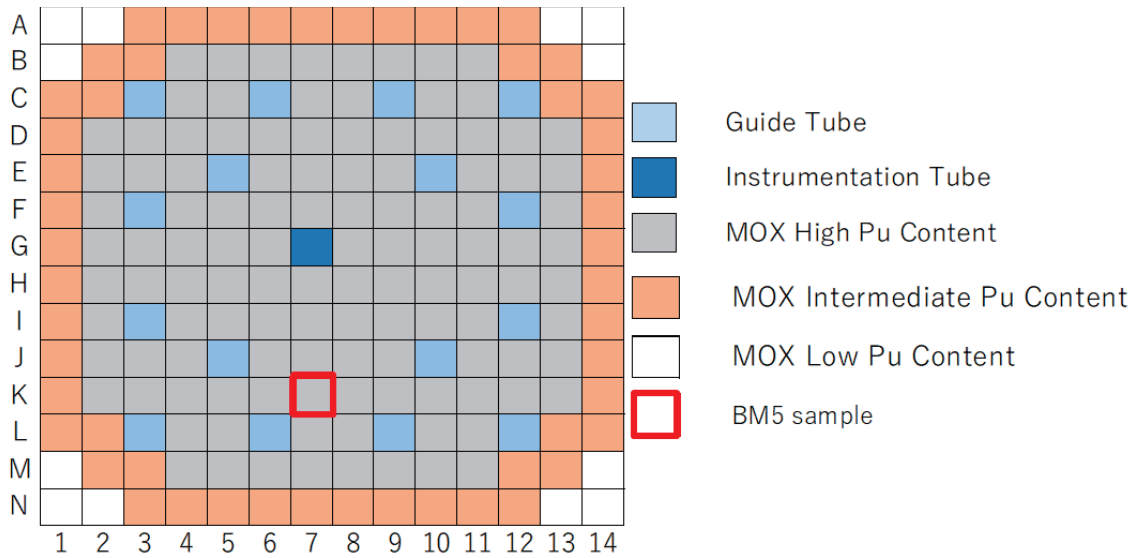


**Fig. 4 Fuel assembly model and position of BM5 sample**

PIE analysis with and without the modification expressed in Case 1 brings a non-negligible impact on the PIE analysis results as shown in Figure 5. The results without the modification are evaluated in the condition that the fission yield of  $^{151m}\text{Ce}$  is neglected (no addition to the fission yield of  $^{151}\text{Ce}$ ). Figure 5 shows that the different modification brings about 10% difference in C/E value of  $^{151}\text{Sm}$ ,  $^{152}\text{Sm}$ ,  $^{151}\text{Eu}$ , which are the daughter nuclides of  $^{151}\text{Cm}$  as shown in Figure 6. These results show that a poor modification brings the misunderstanding for the validity of the data used in the analysis, and proper modification is necessary to check the validity of new fission yield data. To avoid poor modification, the following is preferable that all nuclides are used in the burnup chain.

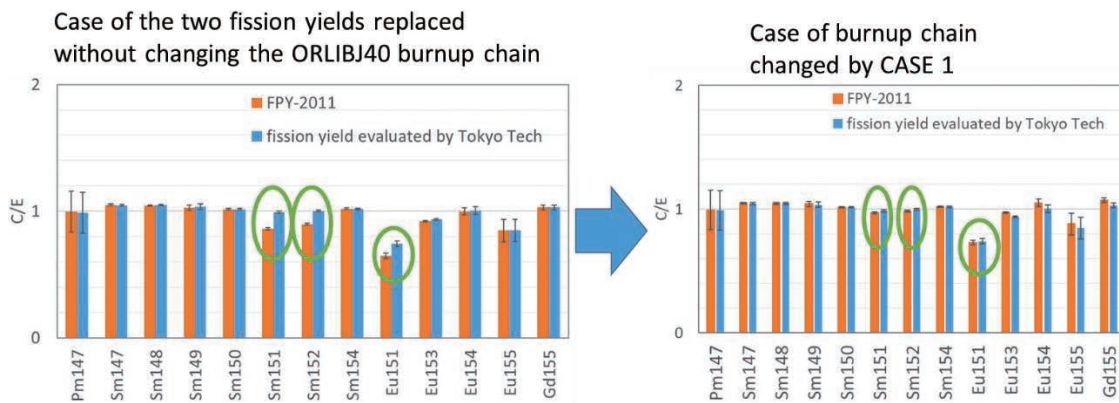


**Fig. 5 Impact on the burnup calculation result**

**Green ellipses show where C/E values are drastically changed by the modification.**

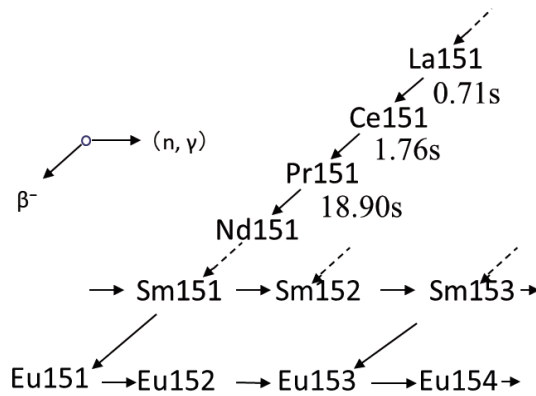


**Fig. 6 Example of burnup chain around Ce151**  
 (Dashed arrows show  $\beta^-$  decay omitting some nuclides.)

#### 4. Conclusion

Recently the new fission yield was evaluated by Tokyo Tech and the fission yield is planned to be adopted in the next version of JENDL. The validation of the data is inevitable before the adoption of new fission yield, and the validation is usually performed with different data where the nuclides stored in each data are not the same. This fact brings the cases where the misunderstanding of the validity is observed by the poor modification. It is also found that the about 10% difference in the C/E value can be observed for daughter nuclides through the PIE analysis with proper or poor modification. Proper modification of burnup chain and fission yield are necessary to obtain reasonable results with the consideration of half-life and decay chain.

#### References

- [1] M.B. Chadwick, P. Obložinský, M. Herman, et al., "ENDF/B-VII.0: Next generation evaluated nuclear data library for nuclear science and technology", Nuclear Data Sheet, 107, p.2931, (2006).
- [2] K. Tsubakihara et al., To be submitted to JNST; S. Chiba, private communication.
- [3] J. Katakura, "JENDL FP Decay Data File 2011 and Fission Yields Data File 2011", JAEA-Data/Code 2011-025, Japan Atomic Energy Agency (2012).
- [4] K. Okumura, K. Sugino, K. Kojima, T. Jin, T. Okamoto, and J. Katakura, "A Set of ORIGEN2 Cross Section Libraries Based on JENDL-4.0: ORLIBJ40", JAEA-Data/Code 2012-032, Japan Atomic Energy Agency (2012) (in Japanese).
- [5] T. Kashima, K. Suyama, and T. Takada, "SWAT4.0 - The Integrated Burnup Code System Driving Continuous Energy Monte Carlo Codes MVP, MCNP and Deterministic Calculation Code SRAC", JAEA-Data/Code 2014-028, Japan Atomic Energy Agency (2015) (in Japanese).
- [6] R.T.Primm III, "ARIANE International Programme Final Report", ORNL/SUB-97-XSV750-1, Oak Ridge National Laboratory (2003).

### 43 Improvement of fuel ion ratio diagnostics performance using anisotropic neutron emission spectrum in NBI heating deuterium-tritium plasma

Tomoki Urakawa and Hideaki Matsuura

Department of Applied Quantum Physics and Nuclear Engineering, Kyushu University,

744 Motoooka Nishi-ku Fukuoka 819-0395, Japan

e-mail : urakawa-0804@nucl.kyushu-u.ac.jp

For the stable operation of the deuterium-tritium (DT) fusion reactor, it is important to know the triton to deuteron fuel-ion density ratio ( $n_T/n_D$ ) during the operation. A method to obtain the  $n_T/n_D$  density ratio from the emission ratio of 14 MeV neutrons from  $T(d,n)^4\text{He}$  reactions and 2.45 MeV neutron from  $D(d,n)^3\text{He}$  reactions has been studied. This method has a serious problem that the detection of DD neutrons is interfered by slowing-down component of DT neutrons. As a solution to this problem, a technic increasing the fraction of the DD to DT reaction rate by NBI heating and utilizing modification of the DT and DD neutron emission spectra by has been studied. Owing to this technic, the measurement has found to be possible even when  $n_T/n_D = 1.0$ . However, the detectable plasma condition is still limited, and further improvement is required. In this study, we calculated the neutron spectrum with the detector by introducing a more realistic angle dependence of neutron production, compared to the previous study. The results showed that the energy region where DD neutrons can be more clearly measured was found and evaluated the effective in improving measurement performance. And it was shown that the fuel-ion ratio diagnosis in ITER class plasma was sufficiently established with the improvement of measurement performance.

#### 1. Introduction

Diagnostic to measure the fuel ion ratio in deuterium-tritium (DT) fusion plasma is important to stably operate and control a fusion reactor. Requirement for fuel ion ratio diagnostics are over the parameter range of  $0.01 < n_T/n_D < 10$ , spatial resolution of  $a/10$ , where 'a' is the minor radius of the plasma [1]. In the ITER, plasma operation over the parameter range of  $0.1 < n_T/n_D < 3.0$  is assumed. Recently, various methods to know the fuel-ion density ratio such as gamma-ray measurement [2], charge exchange recombination spectrometry [3], collective Thomson scattering [4] and neutron measurement [5], have been proposed. The devices for the above measurement will be installed in ITER for the practical examination of the diagnostic [6]. In fuel ion ratio diagnostic using neutron measurement, the intensity of each spectra of the 14 MeV neutrons from  $D(t,n)^4\text{He}$  reactions and 2.45 MeV neutron from  $D(d,n)^3\text{He}$  reactions are measured. Fuel ion ratio is given by

$$\frac{n_T}{n_D} = \frac{R_{DT} \langle \sigma v \rangle_{DD}}{2R_{DD} \langle \sigma v \rangle_{DT}}, \quad (1)$$

where  $R_{DD}$  and  $R_{DT}$  are each DD and DT reaction rates,  $n_T$  and  $n_D$  are the number density of triton and deuteron, and  $\langle \sigma v \rangle_{DD}$  and  $\langle \sigma v \rangle_{DT}$  are the reaction rate coefficients for DD and DT reaction. As a serious problem of this diagnostics, the detection of DD neutron (Signal) is interfered by slowing-down component of DT neutrons (Noise). Due to the above problem, high measurement accuracy for both neutron production rates is required to distinguish between the Signal and Noise. And, it is also important to understand the spectrum of the Noise using neutron transport calculation [7]. As a result, in the case of thermal plasma, it has been reported that the detectable parameter range is  $n_T/n_D < 0.6$  and  $T_i > 6$  keV [1].

In order to improve the measurement performance, a technic using the rise in the fraction of the DD to DT reaction rate and modification of the neutron emission spectra by NBI-heating has been studied [8]. First, the degree of enhancement for the DD reaction rate coefficient is much larger than that for DT due to the cross section of Fig. 1 [9]. Thus, the ratio of DD signal to DT noise (S/N value) is increased. In beam-injected plasma, the shape of neutron emission spectra significantly changed. By considering the modification of the neutron emission spectrum, i.e., shifting the measurement energy region to the higher energy side, we can reduce the Noise to Signal ratio. In Ref [8], possibility of measurement at  $n_T/n_D = 1.0$  was shown by using the method. But, evaluation of the detectable parameter range is still insufficient by only examining Ref [8]. And, further improvement is necessary for measurement of ITER class plasma.

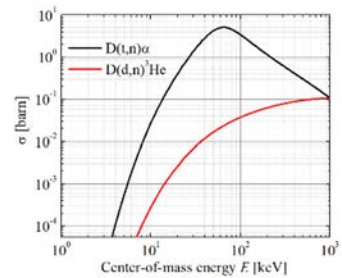


Fig. 1 Cross section for DD and DT reactions as a function of the energy in the CM frame.

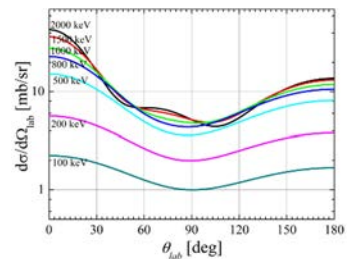


Fig.2 Differential cross section for DD reaction.

In NBI heating plasma, emission spectrum of the particle which produced fusion reaction has anisotropy in addition to modified from Gaussian [10].

Due to anisotropic emission, the population of energetic particle is higher in the NBI incident direction. In the case of  $D(d,n)^3\text{He}$  reaction, anisotropy appears greatly due to differential cross section. Fig. 2 shows differential cross section of  $D(d,n)^3\text{He}$  reaction [11]. Solid lines show incident deuteron energy (100, 200, 500, 800, 1000, 1500 and 2000 keV). The modification from Gaussian to the high energy side is even greater since forward emission is dominant from Fig. 2. Thus, performance of the fuel ion diagnostic using modified neutron emission spectrum measurement may be more improved due to considered anisotropic.

In this study, we introduce the more realistic angle dependence of neutron production by considering the anisotropy of the neutron emission spectra, and calculate the neutron spectra and S/N value with the detector. And, we evaluate the energy region where DD neutrons can be more clearly measured and indicate that consideration of anisotropy is effective for improving measurement performance.

## 2. Calculation model

### 2-1 Double differential neutron emission spectra

In Fig. 3, the double differential emission spectrum for neutron as a function of neutron energy and

emission angle relative to the beam-injection direction in the laboratory system is shown. This neutron emission spectrum was assumed to be obtained from the ITER like plasma sustained by NBI heating. In Fig. 3, plasma parameters are assumed as follow;  $n_e = 5.0 \times 10^{19} \text{ m}^{-3}$ ,  $T_e = 10 \text{ keV}$ ,  $P_{\text{NBI}} = 33 \text{ MW}$ ,  $E_{\text{NBI}} = 1.0 \text{ MeV}$ ,  $\tau_E = 3.0 \text{ s}$  and  $n_T/n_D = 1.0$ . Here  $n_e$  is electron density,  $T_e$  is electron temperature,  $P_{\text{NBI}}$  is beam power,  $E_{\text{NBI}}$  is beam energy,  $\tau_E$  is energy confinement time. In this study, we assumed tangential deuteron beam to the toroidal magnetic field. Beam-particle slowing down is calculated using analytic model described in Ref. [12]. The velocity distribution functions of the triton and deuteron (bulk component) are assumed to be Maxwellian. We calculate this neutron emission spectrum using the method described in Ref. [10]. The double differential neutron emission energy spectrum is written as

$$\frac{d^2 N_n}{dE d\Omega_{lab}}(E, \theta_{lab}) = \frac{1}{1 + \delta_{DD(T)}} \iiint f_D(|\vec{v}_D|) f_{D(T)}(|\vec{v}_{D(T)}|) \frac{d\sigma}{d\Omega} \times \delta(E - E_n) \delta(\Omega_{lab} - \Omega_n) v_r d\vec{v}_D d\vec{v}_{D(T)} d\Omega, \quad (2)$$

where  $E_n$  is the neutron energy in the laboratory system [13];

$$E_n = \frac{1}{2} m_n V_c^2 + \frac{m_{^3\text{He}(\alpha)}}{m_n + m_{^3\text{He}(\alpha)}} (Q_{DD(DT)} + E_r) + V_c \cos \theta_c \sqrt{\frac{2m_{^3\text{He}(\alpha)}}{m_n + m_{^3\text{He}(\alpha)}} (Q_{DD(DT)} + E_r)}, \quad (3)$$

where  $m_n(^3\text{He}, \alpha)$  is the neutron (3-helium,  $\alpha$ -particle) mass,  $V_c$  is the center-of-mass velocity of the colliding particles,  $\theta_c$  is the angle between the center-of-mass velocity and the neutron velocity in the center-of-mass frame,  $Q_{DD(DT)}$  is each reactions  $Q$ -value, and  $E_r$  represents the relative energy given by

$$E_r = \frac{1}{2} \frac{m_D m_{D(T)}}{m_D + m_{D(T)}} |\vec{v}_D - \vec{v}_{D(T)}|. \quad (4)$$

The  $\theta_{lab}$  represents the angle between the direction of emitted neutron and that of beam injection in the laboratory system, and  $\Omega_n$  is a unit vector in the direction of emission of neutron in the laboratory system, which is determined using the classical kinematics as a function of  $\vec{v}_D$ ,  $\vec{v}_{D(T)}$ , and  $\theta_c$ . In Section 3.1, we discuss using only the neutron emission spectrum shown in Fig.1 as a neutron source. In Section 3.2, we calculate the neutron source using analysis models in Ref. [9] and Ref. [12] for each plasma parameter and do the following discussion.

## 2-2 Neutron transport calculation

### 2-2-1 Blanket with detector model

Fig. 4 shows the computational schema of the blanket systems with collimator (detector). In Fig. 4, the collimator direction,  $\varphi$ , was set to be the angle made with respect to the extended line in the NBI incident direction when viewed from the blanket (upper view). The blanket model was employed as the torus form which has a 6.2 m major radius and a 2.0 m minor radius. And, blanket material component and each layer

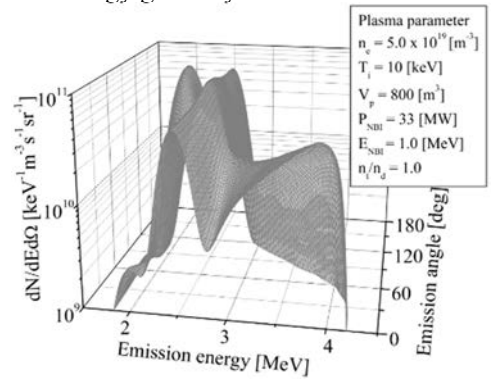


Fig. 3 Double differential emission spectrum produced by the  $D(d,n)^3\text{He}$  reactions as a function of neutron energy and emission angle,  $\theta_{lab}$ , relative to the beam-injection direction in the laboratory system.  $P_{\text{NBI}} = 33 \text{ MW}$ ,  $E_{\text{NBI}} = 1.0 \text{ MeV}$ ,  $T_e = 10 \text{ keV}$ , and  $n_e = 5.0 \times 10^{19} \text{ m}^{-3}$  are assumed.

thickness is shown in Table 1 [13]. The collimator is a pillar 10 cm in inner diameter and 20 cm in outer diameter. And the length of collimator is 225 cm. These conditions were set based on Ref. [8] and Ref. [14].

**2-2-2 Signal and Noise calculation**

Incident DD neutron spectrum in the detector (Signal) and slowing-down component of DT neutrons (Noise) was calculated using the Monte Carlo transport code MVP [15] with the JENDL-4.0 [16] nuclear data library. In this study, we adopted point detector estimators in calculating Signal and Noise. And, Signal and Noise are calculated using a torus volume neutron source with uniform emissivity [17]. The validity of this calculation method is shown in Ref. [1]. Throughout the simulation, the measurement energy range of neutron detection set to  $E_c \pm 120$  keV (Ref. [5]), where  $E_c$  is center energy in the measurement energy range.

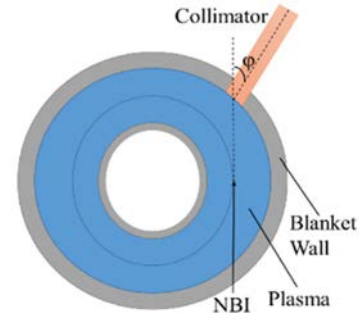


Fig. 4 The model used for MVP neutron transport calculations assuming the ITER condition. The  $\phi$  shows the angle made with respect to the extended line in the NBI incident direction.

Table 1 Blanket component.

	Thickness	Component (vol%)
Be armor	10 mm	Be(100)
Heat sink	22 mm	CuCrZr(82.9), H <sub>2</sub> O(17.1)
First Wall	49 mm	SS316L(N)-IG(84.6), H <sub>2</sub> O(15.4)
Gap	3 mm	
Shield structure	370 mm	SS316L(N)-IG(84.6), H <sub>2</sub> O(15.4)

**3. Result and discussion**

**3-1 Incident neutron spectrum on detector surface**

Fig. 5 shows incident neutron spectrum with the detector. ( $\phi = 0^\circ, 25^\circ, 50^\circ$ ). And, the incident spectrum obtained under the assumption of isotropic emission ( $\phi = 0^\circ, 50^\circ$ ) and the slowing down component of DT neutrons ( $\phi = 0^\circ$ ) is also shown. Since the emission spectrum around the NBI incident direction is measured, the ratio of energetic neutron increases as  $\phi$  increase. In particular, when  $\phi = 0^\circ$ , the peak appears in the high energy region (around 4.0 MeV). This peak is as large as Gaussian formed by thermonuclear reaction. Fig. 6 shows improvement of count due to anisotropic. Now, count is the integral value in the range of  $E_c \pm 120$  keV. Depending on the collimator direction,  $\phi$ , the measurement energy region where count is improved differs. In the case of  $\phi = 50^\circ$ , count is improved about 50% in the 2.4-2.5 MeV region. On the other hand, in the case of  $\phi = 50^\circ$ , count is improved about 8.0 times in the high energy region (around 4.0 MeV). And, the intensity of the incident spectrum obtained under the assumption of isotropic emission is different between  $\phi = 0^\circ$  and  $\phi = 50^\circ$  due to the effect of line of sight. It can be confirmed that the above results are appropriate from the influence of the collimator direction on the intensity of neutron flux and the S/N value discussed in Ref. [7].

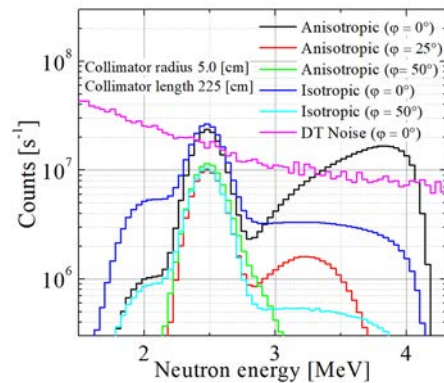


Fig. 5 Incident neutron spectrum with the detector.  $\phi$  shows the angle made with respect to the extended line in the NBI incident direction.  $P_{NBI} = 33$  MW,  $E_{NBI} = 1.0$  MeV,  $T_e = 10$  keV, and  $n_e = 5.0 \times 10^{19} \text{ m}^{-3}$ ,  $n_i/n_d = 1.0$  are assumed.

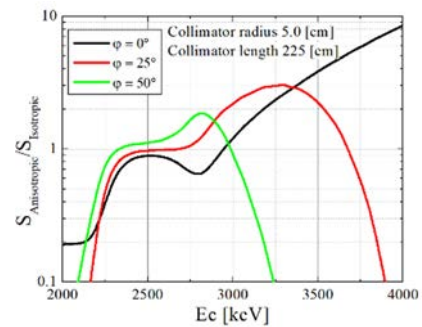


Fig. 6 Improvement of count due to anisotropic. ‘S’ is the integral value in the range of  $E_c \pm 120$  keV.

### 3-2 Improvement of S/N value and distinction of Signal and Noise

Fig. 7 shows S/N value obtained for each incident spectra of Fig.5. Now S/N value is given by

$$\frac{S}{N} = \frac{\int_{E_c-240 \text{ keV}}^{E_c+240 \text{ keV}} F_{DD}(E)dE}{\int_{E_c-240 \text{ keV}}^{E_c+240 \text{ keV}} F_{DT}(E)dE}, \quad (5)$$

where  $F_{DD(DT)}$  is incident DD (DT) neutron energy spectrum on the detector. In Ref. [17], DD neutron and Slowing down component of DT neutron can be distinguished when  $S/N > 0.4$ . But, in this case, high accuracy is required for both of Signal and Noise measurements to decide each spectrum. On the other hands, in Ref. [5], it has been pointed out that DD neutrons can be confirmed sufficiency when  $S/N \gg 1.0$ . Thus, for the above reasons, we defined  $S/N > 1.0$  as 'sufficient condition' and  $S/N > 0.4$  as 'detectable condition' in fuel ion ratio diagnostic.

In the case of measuring neutron emission spectrum Fig. 3 ( $T_i = 10$  keV,  $n_T/n_D = 1.0$ ),  $S/N > 0.4$  can be achieved regardless of the collimator direction,  $\phi$ .  $S/N > 1.0$  can be achieved regardless of the anisotropic consideration when  $\phi = 0^\circ$ . In addition,  $S/N > 2.0$  can be achieved considering anisotropic ( $\phi = 0^\circ$ ) and measuring high energy region (around 4.0 MeV). Thus, the measurement of the anisotropic emission spectrum showed that the S/N was improved about twice. It was shown that 'sufficient condition' is achieved in the ITER class plasma.

### 3-3 Detectable plasma parameter range

Fig. 8 shows S/N values at various ion temperature and fuel ion ratio for anisotropic emission spectrum measurement ( $E_c = 3780$  keV). The diagonal line in Fig. 8 indicates the region where  $S/N > 1.0$ . Due to anisotropic consideration, the parameter range of 'sufficient condition' is  $n_T/n_D < 1.2$  and  $T_i < 20$  keV. In addition, it was shown to achieve detectable condition ( $S/N > 0.4$ ) even when  $n_T/n_D = 3.0$ . This suggests that the fuel ion ratio diagnosis using neutron diagnostic is valid over the entire ITER operating range.

Fig. 9 shows the detectable plasma parameter range under 'sufficient condition'. The solid line shows S/N value (= 1.0) at various plasma parameters for anisotropic emission spectrum measurement. The dashed and dotted lines indicate that obtained when measuring the isotropic emission spectrum and the Gaussian

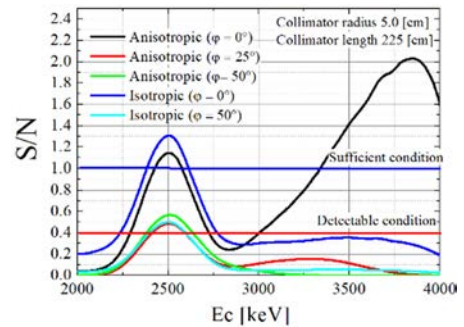


Fig. 7 S/N value dependency on measurement energy range.

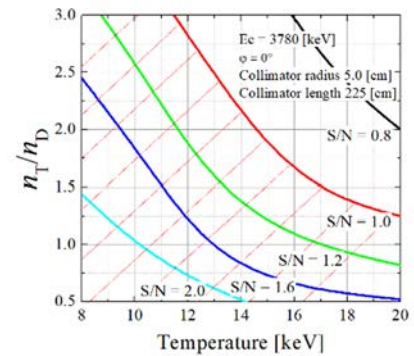


Fig. 8 S/N value at various plasma parameter. Solid lines indicate S/N = 0.8, 1.0, 1.2, 1.6 and 2.0 respectively. Red diagonal lines indicate the range of plasma parameters that satisfy 'sufficient condition ( $S/N > 1.0$ )'.

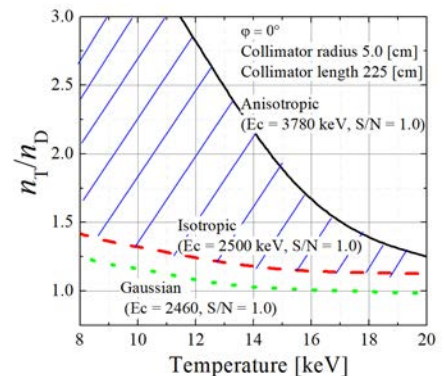


Fig. 9 S/N value (= 1.0) obtained by measuring each spectrum. Blue diagonal lines indicate the plasma parameter region that can be measured by considering the anisotropy of the spectra.

distribution, respectively. Due to anisotropic consideration, parameter range to satisfy the condition is expanded. In particular, the S/N value is well improved in the high  $n_T/n_D$  region. Focusing on the modification from Gaussian reduces the effect of deuteron density reduction on neutron emission rate. These result shows that consideration of anisotropy is effective.

#### 4. Conclusion remarks

In this study, we evaluated the improvement of  $n_T/n_D$  density ratio measurement by anisotropic emission spectra. When the installation direction of the collimator was set to  $\varphi = 0^\circ$  (tangential line), it was found that there was a measurement region where the number of incident neutrons increased by a maximum of about 8 times compared to the assumption of isotropic emission. As a result, the S/N value was doubled compared to the isotropic emission spectrum measurement in the case of  $T_i = 10$  keV,  $n_T/n_D = 1.0$ . And, due to anisotropic neutron emission spectrum measurement, the parameter range of ‘sufficient condition’ ( $S/N > 1.0$ ) is  $n_T/n_D < 1.25$  and  $T_i < 20$  keV. In addition, it was shown to achieve ‘detectable condition’ ( $S/N > 0.4$ ) even when  $n_T/n_D \cong 3.0$ . Therefore, measurement of anisotropic emission spectrum is effective for improving performance of fuel ion ratio diagnosis.

In future work, we need to discuss the plasma parameter range that can be measured in more detail considering the performance of the detector (response function, detection efficiency, etc.). And, discussion of electron density dependence is also needed. In addition, at high  $n_T/n_D$ , precise calculation of DT slowing-down component by neutron transport calculation is required because of  $0.4 < S/N < 1.0$ . Thus, it is also important to improve the accuracy of nuclear data when considering the feasibility of fuel ion ratio diagnostic. And, it is also necessary to study the practicality of this method in the nuclear fusion DEMO reactor.

#### References

- [1] G. Ericsson, et al., Rev. Sci. Instrum. **81**, 10D324 (2010).
- [2] V. G. Kiptily, Nucl. Fusion, **55**, 023008 (2015).
- [3] N. C. Luhmann, et al., Fusion Sci. Technol. **53**, 335-96 (2008).
- [4] L. Bertalot, et al., JINST, **7**, C04012 (2012).
- [5] J. Källne, et al., Rev. Sci. Instrum. **62**, 2781 (1991).
- [6] S. B. Korsholm, et al., Rev. Sci. Instrum. **81**, 10D323 (2010).
- [7] P. Antozzi, et al., Nucl. Instrum. Methods Phys. Res. Sect. A, **368**, 457-472 (1996).
- [8] Y. Kwamoto, et al., J. Plasma Fusion Res. **11**, 2405078 (2016).
- [9] H. S. Bosch and G. M. Hale, Nucl. Fusion, **32**, 611-631 (1992).
- [10] H. Matsuura, et al., J. Plasma Fusion Res. **9**, 48-53 (2010).
- [11] M. Drog and O. Schwerer, Production of monoenergetic neutrons between 0.1 and 23 MeV: neutron energies and cross-sections, Handbook of Nuclear Activation Data (Vienna: IAEA) STI/DOC/10/273, ISBN 92-0-135087-2 (1987).
- [12] John D. Gaffey, Jr., J. Plasma Phys. **16**, 149-169 (1976).
- [13] M. E. Swan, et al., Proceedings of the 22nd IEEE / NPSS symposium on Fusion Engineering, Albuquerque, NM, June 17-21, 1 (2007).
- [14] K. Okada, et al., 32nd EPS Conference on Plasma Phys. Tarragona, 27 June - 1 July 2005 ECA Vol.29C, P-4.096 (2005).
- [15] Y. Nagaya, et al., JAERI 1348 (2005).
- [16] K. Shibata, et al., J. Nucl. Sci. Technol. **48**, 1–30 (2011).
- [17] J. Källne, et al., Rev. Sci. Instrum. **68**, 581 (1997).

# 国際単位系 (SI)

表1. SI 基本単位

基本量	SI 基本単位	
	名称	記号
長さ	メートル	m
質量	キログラム	kg
時間	秒	s
電流	アンペア	A
熱力学温度	ケルビン	K
物質량	モル	mol
光度	カンデラ	cd

表2. 基本単位を用いて表されるSI組立単位の例

組立量	SI 組立単位	
	名称	記号
面積	平方メートル	m <sup>2</sup>
体積	立方メートル	m <sup>3</sup>
速度	メートル毎秒	m/s
加速度	メートル毎秒毎秒	m/s <sup>2</sup>
波数	毎メートル	m <sup>-1</sup>
密度, 質量密度	キログラム毎立方メートル	kg/m <sup>3</sup>
面積密度	キログラム毎平方メートル	kg/m <sup>2</sup>
比体積	立方メートル毎キログラム	m <sup>3</sup> /kg
電流密度	アンペア毎平方メートル	A/m <sup>2</sup>
磁界の強さ	アンペア毎メートル	A/m
量濃度 <sup>(a)</sup> , 濃度	モル毎立方メートル	mol/m <sup>3</sup>
質量濃度	キログラム毎立方メートル	kg/m <sup>3</sup>
輝度	カンデラ毎平方メートル	cd/m <sup>2</sup>
屈折率 <sup>(b)</sup>	(数字の)	1
比透磁率 <sup>(b)</sup>	(数字の)	1

(a) 量濃度 (amount concentration) は臨床化学の分野では物質濃度 (substance concentration) ともよばれる。  
 (b) これらは無次元量あるいは次元1をもつ量であるが、そのことを表す単位記号である数字の1は通常は表記しない。

表3. 固有の名称と記号で表されるSI組立単位

組立量	SI 組立単位			
	名称	記号	他のSI単位による表し方	SI基本単位による表し方
平面角	ラジアン <sup>(b)</sup>	rad	1 <sup>(b)</sup>	m/m
立体角	ステラジアン <sup>(b)</sup>	sr <sup>(e)</sup>	1 <sup>(b)</sup>	m <sup>2</sup> /m <sup>2</sup>
周波数	ヘルツ <sup>(d)</sup>	Hz		s <sup>-1</sup>
力	ニュートン	N		m kg s <sup>-2</sup>
圧力, 応力	パスカル	Pa	N/m <sup>2</sup>	m <sup>-1</sup> kg s <sup>-2</sup>
エネルギー, 仕事, 熱量	ジュール	J	N m	m <sup>2</sup> kg s <sup>-2</sup>
仕事率, 工率, 放射束	ワット	W	J/s	m <sup>2</sup> kg s <sup>-3</sup>
電荷, 電気量	クーロン	C		s A
電位差 (電圧), 起電力	ボルト	V	W/A	m <sup>2</sup> kg s <sup>-3</sup> A <sup>-1</sup>
静電容量	ファラド	F	C/V	m <sup>2</sup> kg <sup>-1</sup> s <sup>4</sup> A <sup>2</sup>
電気抵抗	オーム	Ω	V/A	m <sup>2</sup> kg s <sup>-3</sup> A <sup>-2</sup>
コンダクタンス	ジーメン	S	A/V	m <sup>2</sup> kg <sup>-1</sup> s <sup>3</sup> A <sup>2</sup>
磁束	ウェーバ	Wb	Vs	m <sup>2</sup> kg s <sup>-2</sup> A <sup>-1</sup>
磁束密度	テスラ	T	Wb/m <sup>2</sup>	kg s <sup>-2</sup> A <sup>-1</sup>
インダクタンス	ヘンリー	H	Wb/A	m <sup>2</sup> kg s <sup>-2</sup> A <sup>-2</sup>
セルシウス温度	セルシウス度 <sup>(e)</sup>	°C		K
光照射量	ルーメン	lm	cd sr <sup>(e)</sup>	cd
放射線量	グレイ	Gy	J/kg	m <sup>2</sup> s <sup>-2</sup>
放射性核種の放射能 <sup>(f)</sup>	ベクレル <sup>(d)</sup>	Bq		s <sup>-1</sup>
吸収線量, 比エネルギー分与, カーマ	グレイ	Gy	J/kg	m <sup>2</sup> s <sup>-2</sup>
線量当量, 周辺線量当量, 方向性線量当量, 個人線量当量	シーベルト <sup>(g)</sup>	Sv	J/kg	m <sup>2</sup> s <sup>-2</sup>
酸素活性化	カタール	kat		s <sup>-1</sup> mol

(a) SI接頭語は固有の名称と記号を持つ組立単位と組み合わせても使用できる。しかし接頭語を付した単位はもはやコヒーレントではない。  
 (b) ラジアンとステラジアンは数字の1に対する単位の特別な名称で、量についての情報をつたえるために使われる。実際には、使用する時には記号rad及びsrが用いられるが、習慣として組立単位としての記号である数字の1は明示されない。  
 (c) 測光学ではステラジアンという名称と記号srを単位の表し方の中に、そのまま維持している。  
 (d) ヘルツは周期現象についてのみ、ベクレルは放射性核種の統計的過程についてのみ使用される。  
 (e) セルシウス度はケルビンの特別な名称で、セルシウス温度を表すために使用される。セルシウス度とケルビンの単位の大きさは同一である。したがって、温度差や温度間隔を表す数値はどちらの単位で表しても同じである。  
 (f) 放射性核種の放射能 (activity referred to a radionuclide) は、しばしば誤った用語で"radioactivity"と記される。  
 (g) 単位シーベルト (PV, 2002, 70, 205) についてはCIPM勧告2 (CI-2002) を参照。

表4. 単位の中に固有の名称と記号を含むSI組立単位の例

組立量	SI 組立単位		
	名称	記号	SI 基本単位による表し方
粘力のモーメント	パスカル秒	Pa s	m <sup>-1</sup> kg s <sup>-1</sup>
表面張力	ニュートンメートル	N m	m <sup>2</sup> kg s <sup>-2</sup>
角加速度	ラジアン毎秒	rad/s	m m <sup>-1</sup> s <sup>-1</sup> = s <sup>-1</sup>
角加速度	ラジアン毎秒毎秒	rad/s <sup>2</sup>	m m <sup>-1</sup> s <sup>-2</sup> = s <sup>-2</sup>
熱流密度, 放射照度	ワット毎平方メートル	W/m <sup>2</sup>	kg s <sup>-3</sup>
熱容量, エントロピー	ジュール毎ケルビン	J/K	m <sup>2</sup> kg s <sup>-2</sup> K <sup>-1</sup>
比熱容量, 比エントロピー	ジュール毎キログラム毎ケルビン	J/(kg K)	m <sup>2</sup> s <sup>-2</sup> K <sup>-1</sup>
比エネルギー	ジュール毎キログラム	J/kg	m <sup>2</sup> s <sup>-2</sup>
熱伝導率	ワット毎メートル毎ケルビン	W/(m K)	m kg s <sup>-3</sup> K <sup>-1</sup>
体積エネルギー	ジュール毎立方メートル	J/m <sup>3</sup>	m <sup>-1</sup> kg s <sup>-2</sup>
電界の強さ	ボルト毎メートル	V/m	m kg s <sup>-3</sup> A <sup>-1</sup>
電荷密度	クーロン毎立方メートル	C/m <sup>3</sup>	m <sup>-3</sup> s A
電表面積	クーロン毎平方メートル	C/m <sup>2</sup>	m <sup>-2</sup> s A
電束密度, 電気変位	クーロン毎平方メートル	C/m <sup>2</sup>	m <sup>-2</sup> s A
誘電率	ファラド毎メートル	F/m	m <sup>3</sup> kg <sup>-1</sup> s <sup>4</sup> A <sup>2</sup>
透磁率	ヘンリー毎メートル	H/m	m kg s <sup>-2</sup> A <sup>-2</sup>
モルエネルギー	ジュール毎モル	J/mol	m <sup>2</sup> kg s <sup>-2</sup> mol <sup>-1</sup>
モルエントロピー, モル熱容量	ジュール毎モル毎ケルビン	J/(mol K)	m <sup>2</sup> kg s <sup>-2</sup> K <sup>-1</sup> mol <sup>-1</sup>
照射線量 (X線及びγ線)	クーロン毎キログラム	C/kg	kg <sup>-1</sup> s A
吸収線量率	グレイ毎秒	Gy/s	m <sup>2</sup> s <sup>-3</sup>
放射線強度	ワット毎ステラジアン	W/sr	m <sup>4</sup> m <sup>-2</sup> kg s <sup>-3</sup> = m <sup>2</sup> kg s <sup>-3</sup>
放射輝度	ワット毎平方メートル毎ステラジアン	W/(m <sup>2</sup> sr)	m <sup>2</sup> m <sup>-2</sup> kg s <sup>-3</sup> = kg s <sup>-3</sup>
酵素活性濃度	カタール毎立方メートル	kat/m <sup>3</sup>	m <sup>3</sup> s <sup>-1</sup> mol

表5. SI 接頭語

乗数	名称	記号	乗数	名称	記号
10 <sup>24</sup>	ヨタ	Y	10 <sup>1</sup>	デシ	d
10 <sup>21</sup>	ゼタ	Z	10 <sup>2</sup>	センチ	c
10 <sup>18</sup>	エクサ	E	10 <sup>3</sup>	ミリ	m
10 <sup>15</sup>	ペタ	P	10 <sup>6</sup>	マイクロ	μ
10 <sup>12</sup>	テラ	T	10 <sup>9</sup>	ナノ	n
10 <sup>9</sup>	ギガ	G	10 <sup>12</sup>	ピコ	p
10 <sup>6</sup>	メガ	M	10 <sup>-15</sup>	フェムト	f
10 <sup>3</sup>	キロ	k	10 <sup>-18</sup>	アト	a
10 <sup>2</sup>	ヘクト	h	10 <sup>-21</sup>	ゼプト	z
10 <sup>1</sup>	デカ	da	10 <sup>-24</sup>	ヨクト	y

表6. SIに属さないが、SIと併用される単位

名称	記号	SI単位による値
分	min	1 min=60 s
時	h	1 h=60 min=3600 s
日	d	1 d=24 h=86 400 s
度	°	1°=(π/180) rad
分	'	1'=(1/60)°=(π/10 800) rad
秒	"	1"=(1/60)'=(π/648 000) rad
ヘクタール	ha	1 ha=1 hm <sup>2</sup> =10 <sup>4</sup> m <sup>2</sup>
リットル	L, l	1 L=1 l=1 dm <sup>3</sup> =10 <sup>3</sup> cm <sup>3</sup> =10 <sup>-3</sup> m <sup>3</sup>
トン	t	1 t=10 <sup>3</sup> kg

表7. SIに属さないが、SIと併用される単位で、SI単位で表される数値が実験的に得られるもの

名称	記号	SI単位で表される数値
電子ボルト	eV	1 eV=1.602 176 53(14)×10 <sup>-19</sup> J
ダルトン	Da	1 Da=1.660 538 86(28)×10 <sup>-27</sup> kg
統一原子質量単位	u	1 u=1 Da
天文単位	ua	1 ua=1.495 978 706 91(6)×10 <sup>11</sup> m

表8. SIに属さないが、SIと併用されるその他の単位

名称	記号	SI単位で表される数値
バール	bar	1 bar=0.1MPa=100 kPa=10 <sup>5</sup> Pa
水銀柱ミリメートル	mmHg	1 mmHg=133.322Pa
オングストローム	Å	1 Å=0.1nm=100pm=10 <sup>-10</sup> m
海里	M	1 M=1852m
バイン	b	1 b=100fm <sup>2</sup> =(10 <sup>12</sup> cm <sup>2</sup> ) <sup>2</sup> =10 <sup>-28</sup> m <sup>2</sup>
ノット	kn	1 kn=(1852/3600)m/s
ネーパ	Np	SI単位との数値的關係は、 対数量の定義に依存。
ベレル	B	
デシベル	dB	

表9. 固有の名称をもつCGS組立単位

名称	記号	SI単位で表される数値
エルグ	erg	1 erg=10 <sup>-7</sup> J
ダイン	dyn	1 dyn=10 <sup>-5</sup> N
ポアズ	P	1 P=1 dyn s cm <sup>-2</sup> =0.1Pa s
ストークス	St	1 St=1cm <sup>2</sup> s <sup>-1</sup> =10 <sup>-4</sup> m <sup>2</sup> s <sup>-1</sup>
スチルブ	sb	1 sb=1cd cm <sup>-2</sup> =10 <sup>4</sup> cd m <sup>-2</sup>
フォト	ph	1 ph=1cd sr cm <sup>-2</sup> =10 <sup>4</sup> lx
ガリ	Gal	1 Gal=1cm s <sup>-2</sup> =10 <sup>-2</sup> ms <sup>-2</sup>
マクスウェル	Mx	1 Mx=1 G cm <sup>2</sup> =10 <sup>-8</sup> Wb
ガウス	G	1 G=1Mx cm <sup>-2</sup> =10 <sup>-4</sup> T
エルステッド <sup>(a)</sup>	Oe	1 Oe <sub>e</sub> =(10 <sup>3</sup> /4π)A m <sup>-1</sup>

(a) 3元系のCGS単位系とSIでは直接比較できないため、等号「△」は対応關係を示すものである。

表10. SIに属さないその他の単位の例

名称	記号	SI単位で表される数値
キュリー	Ci	1 Ci=3.7×10 <sup>10</sup> Bq
レントゲン	R	1 R=2.58×10 <sup>-4</sup> C/kg
ラド	rad	1 rad=1cGy=10 <sup>-2</sup> Gy
レム	rem	1 rem=1 cSv=10 <sup>-2</sup> Sv
ガンマ	γ	1 γ=1 nT=10 <sup>-9</sup> T
フェルミ	f	1 フェルミ=1 fm=10 <sup>-15</sup> m
メートル系カラット		1 メートル系カラット=0.2 g=2×10 <sup>-4</sup> kg
トル	Torr	1 Torr=(101 325/760) Pa
標準大気圧	atm	1 atm=101 325 Pa
カロリ	cal	1 cal=4.1858J (「15°C」カロリ), 4.1868J (「IT」カロリ), 4.184J (「熱化学」カロリ)
マイクロン	μ	1 μ=1μm=10 <sup>-6</sup> m

